Precision Measurement of the ^{7}Be Solar Neutrino Interaction Rate in Borexino

Richard Nigel Saldanha

A Dissertation

Presented to the Faculty

of Princeton University

in Candidacy for the Degree

of Doctor of Philosophy

Recommended for Acceptance

by the Department of

Physics

Advisor: Cristiano Galbiati

January 2012

Abstract

Solar neutrinos, since their first detection nearly forty years ago, have revealed valuable information regarding the source of energy production in the Sun, and have demonstrated that neutrino oscillations are well described by the Large Mixing Angle (LMA) oscillation parameters with matter interactions due to the Mikheyev-Smirnov-Wolfenstein (MSW) effect.

This thesis presents a precision measurement of the ^{7}Be solar neutrino interaction rate within Borexino, an underground liquid scintillator detector that is designed to measure solar neutrino interactions through neutrino-electron elastic scattering. The thesis includes a detailed description of the analysis techniques developed and used for this measurement as well as an evaluation of the relevant systematic uncertainties that affect the precision of the result.

The rate of neutrino-electron elastic scattering from 0.862 MeV ^{7}Be neutrinos is determined to be 45.4 ± 1.6 (stat) ± 1.5 (sys) counts/day/100 ton. Due to extensive detector calibrations and improved analysis methods, the systematic uncertainty in the interaction rate has been reduced by more than a factor of two from the previous evaluation. In the no-oscillation hypothesis, the interaction rate corresponds to a 0.862 MeV ^{7}Be electron neutrino flux of $\Phi_{\nu_e} = (2.75 \pm 0.13) \times 10^9$ cm^{-2} sec^{-1}.

Including the predicted neutrino flux from the Standard Solar Model yields an electron neutrino survival probability of $P_{ee} = 0.51 \pm 0.07$ and rules out the no-oscillation hypothesis at 5.1σ. The LMA-MSW neutrino oscillation model predicts a transition in the solar P_{ee} value between low (< 1 MeV) and high (> 10 MeV) energies which has not yet been experimentally confirmed. This result, in conjunction with the Standard Solar Model, represents the most precise measurement of the electron neutrino survival probability for solar neutrinos at sub-MeV energies.

Acknowledgements

The acknowledgements section is often the most widely read portion of a thesis, and since it is not often that one gets to formally recognize those who have greatly influenced them, I would like to take this opportunity to thank not only the people who have directly impacted this work, but also the individuals who have influenced me personally. Much like the rest of this thesis, these acknowledgements, despite their length, do not encompass nearly as much as they should, and for that I apologize.

First and foremost I would like to thank my advisor Cristiano Galbiati and also Frank Calaprice. They took me into the group when I had little research experience and even less knowledge of neutrinos or dark matter, and have been a constant source of advice and encouragement. Their guidance and support has allowed me to work fairly independently and to assume larger roles within the collaboration than is normally deemed appropriate for a graduate student. More importantly they have taught me, by example, that the only real requisite for research is hard work.

Over the years they have also put together an amazing research group here at Princeton. In particular I would like to acknowledge the two other graduate students who have been with me since the start, Alvaro Chavarria and Ben Loer. Having spent many long hours together writing analysis memos, preparing last minute presentations for collaboration meetings and running "mass process cycles", I can confidently say that they are amongst the most talented and fun colleagues I have worked with, and almost all of the analysis techniques I know have been learnt while working with them. I must also thank Alex Wright, to whom a significant portion of this thesis owes its existence. His scrupulousness regarding every detail has made this analysis much stronger and I am grateful for his constant encouragement to persevere with the work, despite pressure from various quarters.

In addition to Alvaro and Ben, I also thank my other office-mates, Pablo Mosteiro and Jingke Xu, and our frequent visitor Allan Nelson. Our daily discussions on soccer,

religion, music, tennis, Apple, videos on the internet and many other topics (most too inappropriate to mention here) often lifted the tedium and ensured that there has never been a dull day at work. I am also grateful to the other members of the group who have contributed to the convivial work environment: Kevin McCarty, Ferenc Dalnoki-Veress, Ernst de Haas, Peter Meyers (whose careful reading of this thesis has greatly improved its clarity), Charles Cao, Jason Brodsky and Emily Lebsack. A special thanks goes to Helen Ju, our group secretary, who works tirelessly to book trips, file reimbursements and keep the group functioning, while still managing to remember everyones birthday and refill the jar of chocolates.

Working on Borexino has involved frequent trips to Italy and my stays have been greatly enhanced by the many wonderful people I have met there. I would specifically like to thank Aldo Ianni for his friendliness and patience in helping me understand various subtleties regarding solar neutrinos, Andrea Ianni for looking after us during our first summer and introducing me to arrosticini, Luca Grandi who has been a great friend both in Italy and Princeton, Alessandro Razeto for his hospitality and continuous computing support, Margherita Buizza Avanzini and Alessandra Re for showing me around Milan (especially the thermal baths) and Chiara Ghiano for being the best neighbour one could hope for in Assergi. In addition to the people mentioned above, our colleagues from other American groups: Amanda Lund, Steve Hardy and Szymon Manecki, have made the summers I spent in Italy some of the most memorable times of graduate school. I would also like to thank the many people in the Borexino collaboration with whom I have worked and had several lively discussions: Andrea Pocar, Laura Cadonati, Gioacchino Ranucci, Gemma Testera, Livia Ludhova, Barbara Caccianiga, Oleg Smirnov and many others. During the five years that I have been a part of the collaboration, there has rarely been a dull moment.

My time in Princeton has been immensely enriched by the friends I have made in graduate school. I would like to specifically thank my roommates Alex Dahlen, Lucas

v

Parker and Silviu Pufu, as well as my extended roommates Tiberiu Tesileanu, XinXin Du and John Appel for the fun times we had skiing, playing Rock Band, apple picking, ice skating and deciding where to eat. I would also like to thank Joshua Ruderman, Siddharth Parameswaran, Colin Parker, Arijeet Pal, Anand Murugan, Justin Brown and many others who participated in the GC party, turkey gutting, Florida road trip, all-you-can-eat sushi dinners, Italian car crash and Friday Beer. To all my teammates from soccer, volleyball, handball, wallyball, kickball and softball, we may not have won anything[1], but it was always a lot of fun. I owe a special debt of gratitude to Emily Grace, who has made this last year wonderful and whose awesome company on "lazy Saturdays" kept me sane during the many months spent writing this thesis.

I would also like to acknowledge my friends and family outside Princeton who have supported me over the years. There are too many to mention, but I would like to thank Vidish Nahar and Bheeshm Chaudhary for our memorable annual vacations that were a welcome break from the routine of graduate school.

Finally I would like to thank my parents, grand parents and brother, without whom none of this would have been possible. Their love and encouragement through-out the years has been a constant source of strength and I shall always be grateful for everything that they have done for me. This thesis is dedicated to them.

---

[1]This changed spectacularly when we became the ISAP World Cup champions just three days before this thesis was submitted !

Contents

Chapter 1

Introduction to Solar Neutrinos

1.1 Neutrinos

Neutrinos are one of the most interesting fundamental particles. First postulated by Wolfgang Pauli in 1930 so as to conserve energy and spin angular momentum in β decays, the neutrino was directly detected in 1956 by Reines and Cowan, a result which eventually lead to the Nobel Prize. Since then neutrinos have been the subject of numerous theoretical and experimental studies and have influenced many fields of research including fundamental particle physics, cosmology, astrophysics and geology. In this chapter we will briefly describe some of the known properties of neutrinos before discussing solar neutrinos in detail.

Neutrinos are fundamental, neutral, spin 1/2 particles. They are not influenced by either the strong or electromagnetic force and due to their small masses are mostly unaffected by gravity. The only force through which neutrinos interact is the weak nuclear force, whose small interaction strength makes neutrinos extremely difficult to detect.

Neutrinos come in three distinct flavors. Each flavor corresponds to one of the charged leptons and they are referred to as electron (ν_e), muon (ν_μ), and tau (ν_τ) neu-

trinos. The number of active neutrino flavors has been precisely determined through measurements of the Z boson decay width (2.984 ± 0.008 [1]) though this does not rule out the possibility of additional, sterile, neutrino flavors. The current best limit for the total number of neutrino flavors comes from cosmological constraints (4.56 ± 0.75 [2]) which indicates a slight preference for an additional sterile neutrino, but is consistent with three active neutrinos at the 95% C.L.

One of the most interesting properties of neutrinos is the fact that the eigenstates of the weak interaction (ν_e, ν_μ and ν_τ) do not coincide with the mass eigenstates (ν_1, ν_2, and ν_3). This mismatch between the basis states leads to the phenomenon of neutrino oscillations, in which neutrinos are observed to change flavors as they propagate between weak interactions. Neutrino oscillations, which are described in detail in a later section of this chapter, have been observed by numerous independent experiments, confirming that neutrinos have a small, but non-zero, mass. While neutrino oscillation experiments can obtain information about the spacing between the mass eigenstates, there are currently only limits on the absolute values of the masses. The current best limits on the effective[1] mass of the different neutrino flavors are $m_{\nu_e} < 2.2$ eV, $m_{\nu_\mu} < 190$ keV and $m_{\nu_\tau} < 18.2$ MeV [3]. More stringent limits on the sum of all the neutrino masses can be obtained from cosmological constraints: $\sum m_{\nu_i} < 0.58$ eV (95% C.L.) [4], and the upcoming tritium β decay experiment KATRIN [5] aims to reach a sensitivity of 0.2 eV for the electron neutrino effective mass. We note that given the known mass-squared differences from oscillation experiments (see Table 1.3), we can place a lower bound on the mass of the heaviest (m_{ν_H}), and intermediate (m_{ν_I}), neutrino mass eigenstates of approximately $m_{\nu_H} > 0.05$ eV and $m_{\nu_I} > 0.009$ eV.

---

[1]The flavor states are linear superpositions of the true mass eigenstates

1.2   Solar Neutrinos

Solar neutrinos are an invaluable tool for studying both stellar astrophysics as well as particle physics. The Sun, with its close proximity to the Earth, provides us with an opportunity to study stellar evolution with a precision that can not be obtained with other stars. In addition to the vast information that can be learnt from the light emitted by the photosphere, neutrinos give us a unique perspective on the interactions that take place in the solar core. Unlike the energy from photons, which takes more than 10,000 years to travel from the core to the surface, neutrinos escape in a matter of seconds, carrying valuable information about the nuclear reactions that fuel the Sun. To quote John Bahcall, a pioneer in the field of solar neutrino physics: "Only neutrinos, with their extremely small interaction cross sections, can enable us to see into the interior of a star."

Solar neutrinos have also provided valuable information on the quantum mechanical phenomenon of neutrino oscillations. At the time the first solar neutrinos were detected, neutrinos were thought to be massless and the idea of neutrino oscillations had only recently been proposed. The field of solar neutrinos has since come a long way with multiple detectors now having measured solar neutrinos originating from different fusion reactions, all confirming neutrino oscillations. While several neutrino species[2] still remain to be detected, one of the driving goals for the current and future set of solar neutrino detectors is to study neutrino interactions with matter. The high density of the solar core combined with the wide range of solar neutrino energies gives us a unique opportunity to study the impact of matter on the effective neutrino oscillation parameters. In the remainder of this chapter we will describe, in some detail, the physics relevant to the production and propagation of solar neutrinos which will later allow us to use the measurement of the ^{7}Be neutrino interaction rate presented in this thesis to further our understanding of solar and neutrino physics.

---

[2]A neutrino species here refers to neutrinos produced in a given nuclear reaction

1.3 Solar Neutrino Production

We know from various pieces of geological and astronomical evidence that the Sun has been shining for several billion years. The only source of energy that can provide the required amount of energy, over such a long period of time, is nuclear fusion. The Sun shines by converting protons (hydrogen) in to α particles (helium). During this process, several neutrinos are produced that are collectively referred to as solar neutrinos. The overall fusion reaction can be summarized as:

$$4p \rightarrow {}^{4}\text{He} + 2e^{+} + 2\nu_e \tag{1.1}$$

The total energy released in the above reaction is roughly 26.73 MeV, of which, on average, only about 0.6 MeV is carried away by neutrinos [6]. The mechanism for nuclear fusion in stars was originally proposed independently by Carl von Weizsäcker [7] and Hans Bethe (in his seminal paper *Energy Production in Stars* [8]). In this section we will briefly describe some of the critical nuclear reactions and their relevance to solar neutrinos. The subject is comprehensively reviewed by Bahcall in [6].

1.3.1 *pp* Chain

In stars the size of our Sun, the principal nuclear reactions by which hydrogen is converted to helium are collectively called the proton-proton (*pp*) chain. The *pp* chain (shown in Figure 1.1) has five different neutrino-producing branches, with each neutrino generally referred to by the name of the parent nuclide. The spectra for the different neutrino species are shown in Figure 1.2.

The chain begins with the fusion of two protons to form deuteron:

$$p + p \rightarrow {}^{2}\text{H} + e^{+} + \nu_e \tag{1.2}$$

$$p + p \rightarrow {}^2H + e^+ + \nu_e \qquad\qquad p + e + p \rightarrow {}^2H + \nu_e$$

99.8%   0.2%

$${}^2H + p \rightarrow {}^3He + \gamma$$

83.3% 10^{-5} %

$${}^3He + {}^3He \rightarrow {}^4He + 2p \qquad\qquad {}^3He + p \rightarrow {}^4He + e^+ + \nu_e$$

16.7%

$${}^3He + {}^4He \rightarrow {}^7Be + \gamma$$

99.9%   0.1%

$${}^7Be + e^- \rightarrow {}^7Li + \nu_e \qquad\qquad {}^7Be + p \rightarrow {}^8B + \gamma$$

$${}^7Li + p \rightarrow {}^4He + {}^4He \qquad\qquad {}^8B \rightarrow {}^8Be^* + e^+ + \nu_e$$

$${}^8Be^* \rightarrow {}^4He + {}^4He$$
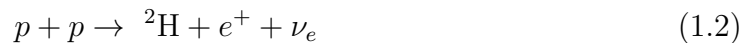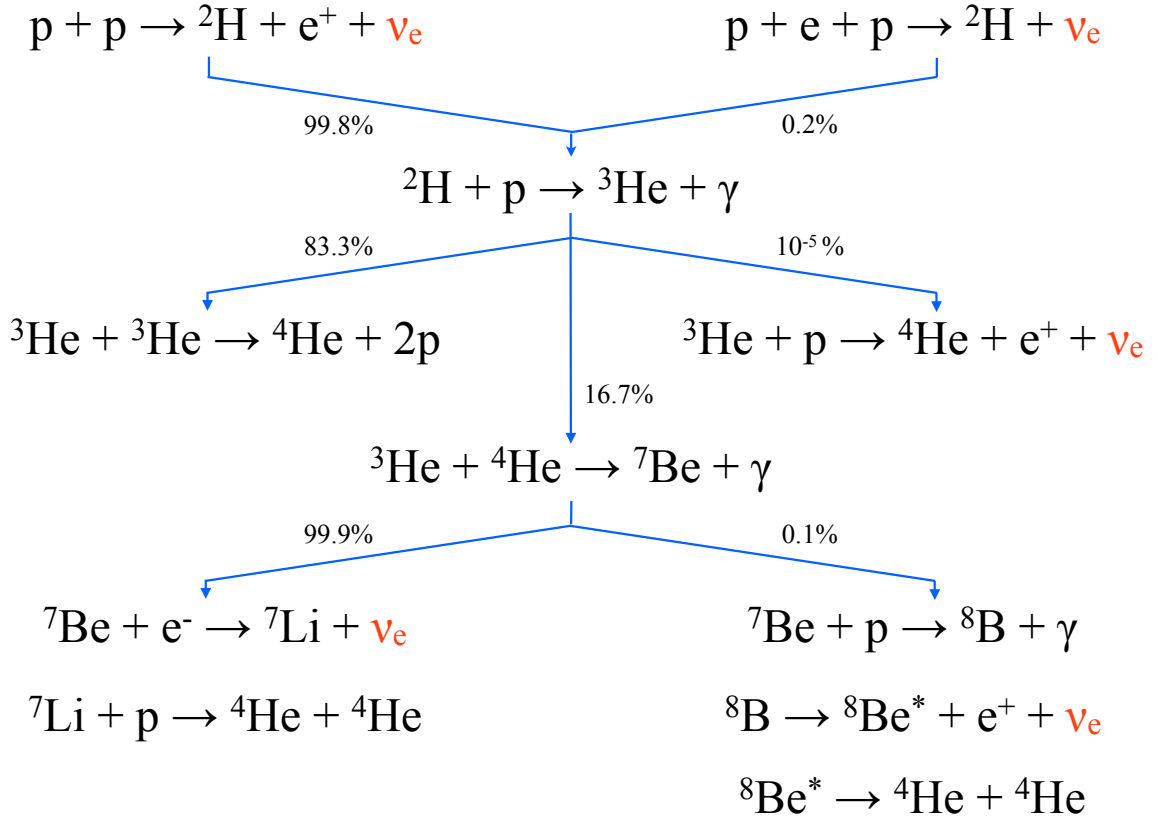
Figure 1.1: Diagrammatic representation of the *pp* chain. Neutrinos produced during the reactions are highlighted in red. The branching fractions are taken from [9].

The conversion of a proton into a neutron takes place through the weak interaction and hence the reaction rate is slow. The emitted neutrino, known as the *pp* neutrino has a continuous spectrum that extends up to an end point of 0.420 MeV.

There is an alternative production mechanism for deuteron:

$$p + e^- + p \rightarrow {}^2H + \nu_e \tag{1.3}$$

This reaction involves the interaction of three particles and is therefore disfavored, by roughly a factor of 400, with respect to the above *pp* interaction. Since there are only two final products, the energy of the *pep* neutrino is fixed ($E_\nu = 1.422$ MeV).
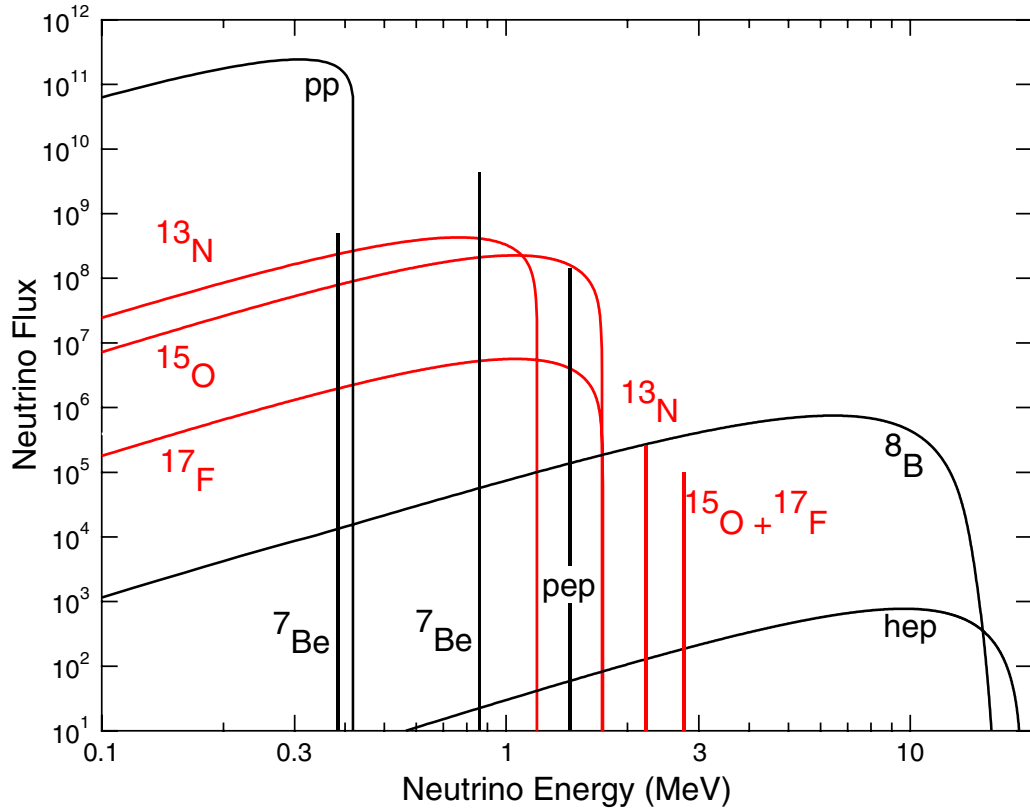
Figure 1.2: Neutrino energy spectra for the different species. Continuous spectra are shown in units of $cm^{-2}sec^{-1} MeV^{-1}$ while line fluxes are in $cm^{-2}sec^{-1}$. Neutrinos originating from the *pp* chain are shown in black while neutrinos from the CNO cycle are shown in red. Flux values are based on an older SSM (see Table 1.2 for the most recent SSM predictions) but the differences are minor. Figure taken from [9].

In the next step the deuteron captures a proton to form ^{3}He:

$$^2\text{H} + p \rightarrow\ ^3\text{He} + \gamma \tag{1.4}$$

This step takes place quickly and produces no neutrinos. The fast rate of this reaction ensures that the concentration of deuteron in the Sun is never high enough for the fusion of two deuterons (directly into ^{4}He) to be feasible.

There are three different possibilities for the ^{3}He nucleus produced above. The first, and main branch ($\sim 85\%$), involves the fusion of two ^{3}He nuclei to form helium,

thereby terminating the *pp* chain:

$$^3\text{He} +^3 \text{He} \rightarrow\ ^4\text{He} + 2p \qquad (1.5)$$

The second possibility, which has a branching ratio of about 15% and is of much greater interest for solar neutrino experiments, is the production of ^{7}Be:

$$^3\text{He} +^4 \text{He} \rightarrow\ ^7\text{Be} + \gamma \qquad (1.6)$$

Finally there is the rare $(10^{-5}\%)$ weak interaction:

$$^3\text{He} + p \rightarrow\ ^4\text{He} + e^+ + \nu_e \qquad (1.7)$$

The *hep* neutrino produced from this interaction has the highest maximum energy (18.77 MeV) of all the solar neutrinos, but it has yet to be observed due to its low flux. This interaction also terminates the *pp* chain.

For the case in which ^{7}Be is produced, the chain can be extended in two possible ways. The dominant (99.9%) mechanism is for ^{7}Be to capture an electron, producing the ^{7}Be neutrino (which is the focus of this thesis):

$$^7\text{Be} + e^- \rightarrow\ ^7\text{Li} + \nu_e \qquad (1.8)$$

$$^7\text{Li} + p \rightarrow\ ^4\text{He} + ^4\text{He} \qquad (1.9)$$

The ^{7}Be neutrino is monoenergetic, though the neutrino can have two different energies depending on the excitation level of the daughter ^{7}Li nucleus. In 89.6% of the cases ^{7}Li is produced in the ground state leading to a 0.862 MeV ^{7}Be neutrino, while the rest of the time the emitted neutrino has an energy of 0.384 MeV.

The other possibility for the ^{7}Be nucleus, though rare (0.1%), is to interact with a proton to form ^{8}B:

$$^7\text{Be} + p \rightarrow\ ^8\text{B} + \gamma \tag{1.10}$$

$$^8\text{B} \rightarrow\ ^8\text{Be}^* + e^+ + \nu_e \tag{1.11}$$

$$^8\text{Be}^* \rightarrow\ ^4\text{He} + ^4\text{He} \tag{1.12}$$

The ^{8}B neutrino has an end point energy of roughly 16 MeV and has been detected by multiple solar neutrino experiments due to its higher energy and non-negligible flux.

While all of the pp chain neutrinos have been jointly detected by radiochemical means, to date only ^{8}B and ^{7}Be neutrinos have been spectrally measured (a brief discussion of previous solar neutrino results is given at the end of this thesis in Section 7.4). An analysis is currently underway by the Borexino collaboration to measure the pep neutrino interaction rate and several experiments in the near future (XMASS [10], CLEAN [11], SNO+ [12], LENA [13], LENS [14]) aim to make measurements of the pp and pep solar neutrinos.

1.3.2 CNO Cycle

In stars larger than the Sun, that have higher core temperatures, the dominant mode of fusion takes place through the CNO cycle. In these reactions, the fusion of protons takes place with the aid of ^{12}C, the most abundant heavy isotope in stars. The contribution of the CNO cycle to the total solar energy is predicted to be only about 1% [9], with the remainder coming from the pp chain.

The interactions corresponding to the CNO cycle are shown in Figure 1.3. There are several other side chains that are only relevant at higher temperatures than that at the solar interior ($\sim 1.6 \times 10^7$ K). In regions of the Sun with temperatures below

$^{12}\text{C} + \text{p} \rightarrow {}^{13}\text{N} + \gamma$ $\longrightarrow$ $^{13}\text{N} \rightarrow {}^{13}\text{C} + \text{e}^+ + \nu_e$

$^{15}\text{N} + \text{p} \rightarrow {}^{12}\text{C} + {}^4\text{He}$ $\qquad$ $^{13}\text{C} + \text{p} \rightarrow {}^{14}\text{N} + \gamma$

99.95%

$^{15}\text{O} \rightarrow {}^{15}\text{N} + \text{e}^+ + \nu_e$ $\longleftarrow$ $^{14}\text{N} + \text{p} \rightarrow {}^{15}\text{O} + \gamma$

0.05%

$^{15}\text{N} + \text{p} \rightarrow {}^{16}\text{O} + \gamma$ $\qquad$ $^{17}\text{O} + \text{p} \rightarrow {}^{14}\text{N} + {}^4\text{He}$

$^{16}\text{O} + \text{p} \rightarrow {}^{17}\text{F} + \gamma$ $\dashrightarrow$ $^{17}\text{F} \rightarrow {}^{17}\text{O} + \text{e}^+ + \nu_e$
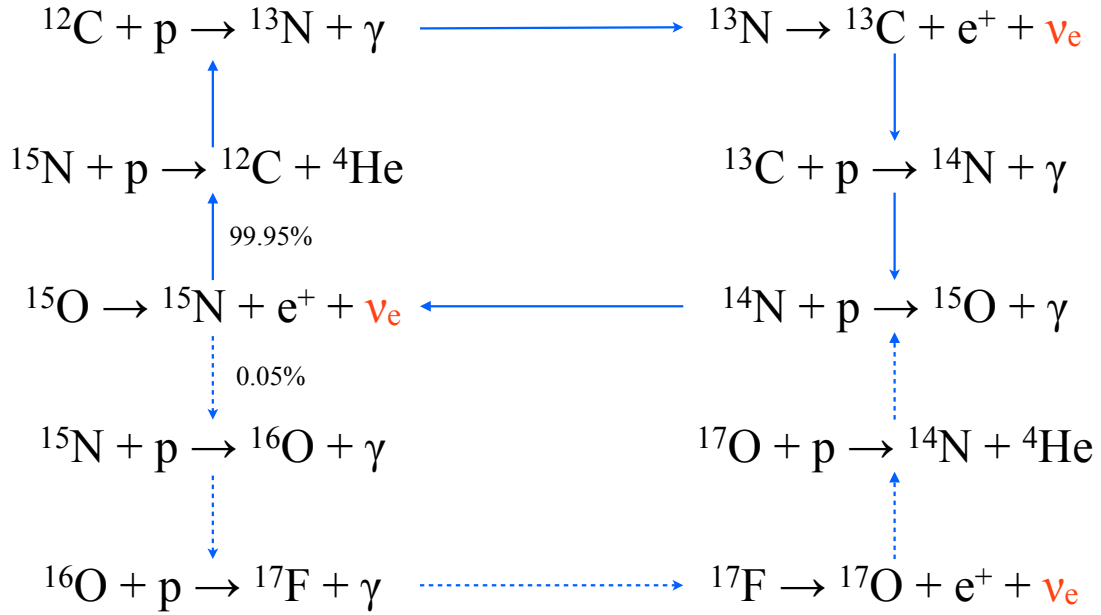
Figure 1.3: Diagrammatic representation of the CNO cycle. Neutrinos produced during the reactions are highlighted in red. The branching fraction for the lower cycle is taken from [9].

10^7 K, the ^{14}N remains largely unburned and some ^{12}C is converted to ^{14}N, leading to a slightly lower ^{15}O neutrino flux compared to the ^{13}N neutrinos. Due to the small probability for ^{15}N to convert to ^{16}O (the lower cycle in Figure 1.3), the flux of ^{17}F neutrinos is significantly smaller.

We note that in addition to the neutrinos produced in the β^+ decays, there are also competing electron capture processes for ^{13}N, ^{15}O and ^{17}F, that produce monoenergetic neutrinos (see Figure 1.2). However the flux ratio of the neutrinos produced by electron capture to β^+ decay is less than 8×10^{-4} [15].

To date there have been no direct measurements of neutrino fluxes from the CNO cycle. Such a measurement would be the first direct evidence of the nuclear processes that are believed to dominate in larger stars and may also help resolve the solar metallicity problem (see Section 1.3.3.2).

1.3.3 Neutrino Fluxes

1.3.3.1 Model Independent Predictions

Without going into the details of the structure and composition of the Sun, there are some basic predictions we can make regarding the neutrino flux on Earth. Using Eq. 1.1 we see that two neutrinos are created during the creation of every helium nucleus and each reaction produces $Q = 26.73$ MeV. If we ignore the energy carried away by the neutrinos themselves, then given the luminosity of the Sun, the total expected flux of solar neutrinos at Earth is:

$$\Phi \geq 2 \times \frac{K_\odot}{Q} \tag{1.13}$$

$$\geq 6.4 \times 10^{10} \text{ cm}^{-2} \text{ sec}^{-1} \tag{1.14}$$

where the solar constant $K_\odot$ is the mean solar photon flux on Earth (see Table 1.1). We note that the inequality arises from assuming that the energy of the neutrinos is negligible. If we assume that the fusion reactions belonging to the pp chain and CNO cycle are indeed the reactions that power the Sun, then by taking into account the neutrino spectra we can place a strict equality relating the weighted sum of the total neutrino fluxes to the solar luminosity. This is referred to as the "luminosity constraint" [16].

We can also place some general limits on the pp chain neutrinos by noticing (see Figure 1.1) that the ^{7}Be, ^{8}B and hep neutrinos all require the production of a ^{3}He nucleus, which is created following the pp and pep reactions. Thus, we have:

$$\Phi_{pp} + \Phi_{pep} \geq \Phi_{Be} + \Phi_B + \Phi_{hep} \tag{1.15}$$

Solar Parameter	Value
Luminosity ($L_\odot$)	3.8418×10^{26} W
	2.3977×10^{39} MeV/sec
Radius ($R_\odot$)	6.9598×10^{10} cm
Mass ($M_\odot$)	1.9884×10^{33} g
Core Temperature	$\sim 1.55 \times 10^7$ K
	~ 1.34 keV
Core Density	~ 153 g/cm^3
Surface Heavy Metal to Hydrogen Ratio (Z/X)	0.0229 (GS98)
	0.0178 (AGSS09)
Mean Distance to Earth (AU)	1.49598×10^{13} cm
Solar Constant ($K_\odot = L_\odot/4\pi(\text{AU})^2$)	8.5339×10^{11} MeV/cm^2/sec

Table 1.1: Relevant solar parameters of the Sun as well as the Sun-Earth system. The solar constant is defined here as the mean solar photon flux on Earth. Values taken from [9,17,18].

1.3.3.2 Standard Solar Model

In order to make precision estimates of the individual solar neutrino fluxes, we must calculate the rate of the corresponding nuclear reaction. For any two reactants, A and B, the rate of the reaction per unit volume, R_{AB}, can be written as:

$$R_{AB} = \frac{n_A n_B \langle \sigma v \rangle_{AB}}{1 + \delta_{AB}} \tag{1.16}$$

where n_X is the number density of species X, and $\langle \sigma v \rangle_{AB}$ is the product of the interaction cross section $\sigma(E)$ with the relative velocity of the two particles v, averaged over the velocity distribution of the particles. The Kronecker delta function in the denominator corrects for over counting when the particles A and B are identical.

Given the high densities and temperatures in the solar interior, the velocity distribution of the interacting particles follow a Maxwell-Boltzmann distribution. Converting to energy (E) we obtain [18]:

$$\langle \sigma v \rangle_{AB} = \left(\frac{8}{\pi \mu (k_B T)^3} \right)^{1/2} \int \sigma(E) E \exp \left(-\frac{E}{K_B T} \right) dE \tag{1.17}$$

where E is the center-of-mass kinetic energy, μ is the reduced mass, k_B is the Boltz-

mann constant, and T is the temperature. The energy distribution peaks at $E = k_B T$ which at the core of the Sun ($T \sim 1.55 \times 10^7$ K) is about 1.3 keV.

The particles at the core of the Sun are in the form of a plasma of ionized atoms. In order for nuclear fusion to take place the particles must first overcome the repulsive Coulomb barrier between them. The typical height of the Coulomb barrier is much higher than the thermal energy of the particles. For example, the Coulomb barrier between two protons is on the order of 550 keV [18], two orders of magnitude larger than the thermal energy at the core. Thus nuclear fusion is only possible due to quantum mechanical tunneling through the potential barrier.

The cross section term is usually factored as:

$$\sigma(E) = \frac{1}{E} \exp(-2\pi\eta) S(E) \tag{1.18}$$

where $\exp(-2\pi\eta)$ with $\eta \equiv Z_A Z_B (e^2/\hbar v)$ is the approximate tunneling probability, known as the Gamow factor, and $S(E)$ is referred to as the astrophysical S-factor. The function $S(E)$ contains all the nuclear effects and, for non-resonant reactions, is a smooth, slowly varying function of energy. This leads to:

$$\langle \sigma v \rangle_{AB} = \left(\frac{8}{\pi \mu (k_B T)^3} \right)^{1/2} \int S(E) \exp \left(-\frac{E}{K_B T} - 2\pi\eta \right) dE \tag{1.19}$$

The functional form of the exponential function in the integrand is shown in Figure 1.4. The combination of the Maxwell-Boltzmann tail and the penetration factor leads to a narrow peak (called the Gamow peak) in the overlap region, centered at:

$$E_0 = \left[\frac{\mu}{2} (\pi \alpha Z_A Z_B k_B T)^2 \right]^{1/3} \tag{1.20}$$

where α is the fine structure constant. It is in this narrow energy window that the nuclear fusion reactions take place. For most of the important interactions in the
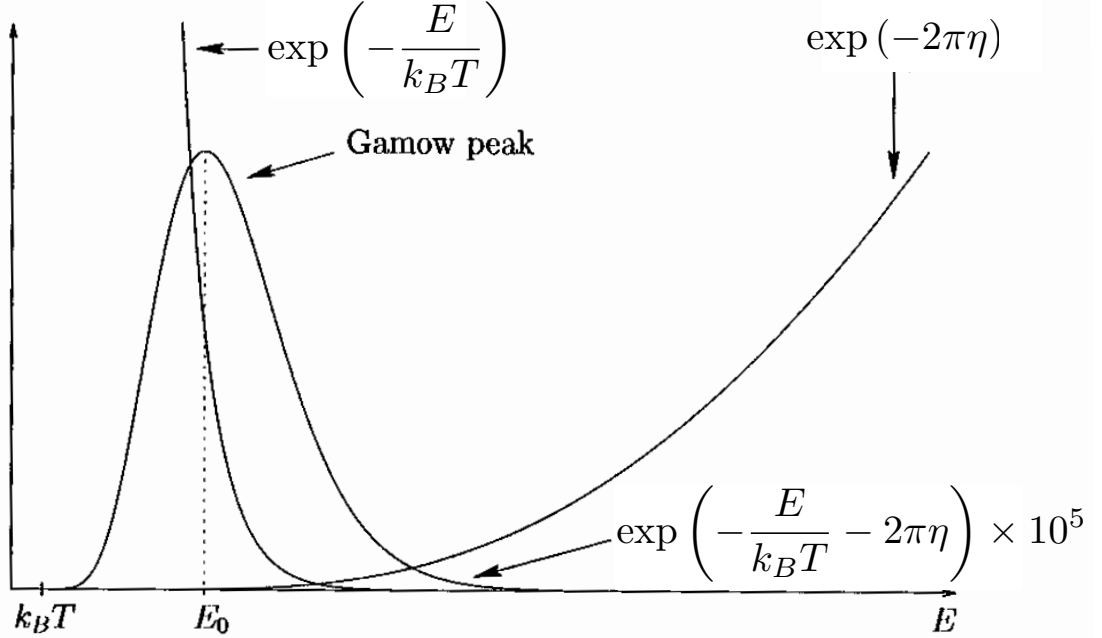
Figure 1.4: Schematic representation of the Gamow peak formed by the product of the Maxwell-Boltzmann distribution tail ($\propto \exp(-\frac{E}{k_B T})$) and the tunnelling probability ($\propto exp(-2\pi\eta)$). The Gamow peak has been enlarged by a factor of 10^5 for visibility. Figure taken from [18].

Sun, E_0 lies between 6 to 10 keV [6]. Since the astrophysical S-factor varies only slowly with energy, it can be replaced with its value at E_0. The final result can be approximated as [6, 18]:

$$\langle \sigma v \rangle_{AB} \propto \frac{\sqrt{E_0/\mu}}{k_B T} S(E_0) \exp\left(-3\frac{E_0}{k_B T}\right) \tag{1.21}$$

Combining Eqns. 1.16 and 1.21, we see that the production rate of solar neutrinos depends on the number density of the corresponding parent nuclides, the details of the nuclear interaction cross section S(E), and the temperature. These parameters can be calculated for each of the nuclear reactions using the Standard Solar Model (SSM).

A SSM is a solar model that is constructed with the best available physics and input data and is required to fit the current observations of the Sun such as the

luminosity, radius and heavy element abundance at the surface. Over the years, as the input data has grown and the computational power available has increased, the SSM has been constantly updated and improved. The inputs to the SSM can be divided into four main categories [6]:

- Nuclear Cross Sections

  The S-factor cannot be calculated theoretically and must be instead measured in the laboratory. Unfortunately, while the reaction rates are large at energies on the order of MeV, they are greatly suppressed by the Gamow penetration factor below $\sim$ 100 keV and become too small to measure. The standard practice is therefore to measure the cross section at as low energies as possible in the laboratory and extrapolate down to the relevant solar temperatures (a few keV). More than a decade following the original critical evaluation and summary of the pp chain and CNO cycle cross sections (Solar Fusion I [19]) a new revised set of recommended values was recently established, Solar Fusion II [9]. The largest effect of the new recommendations is the decrease in the predicted ^{8}B flux by 5% and an increase in the ^{13}N flux. For ^{7}Be, the uncertainty has increased from 6% to 7% [17, 20].

- Surface Heavy Element Abundance

  The initial ratio of heavy (heavier than helium) elements to hydrogen, Z/X, is a crucial input parameter to the solar model and is closely linked to the predicted neutrino fluxes. The present elemental abundances at the solar surface (determined by studying emission spectra across a wide range of wavelengths) are presumed to reflect the initial abundances and solar models are constrained to match the current observations. There are currently two competing values for the surface heavy metal to hydrogen abundance ratio. The first, referred to as GS98, gives a value on the solar surface of $Z/X = 0.0229$ while a later evaluation (AGSS09) estimates $Z/X = 0.0178$ due to a strong reduction in the CNO

and Ne abundances [17, 20]. The main differences between the high-metallicity (GS98) and low-metallicity (AGSS09) models comes from the latter using a 3D hydrodynamics model atmosphere, better selection of spectral lines and a detailed treatment of radiative transport. We note that while the models used in the more recent low-metallicity evaluation are deemed more accurate, they spoil the good agreement between the low-metallicity GS98 SSM and helioseismic measurements [17, 20].

- Radiative Opacity

  Most of the energy transport at the core of the Sun takes place through photon radiation. The radiative opacity depends on both the chemical composition (see above) and the modeling of complex atomic processes. These models are normally carried out using computer programs that include all the known effects from statistical mechanics and atomic physics. A brief summary of the models can be found in [6].

- Equation of State

  The relationship between the pressure and density, referred to as the equation of state, for material near the solar interior is close to that of a perfect gas, with the effects of radiation pressure and electron degeneracy included in the solar models. The uncertainties in the equation of state are small and have a minor effect on the predicted neutrino fluxes [6].

For the purposes of consistency, we have chosen the recent SSM by Serenelli, Haxton and Peña-Garay [17] to use as the reference SSM throughout this work. This solar model uses the latest Solar Fusion II [9] recommendations for the nuclear cross sections and is required to reproduce the current solar luminosity, radius and surface heavy metal to hydrogen abundance ratios as listed in Table 1.1. The predicted neutrino fluxes for both the high (GS98) and low (AGSS09) metallicity abundances are listed

in Table 1.2. Unless specifically mentioned, we have chosen, arbitrarily, to use the high-metallicity (GS98) fluxes as our standard reference.

The high and low metallicity predictions for the individual neutrino fluxes are compared graphically in Figure 1.5. As can be seen, only for the CNO neutrinos are the differences significant compared to the model uncertainties. Thus a precision measurement of the CNO neutrino flux could help resolve the solar metallicity problem.

ν Species	GS98	AGSS09
	Flux $[\mathrm{cm}^{-2}\ \mathrm{sec}^{-1}]$	
pp	$5.98 \times 10^{10}(1 \pm 0.006)$	$6.03 \times 10^{10}(1 \pm 0.006)$
pep	$1.44 \times 10^{8}(1 \pm 0.012)$	$1.47 \times 10^{8}(1 \pm 0.012)$
hep	$8.04 \times 10^{3}(1 \pm 0.30)$	$8.31 \times 10^{3}(1 \pm 0.30)$
$^{7}\mathrm{Be}$	$5.00 \times 10^{9}(1 \pm 0.07)$	$4.56 \times 10^{9}(1 \pm 0.07)$
$^{8}\mathrm{B}$	$5.58 \times 10^{6}(1 \pm 0.14)$	$4.59 \times 10^{6}(1 \pm 0.14)$
$^{13}\mathrm{N}$	$2.96 \times 10^{8}(1 \pm 0.14)$	$2.17 \times 10^{8}(1 \pm 0.14)$
$^{15}\mathrm{O}$	$2.23 \times 10^{8}(1 \pm 0.15)$	$1.56 \times 10^{8}(1 \pm 0.15)$
$^{17}\mathrm{F}$	$5.52 \times 10^{6}(1 \pm 0.17)$	$3.40 \times 10^{6}(1 \pm 0.16)$

Table 1.2: SSM [17] predicted neutrino fluxes for the high metallicity (GS98) and low metallicity (AGSS09) solar abundances. Unless specified, the high metallicity values will be used as reference for this work.
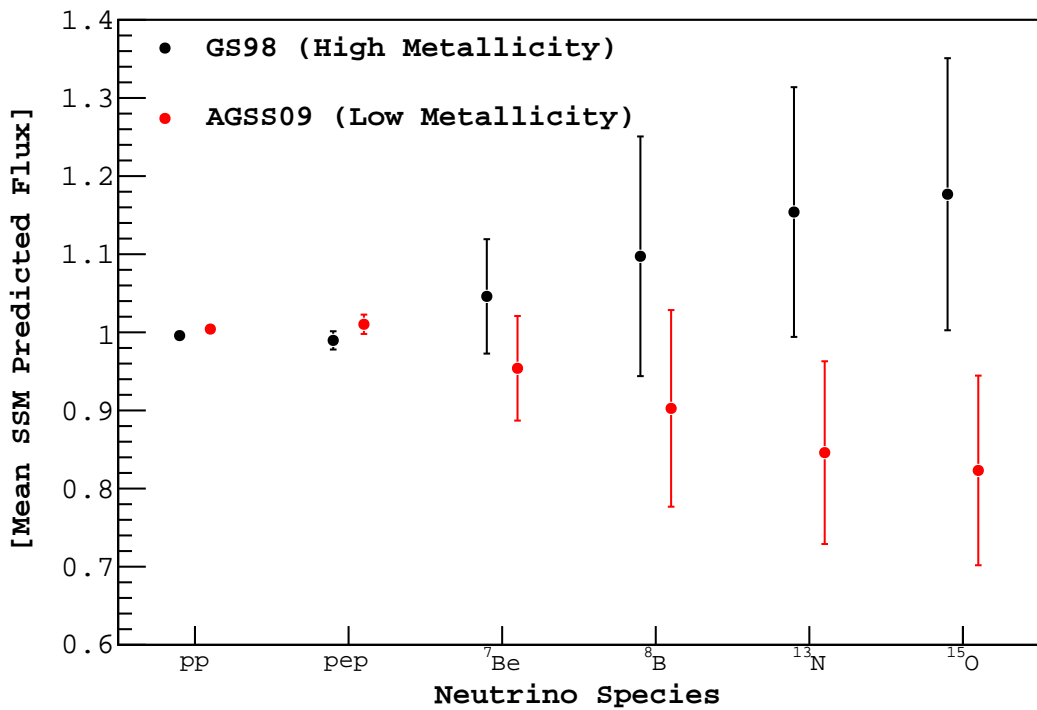
Figure 1.5: SSM predicted neutrino fluxes for the high (black) and low (red) metallicity scenarios [17]. The values (taken from Table 1.2) have been scaled to the mean value for each species.

1.4   Solar Neutrino Propagation

1.4.1   Neutrino Oscillations

The physics of neutrino oscillations describe how neutrinos created in a given flavor eigenstate can, at a later time, have a non-zero probability to be detected in a different flavor eigenstate. The theory of neutrino oscillations is fairly old, first proposed by Pontecorvo in the late 1950's [21–23], and there is a wide, and sometimes conflicting, set of formalisms describing the underlying physics. While a complete derivation of neutrino oscillations would require the use of the wave packet formalism or a field theoretical approach that includes the entanglement with other particles (during production) and the space-time localization of the detection process (for example see [24, 25]) in this section we will follow a simplified approach [1], that nevertheless obtains the correct neutrino oscillation probabilities.

We begin by taking into consideration the fact that the neutrino weak eigenstates do not coincide with the mass eigenstates. The weak eigenstates, $|\nu_\alpha\rangle$, are usually labelled by the corresponding lepton family ($\alpha = e, \mu, \tau$), while the mass eigenstates are labelled $|\nu_i\rangle$ where ($i = 1, 2, 3$). Transformations between the mass and weak eigenstates are described by the unitary Pontecorvo-Maki-Nakagawa-Sakata (PMNS) mixing matrix U:

$$|\nu_\alpha\rangle = \sum_i U_{\alpha i} |\nu_i\rangle \;\Leftrightarrow\; |\nu_i\rangle = \sum_\alpha U_{i\alpha}^\dagger |\nu_\alpha\rangle \tag{1.22}$$

where

$$U = \begin{bmatrix} U_{e1} & U_{e2} & U_{e3} \\ U_{\mu 1} & U_{\mu 2} & U_{\mu 3} \\ U_{\tau 1} & U_{\tau 2} & U_{\tau 3} \end{bmatrix} \tag{1.23}$$

Consider a neutrino produced during a weak interaction, such as a β decay. At the

position, $\mathbf{x} = 0$, and time, $t = 0$, of production, the neutrino will be in a weak eigenstate $|\nu_\alpha\rangle$:

$$|\nu\rangle\,(\mathbf{x} = 0, t = 0) = |\nu_\alpha\rangle \tag{1.24}$$

$$= \sum_i U_{\alpha i}\,|\nu_i\rangle \tag{1.25}$$

As time passes, the neutrino wavefunction will evolve under its free Hamiltonian, whose eigenstates are the mass eigenstates. We will assume a plane-wave solution for each of the neutrino eigenstates (which only accounts for the movement of the center of the corresponding wave packet):

$$|\nu\rangle\,(\mathbf{x}, t) = \sum_i U_{\alpha i} e^{-i(E_i t - \mathbf{p_i} \cdot \mathbf{x})}\,|\nu_i\rangle \tag{1.26}$$

$$= \sum_i U_{\alpha i} e^{-i(E_i t - p_i L)}\,|\nu_i\rangle \tag{1.27}$$

where E_i and $\mathbf{p_i} = p_i \hat{\mathbf{k}}$ are the energy and momentum of the corresponding mass eigenstate, $\mathbf{x} = L\hat{\mathbf{k}}$, and $\hat{\mathbf{k}}$ is the unit vector in the direction of the neutrino momentum. Note that we have not made the common, but questionable [26,27], assumption that the mass eigenstates have identical energy or momentum.

When the neutrino interacts with the detector, the probability for observing the

neutrino in the weak eigenstate $|\nu_\beta\rangle$ is then given by:

$$P(\nu_\alpha \to \nu_\beta) = |\langle \nu_\beta | \nu \rangle (\mathbf{x}, t)|^2 \tag{1.28}$$

$$= \left| \sum_i \sum_j \langle \nu_j | U_{j\beta}^\dagger U_{\alpha i} e^{-i(E_i t - p_i L)} | \nu_i \rangle \right|^2 \tag{1.29}$$

$$= \left| \sum_i U_{\alpha i} U_{\beta i}^* e^{-i(E_i t - p_i L)} \right|^2 \tag{1.30}$$

$$= \sum_i \sum_j U_{\alpha i} U_{\beta i}^* U_{\alpha j}^* U_{\beta j} e^{-i((E_i - E_j)t - (p_i - p_j)L))} \tag{1.31}$$

$$= \sum_i \sum_j |z_{\alpha\beta ij}| \cos\left((E_i - E_j)t - (p_i - p_j)L - arg(z_{\alpha\beta ij})\right) \tag{1.32}$$

where $z_{\alpha\beta ij} \equiv U_{\alpha i} U_{\beta i}^* U_{\alpha j}^* U_{\beta j}$. We can write the oscillatory term as:

$$(E_i - E_j)t - (p_i - p_j)L = (E_i - E_j)\left(t - \frac{E_i + E_j}{p_i + p_j}L\right) + \left(\frac{m_i^2 - m_j^2}{p_i + p_j}\right)L \tag{1.33}$$

As described in [28], the first term can be shown to be small by noting that the distance travelled by the neutrino is related to the time elapsed by:

$$L \sim \overline{v}t \equiv \frac{p_i + p_j}{E_i + E_j}t \tag{1.34}$$

where $\overline{v}$ describes an average wave packet velocity. Using this approximation we have

$$(E_i - E_j)t - (p_i - p_j)L \sim \frac{m_i^2 - m_j^2}{p_i + p_j}L \tag{1.35}$$

$$\equiv \frac{\Delta m_{ij}^2}{2\overline{p}}L \tag{1.36}$$

We can then write the transition probability as:

$$P(\nu_\alpha \to \nu_\beta) = \sum_i \sum_j |z_{\alpha\beta ij}| \cos\left(\frac{\Delta m_{ij}^2}{2\overline{p}}L - arg(z_{\alpha\beta ij})\right) \tag{1.37}$$

As can be seen from Eq. 1.37, a transition to a different flavor state can only take place if there is a non-zero mass difference between the mass eigenstates. Therefore, an observation of a transition between different neutrino flavor states indicates that at least one of the neutrino mass states has a different mass, which in turn implies that at least one of the neutrino masses is non-zero. Thus neutrino oscillations imply massive neutrinos.

Another interesting thing to note is that for antineutrinos, the relationship between the mass and flavor eigenstates is given by:

$$|\overline{\nu}_\alpha\rangle = \sum_i U^*_{\alpha i} |\overline{\nu}_i\rangle \tag{1.38}$$

Following the same derivation as for neutrinos, we obtain:

$$P(\overline{\nu}_\alpha \to \overline{\nu}_\beta) = \sum_i \sum_j |z_{\alpha\beta ij}| \cos\left(\frac{\Delta m^2_{ij}}{2\overline{p}}L + arg(z_{\alpha\beta ij})\right) \tag{1.39}$$

which is identical to the neutrino transition probability except for the change in the sign of the second oscillatory term $arg(z_{\alpha\beta ij})$. Thus, if the PMNS matrix contains complex terms, we have CP violation: $P(\nu_\alpha \to \nu_\beta) \neq P(\overline{\nu}_\alpha \to \overline{\nu}_\beta)$. Of course we still have $P(\nu_\alpha \to \nu_\beta) = P(\overline{\nu}_\beta \to \overline{\nu}_\alpha)$ as a consequence of CPT invariance.

1.4.1.1 Neutrino Oscillation Parameters

For three neutrino flavors, the PMNS matrix can be parameterized by three mixing angles and six phases. If neutrinos are Dirac particles, then there exists only one physical phase, commonly denoted as the CP violating Dirac phase (δ), while Majorana neutrinos have two additional phases (α_i). The most general mixing matrix can

be factored according to these angles and phases:

$$U = \begin{bmatrix} c_{12}c_{13} & s_{12}c_{13} & s_{13}e^{-i\delta} \\ -s_{12}c_{23}-c_{12}s_{23}s_{13}e^{i\delta} & c_{12}c_{23}-s_{12}s_{23}s_{13}e^{i\delta} & s_{23}c_{13} \\ s_{12}s_{23}-c_{12}c_{23}s_{13}e^{i\delta} & -c_{12}s_{23}-s_{12}c_{23}s_{13}e^{i\delta} & c_{23}c_{13} \end{bmatrix} \begin{bmatrix} e^{i\alpha_1/2} & 0 & 0 \\ 0 & e^{i\alpha_2/2} & 0 \\ 0 & 0 & 1 \end{bmatrix}$$

(1.40)

$$= \begin{bmatrix} 1 & 0 & 0 \\ 0 & c_{23} & s_{23} \\ 0 & -s_{23} & c_{23} \end{bmatrix} \begin{bmatrix} c_{13} & 0 & s_{13}e^{-i\delta} \\ 0 & 1 & 0 \\ -s_{13}e^{i\delta} & 0 & c_{13} \end{bmatrix} \begin{bmatrix} c_{12} & s_{12} & 0 \\ -s_{12} & c_{12} & 0 \\ 0 & 0 & 1 \end{bmatrix} \begin{bmatrix} e^{i\alpha_1/2} & 0 & 0 \\ 0 & e^{i\alpha_2/2} & 0 \\ 0 & 0 & 1 \end{bmatrix}$$

(1.41)

where $c_{ij} = \cos\theta_{ij}$, $s_{ij} = \sin\theta_{ij}$ and the phases α_i are meaningful only if the neutrino is a Majorana particle. The current best estimates for the mixing parameters are given in Table 1.3. For historical reasons the combination of values for Δm_{21}^2 and $\sin^2(2\theta_{12})$ are referred to as the Large Mixing Angle (LMA) solution. We note that there is currently no strong evidence for CP violation, so for the remainder of this chapter we will assume that the CP violating phases are small and that the PMNS matrix entries can be considered real.
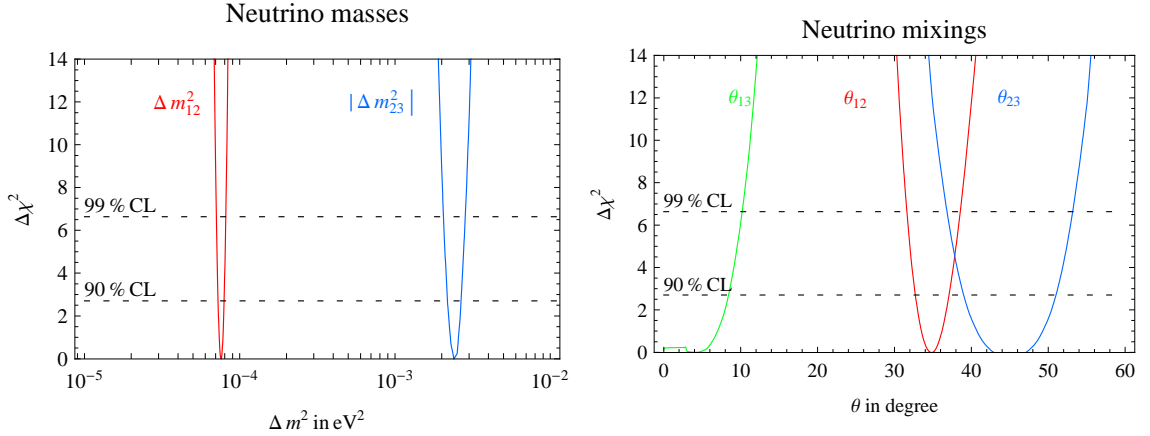

Figure 1.6: Diagrammatic representation of the current best estimates and uncertainties of the neutrino oscillation parameters. See Table 1.3 for exact values. Figure taken from [29]

Parameter	Value	
Δm^2_{21}	$(7.59 \pm 0.20) \times 10^{-5}$ eV	
$|\Delta m^2_{32}|$	$(2.43 \pm 0.13) \times 10^{-3}$ eV	
$\sin^2(2\theta_{12})$	0.87 ± 0.03	$(33° < \theta_{12} < 36°)$
$\sin^2(2\theta_{23})$	> 0.92	$(37° < \theta_{23} < 53°)$
$\sin^2(2\theta_{13})$	< 0.15 (90% CL)	$(0° < \theta_{13} < 11°)$

Table 1.3: Current best estimates for neutrino oscillation parameters taken from the 2010 Particle Data Group [1]. Note that the sign of Δm^2_{32} is not currently known and the limits are only on the absolute value. The third mass squared difference, Δm^2_{13}, is completely determined by the other two. The combination of values for Δm^2_{21} and $\sin^2(2\theta_{12})$ are historically referred to as the Large Mixing Angle (LMA) solution. See Figure 1.6 for a diagrammatic representation of the values and uncertainties.

1.4.1.2 Neutrino Oscillation Experiments

There are many neutrino experiments designed to measure the values of the different oscillation parameters (both the mass-squared differences as well as the mixing angles). The general strategy of most of these experiments is to measure the flux of the different neutrino flavors a certain distance away from a neutrino source with known energy, flux and flavor composition. For example, the KamLAND experiment studies the "disappearance" of electron anti-neutrinos from nuclear reactors while MiniBooNE searches for the "appearance" of electron (anti-)neutrinos in a muon (anti-)neutrino accelerator beam. The oscillation parameters that can be studied with a given experiment depend on the transition being probed as well as the energy of the neutrinos and the distance from the source (baseline).

Since solar neutrinos are all produced in the electron flavor eigenstate, the transition of interest to solar neutrino experiments is the probability of an electron neutrino being detected as a muon or tau neutrino. Given that the maximum energy of a solar neutrino energy is around 20 MeV, below the muon or tau mass, solar neutrino experiments cannot distinguish between muon and tau neutrinos. The transition probability between an electron neutrino eigenstate and either one of the other flavor

eigenstates is given by:

$$P(\nu_e \to \nu_{\mu,\tau}) = 1 - P(\nu_e \to \nu_e) \equiv 1 - P_{ee} \tag{1.42}$$

where P_{ee} is commonly referred to as the electron neutrino survival probability. Using Eq. 1.37 and the parameterization of the PMNS matrix given in Eq. 1.40, we can, after some trigonometric manipulations, write the survival probability as:

$$\begin{aligned}
P_{ee} &= \sum_i \sum_j |z_{eeij}| \cos\left(\frac{\Delta m_{ij}^2}{2\overline{p}}L\right) \\
&= 1 - \cos^4(\theta_{13})\sin^2(2\theta_{12})\sin^2\left(\frac{\Delta m_{21}^2}{4\overline{p}}L\right) \\
&\quad - \cos^2(\theta_{12})\sin^2(2\theta_{13})\sin^2\left(\frac{\Delta m_{31}^2}{4\overline{p}}L\right) \\
&\quad - \sin^2(\theta_{12})\sin^2(2\theta_{13})\sin^2\left(\frac{\Delta m_{32}^2}{4\overline{p}}L\right)
\end{aligned} \tag{1.43}$$

where we have ignored CP violating terms.

It is useful to calculate the different wavelengths associated with the survival probability for solar neutrinos. Plugging in the missing factors of c and $\hbar$ and approximating $\overline{p} \sim \overline{E}/c$, we get $\lambda_{ij} \equiv 4\pi\overline{E}\hbar/\Delta m_{ij}^2 c^3$. As a point of reference, we will consider the monoenergetic ^{7}Be neutrino at 0.862 MeV. Using the values listed in Table 1.3 we obtain the following oscillation lengths:

$$\lambda_{ij} \equiv (4\pi\hbar c)\frac{E}{\Delta m_{ij}^2 c^4} \sim (2.48)\frac{E[\text{MeV}]}{\Delta m_{ij}^2[\text{eV}^2]}m \tag{1.44}$$

$$\lambda_{21} \sim 28 \text{ km } (0.862 \text{ MeV}) \tag{1.45}$$

$$\lambda_{31} \sim \lambda_{32} \sim 880 \text{ m } (0.862 \text{ MeV}) \tag{1.46}$$

Since the production region of neutrinos within the Sun spans a radius of roughly $0.2R_\odot \sim 1.4\times10^5$ km $\gg \lambda_{ij}$, neutrinos produced in different regions arrive at Earth at

different phases and the oscillation probabilities therefore average out. Consequently, for solar neutrino experiments, the observed electron neutrino survival probability is:

$$P_{ee} = 1 \; - \frac{1}{2} \cos^4(\theta_{13}) \sin^2(2\theta_{12}) - \frac{1}{2} \sin^2(2\theta_{13})$$

$$= \cos^4(\theta_{13}) \left(1 - \frac{1}{2} \sin^2(2\theta_{12}) \right) + \sin^4(\theta_{13}) \tag{1.47}$$

$$\sim 0.565 \; (\theta_{13} = 0) \tag{1.48}$$

In the next section we will see how this survival probability is modified in the presence of matter

1.4.1.3 Neutrino Oscillations in Matter

The previous discussion of neutrino oscillations only applies to neutrinos in vacuum. The presence of matter can alter the oscillation parameters due to interactions between the neutrino and the surrounding particles. These interactions modify the Hamiltonian for the neutrino, effectively changing the corresponding propagation eigenstates. Leptonic matter consists exclusively of electrons, which implies that while a ν_μ and ν_τ can only interact through the neutral current interaction, a ν_e will interact through both the neutral and charged current interaction. Since ν_e interact more often than the other flavors, there is an additional phase difference between the flavor eigenstates that leads to modified oscillations. This effect is known as the Mikheyev-Smirnov-Wolfenstein (MSW) effect [30, 31].

To describe this effect, we will follow the derivation given in [32] and first reformulate the description of vacuum oscillations in a manner that can be easily extended to oscillations in matter. As before we will denote the mass eigenstates in vacuum as $|\nu_i\rangle$, but for simplicity we will only consider two neutrino species with mixing angle

θ. The evolution of the mass eigenstates is given by:

$$i\frac{d}{dt}\begin{bmatrix} \nu_1(t) \\ \nu_2(t) \end{bmatrix} = H' \begin{bmatrix} \nu_1(t) \\ \nu_2(t) \end{bmatrix} \qquad (1.49)$$

where H' is the (diagonal) Hamiltonian:

$$H' = \begin{bmatrix} E_1 & 0 \\ 0 & E_2 \end{bmatrix} \qquad (1.50)$$

Transforming to the flavor basis, we have:

$$i\frac{d}{dt}\begin{bmatrix} \nu_e(t) \\ \nu_x(t) \end{bmatrix} = H \begin{bmatrix} \nu_e(t) \\ \nu_x(t) \end{bmatrix} \qquad (1.51)$$

where

$$U = \begin{bmatrix} \cos\theta & -\sin\theta \\ \sin\theta & \cos\theta \end{bmatrix} \qquad (1.52)$$

$$H = UH'U^\dagger \qquad (1.53)$$

$$= \frac{E_1 + E_2}{2} + \frac{\Delta E}{2}\begin{bmatrix} -\cos(2\theta) & \sin(2\theta) \\ \sin(2\theta) & \cos(2\theta) \end{bmatrix} \qquad (1.54)$$

The oscillation length can be obtained by dividing 2π by the difference in the eigenvalues of H':

$$\lambda_{vac} = \frac{2\pi}{\Delta E} \sim \frac{4\pi E}{\Delta m^2} \qquad (1.55)$$

26

and the amplitude of the oscillation is given by $\sin^2(2\theta)$ where

$$\tan(2\theta) = \frac{H_{12} + H_{21}}{H_{22} - H_{11}} \tag{1.56}$$

Thus, from the Hamiltonian, one can obtain the survival probability for electron neutrinos as :

$$P_{ee} = 1 - \sin^2(2\theta)\sin^2\left(\frac{\pi L}{\lambda_{vac}}\right) \tag{1.57}$$

These results are the same as those derived in the previous section, reduced to the case of two neutrino species.

We will now consider oscillations in matter. Since the neutral current interaction with quarks and electrons is the same for all neutrino flavors, these interactions do not introduce any additional phase differences. However, only the electron neutrino can interact with electrons via the charged current interaction. The Feynman diagrams corresponding to the neutral and charged current interactions are shown in Figure 3.2. The contribution of these interactions can be interpreted as effective potential energy terms V_{nc} and V_{cc} (detailed in [33]) corresponding to the neutral current and charged current interactions respectively:

$$V_{nc} = -\frac{1}{\sqrt{2}}G_F n_n \tag{1.58}$$

$$V_{cc} = \sqrt{2}G_F n_e \tag{1.59}$$

where G_F is the Fermi constant ($G_F/(\hbar c)^3 \sim 1.167 \times 10^{-5}$ GeV^{-2}) and n_n and n_e are the number densities of neutrons and electrons respectively. We note that while the effective potential depends on the number density of scatterers (for the neutral current interactions the contributions from protons and electrons cancel each other), it is independent of the energy of the neutrino. Thus in matter, the vacuum Hamiltonian

in the flavor basis (Eqn. 1.54), should be replaced by:

$$H_m = \frac{E_1 + E_2}{2} - \frac{1}{\sqrt{2}} G_F n_n + \frac{\Delta E}{2} \begin{bmatrix} -\cos(2\theta) + 2A & \sin(2\theta) \\ \sin(2\theta) & \cos(2\theta) \end{bmatrix} \quad (1.60)$$

$$\text{where } A \equiv \frac{\sqrt{2} G_F n_e}{\Delta E} \sim \frac{2\sqrt{2} G_F n_e E}{\Delta m^2} \quad (1.61)$$

As in the case of the vacuum oscillations, we can now use this Hamiltonian to construct the electron neutrino survival probability:

$$P_{ee} = 1 - \sin^2(2\theta_m) \sin^2\left(\frac{\pi L}{\lambda_m}\right) \quad (1.62)$$

The oscillation length, obtained from the difference in the eigenvalues of H'_m (the matter Hamiltonian H_m in the mass basis), is given by:

$$\lambda_m = \frac{2\pi}{\Delta E \sqrt{(\cos(2\theta) - A)^2 + \sin^2(2\theta)}} \quad (1.63)$$

$$= \frac{\lambda_{vac}}{\sqrt{(\cos(2\theta) - A)^2 + \sin^2(2\theta)}} \quad (1.64)$$

and the angle that determines the amplitude of the oscillation is:

$$\tan(2\theta_m) = \frac{H_{m(12)} + H_{m(21)}}{H_{m(22)} - H_{m(11)}} \quad (1.65)$$

$$= \frac{\sin(2\theta)}{\cos(2\theta) - A} \quad (1.66)$$

From the above equations, it is clear that both the amplitude and wavelength of the oscillations in matter depend critically on the parameter A, which in turn depends on the product of the matter number density and the neutrino energy, $n_e E$. It is useful to consider some limiting cases for the value of A. At low densities or low neutrino energies, such that $A \ll \cos(2\theta)$, we obtain the standard vacuum oscillation

parameters. At high densities or high neutrino energies, where $A \gg \cos(2\theta)$, the amplitude of the oscillations is suppressed and the survival probability is effectively unity. In these conditions, the electron flavor eigenstate is also an effective mass eigenstate. Interestingly, there is also a resonant condition for $A = \cos(2\theta)$. At resonance, $\sin(2\theta_m) = 1$, which results in a complete conversion of electron neutrinos ($P_{ee} = 0$) at specific positions separated by $\lambda_{m,res} \equiv \lambda_{vac}/\sin(2\theta)$. We also note that at resonance, the mass eigenvalues are the closest to each other and therefore the oscillation length $\lambda_{m,res}$ is the largest.

We can now plug in some numbers for A to determine which of the above situations are relevant to solar neutrinos. The electron number density can be expressed as $n_e = \rho N_A \langle Z/A \rangle$ where ρ is the matter density, N_A is Avogadro's number and $\langle Z/A \rangle$ is the average charge to mass ratio (for electrically neutral matter). At the core of the Sun, $\rho \sim 153$ g/cm^3 and $\langle Z/A \rangle \sim 2/3$ which gives an electron number density of $n_e^{sc} \sim 6 \times 10^{25}$ cm^{-3} [32, 33]. In comparison, in the Earth's core, $\rho \sim 12$ g/cm^3 and $\langle Z/A \rangle \sim 1/2$ giving $n_e^{ec} \sim 4 \times 10^{24}$ cm^{-3} [29]. Table 1.4 gives the values for $A_{ij}(E)$ at the center of the Sun and Earth, where we have rewritten Eq. 1.61 as:

$$A_{ij}(E) \equiv \frac{2\sqrt{2}G_F n_e}{\Delta m_{ij}^2}E \tag{1.67}$$

Region	$A_{21}(E \text{ [MeV]})$	$\cos(2\theta_{12})$	$A_{31}(E \text{ [MeV]})$	$\cos(2\theta_{13})$
Solar Core	$0.205E$	0.36	$0.0064E$	$[0.93 - 1.00]$
Earth Core	$0.012E$	0.36	$0.0004E$	$[0.93 - 1.00]$

Table 1.4: Matter oscillation parameter $A_{ij}(E)$ (Eq 1.67) as a function of energy (in MeV) for different mass-squared differences at the center of the Earth and Sun. Values of $\cos(2\theta_{ij})$, taken from Table 1.3, are shown for comparison.

We can see from the values in Table 1.4, that even in the densest regions of the Sun, $A_{31}(E) \ll \cos(2\theta_{13})$ for $E < 10$ MeV. It can therefore be shown [1,34,35] that the oscillations of solar neutrinos due to Δm_{31}^2 proceed essentially as in vacuum. Thus we

can restrict ourselves to the 2-neutrino oscillations described in the previous section, changing $\Delta m^2 \to \Delta m_{12}^2$ and $\theta \to \theta_{12}$.

For the high energy solar neutrinos ($E > 3$ MeV) we see that at the core of the Earth $A_{21}(E)$ is non-negligible compared to $\cos(2\theta_{12})$ and so Earth-matter effects start to become significant. The day-night asymmetry[3] for solar neutrinos above 5 MeV is predicted to be around 2-5% [37, 38]. For the 0.862 MeV ^{7}Be neutrinos, which are the subject of this study, $A_{21}/\cos(2\theta_{12}) \sim 0.03$ and the predicted day-night asymmetry is less than 0.1% [37].

Thus, for ^{7}Be neutrinos the dominant matter effect comes from interactions within the Sun.

1.4.1.4 Neutrino Oscillations in the Sun

There is an additional complication for solar neutrinos in that the matter density varies as the neutrino propagates from the core to the surface of the Sun. The electron density in the Sun (except for the inner and outer most 10% of the radius) can be modeled fairly accurately as a simple falling exponential [18]:

$$n_e(r) \sim 2.5 \cdot n_e^{sc} e^{-r/r_0} \tag{1.68}$$

where, as before, n_e^{sc} is the electron density at the solar core, r is the radial distance from the core and $r_0 \sim R_\odot/10.5 \sim 6.6 \times 10^4$ km is the characteristic length over which the density changes. If this characteristic length is large compared to the oscillation length, then the mass eigenstates will change adiabatically, ensuring that a neutrino in a given eigenstate will remain in the same state as it traverses through the sun. A non-adiabatic change (jump) between mass eigenstates is most likely to occur when

---

[3]At night, neutrinos must pass through the Earth to reach the detector. If they are affected by interactions with matter in the Earth, it can manifest as a difference in the observed neutrino interaction rates during the day and night. Further details on the day-night effect can be found in [36].

the mass eigenvalues are closest to each other, which, as noted above, happens at resonance. We can express the adiabatic condition as:

$$\gamma \equiv \frac{r_0}{\lambda_{m,res}} \gg 1 \tag{1.69}$$

$$E \ll \frac{\Delta m_{12}^2 c^4 r_0 \sin 2\theta_{12}}{4\pi\hbar c} \tag{1.70}$$

$$E \ll 2 \text{ GeV} \tag{1.71}$$

Thus we can see that for solar neutrinos ($E < 10$ MeV), the adiabatic condition is always satisfied. A more complete derivation of the adiabatic condition can be found in [29, 33].

We can now evaluate the effect of matter on the survival probability for solar neutrinos. Consider an electron neutrino with energy E, produced at the center of the Sun. As described above, matter effects become important when $A_{21}^{sc}(E) = 0.205E$ [MeV] is comparable to $\cos(2\theta_{12}) = 0.36$. We will consider two limiting cases to develop an understanding of the energy dependence of the survival probability.

For low energy neutrinos ($E < 0.1$ MeV), $A^{sc} \ll \cos(2\theta_{12})$ throughout the interior of the sun and the oscillations proceed essentially as in vacuum. The survival probability is given by Eq. 1.47 (reducing to the two neutrino case):

$$P_{ee}(E < 0.1 \text{ MeV}) = 1 - \frac{1}{2}\sin^2(2\theta_{12}) \tag{1.72}$$

$$= 0.565 \pm 0.015 \tag{1.73}$$

At high energies matter effects dominate. Consider a hypothetical solar neutrino with energy in the range of 100 MeV, such that the adiabatic condition still holds. At these energies the mixing angle θ_m, given by Eq. 1.66, is approximately $\pi/2$. This implies that for such a neutrino at the solar core, the electron flavor state ν_e coincides with ν_{2m}^{sc}, the second (matter-modified) mass eigenstate at the solar core. As the

neutrino propagates outward, the density decreases and the eigenstates of the matter-modified Hamiltonian H' (Eq. 1.54) change correspondingly. Due to the adiabatic change in density, the neutrino will remain in the same mass eigenstate ν_{2m}, even as the component of ν_e decreases. Once the neutrino reaches the surface of the Sun ($n_e = 0$), it will continue to propagate to the Earth in the vacuum ν_2 eigenstate. The probability of being detected as an electron neutrino is then simply:

$$P_{ee}(100 \text{ MeV} < E < 1 \text{ GeV}) = |\langle \nu_2 | \nu_e \rangle|^2 \tag{1.74}$$

$$= \sin^2(\theta_{12}) \tag{1.75}$$

$$= 0.320 \pm 0.021 \tag{1.76}$$
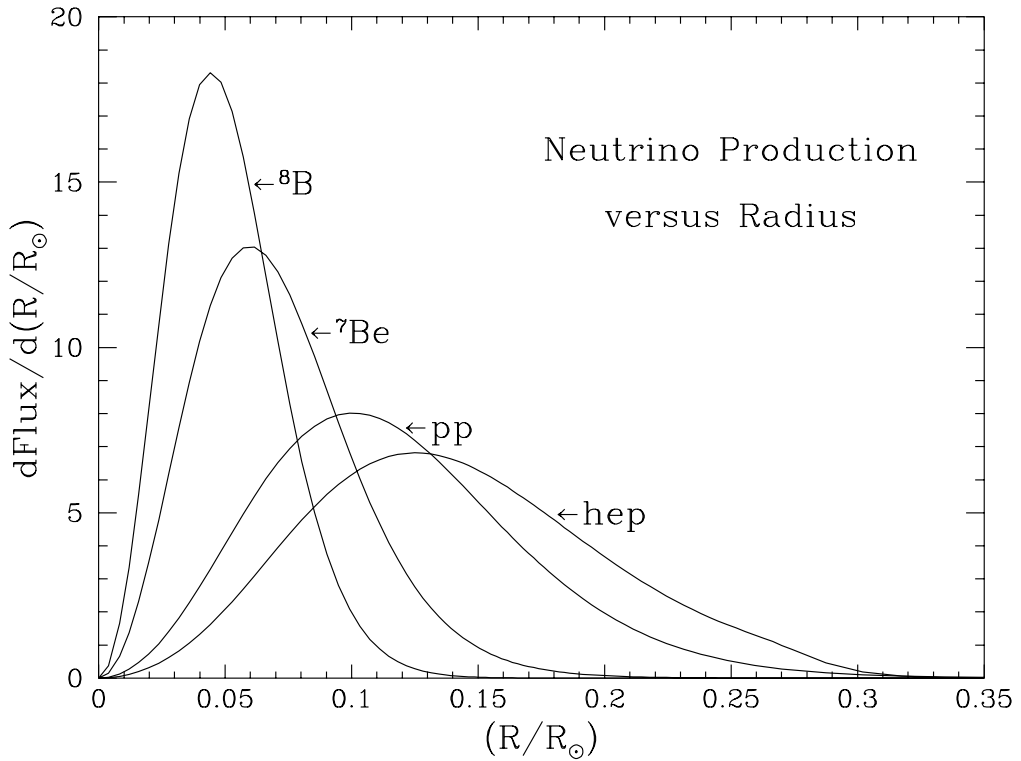
Figure 1.7: Production regions for the different solar neutrino species within the Sun. Figure taken from [39].

Of course most solar neutrinos are produced between these extreme energy ranges.

32

As one would expect, there is a smooth transition between the low and high energy limits of the survival probability, though for intermediate energies the calculation of the survival probability is more complicated. The survival probability depends on not only the energy of the neutrino but also on the electron density at the point of production. Due to the dependence of the nuclear reaction rates on the local temperature, density and chemical composition, the production regions for the different neutrino species varies, as shown in Figure 1.7.

As reference, we use the analytical approximation of the energy-dependent electron neutrino survival probability derived in [40]. As part of the derivation, the survival probability is averaged over the production region of the corresponding neutrino species and non-adiabatic corrections (that were shown to be small above) were neglected. The predicted survival probabilities for the different neutrino species, as calculated by this method, are shown in Figure 1.8. Note that in calculating the values, we have ignored Earth-matter effects and have used the vacuum oscillation parameters in Table 1.3. The uncertainties shown come solely from the uncertainties in the vacuum oscillation parameters. The predicted survival probability for the ^{7}Be neutrinos is $P_{ee} = 0.542 \pm 0.013$ at 0.862 MeV.

1.4.1.5 Non-Standard Interactions

The matter effects discussed in the previous two sections, in conjunction with the vacuum oscillation parameters listed in Table 1.3 are referred to as the LMA-MSW solution, which is the most widely accepted oscillation framework for solar neutrinos. There are however other possible interactions between neutrinos and matter, which lie outside the scope of the Standard Model, that could affect the observed solar neutrino flux. These non-standard interactions (NSIs) are generally described by a four fermion interaction (two of which are neutrinos) that may involve a flavor change [41, 42]. The most common interaction considered (due to the lack of experimental constraints) is
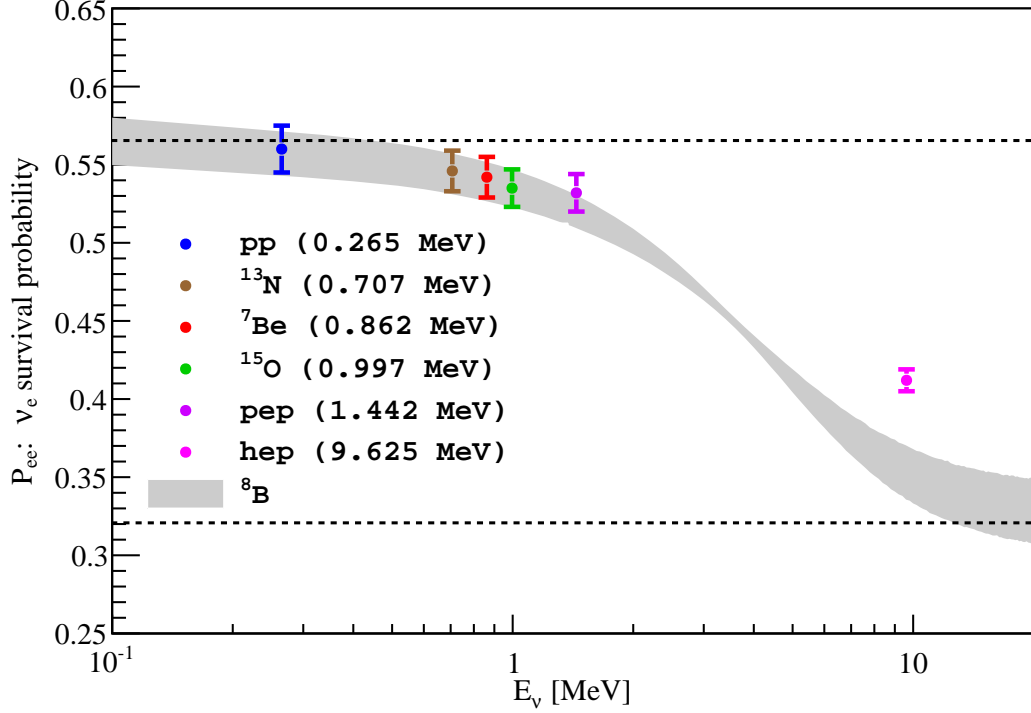
Figure 1.8: LMA-MSW predicted electron neutrino survival probabilities for the different neutrino species. For clarity, the survival probability for *pp*, ^{13}N, ^{15}O and *hep* neutrinos, is only shown at the average neutrino energy. Values are calculated using the analytical approximation in [40], ignoring Earth-matter effects. Uncertainties shown only include the uncertainties in the vacuum oscillation parameters. The upper (lower) black dashed line is the predicted survival probability at the low (high) energy limit.

the interaction of a ν_e with an up or down quark that can cause a flavor transition to a ν_τ. Such a flavor-changing NSI can be shown to mimic the effect of a non-zero θ_{13} value and ease the tension between solar neutrino results and KamLAND data[4] [42].

NSI's can be be parameterized by an additional term to the neutrino matter

---

[4]KamLAND is a reactor neutrino experiment studying the disappearance of electron antineutrinos. KamLAND places strong limits on Δm_{12}^2 while solar neutrino experiments provide the best constraints on θ_{12}. The combined results are used to obtain the parameters of the LMA solution, though there is some tension between the results.

Hamiltonian (see Eq 1.60 for the 2-neutrino MSW Hamiltonian) [41]:

$$H_m^{NSI} = \sqrt{2}G_F n_e \begin{bmatrix} \epsilon_{ee} & \epsilon_{e\mu}^* & \epsilon_{e\tau}^* \\ \epsilon_{e\mu} & \epsilon_{\mu\mu} & \epsilon_{\mu\tau}^* \\ \epsilon_{e\tau} & \epsilon_{\mu\tau} & \epsilon_{\tau\tau} \end{bmatrix} \tag{1.77}$$

where the ϵ_{xy} parameters correspond to the strength of the interaction involving ν_x and ν_y, relative to the standard MSW case ($\epsilon_{ee} = 1$, all others zero). The ϵ_{xy} parameters include effects with both electrons and quarks and hence the magnitude of NSI effects also depend on the chemical composition of the medium.
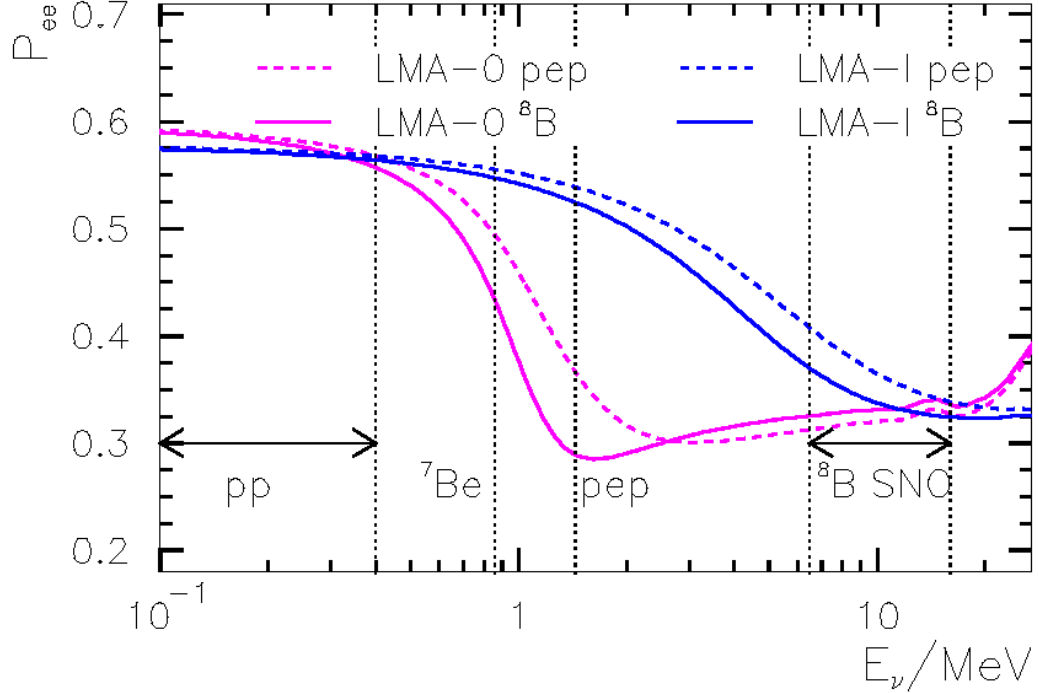

Figure 1.9: Comparison of the energy dependence of the electron neutrino survival probability for the standard LMA-MSW solution (LMA-I, blue curves) and the alternative LMA-0 solution (magenta curves) with non-standard interactions. The solid (dashed) line shows the energy dependence for solar neutrinos with the same production region as ^{8}B (pep) neutrinos. Figure taken from [41].

One set of interaction variables gives rise to an alternative set of neutrino oscillation parameters, $\Delta m^2 = 1.5 \times 10^{-5}$ eV^2 and $\sin^2(2\theta_{12}) = 0.81$, when fitting

KamLAND and solar neutrino data [41]. This is referred to as the LMA-0 solution and its effect on the electron neutrino survival probability is shown in Figure 1.9, in comparison to the standard LMA-MSW prediction (LMA-I). We note that both standard and non-standard matter interactions are constrained at low energy by the vacuum oscillation parameters and in the ^{8}B energy region by the measurements of the SNO experiment (see Section 7.4 for more details). Thus the region of interest is at intermediate energies, in which the ^{7}Be and *pep* neutrinos are produced. It is clear that by making precision measurements of the electron neutrino survival probability at different energies, one can place constraints on the strength of NSIs and perhaps reveal physics beyond the Standard Model.

Chapter 2

Borexino Detector

The Borexino detector is located in the Laboratori Nazionali del Gran Sasso (LNGS), situated under the Apennine Mountains in Italy, approximately 130 km northeast of Rome. The laboratory lies adjacent to a tunnel that is part of the A24 national highway connecting the towns of L'Aquila and Teramo and is thus easily accessible by vehicle. The overhead Gran Sasso mountains provide an average rock coverage of 1400 m (3800 m water equivalent) and act as a cosmic ray shield for the experiments within the laboratory. The Borexino detector is located at the far end of Hall C in the laboratory, next to the prototype CTF detector.

The layout of the detector is based on the principle of graded shielding, with each inner region shielded by the outer sections and exhibiting a lower level of internal radioactive background than the neighboring outer layer. A schematic cross section of the detector is shown in Figure 2.1. Moving from the outermost regions inwards, we first have the external water tank that acts as a Cherenkov detector for the residual muon flux, and provides shielding from external radiation. Located inside the water tank is the Stainless Steel Sphere (SSS) that houses the inner detector. The inner detector is partitioned into three regions: the innermost section, bounded by the Inner Vessel (IV), is filled with scintillator and acts as the active volume of the detector, the
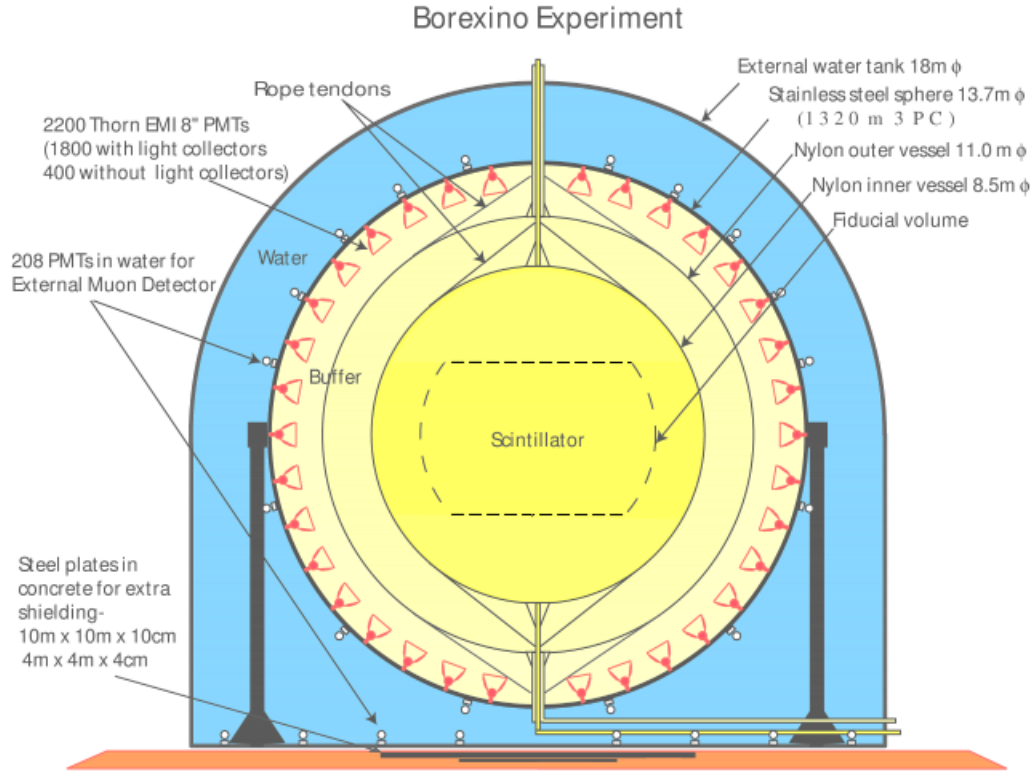
Figure 2.1: Schematic cross section of the Borexino detector. Going from the outside towards the center we have the external water tank (blue) , the Stainless Steel Sphere (with mounted photomultiplier tubes), the outer buffer region, the Outer Nylon Vessel (OV), and the Inner Nylon Vessel (IV). The buffer fluid is shown in pale yellow, while the scintillator fluid that fills the IV is shown in bright yellow. Only events reconstructed within the region demarcated by dashed lines, referred to as the fiducial volume, are used for the ^{7}Be analysis. Figure adapted from [43].

inner buffer, bounded by the Outer Vessel (OV), and the outer buffer region which extends radially from the OV to the SSS. Photomultiplier tubes (PMTs) are mounted on the inner surface of the SSS to detect scintillation light.

In this chapter we will briefly describe the different components of the detector, before discussing the associated electronics and data acquisition system used. Finally we will also describe the source calibration system that played a critical role in the analysis described in this thesis.

2.1 Hardware

2.1.1 Outer Detector

The outer detector (OD) consists of a high dome steel water tank, 18 m in diameter with a maximum height of 16.9 m. It is filled with 2100 tons of ultra-pure water and is instrumented with 208 PMT's to detect Cherenkov light from muons passing through the water. Of the 208 PMT's, 154 are mounted on the outer surface of the Stainless Steel Sphere (SSS), facing radially outward, 34 are positioned in four concentric rings on the floor of the water tank, and the remaining 20 PMT's lie on a 45° inward inclination around the outer edge of the water tank floor. Both the outer surface of the SSS and the inner surface of the water tank are covered with ~ 200 μm thick Tyvek sheets to enhance reflectivity. The overall muon tagging efficiency of the outer detector has been estimated to be (99.33 ± 0.01)%. Further details on the outer detector and the evaluation of the efficiency can be found in [44].

2.1.2 Inner Detector

The inner detector lies within the Stainless Steel Sphere (SSS), which stands in the water tank on 20 steel legs. The SSS has a diameter of 13.7 m and a thickness of 8 mm and provides structural support for the above-mentioned outer detector PMT's, the inner detector PMTs, the nylon vessels, and also counters the large buoyant forces due to the lower density of the scintillator, compared to the water in the OD. In this section we will discuss the major components of the inner detector, with a more detailed description available in [45].

2.1.2.1 Photomultiplier Tubes

The SSS is instrumented with 2212 inward facing photomultiplier tubes to detect scintillation light. The tubes chosen were hemispherical 8″ ETL 9351 photomultipliers

with a projected photocathode area of 366 cm^2. The nominal quantum efficiency for this model of PMT is 26.5% at 420 nm and only phototubes with a quantum efficiency above 21% were accepted for use within the inner detector. It should be noted that these phototubes have a collection efficiency (the probability that a photoelectron leaving the cathode will land on the effective area of the first dynode) of only about 60% [46]. Given the nominal quantum efficiency of 32% at 360 nm, the peak of the scintillation emission spectrum (see Figure 2.4), the overall detection efficiency of the tubes is about 19%. The most relevant parameters of the PMTs for the current analysis are listed in Table 2.1.

Photomultiplier Tube Parameter	Nominal Value	Acceptance Criterion
Quantum Efficiency (420 nm)	26.5%	> 21%
Rise Time	0.67 ns	-
Transit Time Spread (FWHM)	2.8 ns	< 1.3 ns
S.P.E. Peak-to-Valley Ratio	2.5	> 1.5
Dark Current at 10^7 Gain	25 nA	-
Dark Count Rate	-	$< 2 \times 10^4$ Hz

Table 2.1: Parameters for 8″ ETL 9351 photomultiplier tubes used in the Borexino inner detector. The second column gives the nominal values from the manufacturer while the third column gives the criteria used to accept or reject tubes. Values taken from [45].

Of the 2212 photomultipliers, 1839 are also equipped with light concentrators. The light concentrators consist of a curved aluminium surface, 23 cm in height with entry and exit apertures of 16 and 9.5 cm respectively, that is attached to the front face of the PMT glass (see Figure 2.2). The shape of the concentrator is designed [47] such that light incident on the concentrator at angles less than the critical angle, $\delta = 44°$, is almost always reflected on to the exit aperture, while light incident above the critical angle is mostly reflected outwards. This allows the light concentrators to increase the effective photocathode coverage while filtering out light from events in the buffer. The remaining photomultipliers were left without light concentrators so as to help distinguish point-like events in the Inner Vessel from muons passing through the buffer.
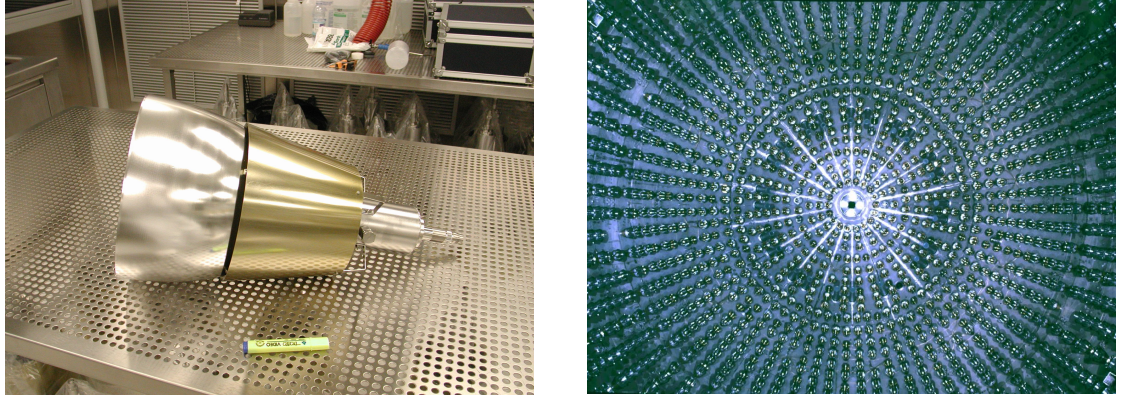
Figure 2.2: Left: One of the photomultiplier tubes used in the inner detector of Borexino. The aluminum light concentrator (silver) can be seen attached to the front face of the tube, below which is a μ-metal magnetic shield. Right: Picture of the inside of the SSS after the installation of the photomultiplier tubes.

The fractional solid angle coverage for an event located at the center of the detector, accounting for the larger effective aperture of PMTs with light concentrators, is 30%. Including a 90% reflectivity for the light concentrators and an average detection efficiency of 19% for the photomultiplier tubes we obtain a predicted photon to photoelectron conversion efficiency of $\sim$ 5.2%. This would correspond to a predicted lightyield of $\sim$ 540 p.e./MeV (assuming a scintillator light yield of 11500 photons/MeV (Section 2.1.2.2) and 2000 working PMT's). This calculation does not take into account losses in the scintillator or photons that are detected after reflecting off the light concentrators (or the SSS) back towards the center of the detector. As we will see in Section 5.2, the observed light yield at the center of the detector (based on source calibration data) is 488.5 ± 1.6 p.e./MeV, scaled to 2000 working PMT's. Given the uncertainty in the numbers used and the lack of a full optical Monte Carlo simulation, this is roughly consistent with the above prediction.

Unfortunately the photomultiplier tubes and light concentrators are the most radioactive components in the inner detector. Even with a large buffer region separating them from the active fiducial volume, they are the source of about 80% of the external backgrounds in the spectral fit range [48].

2.1.2.2   Scintillator and Buffer

The ~ 278 tons of liquid organic scintillator at the center of Borexino forms the active target of the detector. In this section we briefly describe the scintillation process and the physical and chemical properties of the scintillator and buffer fluids used in Borexino.

Scintillation Mechanism   Charged particles passing through the scintillator excite and ionize the scintillator molecules. The molecules, after recombination, then decay back to the ground state through the emission of lower energy scintillation photons. A detailed description of the scintillation mechanism can be found in [49], while here we only discuss the details that are most relevant for the description of the detector and the ^{7}Be analysis.

Most organic scintillators consist of aromatic molecules. These molecules, often containing benzene rings, have delocalized electrons which are free to circulate around the arrangement of atoms. It is the excitation levels of this delocalized electron cloud that is responsible for scintillation. The energy spacing between the states is usually on the order of 5 eV (~ 250 nm) and the excited state of a specific molecule depends on the electron spin. The singlet states, in which the total spin is zero, have a relatively fast ($\sim$ ns) decay time to the ground state emitting what is known as the fast component of scintillation light. Some fraction of the excited singlet states can also de-excite to the ground state non-radiatively. The fraction of fluorescent decays of the singlet state is referred to as the fluorescence quantum efficiency of the scintillator. Following recombination, the scintillator molecules can also be in a triplet state (with total spin 1). The decay of the triplet state back to the ground state is suppressed due to the difference in spin angular momentum, leading to decay time scales on the order of milliseconds to seconds. Due to the long decay time, a much more common channel for the triplet states to de-excite is through collisions with

other molecules in the triplet state. This results in one molecule in the first excited singlet state and the other in the ground state. The excited singlet state molecule can then scintillate back to the ground state as discussed above. The lifetime of this delayed emission is normally on the order of microseconds and is referred to as the slow component of the scintillation light. At low ionization densities, the primary scintillation process is due to molecular excitation of the delocalized electrons into the singlet states (the direct excitation into triplet states is spin-forbidden). At higher ionization densities however, a larger proportion of excited molecules are produced due to the recombination of ions and electrons, which favors the production of the triplet states. Thus, the scintillation light from highly ionizing particles such as αs and protons have a larger slow component than that from electrons. The differing scintillation time profiles of α and β decays allow us to discriminate between the two (Section 4.5), which plays a critical role in the ^{7}Be analysis (see Section 6.4).

The ionizing density of the particle track also affects the amount of light output. For electrons, roughly 5% of the deposited energy is converted into scintillation photons while for highly ionizing particles, such as αs, the output is usually less than a tenth of that. The relationship between particle ionization and light output is described and modeled in Section 5.2.

Scintillator The scintillator used in Borexino is a solution of 1,2,4-trimethylbenzene, commonly referred to as pseudocumene, with 2,5-diphenyloxazole (PPO) dissolved at a concentration of 1.45 g/l. The chemical structure of pseudocumene and PPO are shown in Figure 2.3. While pseudocumene is by itself a scintillating molecule, its scintillation properties are not ideal for a large neutrino detector such as Borexino. The fast component of the scintillation light has a relatively long mean life of 22 ns [50]. The position reconstruction algorithm used in Borexino (described in Section 4.3) is based on a likelihood fit to the scintillation time profile. A large spread
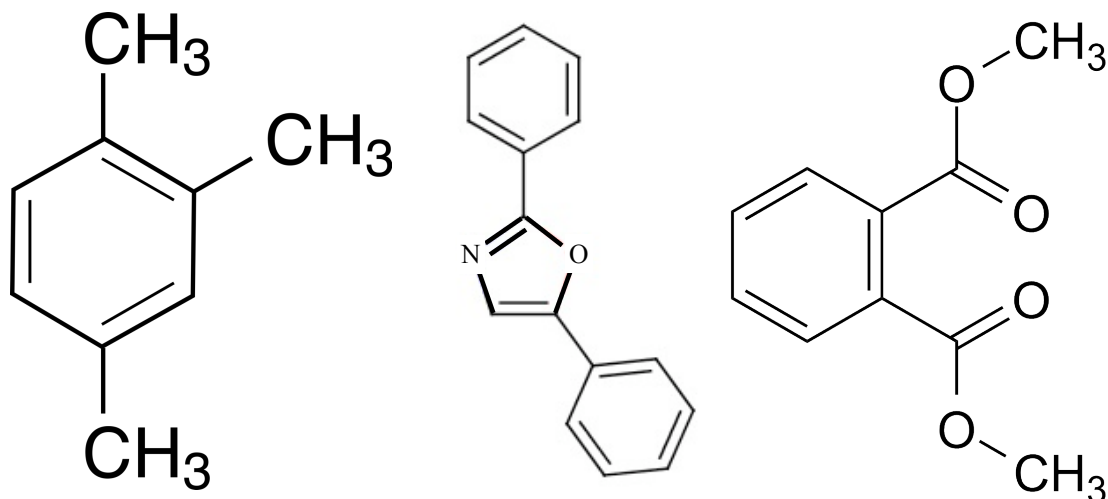
Figure 2.3: Skeletal formula of compounds in the scintillator and buffer fluids. Left: Pseudocumene (1,2,4-trimethylbenzene). Middle: PPO (2,5-diphenyloxazole). Right: DMP (dimethylphthalate)

in the emission times adversely affects the position resolution, making it difficult to precisely determine the location of events. Also detrimental to the position as well as energy resolution is the low fluorescence quantum efficiency of pseudocumene (roughly 40% [43]). This reduces the number of scintillation photons produced for a given energy deposit, a problem that is further compounded by the fact that the peak emission wavelength of pseudocumene, around 290 nm, is not well matched to the photomultiplier quantum efficiency (see Figure 2.4). The addition of PPO to pseudocumene addresses all of these problems. The fluorescence efficiency of PPO is about 80% [50] and the emitted light is peaked at 360 nm, near the maximum efficiency of the photomultipliers (see Figure 2.4). The decay time of PPO is only 1.8 ns [50] and importantly, the energy from the excited pseudocumene molecule can be transferred non-radiatively to the PPO molecule (a process that takes place faster than photon emission). The combination of pseudocumene and 1.5 g/l PPO yields a decay time of 2.5 ns due to the additional time required for pseudocumene to transfer its energy to the PPO [50]. The scintillator light yield was measured to be $(11500 \pm 10\%)$ photons/MeV for a few hundred keV electrons [51] with an index
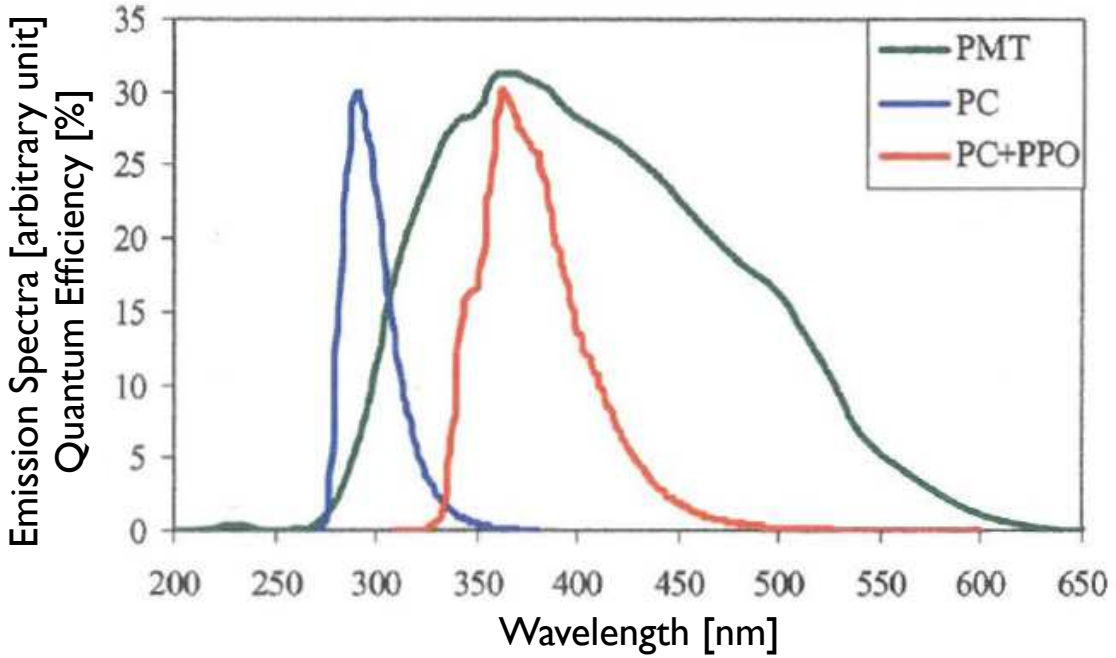
Figure 2.4: Emission spectra for PC (blue) and PC + PPO (red), with arbitrary units on the y-axis. Overlaid is the quantum efficiency for the Borexino inner detector photomultipliers (green). Figure adapted from [43].

of refraction of 1.52 at 425 nm (see later subsection on light propagation for more details).

One of the important parameters of the scintillator for the determination of the ^{7}Be rate and flux is the number density of electrons. The temperature-dependent density for pure pseudocumene is given by [52]:

$$\rho_{PC}(T)[\text{g/cm}^3] = (0.89179 \pm 0.00003) - (8.015 \pm 0.009) \times 10^{-4} \cdot T \qquad (2.1)$$

where T is the temperature in degree Celsius. For a PC + PPO mixture, the density is [53]:

$$\rho_{PC+PPO}(T)[\text{g/cm}^3] = \rho_{PC}(T) \cdot (1 + (3.16 \pm 0.01) \times 10^{-1}\eta_{PPO}) \qquad (2.2)$$

where η_{PPO} is the concentration of dissolved PPO in g/cm^3. Plugging in values

for the temperature of the scintillator in Borexino $T = (15.0 \pm 0.5)°$C and $\eta_{PPO} = (1.45 \pm 0.05) \times 10^{-3}$ g/cm^3 we obtain a final scintillator density value of 0.8802 ± 0.0004 g/cm^3. In order to convert this into the number of electrons per unit mass, we take into account the chemical composition of the scintillator components (including the 1.1% isotopic abundance of ^{13}C) to get $n = (3.307 \pm 0.003) \times 10^{29}$ electrons/ton [54].

Buffer   In order to separate the active volume from the high radioactivity levels of the photomultiplier tubes and light concentrators, an optically transparent, but inactive "buffer" liquid was required to fill the region between the Inner Vessel and the SSS. An important design concern is the buoyancy force on the Inner Vessel. Given the large volume of the Inner Vessel (322 m^3), a density mismatch of 1 part in 1000 gives rise to a net force of over 3000 N. Thus a liquid whose density closely matches that of the scintillator is needed. Also, in order to avoid complications in the position reconstruction of events, it is desirable for the liquid to have an index of refraction that is compatible with the scintillator. The solution that was found that matches all of these requirements is a mixture of pseudocumene with dimethylphthalate (DMP, see Figure 2.3) at a concentration of 5 g/l [55]. The addition of DMP at this concentration was found to quench the light yield by roughly a factor of 28.4±1.4 [55] with respect to pure pseudocumene. Also, both the density (1.19 g/cm^3 [43]) and index of refraction (1.515 [43]) are very similar to that of the scintillator fluid. The density of a mixture of pseudocumene and DMP is given by [53]:

$$\rho_{PC+DMP}(T)[\text{g/cm}^3] = \rho_{PC}(T) \cdot (1 + (2.75 \pm 0.05) \times 10^{-1} \eta_{DMP}) \qquad (2.3)$$

where η_{DMP} is the concentration of dissolved DMP in g/cm^3. Given the concentrations of PPO and DMP in the Inner and Outer vessels respectively, and the average temperature of the scintillator, there is a net upward buoyancy force of $\sim$ 2500 N. We note that following the development of a leak in the inner nylon vessel (see Sec-

tion 2.3) the concentration of DMP in the buffer was reduced to 2 g/l to reduce the buoyant force on the inner vessel. At this level, the DMP was still found to be effective in quenching the scintillation light in the buffer, while the buoyant force was reduced to ~ 250 N.

Light Propagation In order to reconstruct the position of an event (see Section 4.3) it is necessary to estimate the time-of-flight of the scintillation photons from the point of emission to the photomultiplier tubes. This was calculated using the formula $t = d \cdot (n/c)$ where d is the distance travelled, c is the speed of light and n is the index of refraction. In order to determine the index of refraction, several measurements of the scintillator were made using a refractometer, yielding a value of about $n = 1.52$ at 425 nm. However in order to reconstruct events at the correct radius, an effective refractive index of $n \sim 1.7$ had to be used (see Section 4.3.1.1). This discrepancy was not understood and remained a long-standing mystery until recent measurements of the refractive index were made at different wavelengths [56]. The results, shown in Figure 2.5, show a dependence of the refraction index on the wavelength of light, especially at short wavelengths. Due to this dependence, the propagation speed of light (group velocity v_g) differs from the phase velocity, $v_p = c/n$, by:

$$v_g = \frac{v_p}{1 - \frac{\lambda}{n}\frac{dn}{d\lambda}} \tag{2.4}$$

$$n_g \equiv \frac{c}{v_g} \tag{2.5}$$

$$= n - \lambda\frac{dn}{d\lambda} \tag{2.6}$$

where λ is the wavelength in vacuum and we have defined a group velocity refractive index n_g. Figure 2.5 shows the group velocity refractive index of the scintillator using a smooth fit the the measured refractive index data. One can see that near the peak

47
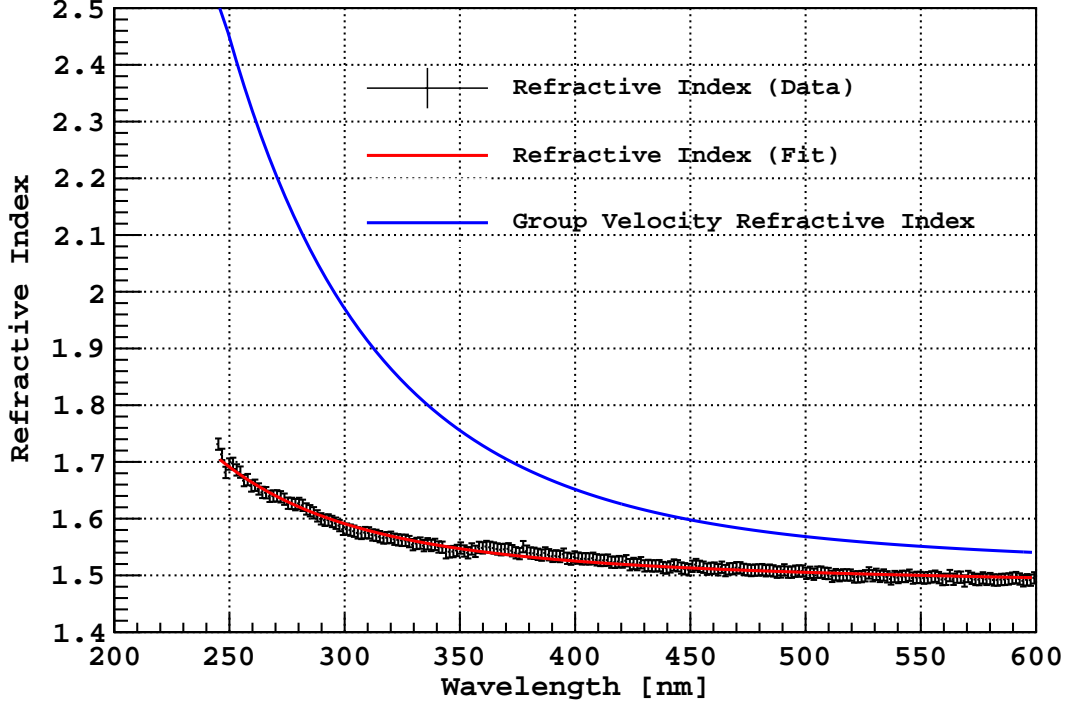
Figure 2.5:   Refractive index of scintillator solution. The black data points show the direct measurements of the scintillator refractive index as a function of wavelength, made with a refractometer. The red line is a fit to the data with the arbitrary function $n^2 = p_0 + p_1/\lambda^2 + p_2/\lambda^4 + p_3\lambda^2 + p_4\lambda^4$. The blue line is the group velocity refractive index, calculated using Eq 2.6 and the fitted curve. Figure adapted from [56].

of the PPO emission spectrum (360 nm) the group velocity refractive index is about 1.7, explaining the use of an effective index of refraction in the position reconstruction algorithm.

2.1.2.3   Nylon Vessels

Within the SSS are two concentric spherical nylon vessels with a thickness of 125 μm. The Inner Vessel (IV) has a diameter of 8.5 m and holds the scintillator, separating it from the buffer liquid surrounding it. The main purpose of the Outer Vessel (OV), which has a diameter of 11.0 m and sits inside the buffer region, is to prevent radon gas from diffusing towards the scintillator. There are several requirements that the nylon vessels must meet. Mechanically they must be able to withstand the buoyant

forces caused by density and temperature differentials on either side of the nylon film. To this end, the nylon vessels have been designed to withstand stresses up to 20 MPa [48] and each vessel is also held in place vertically by two sets of ropes that attach to the vessel end regions. In addition to the mechanical strength, the vessels, especially the IV which separates the scintillator and buffer fluids, should be leak-tight. At the time of installation, the leak rate for the IV and OV were measured at 0.005 cc (PC)/sec and 0.1 cc (PC)/sec respectively for the 1 mbar over-pressure of the IV with respect to he OV [48], at least a factor of two better than the design specifications. Since the IV is in direct contact with the scintillator, not only did the intrinsic radioactive background in the material have to be as low as possible, but the entire process, from fabrication to installation had to be done in a clean environment to avoid surface contamination that can wash off into the scintillator. The estimated count rates from intrinsic backgrounds in the nylon vessel is estimated to be < 0.02 counts/day in the innermost 100 tons of scintillator [48].

2.1.2.4   Vessel Endcaps

The endcap regions at the top and bottom of each of the nylon vessels serve multiple functions. They provide mechanical support for the nylon vessels and ropes as well as serve as a passageway for instrumentation and liquids during purification and refilling operations. Figure 2.7 shows a picture of the bottom endcap of the Inner Vessel during construction. The top endcaps must also allow the insertion of radioactive sources into the scintillator during source calibrations (see Section 2.4). The OV endcaps are composed mainly of stainless steel, while the IV endcaps are constructed mostly of copper and nylon to reduce the radioactive backgrounds. Nevertheless the endcap regions, due to their proximity to the scintillator contribute the highest rates of backgrounds within the Inner Vessel (see Section 3.2.11). In addition, the mechanical structure of the endcaps blocks some of the scintillation light emitted by events located
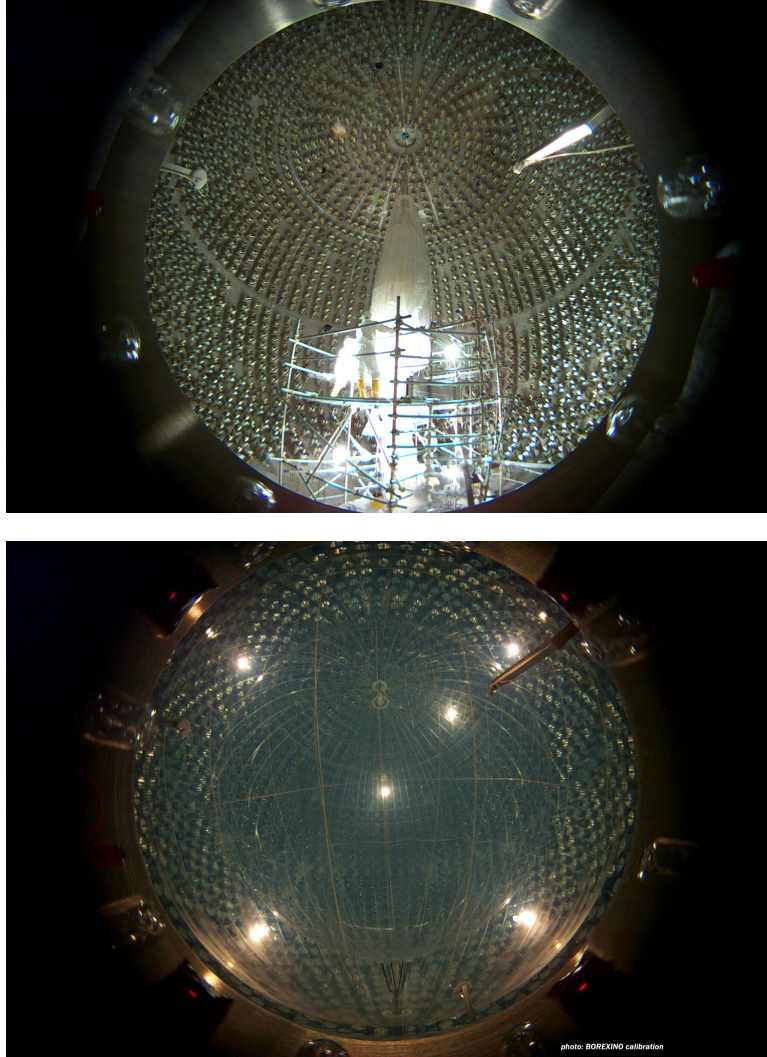
Figure 2.6: Top: Installation of the nylon vessels within the SSS. Bottom: Inner detector on May 15th 2007, a few hours after the filling with scintillator was completed. The data taking period for the ^{7}Be analysis began the next day. Pictures taken by one of the seven cameras installed on the SSS.

near the top and bottom of the IV, leading them to be misreconstructed towards the center of the detector (see Figure 3.16). For this reason the Fiducial Volume used for the ^{7}Be analysis has a vertical cut at $|z| = 1.67$ m in addition to a 3 m radial cut.
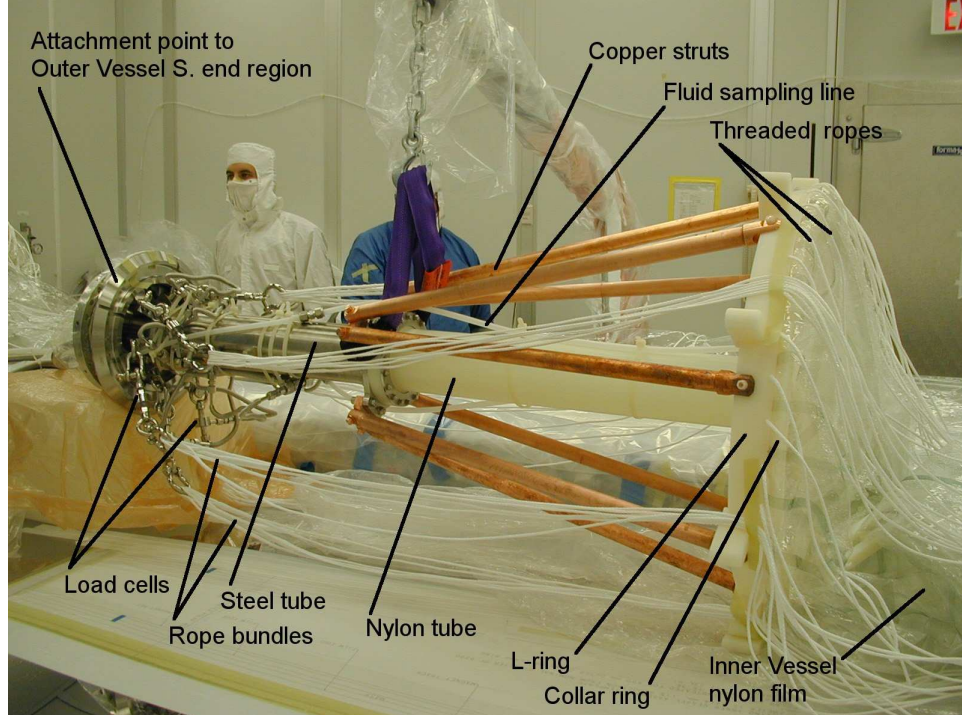
Figure 2.7: The bottom end region of the Inner Vessel during assembly. The stainless steel parts on the left connect to the bottom endcap of the Outer Vessel, with the steel and nylon tubes oriented vertically. The author's advisor can be seen in the white clean room suit. Figure taken from [43].

2.2 Data Acquisition

In this section we will describe the data acquisition system used to readout the signals from the 2212 inner detector and 208 outer detector photomultiplier tubes. Detailed descriptions of the system can be found in [44, 45].

2.2.1 Channel Data

The PMTs are supplied with positive high voltage and are AC coupled to the front-end electronics. The signal from each phototube is split into two, to determine the timing and charge information.

The timing signal is amplified by a low-noise fast amplifier and fed to a discriminator to obtain the photoelectron arrival time. The threshold for the discriminator is set to correspond to roughly 0.2 p.e. [45] and channels whose signal exceeds the

51

threshold are considered hit. We note that in this system, only the timing of the first photoelectron is recorded, and it is this time that is associated with the hit. This creates some complications with data analysis algorithms that depend on the time profile of the pulse shape, such as the position reconstruction (Section 4.3) and the Gatti parameter (Section 4.5). The charge signal is integrated on a gateless charge integrator [57] with a decay time of roughly $\tau_D = 500$ ns [45] and an automatic reset.

Both the timing and charge information are then digitized by a dual input FADC. The output of the timing discriminator is used to generate two pulses $\Delta t = 80$ ns apart. The first of those samples a 10 MHz triangular wave which, along with a counter, is used to determine the timing of the hit with a resolution of better than 0.5 ns [45]. At this time (t_0) the integrated charge signal is also sampled to obtain the baseline integrator output. The second pulse samples the integrator output at a time Δt later. The charge arriving within the time interval $[t_0, t_0 + \Delta t]$ is then calculated as:

$$Q = G^{-1} \left[(V(t_0 + \Delta t) - V_{off}) - (V(t_0) - V_{off})e^{-\Delta t/\tau_D} \right] \quad (2.7)$$

where $V(t)$ is the integrator output voltage at time t, $G = 129$ mV/pC [45] is the integrator gain and V_{off} is the DC offset. The digitized timing and charge information is then stored in a temporary memory buffer, awaiting a trigger signal.

Once the timing discriminator fires, it is automatically disabled for a period of 140 ns. Thus, if a second photoelectron arrives within 140 ns of the first, no new hit is recorded. However, since the charge integration is carried out over a time interval of $\Delta t = 80$ ns, the arrival of multiple photoelectrons within the first 80 ns is recorded in the charge information. We note that in addition to the hardware dead time of 140 ns, there is an additional 40 ns dead time imposed in software to avoid false retriggers. Thus, for any photoelectron produced between 80 and 180 ns of the first

photoelectron on that channel, neither the time nor charge is recorded. The effects of this on the energy reconstruction are discussed in Section 5.1.5.5.

The calibration and alignment of the charge and timing information is facilitated by the use of a fast diode laser whose light is carried simultaneously to each of the PMTs within the SSS by a dedicated system of optical fibers. Details regarding the laser system can be found in [45] while the calibration process is described in Section 4.1.1.

2.2.2 Trigger

The trigger system is set to fire when a fixed number of channels are hit within a given time interval. These values are normally set to 25 hits (roughly corresponding to 50 keV) in a window of 60 ns, though the trigger value for the number of hits is sometimes varied. When the required threshold is met, a trigger signal is generated and sent to all the boards. At this signal all the data within a fixed time interval around the trigger, referred to as the "trigger gate", is recorded. At the start of data taking the length of the trigger gate was set to 6.9 μs, but it was later increased to 16.5 μs. In addition to the trigger signal, the absolute time is read from a GPS clock (with an accuracy of 100 ns) and associated with the given event. The dead time following each trigger was initially 6.1 μs but this was decreased to 2.5 μs at the same time that the length of the trigger gate was enlarged. The typical trigger rate is approximately 26 Hz (see Section 6.2.4 for more details).

Along with the standard inner detector trigger, there are a few other types of events that can create a trigger:

- Outer Detector Trigger

    A event occurring in the outer detector water tank can also create a trigger, regardless of the state of the inner detector. The threshold for the outer detector

is normally set at 6 hits on the outer detector PMTs within 150 ns. For more details on the outer detector electronics we refer the reader to [44, 45].

- Neutron Trigger

  In order to gain information about spallation neutrons produced by muons passing through the detector, a new trigger was introduced in December 2007. Following every outer detector trigger, a special detector trigger is issued, regardless of the inner detector status. In order to have a high efficiency for detecting the neutron capture γs ($\tau_{cap} = 254.5 \pm 0.8$ μs), the length of the trigger gate used is 1.6 ms, roughly 100 times longer than the standard inner detector trigger gate.

- Laser Trigger

  The fast diode laser which is optically connected to each individual PMT in the inner detector is fired in coincidence with a electronic pulse used to trigger the detector.

- Electronic Pulse Trigger

  A pulse from a pulse generator is sent to the test input of each front-end channel, simulating a signal without an input from the photomultiplier tubes.

- Random Trigger

  In this trigger the data from each channel is read out, regardless of the detector status.

The last three triggers listed (laser, electronic and random) are fired every 0.5 s during a run and are used for determining the number of working channels, calibrating the charge and timing of each channel as well as determining the dark rate. These calibrations are described in Section 4.1.1. We emphasize the fact that regardless of the type of trigger, data from both the inner and outer detector is read out and recorded.

2.3　Inner Vessel Leak

In April 2008 a leak developed in the Inner Nylon Vessel, causing scintillator to leak out into the buffer region within the Outer Vessel. In this section we will briefly discuss the possible causes of the leak, how it was discovered, and the steps taken to decrease the leak rate and minimize its effect on data taking and analysis.

2.3.1　Cause

The exact cause of the leak is difficult to pinpoint but it is thought to be due to temperature (and hence density) variations in the scintillator and buffer liquids. In October 2007 it was noticed, that due to the cooling of the scintillator after the initial filling, water had begun to condense out of the scintillator, forming a haze in the Inner Vessel. In order to try and remove the haze, starting in December 2007 the water in the external water tank was heated, conductively heating the scintillator and buffer in the Inner Vessel. While this was effective in removing the haze, the temperature variations caused noticeable changes in the Inner Vessel shape and volume (due to large buoyancy forces) that may have led to an eventual tear in the nylon vessel. There is also a possibility that the leak rate was exacerbated by the turning on of the OPERA magnet. The OPERA experiment, which is also located in Hall C, had their magnet turned on starting June 17th 2008 (note that the magnet had also been previously turned on between Feb 7th and Feb 18th). At the time there was no cooling system in place for the magnet and since the temperature in Hall C was unregulated, this caused an overall heating of the hall. The corresponding increase in temperature inside the detector may have increased the rate of the leak, though the correlation between the operation of the magnet and the leak rate has not been firmly established.

2.3.2 Detection and Analysis

Due to the standard analysis practice of applying a 4.25 m radial cut to restrict the data sample to events within the Inner Vessel (IV), the leak was not detected until September 2008 when a large number of events were found to reconstruct between the Inner and Outer Vessels. At about the same time, samples of buffer taken from the OV showed an abnormally high concentration of PPO confirming that there was in fact a leak in the IV. Subsequent analyses of the event rates in the inner buffer identified the probable leak location as $26° < \theta < 37°$ and $225° < \phi < 270°$, and the start date as approximately April 9th 2008.

2.3.3 Leak Rate and Detector Operations

Soon after the leak was noticed, a series of pictures of the inner detector were taken with the seven CCD cameras mounted on the Stainless Steel Sphere. By comparing the pictures taken by the different cameras one can estimate the volume of the IV (see [58] for a description of the method). Figure 2.8 shows the change in IV volume in time, as estimated from the camera pictures. The large decrease in vessel volume during the early period of the leak is evident and using this method, the leak rate was estimated to be about 1.33 m^3/month [59]. During this period several proposals were put forward in order to reduce the leak rate. The solution that was adopted was to reduce the DMP concentration in the buffer. Distilling the buffer to remove DMP reduces the density difference between the scintillator and buffer fluids, thereby reducing the pressure difference across the leak. Between February 12 2009 and 3rd April 2009 (following two source calibration campaigns and a few scintillator refillings to maintain the sphericity of the IV) the buffer liquid was purified and the DMP concentration reduced from 5 g/l to 3 g/l (first green band in Figure 2.8). This reduced the leak rate to about 0.56 m^3/month [59] as well as greatly reduced the number of events occurring in the buffer (see Figure 3.15). In December 2009 it was

decided to further reduce the DMP concentration to 2 g/l (second green band in Figure 2.8). Following this operation, which concluded at the end of January 2010, the leak rate was further reduced. The most recent estimate for the leak rate is 1.5 m^3/year [60]. A discussion of the event rates due to the leak can be found in Section 3.2.11.1
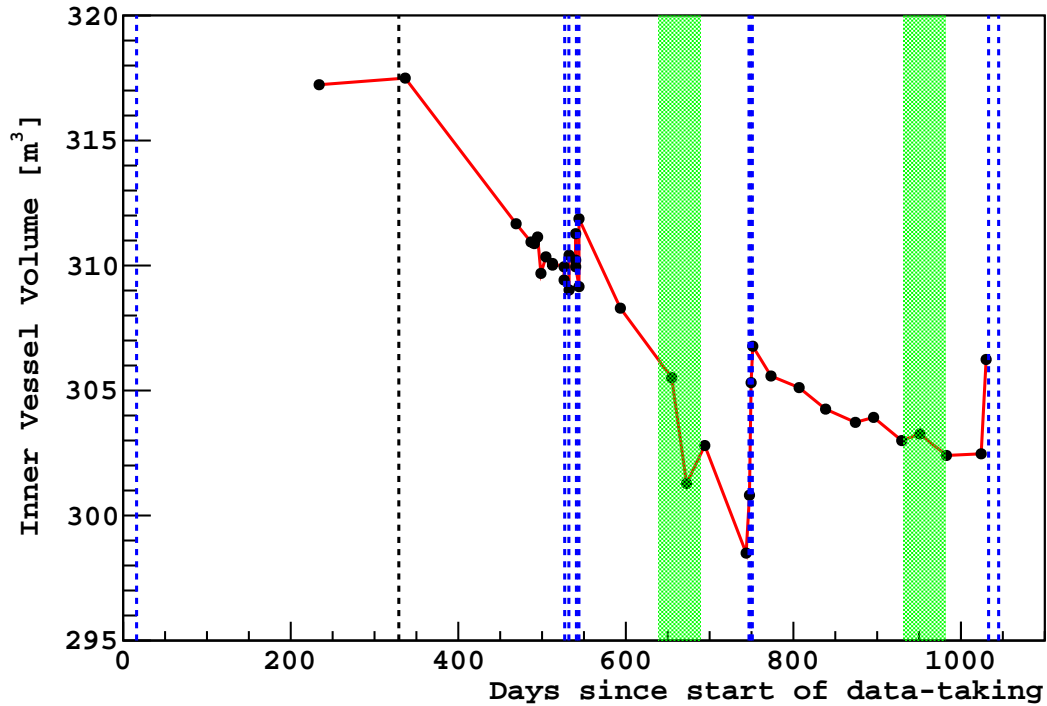

Figure 2.8: Volume of the inner nylon vessel as a function of time. The black points indicate the vessel volume as calculated from pictures of the inner detector by the CCD cameras. The red line is a simple linear interpolation between each set of pictures. The dashed black line marks the best estimate for the start of the leak in the inner nylon vessel. The blue lines indicate refilling of the inner vessel scintillator and the green shaded areas designate buffer purifications and DMP removal. Compare with Figure 3.15 which shows the total event rate in the detector as a function of time.

2.4 Internal Source Calibration

An important requirement for any precision measurement is a detailed understanding of the response of the detector. Analysis of solar neutrino interaction rates in Borexino

depends on two critical factors: the energy and the position of each event. In order to understand the optical and energy response, the detector was designed to allow for the periodic insertion of radioactive sources into the Inner Vessel. However, given the long and difficult history of the Borexino experiment and the remarkably low level of radioactive contamination that was achieved at the time of the first filling, there was a strong reluctance from some members of the collaboration to perform a calibration, for fear of contaminating the detector. With the development of the leak in the Inner Vessel (see previous section) it became clear that some detector operations would need to be performed to reduce the leak rate. In order to make optimal use of the data taken before the leak, a calibration campaign was finally agreed to. Given the success of this first calibration (the radioactive background levels were unaffected [58]), a series of three other calibrations were performed over time. In this section we will briefly describe the source insertion and location systems as well as the four calibration campaigns. The source calibration system was designed and operated by the Virginia Tech group and further details can be found in the Ph.D. thesis of Steven Hardy [58].

2.4.1 Source Insertion Hardware

Extending vertically downwards from a gate valve at the top of the SSS are three concentric tubes that lead to IV (innermost), inner buffer and outer buffer (outermost). The innermost tube that leads to the IV (the one used for the insertion of radioactive sources) has an inner diameter of $4''$ and a length of about 6 m between the top of the gate valve and the bottom of the IV endcap. Located above the water tank, directly above the gate valve is a class 10 clean room containing a custom built glove box for operations related to the insertion and removal of the sources. The sources are lowered into the detector using a series of 1m long, $1.5''$ diameter stainless steel rods. The rods are hollow and weighted to be neutrally buoyant in the Borexino scintillator.

Different numbers of rods can be coupled together to reach different depths within the detector. In order to access positions away from the central vertical axis, a "hinge rod" can be attached, that allows the section of rods below the hinge to rotate up to 90° from the vertical (see Figure 2.9). The angle can be adjusted by means of a 100 ft teflon tube ("tether") that attaches to the lower section of rods (below the hinge), just above the source. By varying the number of rods and the length of the tether, one can therefore reach any position within the 4.25 m radius Inner Vessel. The tether also acts as a conduit for a fiber optic cable that was used to transmit red laser light for the purpose of locating the source (see Section 2.4.2). The tether terminates in a piece of Pyrex tubing that contains a white teflon diffuser for the laser light (see Figure 2.10). In addition to the fiber optic cable, a 30 m long tape measure is also inserted into the tether to aid in the measurement of the tether length. At the end of the last rod is a specially designed coupler that connects the rods, tether and source vial. The source vials used were 1″ diameter quartz spheres with a neck that transitions to Pyrex to help in sealing (see Figure 2.10).

2.4.2 Source Location System

In order to accurately calibrate the position reconstruction algorithm (see Section 4.3) the location of the source was required to be known with an accuracy of 2 cm. While the length of the insertion rods is known to much greater accuracy, this only gives the position of the source relative to the glove box on top of the external water tank, whose position relative to the SSS is not known to the required precision. In addition, for sources located off-axis, the flexibility of the teflon tether tubing means that the angle of the lower arm is not well known. Given these constraints, a camera-based optical source location system was adopted.

There are seven cameras mounted at different position on the SSS. The cameras are commercial grade digital cameras with a CCD resolution of 2.3 million pixels and
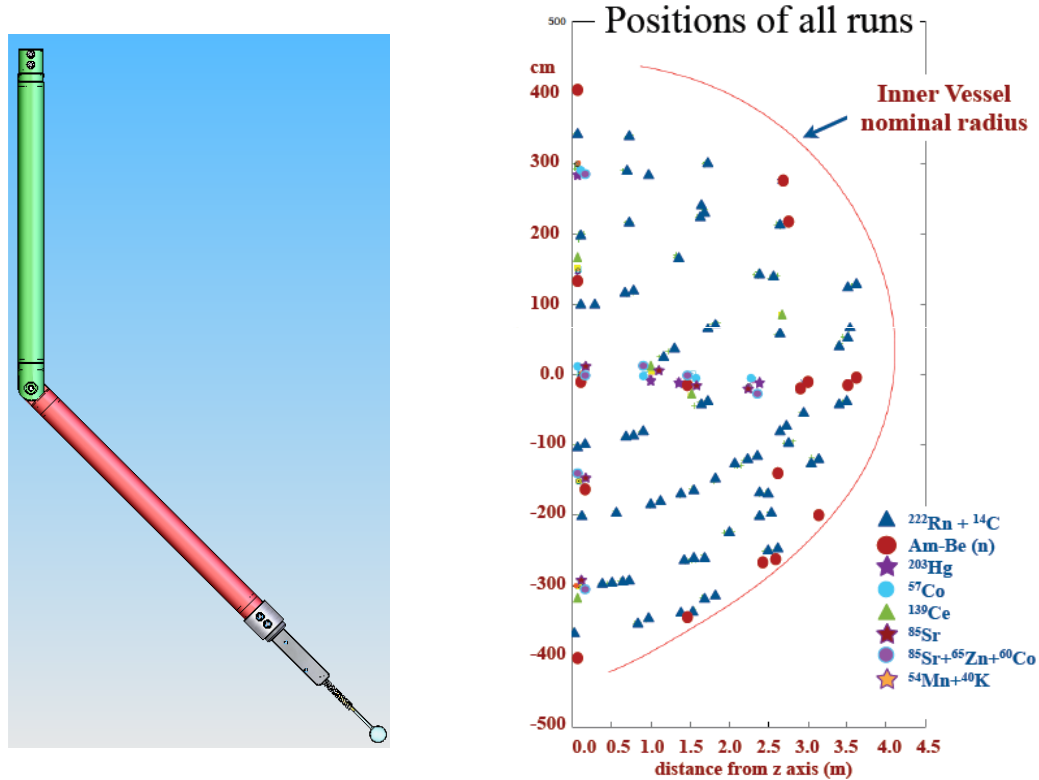
Figure 2.9:   Left: Drawing of the hinge rod, source coupler and source vial. Figure taken from [58]. Right: Source locations used within the Inner Vessel for the various different sources.
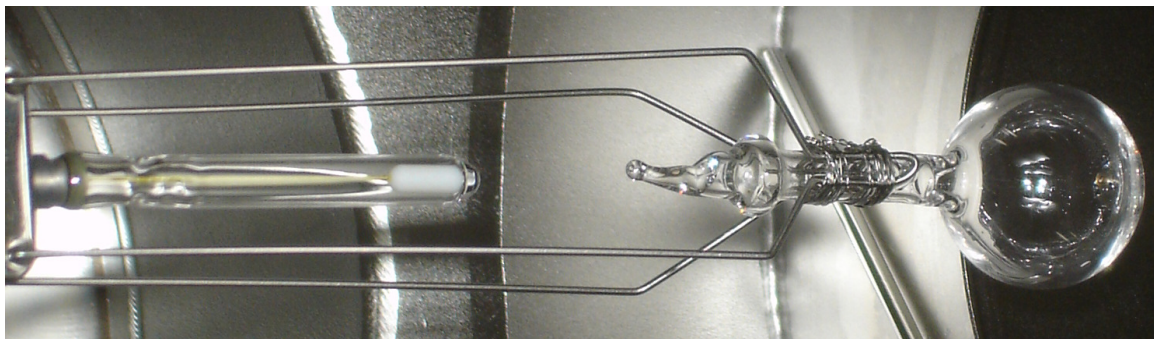
Figure 2.10:   Photograph of calibration source before deployment. Starting from the left, one can see the bottom of the source coupler, the termination of the Teflon tether with a Pyrex tube. The white Teflon diffuser can be seen inside the Pyrex tube, at the bottom. The quartz source vial (far right) is attached to the source coupler by long U-shaped stainless steel wires.

a fish eye lens that enables the entire Inner Vessel to lie within the field of view. Around each camera mount is a ring of eight 50 W halogen bulbs that are used to illuminate the inner detector while pictures of the inner nylon vessel are being taken.

Since the camera and lens assembly shift slightly every time the camera is powered on or off, or a picture is taken, it is necessary to calibrate each picture individually. This is done with the help of red LED's that were installed on each camera which, following a process of "tweaking" [58], allows for the comparison of pictures taken at different times.

The location of the laser diffuser attached above each source is determined using a ray tracing algorithm that combines pictures from different cameras with varying perspectives. This algorithm is able to locate the source with a precision of greater than 2 cm [58], which is extremely useful in tuning the position reconstruction algorithm and determining the fiducial volume uncertainty (see Section 4.3.1.1).

2.4.3 Calibration Campaigns

Between 2008 and 2009, four different internal source calibration campaigns were carried out. In all, 19 different sources were used at 295 different locations within the Inner Vessel, with about 35 days of data-taking recorded [58]. In this section we will briefly describe the different sources used and their contribution to the ^{7}Be analysis.

For the first calibration campaign in October 2008, sources were only deployed "on-axis" and the hinge and tether system was not used. Once the system was proven, the following three campaigns included source locations throughout the Inner Vessel. Figure 2.9 (right), shows the positions of the different sources used in all the campaigns, with a large amount of data taken along the z-axis and the equator.

Four different types of radioactive sources were used within the detector: βs αs, γ-rays and neutrons. A list of all the sources and their corresponding energies are listed in Table 2.2. The β and α sources were usually dissolved in scintillator, and due to their short range, deposited their energy within the source vial itself. Since the scintillator used in the vial was not the exactly the same as the one within the Inner Vessel, the relative quenching and light yield was found to be different from

the intrinsic radioactive contaminants within the IV. On the other hand the longer range of the γ rays sources meant that most of the energy deposition took place within the IV scintillator. In order to prevent pileup with simultaneously emitted βs, the γ sources were usually dissolved in a non-scintillating aqueous solution. For the ^{241}Am-^{9}Be neutron source, a special Delrin source holder was used with 3 mm of lead shielding to absorb the accompanying 60 keV x-ray.

The β and α emissions from the ^{222}Rn source were an important tool in tuning and evaluating the performance of the position reconstruction algorithm due to the widespread deployment of the source within the detector. By comparing the reconstructed position of the sources to the location of the source, as determined by the CCD cameras, we were able to determine the uncertainty and bias of the position reconstruction algorithm and hence evaluate the true volume of scintillator enclosed within the fiducial cuts (see Section 4.3.1.1).

The γ ray sources were used for calibrating the energy response of the detector. Since the γ rays escape the source vial and deposit most of their energy in the IV scintillator, complications arising from the use of a different scintillator (as in the case of the β and α sources) are avoided. Additionally, the monoenergetic peaks allow for easy identification of the source spectra above the background and accurate energy evaluation. The γ sources were specifically chosen to have energies that spanned the entire range of interest for the ^{7}Be analysis. The calibration of the γ and β energy scale (using Birk's quenching model) at the center of the detector is described in detail in Section 5.2. Since the γ rays sources were not used at as many locations, the spatial variation in the detector energy response was studied using the relative peak positions of the ^{214}Po αs from the ^{222}Rn source (see Section 5.3). The γ sources were also useful in testing the model of the detector energy response to monoenergetic events (see Section 5.1) The neutron source was mainly used to study the energy response at higher energies, and was not used for this analysis.

Particle Type	Radioactive Isotope	Energy [MeV]	Calibration Campaign
β	^{14}C	0.156	I, II, III, IV
β	^{214}Bi (^{222}Rn)	3.27	I, II, III, IV
α	^{214}Po (^{222}Rn)	7.69	I, II, III, IV
γ	^{57}Co	0.122	IV
γ	^{139}Ce	0.165	IV
γ	^{203}Hg	0.279	III
γ	^{85}Sr	0.514	I, III, IV
γ	^{54}Mn	0.834	I, III
γ	^{65}Zn	1.12	III
γ	^{60}Co	1.17, 1.33	III
γ	^{40}K	1.46	III
n	^{241}Am-^{9}Be	11	II, III, IV

Table 2.2: List of radioactive isotopes used in the source calibration campaigns. The energies listed for β and neutron (n) emitters is the maximum energy. The calibration campaigns are numbered in chronological order with I referring to the first, on-axis, calibration.

Chapter 3

Signals and Backgrounds
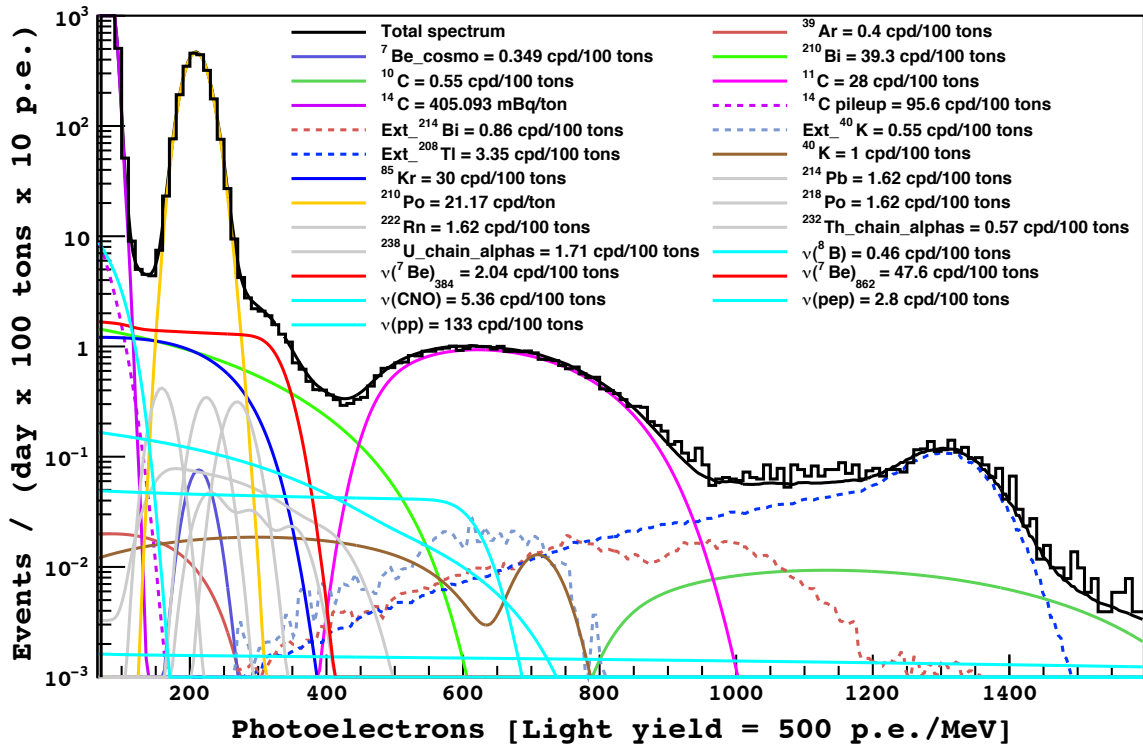
Figure 3.1: Simulated spectra of the various signals and backgrounds in the fiducial volume of the Borexino detector. Rates, given in the legend, are determined using estimates from both theory and data (see the text in this section for a detailed discussion of each component). The total spectrum is shown in black (smooth line), while the true data (black histogram), after all selection cuts, is superimposed.

3.1　Solar Neutrinos

Solar neutrinos passing through the Borexino detector are detected through their interactions with the liquid scintillator contained in the Inner Vessel. The neutrinos can scatter elastically with electrons, protons and neutrons in the scintillator, imparting energy to the target particle. The recoiling particle then ionizes the scintillator molecules around it (either directly for electrons and protons, or through the scattering with protons, for recoiling neutrons) producing light that is detected. The maximum kinetic energy, T_{max}, is imparted to the recoiling particle when the neutrino scatters backwards, and can be calculated using relativistic kinematics:

$$T_{max} = \frac{2E_\nu}{mc^2 + 2E_\nu} \cdot E_\nu \tag{3.1}$$

where E_ν is the neutrino energy and m is the mass of the particle. The vast majority of solar neutrinos have energies below 2 MeV, which gives a maximum recoil energy of ~ 8 keV for protons and neutrons. Considering that the scintillation light from protons is quenched, with respect to electrons, by roughly a factor of 5 (at 1 MeV), even proton recoils from the highest energy *hep* neutrinos have an electron-equivalent energy under 150 keV and are lost below the ^{14}C background. Therefore the most relevant interaction for solar neutrinos in Borexino is elastic scattering off electrons. Solar neutrinos can also interact through quasi-elastic scattering of a carbon nucleus. The threshold energy for ^{12}C (^{12}C $+ \nu_e \rightarrow$ ^{12}N $+ e^-$) is 17.4 MeV, higher than all but the most energetic *hep* neutrinos, but the threshold for the corresponding interaction on ^{13}C is only 2.2 MeV. The natural relative abundance of ^{13}C in the scintillator is about 1.1%, which gives an expected rate of interactions from ^{8}B neutrinos of ~ 2.5/year/100 tons [61]. While this is an extremely low rate of events, the delayed coincidence between the emitted electron and the positron from the decay of ^{13}N may enable us to distinguish it from other backgrounds. An analysis of this signal is

currently underway by the collaboration, but it will not be discussed further in this thesis.

### 3.1.1 Neutrino - Electron Elastic Scattering
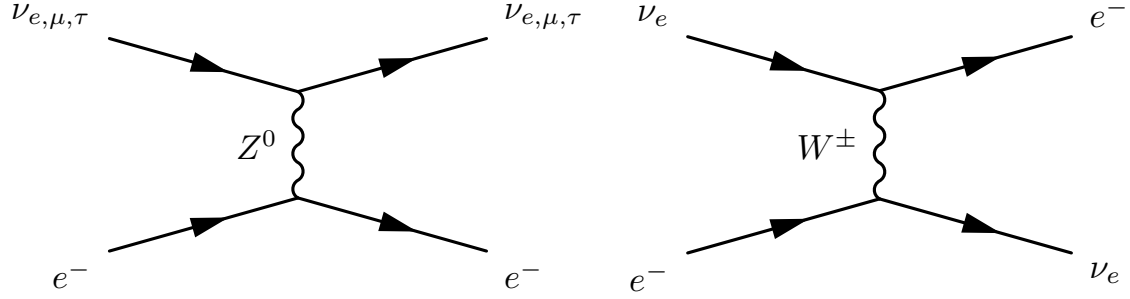
Figure 3.2: First-order Feynman diagrams for neutrino-electron elastic scattering. Left: Neutral-current scattering through the exchange of a Z^0 boson. All neutrino flavors can participate in this interaction. Right: Charged-current scattering through the exchange of a charged W boson. Only electron neutrinos may interact through this channel.

The elastic scattering of neutrinos and electrons can take place through either a neutral or charged current interaction. All neutrino flavors can scatter through the neutral current interaction (shown on the left in Figure 3.2), but only electron neutrinos can also scatter off electrons by exchanging a W boson (Figure 3.2, right). To first order, ignoring radiative corrections, the differential cross section for producing a recoiling electron with kinetic energy T when scattering off a neutrino with energy E_ν is:

$$\frac{d\sigma}{dT}(T, E_\nu) = \frac{\sigma_0}{m_e c^2} \left[g_L^2 + g_R^2 \left(1 - \frac{T}{E_\nu} \right)^2 - g_L g_R \frac{T}{E_\nu} \frac{m_e c^2}{E_\nu} \right] \tag{3.2}$$

$$\sigma_0 \equiv \frac{2 G_F^2 m_e^2}{\pi \hbar^4} = 8.81 \times 10^{-45} \text{ cm}^2 \tag{3.3}$$

where m_e is the mass of the electron and G_F is the Fermi constant. The parameter $g_R = \sin^2 \theta_W \sim 0.2312$ (θ_W is the weak mixing angle) for all neutrinos while $g_L = \sin^2 \theta_W \pm 1/2$ where the plus sign corresponds to electron neutrino scattering and the

minus sign is for muon and tau neutrino scattering.

The kinetic energy of the recoiling electron is related to the electron scattering angle θ (with respect to the incoming neutrino) through the relation:

$$T = \frac{2E_\nu^2 \cos^2 \theta}{(1 + E_\nu)^2 - E_\nu^2 \cos^2 \theta} \tag{3.4}$$

As mentioned earlier, the maximum energy T_{max} is imparted to the electron for a back-scattering neutrino ($\theta = 0$). Integrating the differential cross section from $T = 0$ to T_{max} for a given neutrino energy gives:

$$\sigma(E_\nu) = \sigma_0 \frac{T_{max}}{m_e c^2} \left[(g_L^2 + g_R^2) - \left(g_R^2 + g_L g_R \frac{m_e c^2}{2E_\nu} \right) \frac{T_{max}}{E_\nu} + g_R^2 \frac{T_{max}^2}{3E_\nu^2} \right] \tag{3.5}$$

Radiative corrections to the above first-order total cross section are on the order of a few percent [62].

3.1.1.1 ^{7}Be Neutrinos

^{7}Be neutrinos are produced following the capture of an electron on a ^{7}Be nucleus. Since the final state contains only two particles (the ^{7}Li daughter and the neutrino) the neutrinos produced are monoenergetic. The principal production branch leads to a 0.862 MeV neutrino, though the ^{7}Li can also be produced in an excited state (B.R. 10.4%) giving rise to a 0.384 MeV neutrino. The monoenergetic 0.862 MeV ^{7}Be neutrinos produce a fairly flat electron recoil spectrum with a sharp, Compton-like, edge at $T_{max} = 0.665$ MeV (the corresponding edge for the 0.384 MeV neutrinos occurs at 0.231 MeV).

As can be seen from Eqs. 3.2 and 3.5, the cross section for the interaction depends on the flavor composition of the ^{7}Be neutrinos as they pass through the detector. Table 3.1 lists the total cross sections for different neutrino flavors and energies. At

0.862 MeV, the ratio of the cross sections for electron and other neutrino flavors is:

$$\frac{\sigma_{\nu_e}(0.862 \text{ MeV})}{\sigma_{\nu_{\mu,\tau}}(0.862 \text{ MeV})} \sim 4.51 \tag{3.6}$$

Since solar neutrinos are produced as electron neutrinos, and the cross sections for muon and tau neutrinos are identical, the flavor composition of the neutrinos can be expressed in terms of the electron neutrino survival probability P_{ee} (assuming three flavors of neutrinos). P_{ee} is calculated in the LMA-MSW solution using the analytical expression derived in [40]. As part of the derivation, non-adiabatic corrections for the propagation of neutrinos are shown to be small (see Section 1.4.1.4) and the survival probability is averaged over the production region of the corresponding neutrino species. We have ignored Earth-matter effects (see Section 1.4.1.3) and have used the vacuum oscillation parameters $\Delta m^2 = (7.59 \pm 0.20) \times 10^{-5}$ eV^2 and $\sin^2(2\theta) = 0.87 \pm 0.03$ [1] to obtain a value of $P_{ee} = 0.542 \pm 0.013$ at 0.862 MeV. The oscillated differential electron recoil spectrum, including radiative corrections [62], is shown in Figure 3.3 for both branches of ^{7}Be neutrinos combined and the oscillated total cross sections for ^{7}Be neutrinos, are listed in Table 3.1. We note that the global best values for some of the constants and parameters used in calculating the radiative corrections in [62] have changed since publication. The latest values [63], used here, are listed in Table 3.2.

The total rate of ^{7}Be interactions in Borexino, per target mass, is given by:

$$R = \Phi \left(P_{ee}\sigma_{\nu_e} + (1 - P_{ee})\sigma_{\nu_{\mu,\tau}} \right) n \tag{3.7}$$

$$\equiv \Phi \sigma_{\nu_{osc}} n \tag{3.8}$$

where Φ is the flux of neutrinos at the Earth, σ_{ν_x} are the total cross sections discussed above (listed in Table 3.1) and n is the number of electrons per unit mass of scintillator. The standard convention in Borexino is to express this rate in terms
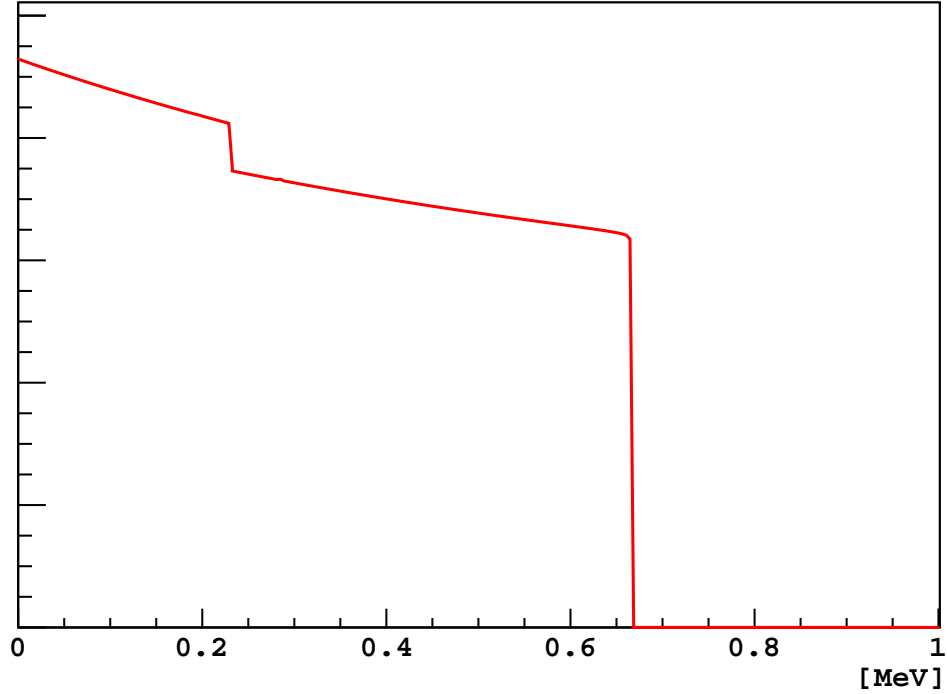
Figure 3.3: Electron recoil spectrum for ^{7}Be oscillated neutrinos. The sharp edge at 0.231 MeV is from the 10.4% 0.384 MeV branch, while the edge at 0.665 MeV is from the 0.862 MeV neutrinos. The scale on the y-axis is arbitrary.

of counts per day per 100 tons (cpd/100 tons). For the 862 keV branch, using the high metallicity Standard Solar Model (GS98) [17] and the LMA-MSW oscillation framework [40], the corresponding numbers are $\Phi = 0.896 \times (5.00 \pm 0.35) \times 10^9$ cm^{-2} s^{-1} and $P_{ee} = 0.542 \pm 0.013$. The electron density of the scintillator is $n = (3.307 \pm 0.003) \times 10^{31}/100$ tons. Plugging in these numbers into Eq. 3.7, taking into account the uncertainties and correlation between the different cross sections, gives an expected rate of 47.6 ± 3.4 cpd/100 tons. For the low metallicity Standard Solar Model (AGSS09) the neutrino flux is $\Phi = 0.896 \times (4.56 \pm 0.32) \times 10^9$ cm^{-2} s^{-1} [17], which translates into an expected rate of 43.4 ± 3.1 cpd/100 tons. Figure 3.4 shows the predicted rate, assuming the high metallicity Standard Solar Model flux, for different values of the electron neutrino survival probability. The rate varies from 16 cpd/100 tons, in the case of the neutrinos having completely converted to

Scattering	E_ν [MeV]	Cross Section [cm^2]
ν_e-e	0.384	$(1.91389 \pm 0.00080) \times 10^{-45}$
$\nu_{\mu,\tau}$-e	0.384	$(0.50816 \pm 0.00026) \times 10^{-45}$
ν_{osc}-e	0.384	$(1.28834 \pm 0.00035) \times 10^{-45}$
ν_e-e	0.862	$(5.7828 \pm 0.0025) \times 10^{-45}$
$\nu_{\mu,\tau}$-e	0.862	$(1.28204 \pm 0.00077) \times 10^{-45}$
ν_{osc}-e	0.862	$(3.7215 \pm 0.0011) \times 10^{-45}$

Table 3.1: Neutrino-electron scattering cross sections for the two branches of ^{7}Be neutrinos. Cross sections are calculated using radiative corrections [62] with updated values (see Table 3.2). $\nu_{osc} - e$ refers to the average cross section obtained for a electron neutrino survival probability of 0.555 at 0.384 MeV and 0.542 at 0.862 MeV, assuming three neutrino flavors. The uncertainties for the oscillated cross sections are fractionally smaller due to anti-correlation ($\rho = -0.74$) between the ν_e and $\nu_{\mu,\tau}$ uncertainties.

Constant / Equation	Value Used
G_F	1.166364(5)
$\sin^2(\theta_W)$	0.23116(13)
(A3)	1.0127 ± 0.0002
(A4)	$0.9786 + 0.0097$ I(T) ± 0.0003
(A7)	$0.9965 - 0.00037$ I(T) ± 0.0003

Table 3.2: Updated values for the constants and expressions used with the formulae in [62], to calculate the neutrino-electron scattering cross-sections with radiative corrections. The (Ai) terms refer to specific equations in Appendix A of [62], while the new values are taken from [63].

ν_μ and ν_τ, to 74 cpd/100 tons in the absence of oscillations. The 1σ range for the expected rate, considering only the uncertainties in the neutrino mixing parameters [1], is 47.6 ± 0.7 cpd/100 tons.

We note that for the sake of convenience while fitting, the 0.384 and 0.862 MeV branches are combined into a single spectrum. As mentioned earlier, the production ratio between the two branches is 10.4 : 89.6. Accounting for the energy dependent survival probability and cross-sections, the ratio between the interaction rates is 3.9 : 96.1.
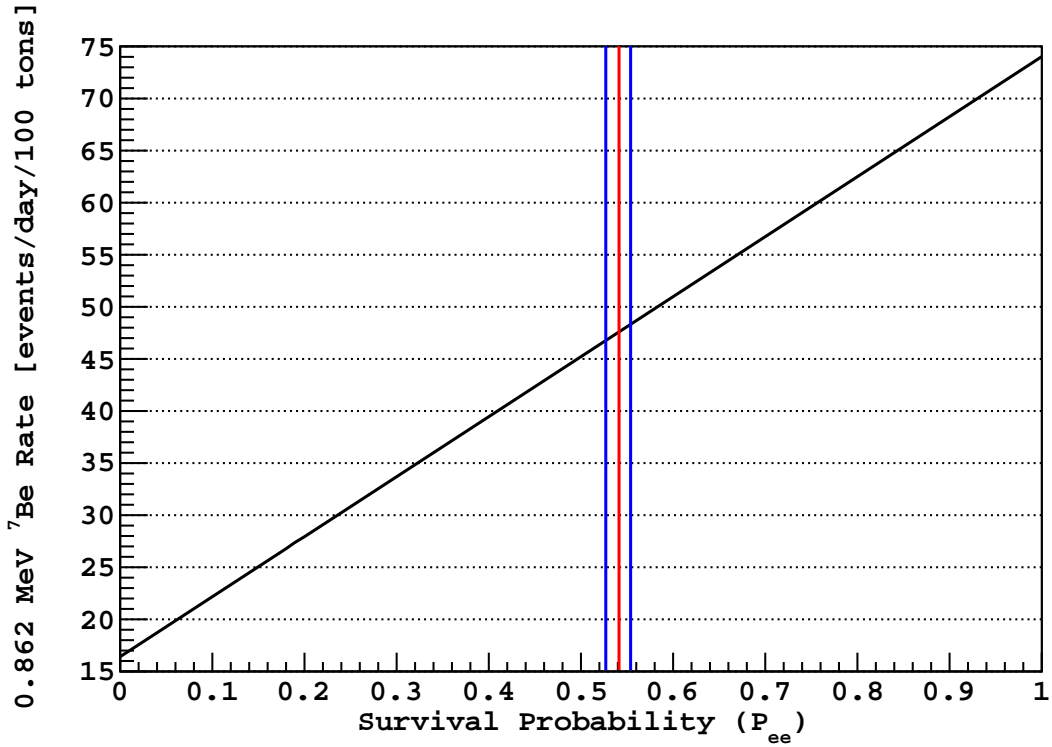
Figure 3.4: Predicted ^{7}Be rate (0.862 MeV branch) as a function of the electron neutrino survival probability P_{ee}, assuming three neutrino flavors. The ^{7}Be neutrino flux is taken to be $0.896 \times 5.00 \times 10^9$ cm^{-2}s^{-1} [17]. The red line indicates the central value for the survival probability in the LMA-MSW solution [40], while the blue lines are the 1σ errors obtained from the uncertainty in the neutrino oscillation parameters [1].

3.1.1.2 Other Solar Neutrinos

For the other monoenergetic solar neutrino species, *pep* (1.445 MeV), the spectrum is calculated in the same way as for the ^{7}Be neutrinos, using the appropriate electron neutrino survival probability of 0.531. For neutrinos emitted with a continuous spectrum (*pp*, ^{8}B, ^{13}N, ^{15}O, ^{17}F) the neutrino-electron scattering cross section has to be integrated over the neutrino energy spectrum also taking into account the energy-dependent neutrino survival probability:

$$R = \Phi n \int S_\nu(E) \left(P_{ee}(E)\sigma_{\nu_e}(E) + (1 - P_{ee}(E))\sigma_{\nu_{\mu,\tau}}(E) \right) dE \qquad (3.9)$$

where $S_\nu(E)$ is the normalized energy spectrum of the neutrino and the integral is performed over the neutrino energy range. The shape of the neutrino energy spectra were obtained from [39] and the expected rates for the various species are given in Table 3.3. We note that for convenience during fitting, we have combined the ^{13}N, ^{15}O and ^{17}F recoil spectra into a single spectrum, referred to as the CNO spectrum. For most of the analysis, the rate of the CNO species is fixed to the sum total of the constituent neutrino spectra. The assumed rate of the solar neutrino species are varied during systematic tests (see Section 6.8.3.1) but due to the strong correlations between the three neutrino rates ($\rho = 0.99$ [64]) the shape of the spectrum is unaffected.

Neutrino Species	Expected Rate [cpd/100 tons]
pp	133.0 ± 0.8
pep	2.80 ± 0.03
CNO	5.36 ± 0.78
^{8}B	0.46 ± 0.06

Table 3.3: Expected neutrino interaction rates assuming the high metallicity (GS98) SSM neutrino fluxes [17] and the LMA-MSW solution [40] using oscillation parameters from [1]. Uncertainties given only include the uncertainty in the SSM fluxes.

The energy spectra for the different solar neutrino species are shown in Figure 3.5, after including the effects of the detector energy response.

3.2 Backgrounds

In scintillator detectors there is no way to individually distinguish electron recoils produced by scattering neutrinos from electrons either emitted during β decay or Compton scattered off γ rays. Thus all neutrino interaction rates must be measured using statistical fits to the data. The ^{7}Be analysis is based on fitting the energy spectrum of all events within a given fiducial volume (FV). In order to obtain a measurement with high precision, it is therefore necessary to keep the background that overlaps with the ^{7}Be recoil spectrum as low as possible. In this section we
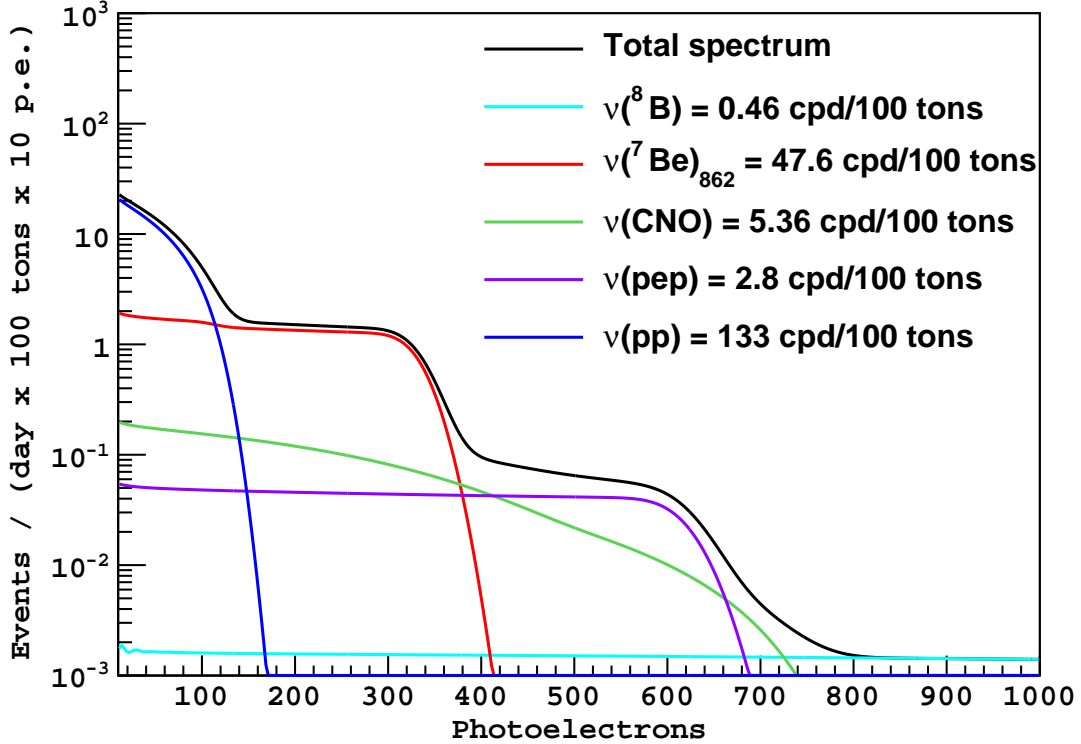
Figure 3.5: Simulated energy spectra (including detector energy response) for solar neutrinos in Borexino. Rates are fixed to the SSM prediction [17] in the LMA-MSW solution [40] using oscillation parameters from [1].

discuss the various backgrounds present in Borexino and their effect on the final measurement.

3.2.1 ^{14}C

^{14}C is a naturally occurring radioactive isotope of carbon. It is produced in the upper layers of the atmosphere through the interaction of cosmogenic neutrons with nitrogen. The ^{14}C then reacts with oxygen to form carbon dioxide which is absorbed by plants, and consequently other organic material. Even though ^{14}C has a geologically short half-life ($\sim$ 5730 years), it is constantly being replenished by the cosmic ray flux. The ratio of ^{14}C to ^{12}C in the atmosphere, as well as all living things, is therefore constant ($\sim 10^{-12}$ g/g). Once the organism has died the ^{14}C begins to decay as there

is no further intake of carbon from the atmosphere. The presence of ^{14}C in organic matter is an invaluable tool for historians as it allows for the method of radiocarbon dating. However for low background experiments using organic scintillator, ^{14}C is as an unavoidable background that limits the energy threshold that can be reached. ^{14}C is chemically identical to ^{12}C and thus it can not be removed from organic scintillators through purification. In order to reduce the levels of contamination, the Borexino scintillator is derived from petroleum from deep underground where the levels of ^{14}C are reduced by roughly a factor of a million ($\sim 3 \times 10^{-18}$ g/g). Since the petroleum has been underground for millions of years, the remaining trace amounts of ^{14}C are possibly due to underground production of neutrons.

Even with the large reduction in contamination, ^{14}C, a β emitter, is by far the largest background in Borexino. The ^{14}C rate is roughly 40 Hz/100 tons ($\sim 75,000$ times higher than the expected ^{7}Be signal rate), though a hardware trigger threshold at ~ 50 keV reduces the trigger rate to roughly 29 Hz in the Inner Vessel. Fortunately the endpoint of the ^{14}C β decay is at 156 keV, low enough (even after the smearing effects of the detector energy resolution) that we can safely start the ^{7}Be analysis beyond the ^{14}C spectrum without losing too much statistics. However, the prospect of observing the low energy pp neutrino spectrum in Borexino is severely hampered by the high ^{14}C rate in that energy region.

3.2.2 Pileup

The length of the trigger acquisition window (~ 16.5 μs) is long compared to the typical duration over which photons from a scintillation event are detected (~ 1 μs). It sometimes happens that two distinct physical events, located in different regions of the detector, record hits during the same trigger gate and therefor a special software clustering algorithm (see Section 4.2) is needed to assign hits to specific events. Since the current clustering algorithm is based only on the temporal distributions of hits, it

is not possible to perfectly separate events whose hits overlap in time. For the purpose of accurate energy reconstruction, this sets a lower limit of ($\sim$ 1 μs) for the time separation between two events. For events that are separated by less than 1 μs but more than 250 ns, we may not be able to correctly assign hits but, due to the distinct shape of the scintillation time profile, we can still detect the presence of two individual events and simply reject the two events, at the cost of some livetime. For events separated by less than 250 ns, even detecting two distinct pulses becomes difficult and all the hits are often mistakenly regarded as coming from a single event. We refer to these events as pileup. Pileup events are an extremely dangerous background since their unusual time profile makes them difficult to model both analytically or through Monte Carlo simulations. We will discuss some of their properties below.

Since the trigger rate of the detector is dominated by ^{14}C, the most common source of pileup events are two ^{14}C events occurring at nearly the same time. The rate of these events can be easily calculated. The rate of ^{14}C decays in the detector is approximately 40 Hz/100 tons or $\lambda = 111$ Hz in the entire Inner Vessel (278 tons). If we assume that any two events with a time separation of less than T $= 250$ ns (see Section 4.2.1) will cause a pileup event, then the probability of having pileup in any given trigger is $1 - e^{-2\lambda T} = 5.56 \times 10^{-5}$. Given an average detector trigger rate of 26.2 Hz, this implies a total ^{14}C pileup rate of 125.9 events/day. The corresponding rate for the ^{210}Po contribution to the pileup rate, is 0.29 events/day, assuming a ^{210}Po rate of 8000 cpd/100 tons.

While the total rate of pileup events is easy to estimate, it is unclear how many of these events pass the selection cuts (many of which are based on the time profile of hits) used for the ^{7}Be analysis. The most important of these cuts is the fiducial volume cut, which selects only those events that reconstruct within a specific volume of the inner detector. The reconstruction of the position of an event (described in detail in Section 4.3) assumes a specific time profile of hits obtained from single

scintillation events, and it is difficult to predict how it performs on pileup events. The reconstructed position of a pileup event depends on both the relative time and energies of the component events as well as their true individual locations. If the overall distribution of reconstructed pileup events is uniform within the Inner Vessel, then the pileup rate corresponds to 45.3 cpd/100 tons. In the extreme case where every pileup event reconstructs within the fiducial volume (75.7 tons), the rate of pileup events in the final energy spectrum would be 166.3 cpd/100 tons. We can use a simple model to study the behavior of the distribution of pileup events, by assuming that the reconstructed position will be the weighted average of the two constituent events, where the weight is the fractional energies of the respective interactions. In this basic model we ignore the effect of the relative time of the two events (which is a crucial part of the position reconstruction algorithm). The result of such a simulation yields 57.5% of pileup events reconstructing within the fiducial volume, corresponding to a spectrum rate of 95.6 cpd/100 tons. The different estimations of the pileup rates in the final energy spectrum are summarized in Table 3.4. Predictions regarding the fraction of pileup events passing other selection cuts suffer similar uncertainties.

Pileup Dist.	Rate in FV [cpd/100 tons]	Rate above Given Threshold (in p.e.) [cpd/100 tons]					
		100	120	130	135	140	145
	1	0.0199	0.0032	0.0010	0.0006	0.0003	0.0002
Uniform	45.3	0.903	0.143	0.047	0.026	0.014	0.007
W. Avg.	95.6	1.905	0.302	0.099	0.054	0.029	0.014
All in FV	166.3	3.314	0.526	0.173	0.095	0.050	0.025

Table 3.4: Estimated pileup rates assuming different distributions of reconstructed events. W. Avg. refers to a model where pileup events are reconstructed at the average position of the two events, weighted by their relative energies. The second set of columns gives the rate of fiducial volume events above the corresponding threshold energy (including detector resolution effects). The threshold used for the standard [7]Be analysis fit is 145 p.e. See Figure 3.6 for comparison to the [7]Be recoil spectrum.

Given the large variation in the estimation of the rate of pileup events, it would be nice to be able to obtain the rate directly from a fit to the energy spectrum.
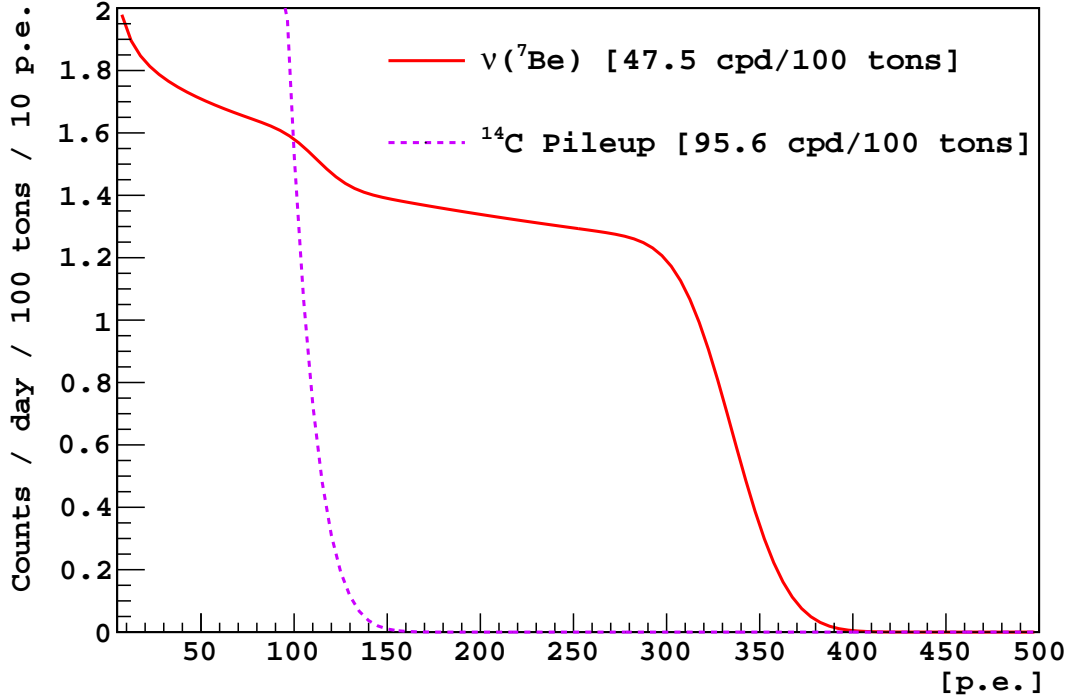
Figure 3.6: ^{14}C pileup spectrum, with the rate calculated assuming a weighted average reconstruction model (see text for details). As a comparison, the ^{7}Be electron recoil spectrum is also shown with the expected rate from the Standard Solar model assuming the LMA-MSW solution. The standard ^{7}Be analysis fit begins at 145 p.e.

Unfortunately most of the ^{14}C pileup spectrum is obscured by the much higher rate ^{14}C, and the tail beyond the end point of ^{14}C is a featureless falling spectrum that very closely matches the shape of the pp neutrino spectrum. As a further complication, many of the selection cuts distort the shape of the pileup spectrum, making it difficult to model analytically. We have therefore chosen to start the fit region above the ^{14}C pileup energy region. The original energy spectrum for ^{14}C pileup events, before any selection cuts, is simply the convolution of the ^{14}C energy spectrum with itself. In Table 3.4 we give the fraction of the spectrum (including the effect of the energy resolution of the detector) above different threshold energies, while in Figure 3.6 we compare the spectrum with the ^{7}Be electron recoil spectrum. The standard fit for the ^{7}Be analysis uses a fit starting point of 145 p.e. which gives a ^{14}C pileup rate of less

than 0.025 cpd/100 tons in the fit region. The ^{7}Be spectrum at 145 p.e. is roughly 40 times higher than the ^{14}C pileup spectrum.

We note that since pileup events are the combination of two distinct events separated by a short time interval, they sometimes appear as a single event with a long tail, mimicking α decays. This causes problems for selection cuts that are based on the time profiles of events such as the Gatti parameter (see Sections 4.5 and 6.4.1.3). For this reason, separation of α and β events is normally only carried out above 145 p.e.

3.2.3 ^{85}Kr

^{85}Kr is one of the most dangerous backgrounds in Borexino. A β emitter with a Q-value of 687 keV, its spectral shape is very similar to the electron recoil spectrum for ^{7}Be neutrinos (see Figure 3.1). ^{85}Kr can be produced naturally from cosmic ray interactions but the current levels are mostly a product of fission in nuclear reactors. As a result of nuclear weapons tests starting in the 1940's, about 5 million curies of ^{85}Kr were released into the atmosphere. In 1962 atmospheric testing was banned, but significant amounts were also later released in the Three Mile Island and Chernobyl accidents. The current level of ^{85}Kr contamination in the air is on the order of 1 Bq/m^3, which is increasing at a rate of roughly 0.03 Bq/m^3/yr [65, 66] due to nuclear reactors. The design level for the Borexino scintillator was less than 1 decay of ^{85}Kr /day/100 tons. In order to achieve this low rate (~ 0.1 μBq/m^3), the scintillator was stripped with specially prepared ultra low Ar/Kr nitrogen (0.06 ppt Kr). Unfortunately, due to a small air leak during the filling, the level of ^{85}Kr in the detector has been measured to be 30 times higher than the design level (30 cpd/100 tons).

Besides fitting the spectral shape, there is another method that can be used to estimate the ^{85}Kr contamination. As can be seen in the decay scheme of ^{85}Kr (Fig-

9/2+ ——————————— 0.0   10.756 Y 18

$^{85}_{36}$Kr$_{49}$

Q(gs)=687.4 keV 20   I(%)   Logft

β- : 100 %   0.434   9.510   9/2+ ———————————— 514

                                              362.8

                                                   514

          ≤2.4E-7 ≥16.7   1/2- ———————————— 281

                                       129.8

                             3/2- ———————————— 151.2

                                       151.2

          99.563   9.4475   5/2- ———————————— 0.0   STABLE

                             $^{85}_{37}$Rb$_{48}$
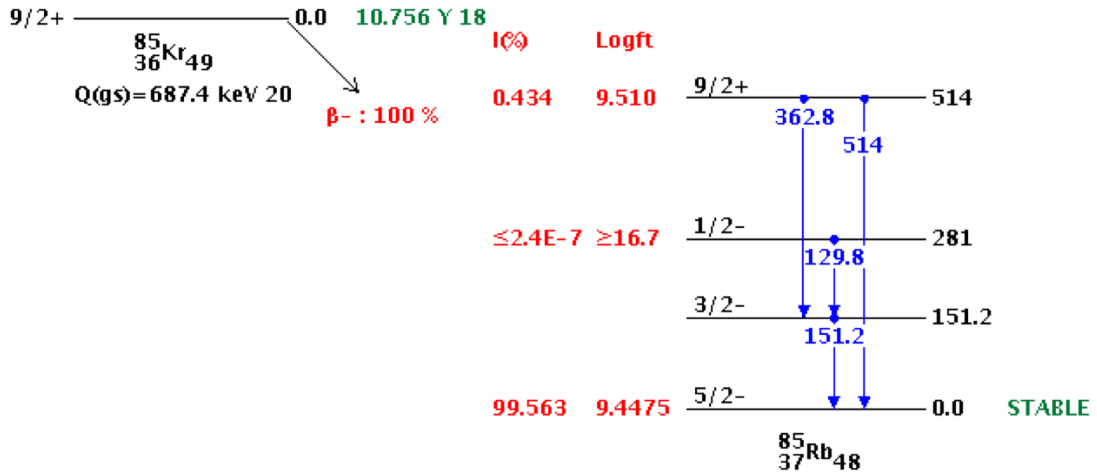
Figure 3.7: Decay scheme for ^{85}Kr. The most common β decay (99.563%) is to the ground state of ^{85}Rb which is stable. There is a small branch (0.434%) to the meta-stable state ^{85m}Rb which then decays to the ground state with the emission of a 514 keV γ ray. This delayed coincidence ($\tau = 1.46\mu$s) allows us to estimate the contamination rate of ^{85}Kr, independent of the spectral fit.

ure 3.7), there is a small β decay branch to a meta-stable state of rubidium, ^{85m}Rb. This is then followed (with a mean-life of 1.46 μs) by the decay to ^{85}Rb with a γ emission at 514 keV. By looking for the delayed coincidence between the β and γ events, and accounting for the branching ratio, one can calculate the total ^{85}Kr contamination in the scintillator. Such an analysis was performed on all the data in a 3.8 m fiducial volume [67]. There are two important factors that make such an analysis difficult. The first, is the small branching ratio (0.434%) such that only 1 in every 230 ^{85}Kr decays occurs in the coincidence channel. The small number of such events (0.13 cpd/100 tons) means that the statistical uncertainty of the method is large. The second problem is the low energy of the β decay (Q-value = 173 keV) in the coincidence branch. Setting the analysis threshold at 40 p.e. (below which hardware trigger threshold effects become important) implies that only 19% of the coincidences will be detected, further reducing the statistics available. Using other energy and coincidence cuts to reduce backgrounds (see [67] for details), a total of 19 events were found in 750 days of data. Including the efficiency of the cuts and

accounting for random fake coincidences between ^{14}C and ^{210}Po events, the total rate of ^{85}Kr in the scintillator was estimated to be 29.2 ± 6.1 cpd/100 tons. To try and increase the efficiency of the low energy cut on the β decay, a separate analysis was done in which no energy threshold was used, and the effect of trigger threshold was evaluated, run-by-run, using the ^{14}C spectrum. This analysis yielded roughly 10 more events to give a ^{85}Kr rate of 30.4 ± 5.3 cpd/100 tons. The systematic uncertainty for this measurement was estimated to be 1.3 cpd/100 tons. As we shall see, this is in good agreement with the results obtained from the spectral fit.

3.2.4 ^{210}Pb and Daughters

^{210}Pb is a β emitter in the ^{238}U decay chain (see Figure 3.9). Due to its long half-life (22 years) and tendency to adsorb on to surfaces, it is often found out of secular equilibrium with the ^{222}Rn section of the chain above it. While ^{210}Pb itself is not a problem, since its endpoint (Q-value = 63.5 keV) is well below the energy region of interest for solar neutrinos, its daughters, ^{210}Bi and ^{210}Po, are a major source of background in Borexino.

3.2.4.1 ^{210}Bi

^{210}Bi is a β emitting daughter of ^{210}Pb whose spectrum (Q-value = 1.16 MeV) spans the energy range of interest for both ^{7}Be and *pep* solar neutrinos. At the start of data-taking, following the initial filling, the ^{210}Bi rate was found to be 10±6 cpd/100 tons [68]. However, over time, the ^{210}Bi contamination has been steadily increasing (see Section 6.8.1.1), and at the start of the May 2010 the rate was found to be ∼ 75 cpd/100 tons. The reason for this increase is not currently well understood. It was noticed [58] that the start of the increase in the observed ^{210}Bi rate seems to coincide with the turning on of the water loop in the external water tank. In December 2007, in order to remove haze in the scintillator caused by water condensation, the water

in the water tank was heated so as to raise the temperature of the scintillator. This heating caused convection currents within the Inner Vessel that could have facilitated desorption of ^{210}Pb from the nylon vessel surface, into the fiducial volume. ^{210}Bi is a critical background for detecting *pep* neutrinos and efforts are ongoing to reduce the contamination through the purification of the scintillator.

3.2.4.2 ^{210}Po

After ^{14}C, ^{210}Po is the largest background in the Fiducial Volume. ^{210}Po is an α emitter in the ^{238}U decay chain (see Figure 3.9) with an energy of 5.31 MeV. Due to the quenching of αs with respect to electrons, the ^{210}Po peak falls squarely over the ^{7}Be spectrum (see Figure 3.1). Even though it is a direct daughter of ^{210}Bi, the rate of ^{210}Po was about 800 times higher than ^{210}Bi at the start of data-taking. It is thought that this high rate (out of equilibrium with the rest of the decay chain) is due to ^{210}Po washing off the surfaces of the scintillator storage tanks and pipes. Figure 3.8 shows the rate of ^{210}Po within the fiducial volume as a function of time. At the start, soon after filling, the ^{210}Po rate was about 8000 cpd/100 tons. The rate then decays away exponentially due to the 138 day half-life. The sharp increase in rates at around 530, 750 and 1030 days are due to refilling operations. These increases support the notion of ^{210}Po washing off the surfaces of the scintillator handling equipment. The average contamination during the period used for the ^{7}Be data analysis is $\sim$ 2100 cpd/100 tons. Luckily, due to the different ionizing properties of αs and βs, we can statistically separate the two using pulse shape discrimination, effectively removing α decays from the final spectrum. This technique is described in detail in Sections 4.5 and 6.4.
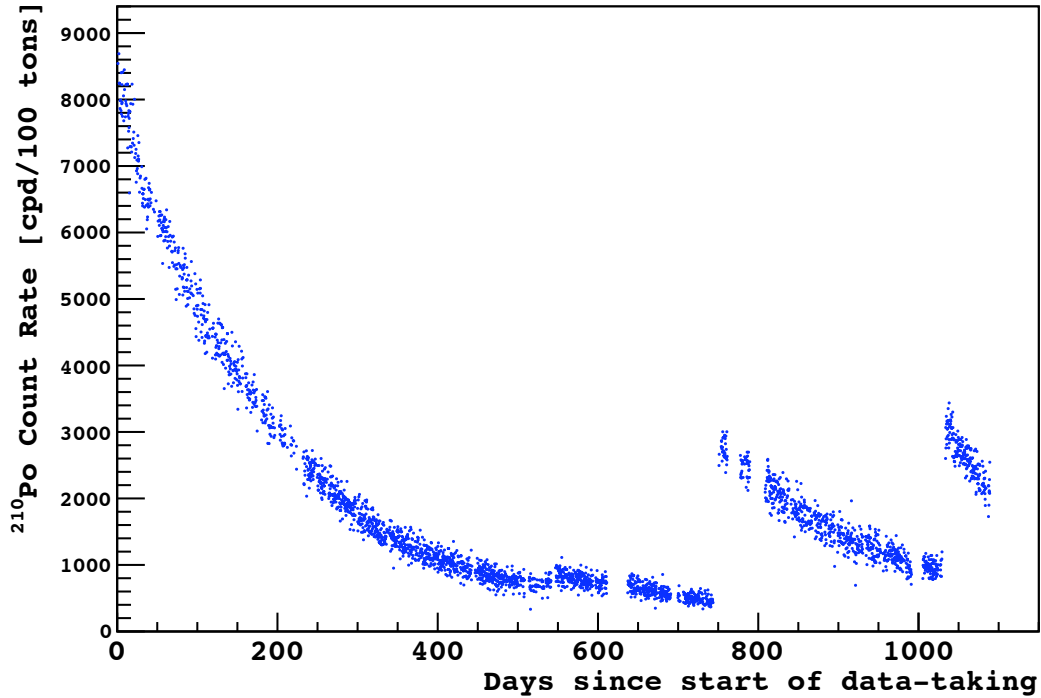
Figure 3.8: Rate of ^{210}Po decays in the fiducial volume, calculated on a run-by-run basis for runs longer than 3 hours. The exponential decay is due to the 138 day half-life while the sharp increases 530, 750 and 1030 days after the start of data-taking are due to scintillator refilling operations. The average contamination during the ^{7}Be analysis period (0 - 990 days) was $\sim$ 2100 counts/day/100 tons.

3.2.5 ^{11}C

^{11}C is a cosmogenic isotope of carbon. It's production in underground detectors is triggered by the residual flux of high energy muons passing through the scintillator. According to estimates [69], in 95% of the production channels a neutron is also produced in the final state:

$$\mu \ (+ \ \text{secondaries}) +^{12} \text{C} \rightarrow \mu \ (+ \ \text{secondaries}) +^{11} \text{C} + n \qquad (3.10)$$

The neutron produced is then captured, emitting a γ ray while the ^{11}C decays through positron emission. Though its half-life is only 20 minutes, the constant rate of muons ($\sim$ 4250 a day through the Inner Vessel) produces a fairly steady rate of ^{11}C. Prior

to the start of Borexino, estimates of the ^{11}C production rate based on independent muon beam experiments [70] and simulations [69] predicted a rate of about 15 to 17 counts/day/100 tons. However the rate measured by Borexino is at least 65% higher at roughly 28 counts/day/100 tons. This higher production rate has been recently confirmed by the KamLAND experiment [71].

^{11}C is a positron emitter, which means that its β decay spectrum (Q-value 960 keV) is shifted to higher energies by the simultaneous detection of the positron annihilation γs. While this conveniently pushes the spectrum past the edge of the ^{7}Be shoulder, it makes ^{11}C the dominant background for the detection of *pep* neutrinos. For this reason several methods have been developed to try and reduce this background. The most common method is to use the threefold coincidence between the parent muon, the associated neutron and the ^{11}C beta decay. In order to efficiently tag ^{11}C decays it is important to reconstruct the track of the through-going muon. A description of the muon tracking algorithm developed for this purpose is described in Section 4.6, and an overview of the method is given in [72]. Another technique to try and distinguish ^{11}C decays is based on the fact that ^{11}C is a positron emitter. The emitted positron can sometimes form ortho-positronium, which has a mean life of a few nanoseconds. This delay between the deposition of the positron kinetic energy and the positron annihilation γs can alter the time profile of the detected scintillation light. We also note that unlike the point-like emissions of β decays, the 511 keV annihilation γs are produced back to back and deposit their energies at slightly different locations. These modifications in the scintillation time profiles allow us to separate, statistically, the ^{11}C decays from other signals in that region. An analysis is currently underway and we hope to publish the results soon, though the details of the study will not be discussed in this thesis.

3.2.6 Heavy Element Decay Chains

A lot of the naturally occurring radioactive isotopes belong the the decay chains of heavy elements. Of the different decay processes, only α decays change the mass number of the parent isotope, decreasing it by four. The isotopes in each decay chain therefore share the same mass number modulo four. The four decay chains are commonly referred to as the uranium, thorium, actinium and neptunium chains. Of the four, the relevant chains for Borexino are the uranium and thorium chains. The natural abundance of ^{235}U, the parent isotope of the actinium chain, is only 0.7% compared to 99.3% for ^{238}U, the parent of the uranium chain. Since the equilibrium rate for the uranium chain is less than 1 cpd/100 tons, the contribution of isotopes from the actinium chain is expected to be negligible. Due to the relatively short, on a geological time scale, half-lifes of all the nuclides in the neptunium decay chain, isotopes from the chain do not occur naturally. The one exception is ^{209}Bi which occurs at the final step of the chain, though the energy of the α decay falls below the analysis threshold. We note that even though the energy of the α decays in these decay chains is well above the region of interest for ^{7}Be neutrinos, the scintillation light produced by αs is quenched by roughly a factor of 13 with respect to the β decays. Thus many of the α decays overlap directly with the low energy solar neutrinos.

3.2.6.1 ^{238}U

^{238}U is a primordial radioactive isotope with a half-life of 4.5 billion years. It is the most common isotope of uranium, with a natural abundance of 99.3%. The typical concentration in rock is around 2.5 ppm by weight which leads to an activity of around 30 Bq/kg. The total activity due to ^{238}U however is higher due to the subsequent decays of its radioactive daughters. The main decay branches of the ^{238}U decay chain are shown in Figure 3.9. The decay chain includes includes 8 α decays (shown in yellow) and 6 β decays (blue) ending with the stable ^{206}Pb. Two of the most

84
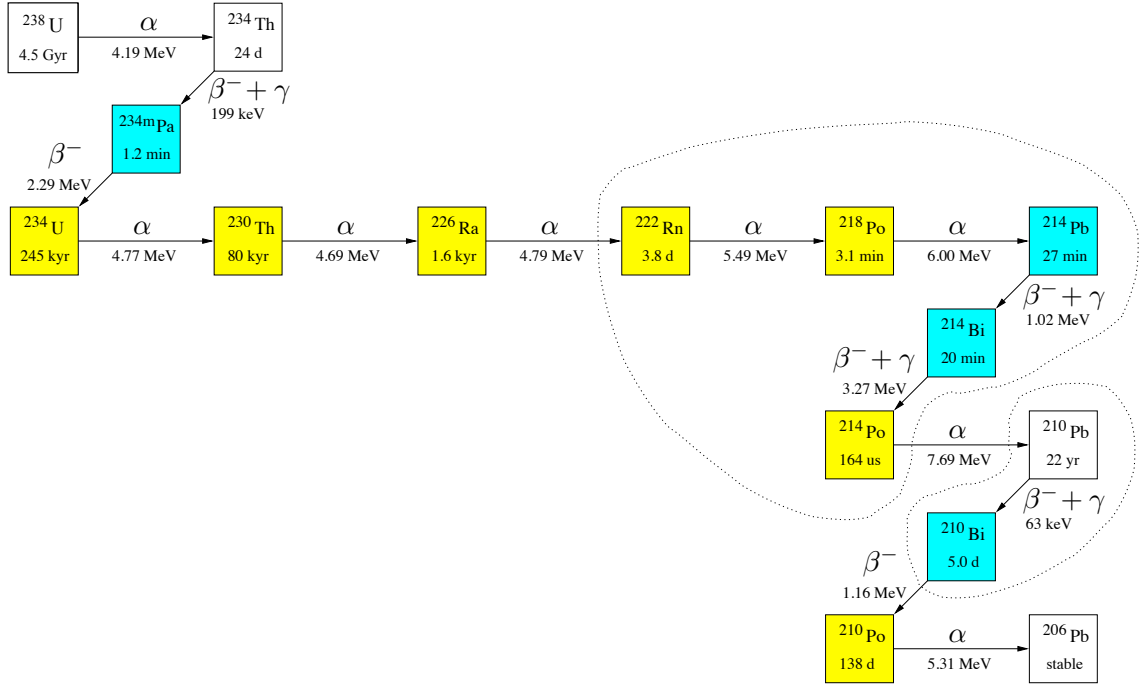
Figure 3.9: Radioactive decay chain of ^{238}U. Energies shown are Q values for β emitters and α kinetic energy for α emitters. Times shown are half-lifes. Isotopes in yellow are α emitters, while β emitters are shown in blue. Decays with energies below the fit region are shown in white. Secular equilibrium is likely to hold only within the sets of isotopes grouped by dotted lines. Figure adapted from [43]

important isotopes for Borexino are ^{222}Rn and ^{210}Pb. ^{210}Pb and its daughters are discussed above in Section 3.2.4, and the ^{222}Rn decay chain is described here.

^{222}Rn is a particularly dangerous radioactive isotope for Borexino. As a noble gas, it can travel far and permeate through most materials, though its spread is limited by its half-life of 3.8 days. Due to this diffusion, it is often found to be out of secular equilibrium with its parent isotopes. The decay rate of the ^{222}Rn chain can be estimated by studying the rate of delayed coincidences between ^{214}Bi and ^{214}Po decays. Due to the short livetime of ^{214}Po, the two decays occur very close together in space and time, making them easy to identify over other backgrounds. By searching for these coincidences within the fiducial volume we have estimated a decay rate of 1.62 ± 0.06 cpd/100 tons for the ^{222}Rn chain during the analysis exposure (details in Section 6.3.1) .

The distribution of ^{214}Bi-Po coincidences, both in time and space, is far from uniform, as can be seen from Figures 3.10 and 3.11. Soon after the initial filling (1st June 2007), a small amount of additional scintillator was added to the top of the inner vessel leading to a large increase in the number of observed ^{214}Bi-Po coincidences. Increases in rate (followed by an exponential decay with the characteristic 3.8 day half-life of ^{222}Rn) are also seen in correlation with later detector operations such as refilling and source insertions. This indicates that the equilibrium of the ^{238}U decay chain is being broken due to contamination of the scintillator with ^{222}Rn in the air. In order to estimate the intrinsic ^{238}U contamination in the scintillator, the rate of ^{214}Bi-Po coincidences during stable detector operations was studied and the equilibrium contamination was found to be 0.57±0.05 cpd/100 tons [73]. The corresponding contamination for ^{238}U in the scintillator is $(5.3 \pm 0.5) \times 10^{-18}$ g/g, assuming secular equilibrium across all the isotopes before ^{222}Rn. Since the half-lifes are all fairly long, it is quite possible that secular equilibrium is also broken elsewhere. Further discussion about the ^{238}U contamination, as measured from the spectral fits, can be found in Section 6.7.

3.2.6.2 ^{232}Th

^{232}Th is also a primordial isotope with a half-life of 14 billion years (more than three times the age of the Earth). Thorium is one of the few natural elements that is mononuclidic - the natural abundance of ^{232}Th is essentially 100%. ^{232}Th is found in the Earth's crust at a typical concentration of 10 ppm, by weight, with an activity of 41 Bq/kg. Since it is the progenitor of the chain, the total activity due to ^{232}Th is higher when taking into account its radioactive daughters. The main decay branches of the ^{232}Th decay chain are shown in Figure 3.13. The decay chain includes includes 6 α decays (shown in yellow) and 4 β decays (blue) ending with the stable ^{208}Pb. After ^{232}Th the decay chain proceeds fairly quickly compared to the ^{238}U chain and
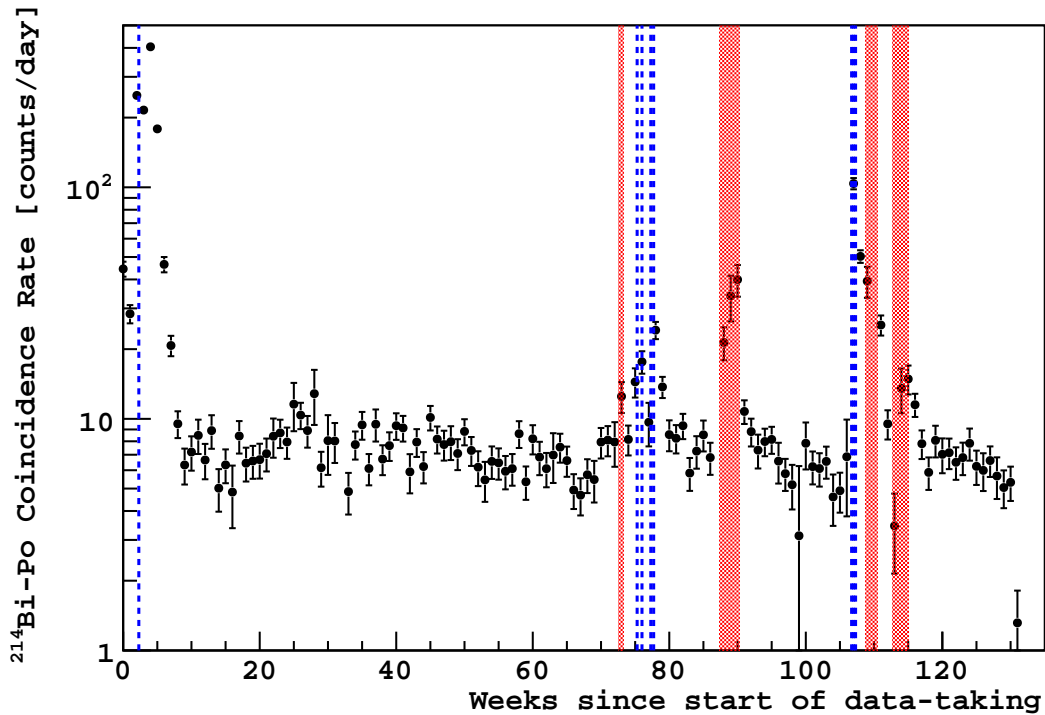
Figure 3.10: Rate of detected ^{214}Bi-Po coincidences within the Inner Vessel as a function of time since the start of data taking (16th May 2007). The blue dashed vertical lines indicate refilling of the inner vessel scintillator and the red shaded periods designate source insertions during calibration campaigns. The large increase shortly after the start was due to refilling of the scintillator on 1st June 2007 (see Figure 3.11 for the spatial distribution of these events).

the longest half-life following the decay of ^{228}Th is 3.7 days. Due to the short isotope half-lifes, the nuclides after ^{228}Th are usually found in secular equilibrium even though the equilibrium can sometimes temporarily be broken due to diffusion of ^{220}Rn. The activity of the chain can be estimated through the number of delayed ^{212}Bi-Po coincidences detected (see Section 6.3.2). The spatial distribution of these coincidences is shown in Figure 3.12 where it can be seen that the rate is highest near the nylon vessel, especially at the bottom. Considering only coincidences occurring in a 3.3 m sphere, during stable detector running, gives an equilibrium rate of (0.13 ± 0.03) cpd/100 tons [73] corresponding to a ^{232}Th contamination of $(3.8 \pm 0.8) \times 10^{-18}$ g/g assuming secular equilibrium throughout the chain. Further discussion about the

87
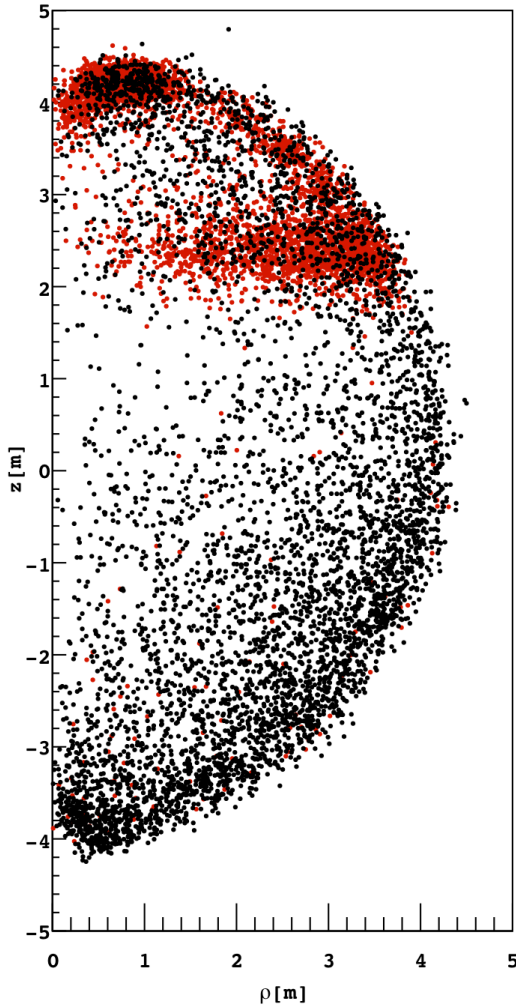
Figure 3.11: Spatial distribution of ^{214}Bi-Po coincidences within the Inner Vessel, given in cylindrical coordinates. Points in red are coincidences detected soon after the refilling operation on 1st June 2007 (see Figure 3.10). Events occurring near the nylon vessel are degraded in energy.
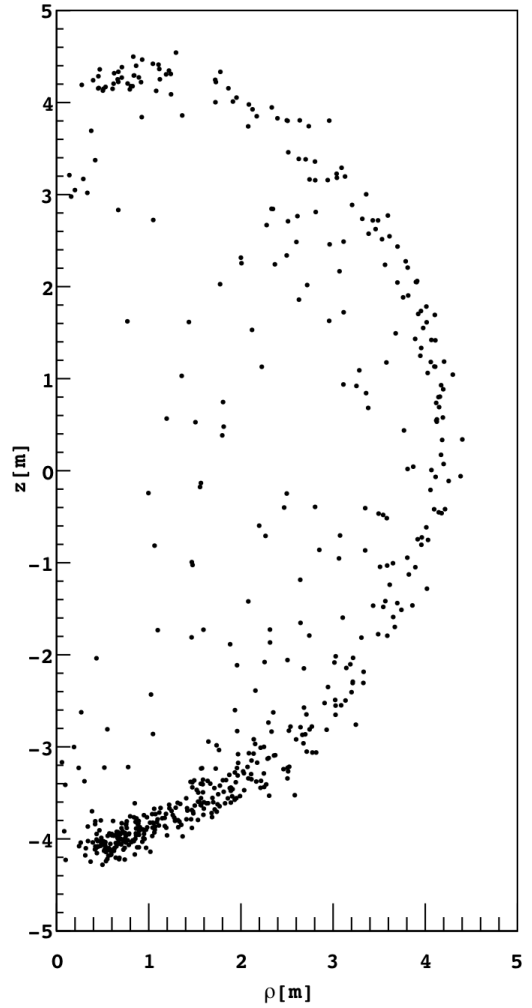
Figure 3.12: Spatial distribution of ^{212}Bi-Po coincidences within the Inner Vessel, given in cylindrical coordinates. Rates of coincidences are highest near the nylon vessel ($r \sim 4.25$ m), particularly near the bottom. Events occurring near the nylon vessel are degraded in energy.

^{232}Th contamination in the scintillator, as measured from the spectral fits, can be found in Section 6.7.

Figure 3.1 shows the contribution of the α decays in the ^{238}U and ^{232}Th to the total energy spectrum (besides ^{238}U and ^{232}Th which are below the fit threshold and
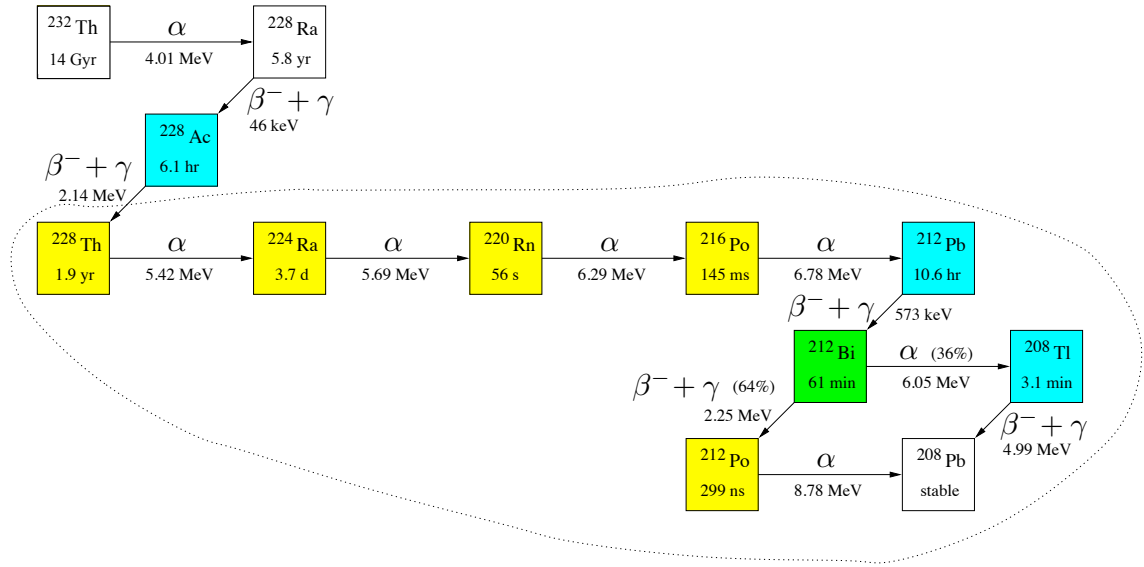
Figure 3.13: Radioactive decay chain of ^{232}Th. Energies shown are Q values for β emitters and α kinetic energy for α emitters. Isotopes in yellow are α emitters, while β emitters are shown in blue. Decays with energies below the fit region are shown in white. ^{212}Bi, which can decay through either α or β emission, is shown in green. Times shown are half-lifes. Secular equilibrium is likely to hold only within the sets of isotopes grouped by dotted lines. Figure adapted from [43]

were therefore not included in the simulation program). Most β decays were not included due to their small contribution to the spectrum (the events are spread over a much larger energy range than the monoenergetic αs). A detailed discussion of the isotopes included in the fit is given in Section 6.6.3.

3.2.7 ^{40}K

^{40}K is a primordial nuclide with a half-life of 1.25 billion years and a natural abundance of 0.012%. ^{40}K can enter into the scintillator primarily in two ways. The first is through micron or sub-micron dust particulates. The fraction of potassium in the crust is about 2.5% by weight which works out to a rate of roughly 800 Bq/kg. This is an extremely high rate and care was taken to reduce the contamination from particulates through water extraction, distillations and filtration [74]. It was also found that commercially available PPO, the wavelength shifter added to the scintillator, had a

potassium contamination at the level of parts per million. Given the PPO concentration of 1.5 grams/liter of scintillator, this equates to $\sim 10^{-9}$ g-K/g-scintillator or roughly 2.7×10^5 cpd/100 tons, nearly 6000 times the expected rate of ^{7}Be. The maximum concentration of potassium that was considered acceptable during the design was set at $\sim 10^{-14}$ g-K/g-scintillator, and the background due to ^{40}K was reduced through water extraction of the PC-PPO solution [74].

Unfortunately the efficiency of these methods at removing ^{40}K is unknown and so we cannot *a priori* calculate the expected rate in the scintillator. For this reason we have included the spectrum as a free parameter in all spectral fits. Figure 3.1 shows the shape of ^{40}K spectrum at an arbitrary rate of 1 cpd/100 tons. In addition to the pure β emission of ^{40}K, there is a 10.7% branching ratio for electron capture to an excited state of ^{40}Ar. This results in the emission a monoenergetic 1.46 MeV γ ray which helps distinguish the ^{40}K energy spectrum from the other β spectrum, though it does also mean that ^{40}K decays at the vessel end-caps or in components on the SSS may deposit energy within the fiducial volume (see Section 3.2.11).

3.2.8 ^{39}Ar

^{39}Ar, like ^{14}C, is produced primarily through cosmic ray activity in the atmosphere. It is a pure β emitter with a Q-value of 565 keV. With an endpoint close to the 665 keV ^{7}Be shoulder and no accompanying γ rays or delayed coincidence, it would be extremely hard to disentangle the ^{39}Ar spectrum from that of ^{7}Be. Therefore great care was taken in ensuring that the contamination was as low as possible. The argon levels in the specially prepared low Ar/Kr nitrogen used for the stripping of the scintillator was around 0.005 ppm (by volume). When mixed in equal volumes of gaseous nitrogen and pseudocumene, argon will partition itself in the ratio 4.1:1 [75]. Given an activity of 1.4 Bq/m^3 in atmospheric argon this translates to an expected rate of less than 0.02 cpd/100 tons in the scintillator. However, as was observed by

the high ^{85}Kr rate, there appears to have been a small air leak during the vessel filling. The activity of ^{39}Ar in air (13 mBq/m^3 [75]) is roughly 75 times lower than that of ^{85}Kr (1 Bq/m^3). Assuming that all the ^{85}Kr contamination ($\sim$ 30 cpd/100 tons) in the scintillator came from the air leak, and that the ratio of ^{39}Ar to ^{85}Kr was the same as in the atmosphere, the expected ^{39}Ar contamination is $\sim$ 0.4 cpd/100 tons. Since the contribution of ^{39}Ar to the spectrum is negligible (see Figure 3.1), we have not included it in the spectral fits for the ^{7}Be analysis.

3.2.9 Muons

Even though the Borexino detector is situated under roughly 1400 meters of rock (3500 m.w.e) the rate of cosmic muons is still non-negligible. With a residual muon flux of $\sim$ 1.2/m^2/hr [44], the rate of muons passing through the inner detector is roughly 4250/day. The average muon energy has been measured to be 270 GeV [76] and a muon passing through the center of the detector can deposit hundreds of MeV of energy. The direction of the muons is strongly peaked in the downward direction, with azimuthal variations depending on the topology of the overhead Gran Sasso mountain [44].

There are two independent methods used to detect muons. The first relies on the outer water tank which detects Cherenkov light produced by muons going through the water. The second used information from the inner detector. Since the scintillation light produced by muons originates from a track rather than the point-like emissions of other interactions, muons can be effectively tagged by studying the time profile of detected light, combined with the total deposited energy. The muon detection efficiency of the inner and outer detectors has been studied in detail [44] and has been estimated to be $(99.972 - 99.992)\%$ combined. This yields a residual muon rate of $\sim$ 0.77/day through the inner detector. Since muons have a very distinct scintillation time profile, many of the other selection cuts also preferentially remove muons from

Isotope	Mean Life	Energy [MeV]	Production Rate [cpd/100 tons]
^{12}N	15.9 ms	17.3 (β^+)	0.058 $\pm$ 0.013
^{12}B	29.1 ms	13.4 (β^-)	1.41 $\pm$ 0.04
^{8}He	171.7 ms	10.7 ($\beta^- \gamma n$)	0.026 $\pm$ 0.012
^{9}C	182.5 ms	16.5 (β^+)	0.096 $\pm$ 0.031
^{9}Li	257.2 ms	13.6 ($\beta^- \gamma n$)	0.071 $\pm$ 0.005
^{8}B	1.11 s	18.0 ($\beta^+ \alpha$)	0.273 $\pm$ 0.062
^{6}He	1.16 s	3.51 (β^-)	0.395 $\pm$ 0.027
^{8}Li	1.21 s	16.0 ($\beta^- \alpha$)	0.40 $\pm$ 0.07
^{11}Be	19.9 s	11.5 (β^-)	0.035 $\pm$ 0.006
^{10}C	27.8 s	3.65 ($\beta^+ \gamma$)	0.54 $\pm$ 0.04
^{11}C	29.4 min	1.98 (β^+)	27.65 $\pm$ 4.45
^{7}Be	76.9 days	0.478 (EC γ)	3.35 $\pm$ 0.22

Table 3.5: Cosmogenic isotopes in Borexino. Production rates are obtained from [77] when available, otherwise calculated directly from [71] using data if present or otherwise FLUKA calculations.

other signals and backgrounds. The total estimated muon rate in the ^{7}Be energy spectrum, after all cuts is < 0.01 counts/day. Details regarding the muon cut can be found in Section 6.2.2 and the residual rates are discussed in Section 6.2.3.2.

3.2.10 Cosmogenic Isotopes

Radioactive isotopes can also be produced *in situ* due to the passage of muons through the detector. The dominant isotope produced in organic scintillators is ^{11}C (discussed in an earlier section), but due to the high energy of the muons, there are many other radioactive isotopes that are produced through the spallation of the carbon nucleus. Using a combination of FLUKA simulations and the measurements of the KamLAND collaboration [71], the rate of cosmogenic isotopes in Borexino can be estimated by extrapolating to the mean muon flux and energy at Gran Sasso. Details of the extrapolation can be found in [77], and the resulting rates are given in Table 3.5.

A majority of the isotopes are relatively short-lived (compared to the incident muon rate) and so the contribution of cosmogenic isotopes can be greatly reduced by

removing all events that occur soon after a muon has passed through the detector. The typical length of such a veto is 300 ms, which, as will be shown in Section 6.2.3.2, reduces the cosmogenic activity for all but the longest lived isotopes (^{10}C, ^{11}C and ^{7}Be) to a negligible rate. The spectra of these long-lived cosmogenic isotopes are shown in Figure 3.1.

3.2.11 External Backgrounds

External background refers to all events produced outside the scintillator. The main source of external backgrounds are radioactive decays in the detector hardware surrounding the scintillator. This includes the nylon vessels, the vessel support structure, photomultiplier tubes, light cones and other hardware mounted on the Stainless Steel Sphere (SSS). Since the radioactive decays occur outside the scintillator, at least a meter away from the fiducial volume, the only background that can travel into the fiducial volume and deposit energy are γ rays (the rate of radiogenic neutrons is negligible [78]). Figure 3.14 shows the distribution of all detected events in the scintillator for different energy regions. The Inner Vessel is clearly visible as a ring (at $r \sim 4.25$ m) of higher activity. Also distinctly visible are the vessel end caps (IV endcaps at $z = \pm 4.25$ m, OV endcaps at $z = \pm 5.5$m) which contribute to the highest activity regions in the scintillator. The high rate of events occurring outside the Inner Vessel, above the top endcap, most prominently seen in the 145 - 300 p.e. region is due to the leak events which are discussed in Section 3.2.11.1. The higher rate of events at the nylon vessel in the top hemisphere, compared to the bottom, is due to the nylon vessel being shifted slightly upwards. The top of the vessel is therefore slightly closer to the SSS and records a higher rate of external background events. It can be seen that the fiducialization of the inner vessel is extremely effective in reducing the external backgrounds. The standard fiducial volume used for the ^{7}Be analysis is $r < 3.021$ m and $|z| < 1.67$ m. The contribution of the residual external background

within this fiducial volume is discussed below.
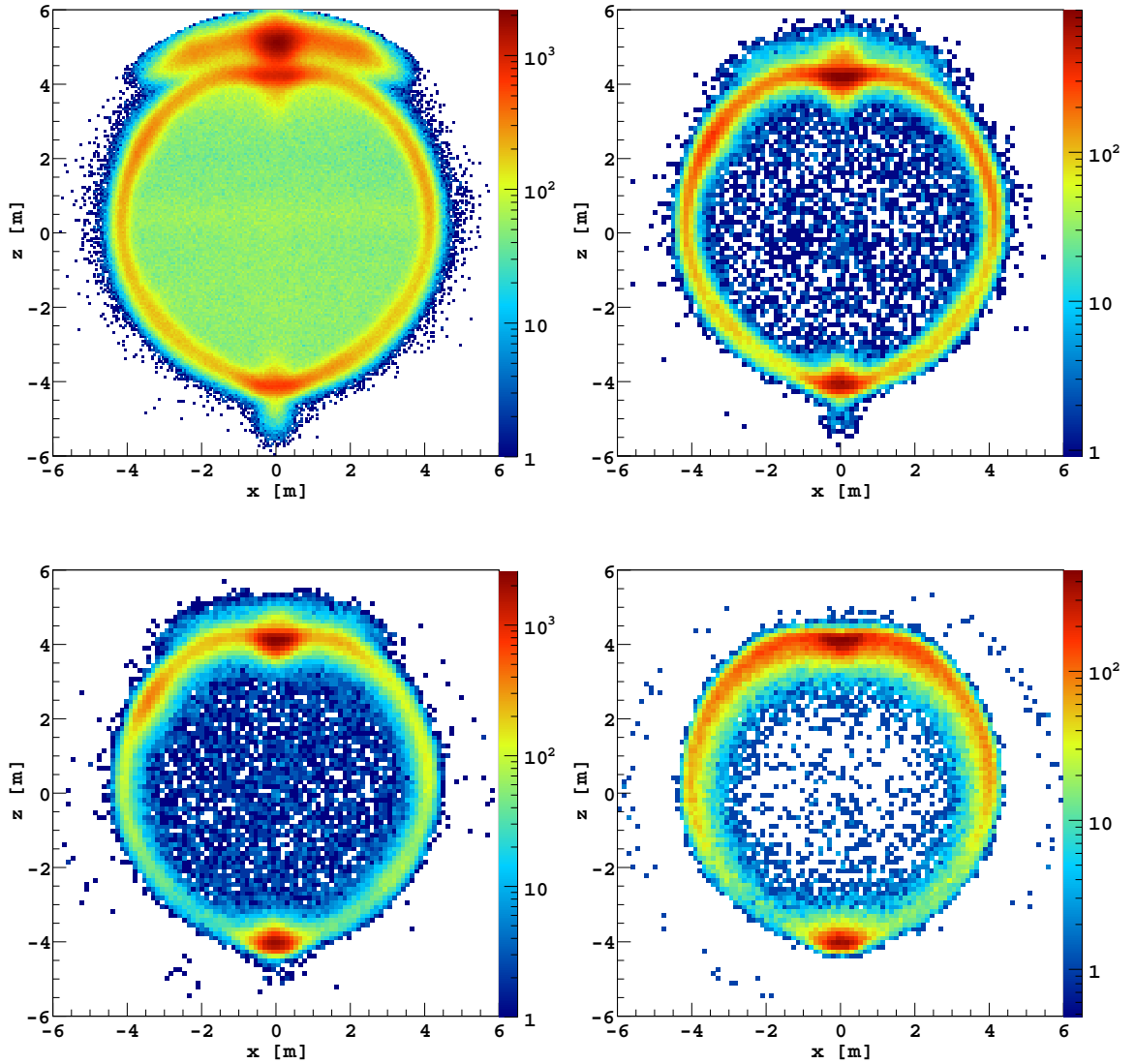
Figure 3.14: Spatial distribution (in the $x - z$ plane, $|y| < 0.5$ m) of all reconstructed events (besides muons) in different energy regions. Top Left: 145 - 300 p.e. (290 - 600 keV) ^{210}Po peak region. Top Right: 300 - 375 p.e. (650 - 850 keV) ^{7}Be shoulder. Bottom Left: 425 - 650 p.e. (850 - 1300 keV) ^{11}C energy region. Bottom Right: 900 - 1500 p.e. (1800 - 3000 keV) ^{208}Tl. Events occurring outside the Inner Vessel ($r = 4.25$), near the top endcap ($z = 4.25$), most clearly seen in the top left figure, are due to the tear in the nylon vessel (see Section 3.2.11.1).

During the construction of Borexino, careful measurements of the radioactivity of each of the components were made [48,79]. Table 3.6 lists the estimated backgrounds in the fiducial volume from the different components, in the energy region of the fit.

94

The values are obtained from [48] but we have adjusted the rates from the end regions. The volume considered in that study had a radius of 3 m, however the fiducial volume for the ^{7}Be analysis has additional vertical cuts at $z = \pm 1.67$ m. This increases the minimum distance from the endcaps to the fiducial volume by $l = 1.33$ m. We have therefore scaled the rates by a factor of $e^{-l/\lambda_{att}}$ where $\lambda_{att} = 0.27$ m is the attenuation length of a ^{208}Tl, 2.615 MeV, γ ray [80].

Source	^{7}Be Range [cpd/100 tons]	Fit Range [cpd/100 tons]
End Regions	0.013	0.017
Nylon Vessel	0.08	0.12
Stainless Steel Sphere	1.4	2.4
Total	1.5	2.5

Table 3.6: Estimates of external background rates in the ^{7}Be analysis fiducial volume based on measured radioactivity of individual components [48]. Rates from end cap regions have been scaled down by a factor of $e^{-l/\lambda_{att}}$ where $l = 1.33$ m and $\lambda_{att} = 0.27$ m, to account for vertical cuts at $z = \pm 1.67$ m. Stainless Steel Sphere also includes the PMTs and light cones mounted on the sphere. The ^{7}Be range assumed is 250 - 800 keV, while the entire fit range corresponds to 250 - 1300 keV

Source	^{7}Be Range [cpd/100 tons]	Fit Range [cpd/100 tons]	Total [cpd/100 tons]
^{40}K	0.05	0.36	0.55
^{214}Bi	0.15	0.86	4.04
^{208}Tl	0.03	0.16	3.35
Total	0.23	1.38	7.94

Table 3.7: Estimates of external background rates in the ^{7}Be analysis fiducial volume based on fits to high energy regions of the spectrum [81, 82]. The ^{7}Be range assumed is 250 - 800 keV, while the entire fit range corresponds to 250 - 1300 keV

The dominant contribution of external backgrounds that deposit energy within the fiducial volume comes from ^{208}Tl, ^{214}Bi and ^{40}K in the photomultipliers and related parts. Using the *g4bx* Monte Carlo program, γ rays from these species were simulated on the SSS and propagated towards the inner vessel. The energy spectra of the events that reconstruct within the fiducial volume is shown in Figure 3.1. The rates were determined by fits to higher energy regions of an ongoing ^{8}B neutrino analysis [81]

as well as ^{11}C subtracted spectra used to study *pep* neutrinos [82], extrapolated to the fiducial volume used in this analysis. The total rate from these fits (listed in Table 3.7) is roughly a factor of two lower than the estimates in [48], and the origin of this difference is not currently known. Since the external background is hard to model analytically, and there is a fairly large uncertainty in the rate, we have excluded them from the fit and set the end point of the fit range at 650 p.e. Below this energy the combined rate of the external background is more than 15 times lower than the total rate of detected events throughout the spectrum, and small compared to other components within the fit range. Systematic tests on the effect of the external background were made by varying the end point of the fit (see Section 6.8.3.1) and the outcome was included in the uncertainty of the final result.

3.2.11.1   Nylon Vessel Leak

Due to the tear in the inner nylon vessel that occurred around the 9th of April 2008 (see Section 2.3), PPO from the inner detector leaked into the buffer fluid in the outer vessel. The presence of PPO in the buffer reduced the quenching effect of the DMP causing the events in the buffer to become visible. This caused a large increase in the number of detected events, as can be seen in Figure 3.15. Thanks to several detector operations involving reduction of the DMP concentration in the outer buffer, purification of the outer buffer and refilling of the inner vessel, the leak rate was greatly reduced and the PPO in the outer vessel removed. These operations are marked in Figure 3.15 and discussed in Section 2.3. Figure 3.16 shows the spatial distribution of events during different periods of the data-taking with respect to the leak and the following operations. Events shown are in the low energy region (95 - 130 p.e.) where the rate of events in the buffer is highest. As can be seen from the comparison of the figures, there is a marked increase in the number of events in the outer buffer ($r > 4.25$ m) following the leak. Once the PPO escapes from the inner

vessel it rises to the top of the outer vessel due to its lower density. The rate of buffer events is then seen to decrease following each of the two cycles of buffer purification. By comparing the rate of all events to those that are selected for the ^{7}Be analysis (see Figure 3.15) we note that the rate of events in the fiducial volume ($r < 3.02$ m, $|z| < 1.67$ m) does not seem to be affected by the leak due to the accurate position reconstruction of events.
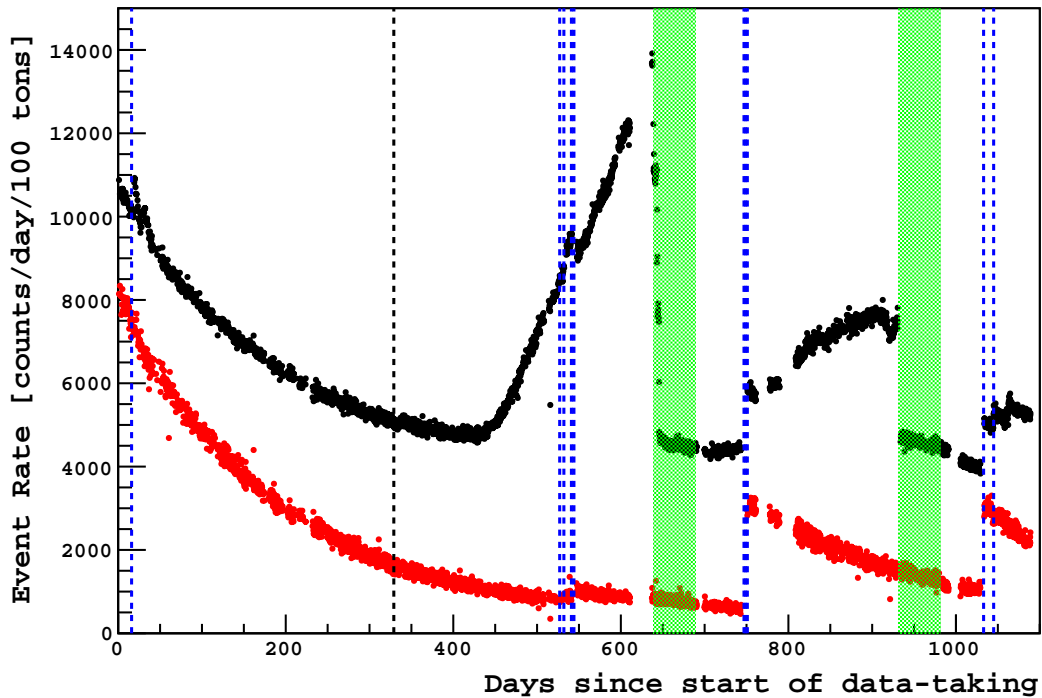

Figure 3.15: Event rates (above 95 p.e.) as a function of time, calculated on a run-by-run basis for runs longer than 3 hours. The black data points indicate the total rate for all detected events, scaled down by a factor of 5, while the red data points show the rate only for events that are selected for the ^{7}Be analysis (the time profile is dominated by the decay of ^{210}Po). The dashed black line marks the best estimate for the start of the leak in the inner nylon vessel. The blue lines indicate refilling of the inner vessel scintillator and the green shaded areas designate buffer purifications. Compare with Figure 2.8, which shows the volume of the Inner Vessel as a function of time.
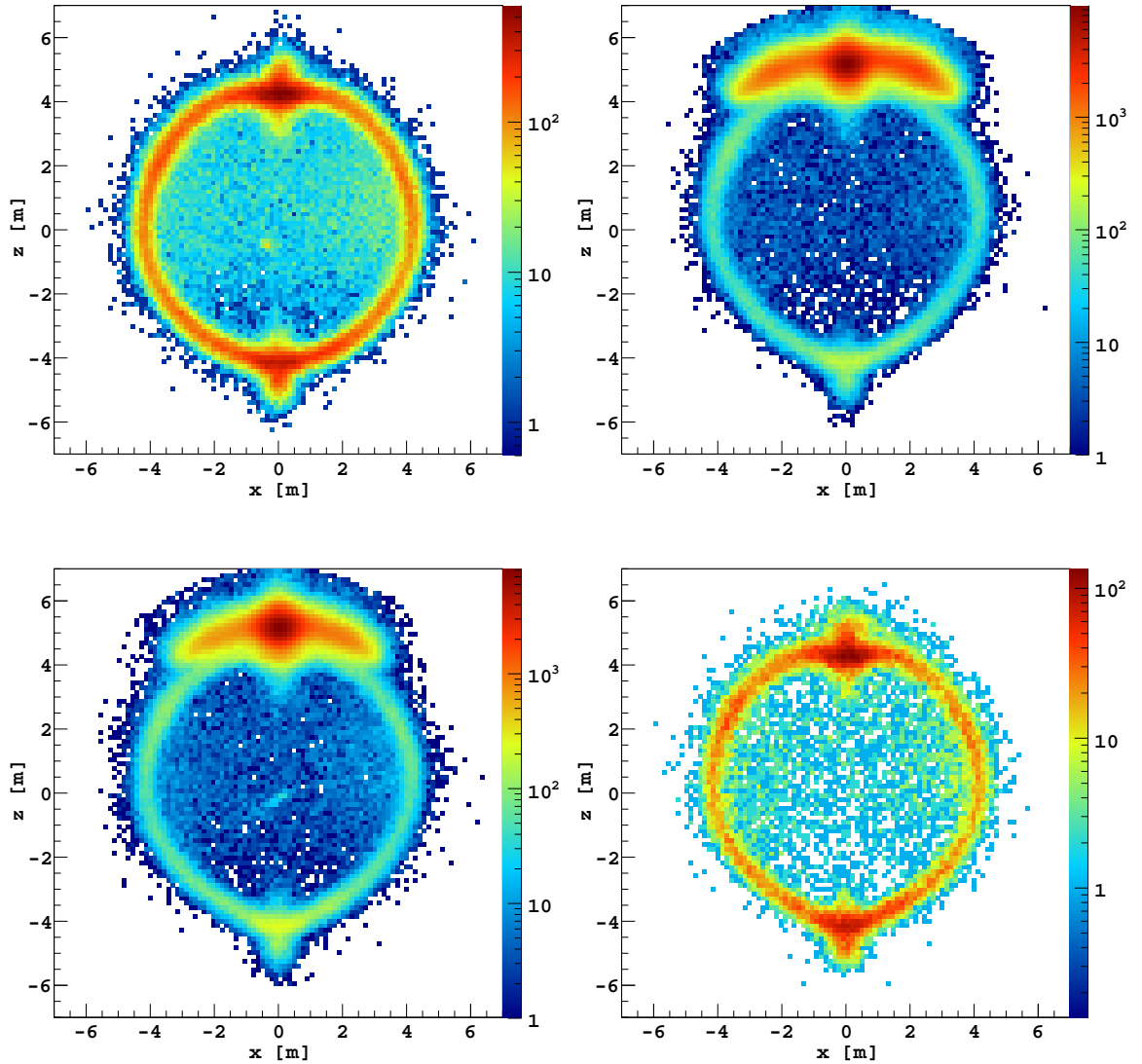
Figure 3.16: Spatial distribution (in the $x - z$ plane, $|y| < 0.5$ m) of all reconstructed events (besides muons) in the 95 - 130 p.e. energy region during different periods with respect to the leak and corresponding detector operations. Events occurring outside the Inner Vessel ($r = 4.25$), near the top endcap ($z = 4.25$), are due to the tear in the nylon vessel. Top Left: Days (1 - 329) Prior to the leak. Top Right: Days (450 - 627) During the period with the highest leak rate. Bottom Left: Days (689 - 930) Following the first buffer purification in which the DMP concentration was also reduced from 5 g/l to 3 g/l. Bottom Right: Days (932 - 990) During and after the second buffer purification, until the end of the ^{7}Be analysis period. The DMP concentration was further reduced to 2 g/l. See Figure 3.15 for the event rates as a function of time.

Chapter 4

Event Reconstruction

All the necessary information required to analyze an event in the inner detector can be extracted from three simple pieces of data: The list of PMT's that were hit during the event, the time of each of the PMT hits and the charge recorded by each PMT. Using this information we reconstruct the energy and position of the event, pulse shape timing information for particle-type identification and spatial pattern information for electronics noise discrimination. These tasks are performed by a dedicated piece of reconstruction software called *MOE-Echidna*. The history of this software is quite interesting and worth describing in order to understand some of the idiosyncrasies present in the current ^{7}Be analysis.

4.0.12 Mach4

In early 2007, due to some of the drawbacks of the *Echidna* reconstruction code used by the European collaborators and differing opinions regarding the openness and availability of the code to the collaboration, the American collaborators from Princeton and Virginia Tech decided to write a software reconstruction program from scratch. The goal of *Mach4* was to create an open source, efficient piece of reconstruction code that could quickly process the raw data and convert it into a simple

output format that could be easily used for data analysis. The basic structure and functionality of the code was completed in just a few weeks and on April 26th 2007, exactly one month after the first *Mach4* meeting, even before the filling of the detector with scintillator was complete, evidence of the first ever real time detection of ^{7}Be neutrinos was found in the data. Figure 4.1 shows the original authors of the *Mach4* team celebrating this achievement. *Mach4* has changed a lot since those early day but the basic philosophy has remained the same. The code is continuously under development and every six months or so the current version of the code is tagged (referred to as a cycle) and an entire reprocessing of the data is done. The version of the code used for this analysis is cycle-97.

4.0.13   MOE-Echidna

As time passed, relations between the two groups improved and it was decided to merge the *Echidna* and *Mach4* codes, enabling us to combine the best parts of each of the reconstruction programs. Unfortunately due to the differing structure of the two codes a complete merging was not possible. After various different attempts it was finally decided to have both programs use the same *Echidna* low level reconstruction (described below). All other sections are kept separate, though the variables are stored in a single output ROOT [83] file. This combination is generally referred to as *MOE-Echidna* where *MOE* is an acronym for *Mach4 Over Echidna*. As implied by the name, *MOE* is the *Mach4* reconstruction code running on top of the Echidna low level reconstruction. Due to the way the merging was done, there are many variables that exist in both codes and are very similar, though not exactly the same. Where necessary we will specify which code created the variable, though by default we will discuss the *MOE* variables. As mentioned above, the version of Mach4/MOE used in this analysis was cycle-97 and the version of Echidna was cycle-12.

Figure 4.1: Original *Mach4* authors celebrating the discovery of the first evidence of ^{7}Be neutrinos in the data on April 29th 2007. From back to front, left to right: Tiberiu Tesileanu, Katerina Visnjic, Joshua Ruderman, Richard Saldanha, Steve Hardy, Rachel Loer, Ben Loer, Cristiano Galbiati, Frank Calaprice, Kevin McCarty, Allan Nelson. The laptop on the table is displaying a plot of the Borexino energy spectrum with what appears to be the ^{7}Be shoulder.

4.1 Low Level

Low level reconstruction refers to conversion of the raw data acquired by the detector into the three critical pieces of information: hit times, charge and position. Unfortunately due to the outdated nature of the Borexino electronics, this information cannot be easily extracted directly from the raw data. The low level reconstruction can be split into two categories, precalibration and event reconstruction.

4.1.1 Precalibration

Before one can make sense of the recorded event information, a set of calibrations need to be performed. The calibrations are done with the help of a dedicated laser

system and special data acquisition triggers that are described in Section 2.2.

- Time Calibration

  The precise time of arrival of each of the detected photons is critical for an accurate reconstruction of the position of each event. The timing across the different channels is aligned by using an electronic pulse generator that simultaneously pulses the test input of each front-end channel. Once the signals from the front-end boards are aligned, the next step is to align the signals from the phototubes to account for possible difference in PMT response times and cable lengths. The timing of each of the phototube signals is aligned with the help of a fast (50 ps width) diode laser. The light from this external laser source is carried along a system of optical fibers to each of the photomultiplier tubes on the Stainless Steel Sphere, such that the laser light reaches the PMT's at the same time, within a precision of much better than 1 ns. By simultaneously delivering a signal to trigger the laser, and to dedicated electronics reference channels, one can align the different PMT signals in time. The typical distribution of PMT signals has a width of $\sim$ 4 ns before alignment and $\sim$ 1.6 ns after alignment. This alignment is performed once a week with a dedicated laser run where the laser is pulsed at $\sim$ 100 Hz for approximately 250,000 events. Details regarding the hardware and implementation of laser calibration system can be found in [45].

- Charge Calibration

  In order to convert the charge output by the PMT's into photoelectrons, one must know the amount of charge that corresponds to a single photoelectron. This conversion factor varies slightly for different phototubes and must be calculated individually for each of the tubes. The charge calibration is performed using the same pulsed laser system (described above) used for the timing calibration. The strength of the 394 nm diode laser is usually set such that the

mean number of photoelectrons detected by each phototube during each pulse is between 0.01 and 0.05 p.e. This reduces the probability of detecting multiple photoelectron in a single pulse while still ensuring that the contamination from dark noise is less than 1% [84]. The charge output of each tube is digitized and histogrammed for each laser pulse. The histogram is then fit to the sum of two Gaussians which represent the single and double photoelectron response. The mean and variance of the second Gaussian are fixed to twice the mean and variance of the first Gaussian, though the amplitude is left free. For each channel the mean position of the first Gaussian (in ADC counts) is then stored as the mean value of the single photoelectron.
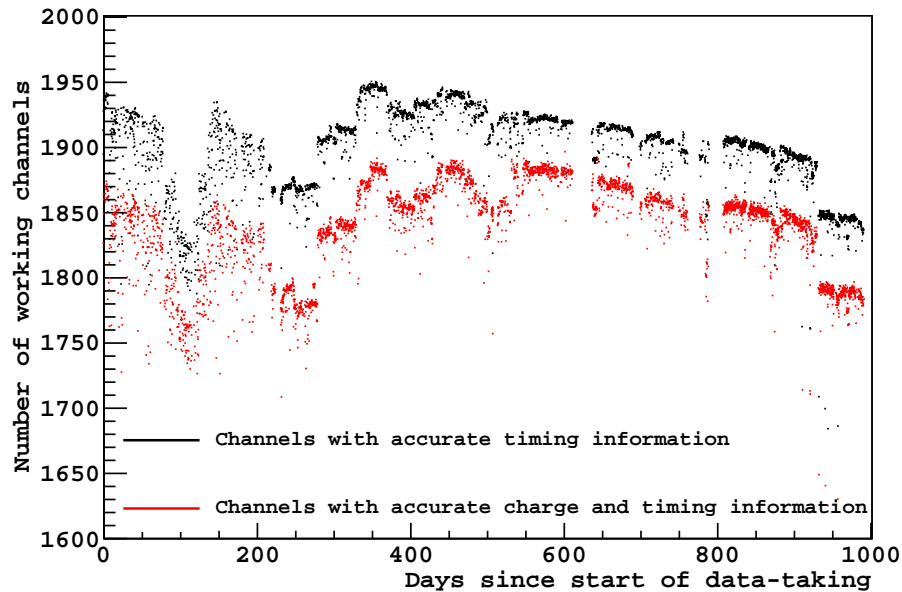
Figure 4.2: Number of working channels as a function of time. Number of channels with reliable timing information (N_{live_pmts}) is shown in black, while the number of channels with reliable timing and charge information ($N_{good\_charge\_chans}$) is shown in red. Sudden discrete jumps in the number of working channels are due to electronics problems and repairs.

- Working Channels

  Of the 2212 PMT's that were installed on the Stainless Steel Sphere, 175 of them were dead before the start of data taking, mostly due to loss of vacuum during

delays in the detector construction, defects or cracks in the waterproof sealing, or damaged connectors. Since then the failure rate of PMT's has plateaued out to around 3 failures per month [45]. In addition to these non-functional PMT's, due to various electronics problems, channels may have unreliable timing or charge information. A distinction is made between those channels that do not have accurate timing information and those that have accurate timing information but no charge information. Channels that do not have accurate timing information are not used at all, since without the time of a given hit, it is difficult to assign the hit to a particular event. Channels that have usable timing information but no charge information are still kept and used for the purposes of position reconstruction etc, but are not used in the determination of the energy of the event. Thus two separate list of working channels are kept with the total number of channels with accurate timing information referred to as N_{live_pmts} and the total number of channels with working charge readout referred to as $N_{good\_charge\_chans}$. We also note that during regular data taking runs, every half a second an electronic pulse trigger, a timing laser trigger and a random trigger are fired. The electronic pulse and timing laser trigger help determine if a channel is working during a run. If at any point during the run the channel stops recording data during these service triggers, the channel is marked as dead. Since it is difficult to determine exactly when the channel started misbehaving, the channel is removed from the list of working channels for the entire run. The number of working channels of each type, as a function of time, is shown in Figure 4.2.

- Dark Noise

  The dark noise rate of each individual channel is determined with the help of random triggers fired during a regular data taking run. Figure 4.3 shows the typical rate of dark noise per channel for runs during the analysis period for ^{7}Be.
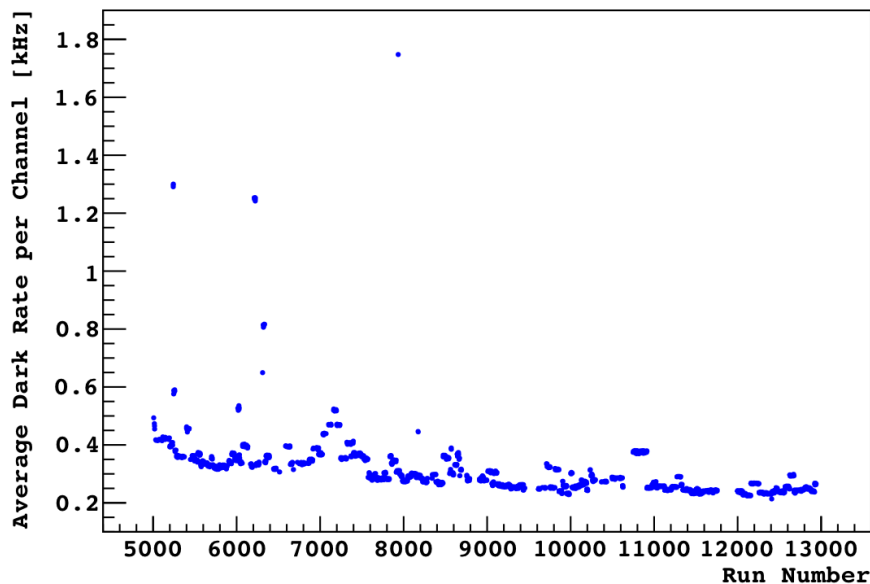
Figure 4.3: Average channel dark rate for each run during the ^{7}Be analysis period.

The average dark noise rate per channel varied by run from 0.21 to 1.75 kHz with a mean rate of 0.30 kHz. The average dark rate from all valid channels was ~ 550 kHz, which corresponds to an average of 9 random hits in a 16.5 μs trigger gate window. The expected number of dark noise hits occurring during a given event is subtracted from the total number of observed hits in order to improve the accuracy of the energy reconstruction.

4.1.2 Event Reconstruction

For each trigger gate, the raw data is converted into a list of hits. Each hit contains information regarding the channel it was recorded on, the time of the hit and the charge corresponding to the hit. The times are stored relative to the start of the trigger gate and the charge is stored in units of single photoelectrons. If the hit occurs on an non-working channel, or if the there is no accurate timing information then the hit is marked as invalid. If the hit has no charge information then an estimate of the charge q_{avg} is made by averaging the charge recorded on all other hits (with

valid charge) in a 15 ns window around the hit.

4.2 Clustering

Since the length of the trigger gate is 16.5 μs while the typical duration of hits related to a single physical event is ~ 1 μs, not all the hits in a single trigger gate correspond to the same event. There are hits due to random dark noise, or sometimes even two unique events recorded within the same trigger gate. The process of assigning individual hits to a specific event is referred to as clustering.

The general algorithm used for clustering is common to all trigger types though the specific implementation depends on whether it is a regular trigger, a trigger tagged by the outer detector as muon event, or a dedicated trigger for cosmogenic neutron captures.

First, all valid hits in the given trigger gate are binned in a histogram with a bin width of 16 ns. Then the rate of noise is estimated, either from the low level reconstruction or from the distribution of hits in the current trigger gate. Once the noise level has been determined, a moving window of length w_{start} is created. Starting from the start of the trigger gate, the window is moved one bin at a time through the trigger gate. When the number of hits in the moving window exceeds the noise level by a given threshold thr_{start}, the start of the cluster is identified. With the start identified, a second moving window of length w_{end} is setup. This second window continues to move through the trigger gate, beginning with the cluster starting point, as long as the number of hits in the window exceeds the noise level by a threshold thr_{end}. The bin at which the number of hits falls below the threshold is marked as the temporary end of the cluster. The process of looking for the start of another cluster then begins again, with the search point starting at the temporary end of the previous cluster.

When the moving window has passed through the entire trigger gate and the start and temporary end of each cluster has been identified, a second pass through the trigger gate is made to finalize the end points of each cluster. First, if the number of hits, h, between the start and temporary end of a cluster is less than 20 hits we discard the cluster. Thus 20 hits represents the nominal software threshold for an event. If, as is most often the case, there is only a single cluster in the trigger window, then an additional time period is added to the end of the cluster to ensure that we do not miss the last few hits of an event. The length of this additional "tail" is energy dependent (the dependence is described in detail at the end of this section) and is given by:

$$\text{tail} = \max\left(512 \text{ ns}, \ 512 \text{ ns} \cdot \left(1 + \log\left(\frac{h}{100}\right)\right)\right) \tag{4.1}$$

If however there is another cluster that starts soon after the temporary end of the previous cluster, the tail only extends up until the start of the next cluster.

In the following paragraphs we describe the specific implementations of the above algorithm for the different trigger types:
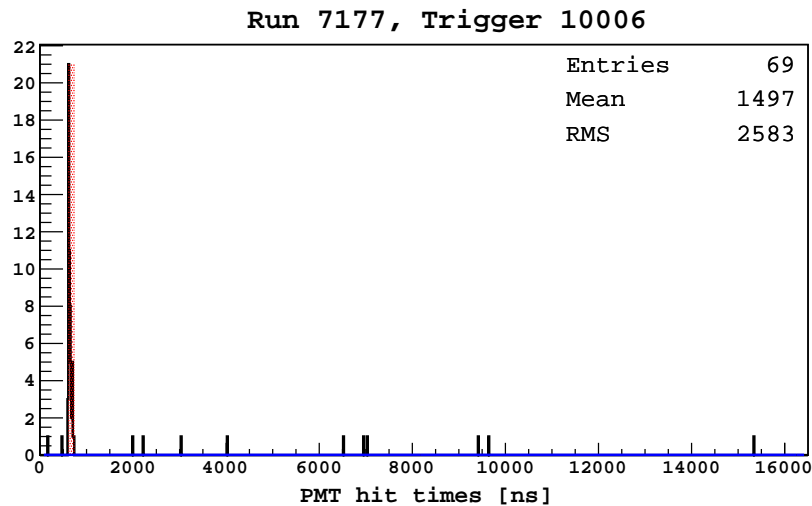

Figure 4.4: Cluster (red shaded region) in a regular trigger gate for a low energy ^{14}C event.
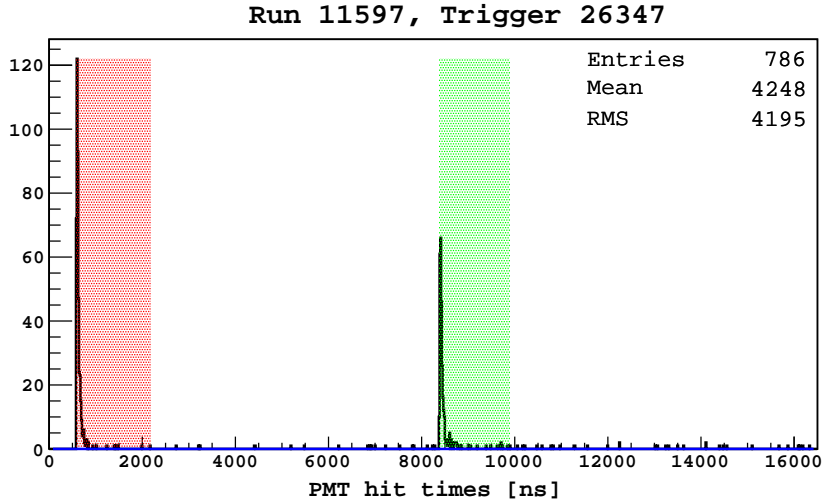
Figure 4.5: Clustering in a regular trigger gate for a ^{214}Bi-Po β(red)-α(green) coincidence event.

- Regular Triggers (`trigger_type = 1`)

  For regular triggers the expected number of "dark" noise hits is determined by the precalibration described above. The dark noise is negligible on the time scale we are interested in. For example, even in the runs with the highest dark rates ($\sim$ 3 kHz), the expected number of hits in 50 ns is 1.5×10^{-4}. Since scintillation light pulses have a very sharp rise, the start threshold, thr_{start}, is simply defined in terms of hits rather than a number of standard deviations above the noise. For the end of the cluster, which for scintillation pulses follows a slow exponential decay, the threshold is set at 3σ above the average dark noise level. The complete list of parameter values is listed in Table 4.1. Figures 4.4 and 4.5 show the outcome of the clustering algorithm for a low energy ^{14}C event and a ^{214}Bi-Po coincidence respectively.

- Muon Triggers (`BTB&4 = 1`)

  Muons passing through the scintillator deposit a large amount of energy. The resulting scintillation often swamps the electronics which leads to large amounts of after-pulsing and other electronics noise following a muon. This noise can last

108

for up to a few milliseconds making it difficult to identify clusters corresponding to physical events above the noise. During this period clustering is important to identify short-lived cosmogenic isotopes produced by the muon or, more importantly, tag them through the associated neutron captures. Because the noise varies with time (see Figure 4.6), we do not calculate a fixed noise level but instead use a moving average. Since the noise level varies much slower than the sharp rise of a scintillation pulse we calculate the dark noise in any bin to be the average number of hits in the current and previous 4 bins. However if the current bin has many more hits than the calculated noise level in the previous bin (for example at the start of a scintillation pulse) then the noise level is simply set to the average over the previous 5 bins. Thus the noise level follows the pattern of hits, except under pulses with steep rises, where a constant extrapolation is used. For the start and end searches, the parameters are given in Table 4.1. We note that for muon triggers no "tail" is added due to the high noise levels. Figure 4.6 shows a muon trigger with a neutron capture.

- Neutron Triggers (`trigger_type = 128`)

  Neutron triggers are special extra-long triggers gates (1.6ms) that are opened after every muon trigger, in order to detect neutron captures. Since the neutron trigger starts soon after the muon trigger, there is still a lot of electronics noise. However, by this time the noise can be well modeled by falling exponentials, unlike during the early part of the muon trigger. The noise is normally fit to the sum of three exponentials, though for muons that do not deposit much energy a constant noise level is used. For the start and end searches, the parameters used are given in the Table 4.1. Figure 4.7 shows a neutron trigger with a large number of neutron captures.
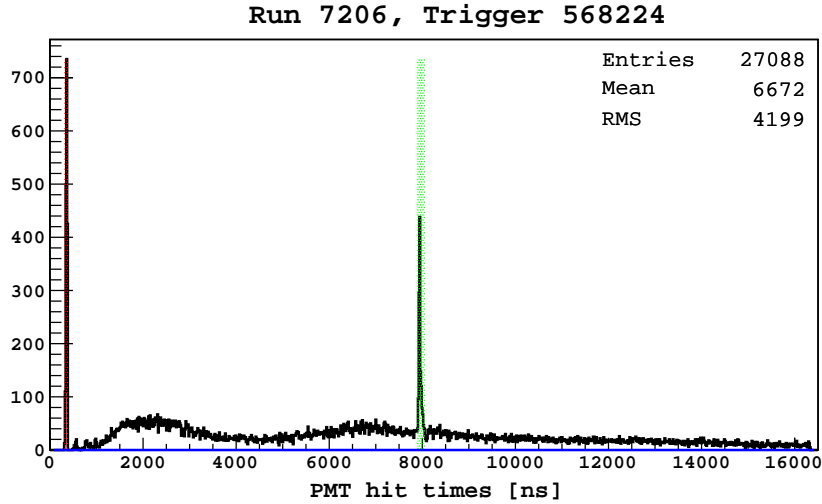
Figure 4.6: Clustering in a muon trigger gate. The sharp spike at ~ 500 ns (red) is the muon event with a probable neutron capture at ~ 8000 ns (green). The electronic noise is clearly visible as a slowly varying background.
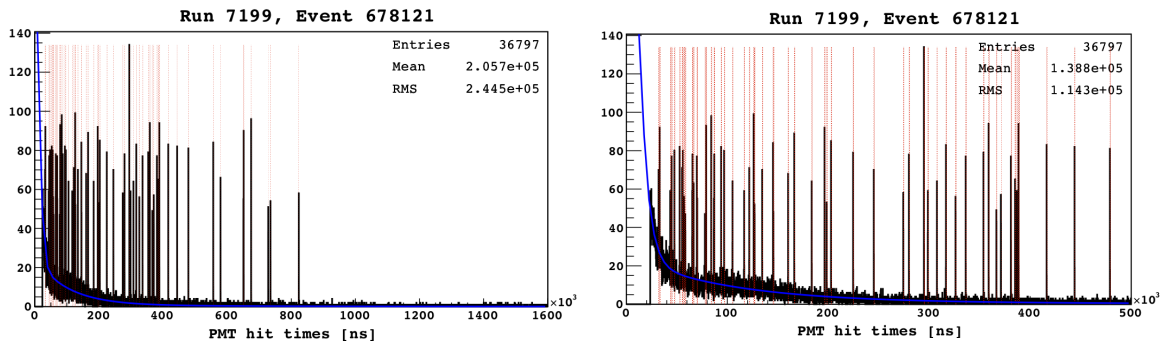
Figure 4.7: Left: Clustering in a neutron trigger window with high multiplicity of neutron captures. The clustered regions are shaded in red. The blue line shows the exponential fit to the noise level. Right: Expanded view of the first 500 μs

4.2.1 Performance and Future Improvements

The performance of the clustering algorithm is difficult to quantify. One test of the algorithm is how well it separates two distinct physical events falling within the same trigger gate. Figure 4.8 shows the distribution of the difference in time, Δt, between the first and second clusters in triggers that have two clusters. Given that the rate of events above the clustering threshold is ~ 75 Hz (dominated by low energy ^{14}C), the expected distribution should be exponential with a characteristic decay time of ~ 13 ms - essentially constant over the length of the trigger gate (16.5 μs). The distribution

Trigger Type	Noise Level	thr_{start} (hits/σ above noise)	w_{start} [ns]	thr_{end} (σ above noise)	w_{end} [ns]
Regular	Constant	9	48	3σ	96
Muon	Moving Avg.	$\max(50, 3\sigma)$	48	1σ	48
Neutron	3 exp.	3σ	48	1σ	96

Table 4.1: Parameter values used for clustering in different types of triggers. See text for details regarding the algorithm.
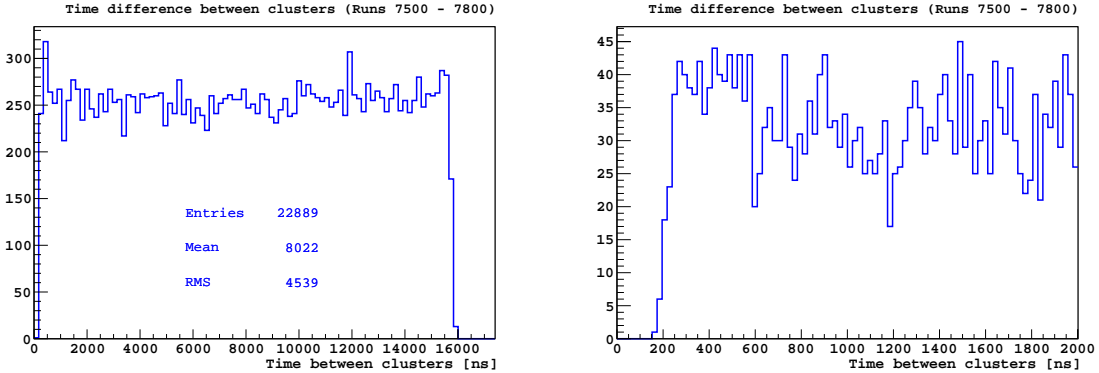
Figure 4.8: Left: Difference in time between the first and second clusters in regular triggers that have two clusters. Right: Expanded view of first 2 μs. Cut-off at $\sim$ 250 ns indicates limit of clustering algorithm sensitivity.

in Figure 4.8 is indeed flat, with a sharp drop-off below $\Delta t \sim 250$ ns. This implies that the algorithm cannot distinguish clusters that are less than 250 ns apart. There is also a slight excess of events with 250 ns $< \Delta t < 600$ ns. One possible reason for this is that events just below the clustering threshold (20 hits) have a higher probability of being clustered if they are sitting on the tail of a previous event. Further investigation is required.

One of the parameters of critical importance is the length of the cluster. The values used in the current version of *Mach4*, especially the length of the tail added, were chosen empirically after experimenting with different options. Figure 4.9 shows the relationship between the cluster length and the total number of hits in the cluster for regular triggers. The effect of the logarithmic tail (Eq. 4.1) is evident. The longer cluster lengths in the ^{210}Po peak region (150 - 200 hits) are due to the larger slow
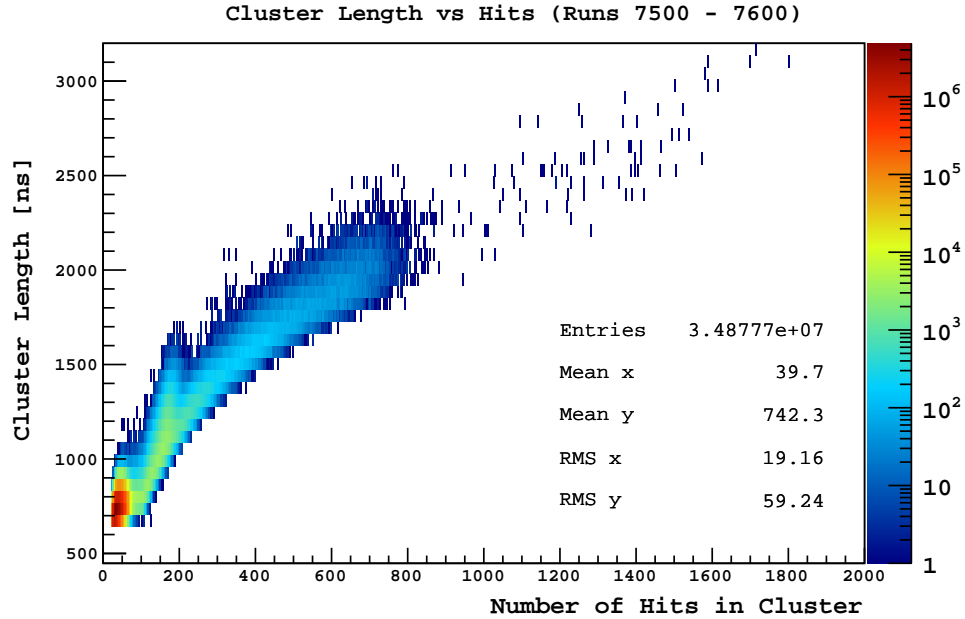
Figure 4.9: Cluster length versus the number of total hits in the cluster for regular triggers. An additional cut was placed on the mean of the cluster emission time to remove muon events that were not tagged by the outer detector. The dependence is dominated by the logarithmic tail (Eq. 4.1) added to each cluster. The increase in the 150 - 200 hit region is due to the longer scintillation time profile of (^{210}Po) αs.

component of α scintillation light as compared to βs. It should be noted that the cluster length shown in this figure is the length in time during which the cluster was defined. In contrast, the cluster length stored in *Mach4* is the time between the first and last hit during this period - which can be considerably shorter. An additional cut on the mean of the cluster emission time was used to remove muon events that were not tagged by the outer detector.

It was noticed, during a particularly unsuccessful process cycle, that shorter tails drastically reduced the ability to separate α and β events using the Gatti parameter (described later in this section). Even though there are indications that not all the hits related to the event are currently being included (for example see the α cluster in Figure 4.5), longer cluster lengths have not yet been tried.

There is also a debate regarding whether the cluster length should be fixed, irrespective of energy, as is done in *Echidna*, or whether it should be energy dependent,

as in *Mach4*. We will motivate the *Mach4* energy-dependent length here. For simplicity consider events at the center of the detector, so that we can neglect transit time effects. In this case the hit time distribution for an event occurring at time $t = 0$ follows the emission time distribution $p(t)$, which we will assume to be exponential $p(t) = \Theta(t)\frac{1}{\tau}e^{-t/\tau}$ (the fast component has a negligible effect on the cluster length). The start and end of the cluster are defined as the first and last hit of the event respectively and the length of the cluster is the time difference between the two. Consider an event with n hits. The probability distributions for the first and last hit are given by the order statistics [85] of the distribution:

$$p_{(1,n)}(t) = n \cdot p(t) \cdot \left(\int_t^\infty p(t')dt' \right)^{n-1} \tag{4.2}$$

$$= \frac{ne^{-\frac{nt}{\tau}}}{\tau} \tag{4.3}$$

where $p_{(1,n)}(t)$ is the probability distribution for the first of n hits. The formula above can be easily obtained by noting that for the first hit to occur at time t, you need one hit to occur at time t, and all $(n-1)$ other hits to occur at times $t' > t$. The factor n comes from the fact that you can pick the first hit in n ways. Similarly, for the last hit:

$$p_{(n,n)}(t) = n \cdot p(t) \cdot \left(\int_{-\infty}^t p(t')dt' \right)^{n-1} \tag{4.4}$$

$$= \frac{ne^{-\frac{t}{\tau}} \left(1 - e^{-\frac{t}{\tau}} \right)^{n-1}}{\tau} \tag{4.5}$$

113

The average length a cluster with n hits, $\overline{l(n)}$, is then given by:

$$\overline{l(n)} = \int_0^\infty p_{(n,n)}(t)t\,dt - \int_0^\infty p_{(1,n)}(t)t\,dt \tag{4.6}$$

$$= \tau \sum_{k=1}^{n} \frac{1}{k} - \frac{\tau}{n} \tag{4.7}$$

$$= \tau \left(\ln(n) + \gamma + \mathcal{O}(n^{-1}) \right) \tag{4.8}$$

where $\gamma \sim 0.577$ is the Euler-Mascheroni constant. Thus we see that the average cluster length has a logarithmic dependence on the number of hits.

The current clustering uses only the timing information of the hits to split events into individual clusters. While this works well in the energy range used for the ^{7}Be analysis, at low energies pileup of ^{14}C events becomes a significant problem. In the future, in order to reduce the rate of pileup events, as will probably be necessary for an analysis of the pp solar neutrinos, an algorithm that also takes into account the spatial information of the hits should be implemented. For example, a trigger that has all the hits clustered in a short time period but located on two spatially distinct groups of PMTs could be fairly easily identified as pileup. Some of the current variables that take into account the available spatial information of the hits are discussed in Section 4.7.

4.3 Position Reconstruction

One of the most powerful background reduction techniques available is the fiducialization of the Inner Vessel. By reconstructing the position of individual events one can reject background γ rays originating on or near the Stainless Steel Sphere and vessel end caps (see Section 3.2.11). The position reconstruction algorithm uses the timing information available for each hit as well as the known positions of the PMT's to determine the most likely position of the event.

Consider an event that produces n detected hits. We will denote the vector of hits as $\{\mathbf{x_i}, t_i\}$ where $\mathbf{x_i}$ is the position vector of the PMT that detected the ith hit and t_i is the detection time of the hit, for $i = 1$ to n. The likelihood that the event occurred at $(\mathbf{x_0}, t_0)$ is then given by:

$$\mathcal{L}\left((\mathbf{x_0}, t_0)|\{\mathbf{x_i}, t_i\}\right) = P\left(\{\mathbf{x_i}, t_i\}|(\mathbf{x_0}, t_0)\right) \qquad (4.9)$$

where we interpret the right hand side of the above equation as the probability of an event occurring at $(\mathbf{x_0}, t_0)$ creating the observed hit pattern $\{\mathbf{x_i}, t_i\}$. In evaluating this probability we will only consider the timing information and ignore factors corresponding to the angle subtended by the different PMT's and PMT's that did not register hits. A detailed description of these factors is given in [43]. We note that when these factors were included in the position reconstruction algorithm, no improvement in the performance was observed. We will also ignore any effects of scattering[1] and assume that all the emitted photons travel at a speed given by c/n_{eff} where $n_{\text{eff}} = 1.68$ is the effective index of refraction discussed in Section 2.1.2.2. The time of flight between the position of the event and the ith PMT is given by:

$$t_f(\mathbf{x_0}, \mathbf{x_i}) = |\mathbf{x_0} - \mathbf{x_i}| \cdot \frac{c}{n_{\text{eff}}} \qquad (4.10)$$

which allows us to convert the detection time of each photoelectron into a photon emission time $t_e = t_i - t_f$. We note that t_e is not the true emission time of the photon since it includes delays due to the PMT transit time and other electronics. However, as long as these delays are the same for all channels, they only cause an offset in the timing for all events and do not affect the position reconstruction algorithm. If we

---

[1]The emission time profile features a sharply rising peak followed by a long tail (see Figure 4.10) and so the likelihood is dominated by the arrival time of the earliest photons. Photons that undergo large angle scattering therefore do not greatly affect the algorithm. For details on the scattering and absorption lengths of the scintillator, see [51].

know the probability distribution for the scintillator emission time profile $P(t)$, we can write the likelihood as:

$$\mathcal{L}\left((\mathbf{x_0}, t_0)|\{\mathbf{x_i}, t_i\}\right) \equiv \prod_{i=1}^{n} P(t_i - t_f(\mathbf{x_0}, \mathbf{x_i}) - t_0) \tag{4.11}$$

where we have assumed that the timing of the emitted photons are independent of each other. By varying the parameters of the event location $(\mathbf{x_0}, t_0)$, we define the reconstructed position as the position and time that maximizes the likelihood function.

There is an additional complication that arises due to the characteristic of the Borexino electronics. As is described in Section 2.2, for a given channel, we do not detect the time of each photoelectron, but rather the time of the first photoelectron and the total integrated charge on the channel. Thus, while we know the total number of photoelectrons on each channel, we do not know the timing of each of them.

The timing probability distribution of the first of many recorded photoelectrons is skewed towards earlier times as compared to the probability distribution for a single photoelectron. This can be easily understood by comparing the case with one and two detected photoelectrons. In the case of a single photoelectron, the probability that the first (and only) photoelectron will have a value below the mean value of the distribution is 1/2. For two photoelectrons however, the probability that the photoelectron with the earliest time will have a value below the mean is 3/4. The exact analytical expression for the probability distribution of the first of p detected photoelectrons (known as the first-order statistic [85]) can be easily computed as:

$$P_{(1,p)}(t) = p \cdot P(t) \cdot \left(\int_{t}^{\infty} P(t')dt'\right)^{p-1} \tag{4.12}$$

where $P_{(1,p)}(t)$ is the probability distribution for the first of p photoelectrons and $P(t)$ is the probability distribution for a single photoelectron. As described in Section 4.2,

116

the above formula can be obtained by noting that for the first hit to occur at time t, you need one hit to occur at time t, and all $(p - 1)$ other hits to occur at times $t' > t$. The factor p comes from the fact that you can pick the first hit in p ways. We therefore need to modify the likelihood function defined above as follows:

$$\mathcal{L}\left((\mathbf{x_0}, t_0) | \{\mathbf{x_i}, t_i, p_i\}\right) \equiv \prod_{i=1}^{n} P_{(1, p_i)}(t_i - t_f(\mathbf{x_0}, \mathbf{x_i}) - t_0) \qquad (4.13)$$

where p_i is the number of detected photoelectrons on the ith channel. The different multi-photoelectron probability distributions $P_{(1,p)}(t)$ for $p = 1$ to 10 are shown in Figure 4.10.
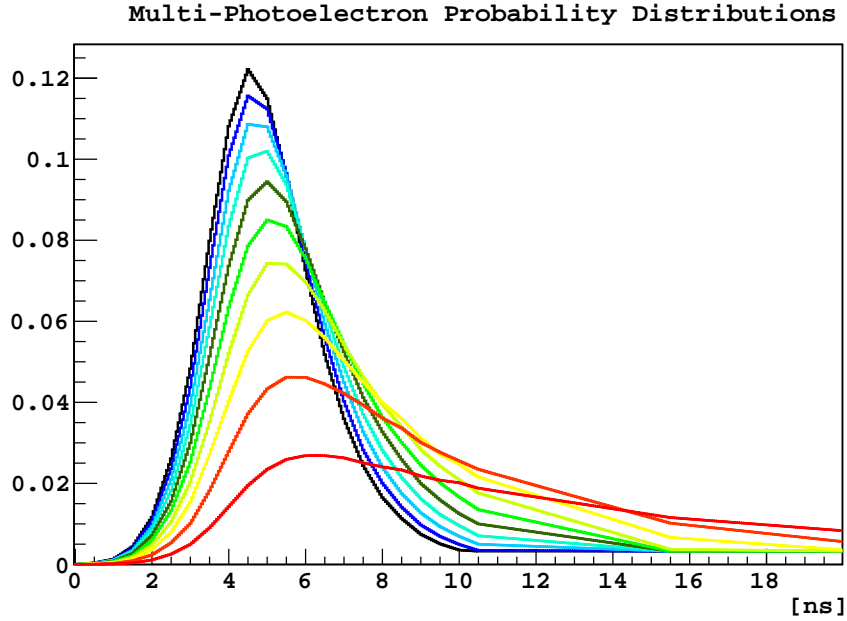

Figure 4.10: Probability distributions, $P_{(1,p)}(t)$, for the emission times of the first of $p = 1$ (red, broadest) to 10 (black, narrowest) photoelectrons, used in the likelihood function of the position reconstruction algorithm.

4.3.1 Performance

The position reconstruction implementation that was used for the ^{7}Be analysis was the `lngs` position reconstruction within *Echidna*. While the basic idea is the same as the implementation in *Mach4*, it was found that the `lngs` algorithm had a smaller uncertainty in the reconstructed position, and was therefore preferred. In this section we will briefly evaluate the performance of the `lngs` position reconstruction using the source calibration data.

4.3.1.1 Evaluation of Fiducial Volume

In order to calculate the rate of ^{7}Be neutrino interactions in terms of a quantity that can be compared with the theory (as well as other experiments), one needs to know the mass of the target used. It is therefore of critical importance to accurately determine the volume of the scintillator that lies within the defined fiducial cuts. The standard fiducial volume used for the ^{7}Be analysis is defined as the central region of the detector bounded by a reconstructed radius of 3.021 m and vertical cuts at $z_{recon} = \pm 1.67$ m. This corresponds to a nominal volume of 86.01 m^3, if there is no bias in the reconstruction.

We can evaluate possible biases and uncertainties related to the reconstruction of the fiducial volume by comparing the reconstructed positions of the inserted sources to the positions as determined by the CCD cameras. As described above, the position reconstruction algorithm is based on a time-of-flight method for the scintillation light, while the cameras use a ray-tracing algorithm to reconstruct the position of the source. These methods are fairly independent (though both are sensitive to changes in the index of refraction) and their uncertainties should be uncorrelated. However, following the initial calibration campaigns the refractive index n_{eff} used in the position reconstruction algorithm was tuned to match the camera reconstruction. Due to this tuning, we must also evaluate the uncertainty of the source location with the cameras

independently. It should be pointed out that the following discussion and evaluation of the fiducial volume uncertainty is based on the same data that was used for the recent publication [86] but the method adopted, as well as the final result, differs slightly.
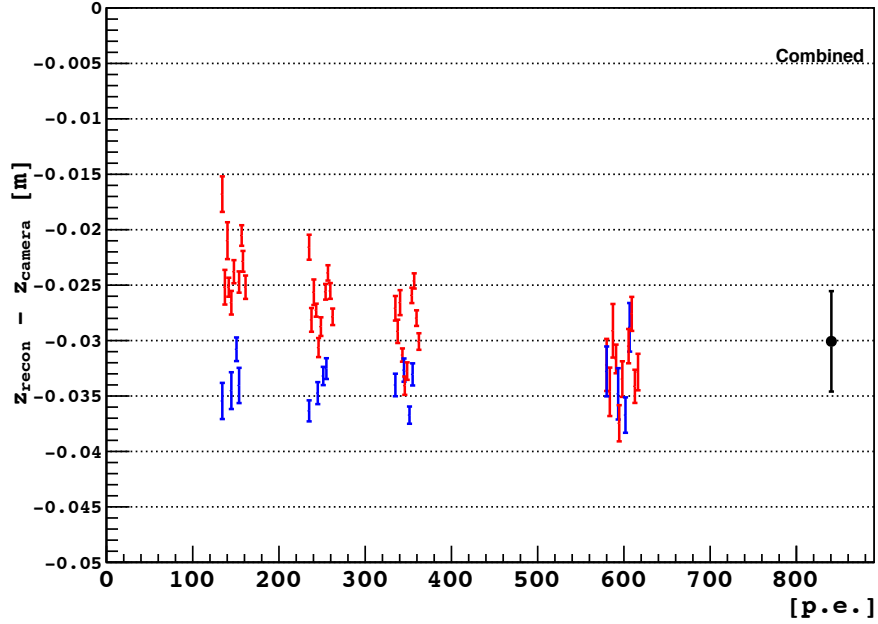
Figure 4.11: Difference between the z positions for sources at different energies, as determined by the position reconstruction algorithm z_{recon} and the CCD cameras z_{camera}. Sources in the northern hemisphere are shown in blue, while sources in the southern hemisphere are shown in red. The data point on the extreme right of the plot is the combined average of all points. Data taken from [56].

Comparison between CCD cameras and position reconstruction algorithm

Since we are only interested in the total volume enclosed by the fiducial cuts we shall focus our attention on the 33 different source locations near the boundary: $r \sim 3$ m, $|z| \sim 1.7$ m. While the position of the sources, as determined by the camera, agree fairly well with the position reconstruction along the x and y directions, there is a significant offset along the z (vertical) direction. Figure 4.11 shows the difference in z (Reconstructed - Camera), for source events located at $|z| \sim 1.7$ m, at different energies. We see that the reconstructed z position is consistently lower than the value

119

from the CCD cameras by 3.0 ± 0.5 cm. A simple translation along the z direction, though currently not understood, would only imply a shift in the coordinate system between the cameras and reconstruction software and would not affect the fiducial volume. What we are really interested in are relative differences, such as radial deformations, that alter the volume of scintillator enclosed between the fiducial cuts. We point out that at low energies the observed z shift is larger at the top (3.4 ± 0.2 cm) than at the bottom (2.3 ± 0.3 cm), whereas at around 600 p.e., the respective values (3.3 ± 0.3 cm, 3.2 ± 0.3 cm) are essentially identical.

In Figure 4.12, we have plotted the difference (Reconstructed - Camera) along the
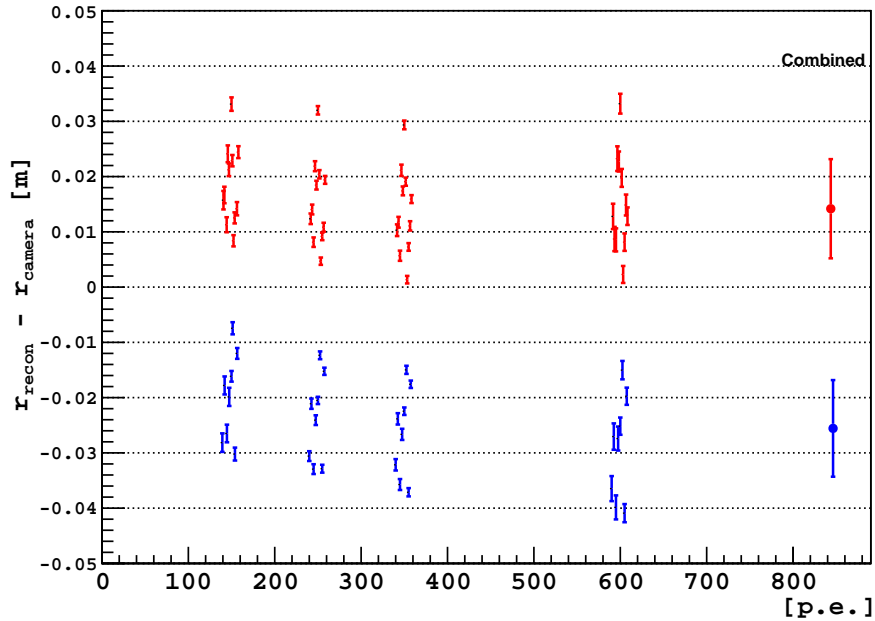
Figure 4.12: Difference between the radial positions for sources at different energies, as determined by the position reconstruction algorithm r_{recon} and the CCD cameras r_{camera}. Sources in the northern hemisphere are shown in blue, while sources in the southern hemisphere are shown in red. The data points on the extreme right of the plot are the combined average over the individual hemispheres. Data taken from [56].

radial direction for sources at $r \sim 3$ m. As one would expect, given the offset in z, sources in the top hemisphere (blue) are reconstructed at a lower radius than from the camera, while the opposite is true for sources in the lower hemisphere (red). However

we note that the absolute value of the average difference in radial position is slightly larger for sources in the top hemisphere (-2.6 ± 0.9 cm) than for sources in the bottom (1.4 ± 0.9 cm). For a simple translation along the vertical axis, we would expect them to have the same magnitude.

A more careful study is needed to determine if this difference is indeed statistically
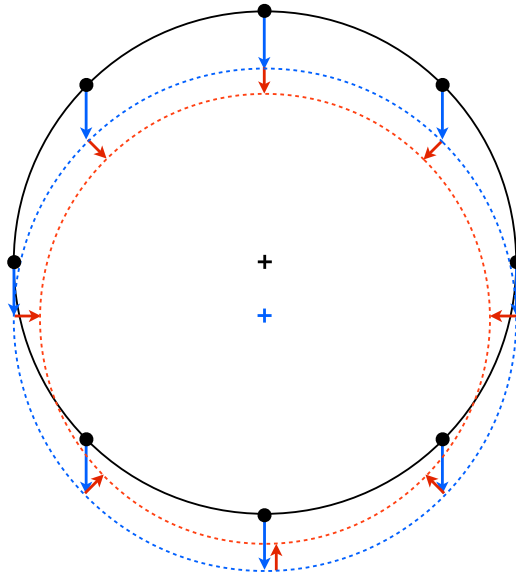
Figure 4.13: Schematic drawing modeling the relative differences between the CCD camera positions and the position reconstruction. The black points represent different source positions located on a sphere near the fiducial volume edge, in the reference frame of the cameras (centered on black cross). The blue arrows indicate the downward shift of the source positions in the reference frame of the reconstruction software (centered on blue cross), such that the black spherical volume has been translated to the dashed blue sphere. Red arrows indicate inward radial shift of reconstructed positions from the true radius. The effective sphere enclosed by the sources is the shown by the (smaller) dashed red sphere.

significant, but for the purpose of this analysis, we propose the following extremely simplified model, in order to obtain a rough estimate of the uncertainties in the fiducial volume. Suppose that in addition to the offset in the vertical direction, there is also a small radial shift, such that the reconstructed position is always at a smaller radius than the position from the cameras. The situation is illustrated in Figure 4.13. The

black points indicate source positions located on a sphere near the fiducial volume edge, in the reference frame of the cameras. The blue arrows indicate the downward shift of the source positions in the reference frame of the reconstruction software, such that the black spherical volume has now been translated to the dashed blue sphere. The volume of the blue sphere is clearly still the same as the black one, and the magnitude of the decrease in radius (with respect to the camera center) of sources in the top hemisphere is equal to the increase in radius of sources in the bottom. We now imagine that there is also an inward radial shift (indicated in red) in the reference frame of the reconstruction software. The volume enclosed is now smaller, proportional to the cube of the fractional decrease in radius. We note that at the top the radial shift acts in the same direction as the vertical shift, magnifying the effect, while at the bottom they oppose each other. This would explain the relative differences between the top and bottom hemisphere shown in Figures 4.11 and 4.12. This does not however explain the energy-dependent z shift in the southern hemisphere shown in Figure 4.11.

We can obtain the size of the radial shift by averaging the change in radius of the source positions in the top and bottom hemispheres. Applying this model to the data presented in Figure 4.12, we obtain a radial shift of -0.6 ± 0.6 cm at a radius of ~ 3 m, giving a relative radial bias of $\Delta r/r = (-0.2 \pm 0.2)\%$. Alternatively, we can calculate the radial shift from the difference in the z shifts at the top and bottom. Using the low energy data in Figure 4.11 we get a radial shift of -0.6 ± 0.2 cm at $|z| \sim 1.7$ m, which equates to a relative radial bias of $\Delta r/r = (-0.3 \pm 0.1)\%$. The high energy data in Figure 4.11 however indicates a negligible radial shift of $\Delta r/r = (0.0 \pm 0.1)\%$.

Given the spread in calculated values for the radial shift and our lack of understanding of the underlying cause, we have decided to adopt an estimate of $\Delta r/r = (-0.15 \pm 0.25)\%$. For a sphere of radius 3.021 m, a radial shift inwards in the software reconstruction reference frame of this magnitude implies that the true fiducial volume

is larger than the nominal one by (0.45 ± 0.75) %.

Uncertainty in reconstruction with CCD cameras   Prior to the calibration campaigns, the performance of the position reconstruction algorithm was evaluated and tuned using backgrounds intrinsic to the scintillator such as ^{14}C, ^{222}Rn daughters and external backgrounds (see for example, [87]). During this period it was noticed that reconstructing events using the phase velocity of the scintillation light $(n = 1.53)$ led to a strong outward radial bias. The index of refraction was therefore tuned to a value of $(n = 1.70)$ such that the known radius of the Inner Vessel could be reproduced. The relationship between the reconstructed radius of an event and the index of refraction can be understood using a simple model. Consider an event located off-center that simultaneously emits light in all directions. If we look at the time difference, Δt, in the arrival time of the light at photomultipliers located opposite to each other, on the diameter passing through the event position, we can calculate the radius of the event using the formula:

$$r_{rec} = \frac{c\Delta t}{2} \cdot \frac{1}{n} \qquad (4.14)$$

where c is the speed of light and n is the refractive index used. Thus, by modifying the refractive index one can adjust the reconstructed radial position of events:

$$\frac{r'_{rec}}{r_{rec}} = \frac{n}{n'} \qquad (4.15)$$

The magnitude of the radial shift given by the back of the envelope calculation in Eq. 4.15 agrees with the changes seen when switching between $n = 1.53$ and $n = 1.70$ [87]. Following the calibration campaigns, the effective refraction index was further tuned from $n = 1.70$ to $n = 1.68$ in order to agree with the source positions as reconstructed by the CCD cameras. Using Eq. 4.15, this corresponds to a 1.2%

123

increase in radius at 3 m, or a decrease in fiducial volume of about 3.6%. This is not a small effect and raises the question of how accurately the CCD cameras reconstruct the true position of the sources. If there is in fact a radial bias in the CCD camera reconstruction, then the same bias will also be incorporated into the position reconstruction.

Fortunately the source insertion hardware provides us with an additional handle on the systematics associated with the CCD camera reconstruction. Using the known lengths of the stainless steel rods used to insert the source into the inner vessel, we can measure differential lengths along the z-axis to within ± 2 mm. This high accuracy allows us to place stringent limits on the radial bias, as described below. We note that since the absolute position of the source insertion point in the CR4 glovebox is not known to the same accuracy, we can only measure differences in length. Also, the larger uncertainty in the length of the tether for off-axis calibrations restricts us to data along the z-axis.
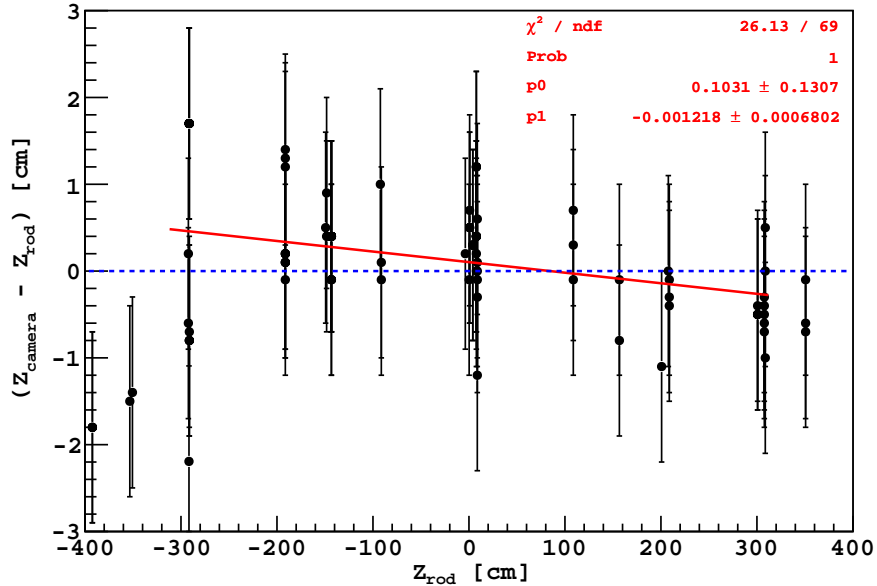

Figure 4.14: Difference between the z positions for sources located along the z-axis, as determined by the CCD cameras z_{camera} and the length of the source insertion rods z_{rod}. Error bars are set equal to ± 1.1 cm, using the value from [88]. The red line shows a linear fit to the data between ± 3 m, while the dashed blue line indicates perfect agreement.

Figure 4.14 shows the difference ($z_{camera} - z_{rod}$) between the predicted z positions of the source versus the z position from the insertion rods. The spread in points at fixed z positions is due to differences in the camera reconstruction for different runs. The error bars are set to ± 1.1 cm from tests of the camera location system along the z-axis, prior to filling [88]. No error is assigned to the position obtained from the insertion rods. We note that the outlying points near $z = -400$ cm are currently not well understood. Fitting the data between ± 3 m to a straight line (shown in red) indicates that the data prefers a small z bias: $\Delta z/z = (-0.12 \pm 0.07)\%$ with the camera positions pushed toward the center with respect to the rod positions. Note that we are not concerned about the offset between the two at $z = 0$ (which is related to an offset in the two coordinate systems) but in the slope between the points. Assuming that this trend also holds along the x and y axis, an inward radial bias of $\Delta r/r = -(0.12 \pm 0.07)\%$ corresponds to a $(0.36 \pm 0.21)\%$ larger fiducial volume. We point out that the small value of χ^2 for the fit indicates that the error bars on the CCD camera positions are slightly conservative.

Resolution   The resolution of the position reconstruction was studied using the localized source calibration data. Figure 4.15 shows the resolution in the x, y, and z (vertical) directions for sources of different energies located at the center of the detector. The resolution along the z direction is worse due the larger spacing between the phototubes in the vertical direction. The typical resolution at the ^{7}Be shoulder energy is $\sim 11 - 12$ cm in each direction and there is no significant reduction in the resolution throughout the fiducial volume. Since the distance between the edge of the fiducial volume ($r = 3$ m) and the inner vessel ($r \sim 4.25$ m) is large compared to the resolution, the effect of the resolution on the fiducial volume is negligible ($< 0.01\%$). Figure 4.16 shows a simulated distribution of reconstructed positions for events uniformly distributed within a 4.25 m sphere. One can see that even for a
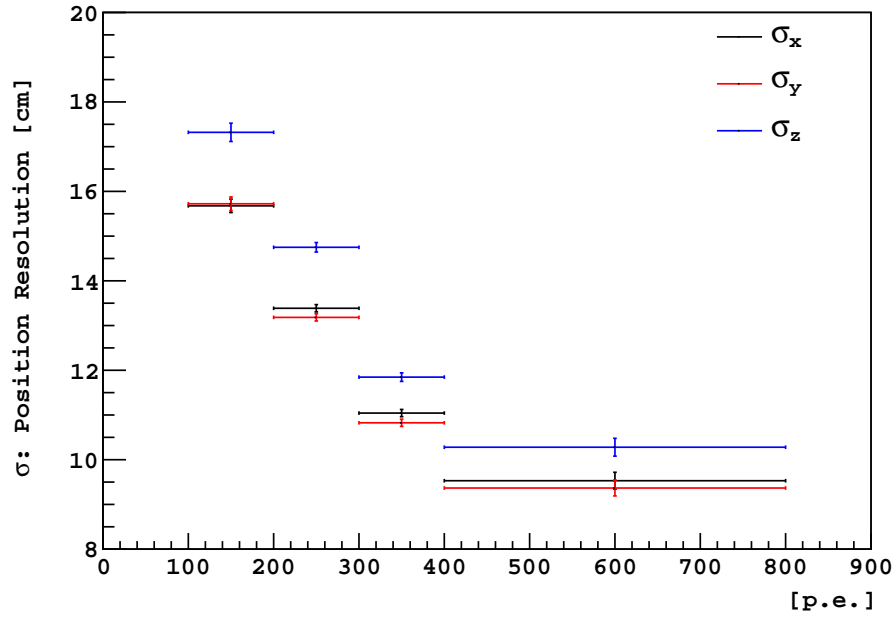
Figure 4.15: Position reconstruction resolution as a function of the number of detected photoelectrons for sources located at the center of the detector. The resolution is shown separately for each coordinate axis.

resolution of 18 cm, the number of events reconstructing within a 3 m sphere stays constant (as many events are pushed out of the fiducial volume as are pulled in).

Overall Uncertainty in Reconstructed Fiducial Volume   Combining the overall uncertainty of the previous sections, summarized in Table 4.2, we obtain an overall change of $(0.81 \pm 0.78)\%$ from the nominal fiducial volume.

Source	Change in Volume %	Uncertainty %
Reconstruction - Camera Comparison	+0.45	0.75
Camera - Hardware Comparison	+0.36	0.21
Reconstruction Resolution	< 0.01	-
Total	+ 0.81	0.78

Table 4.2: Summary of uncertainties in the reconstructed fiducial volume.

126
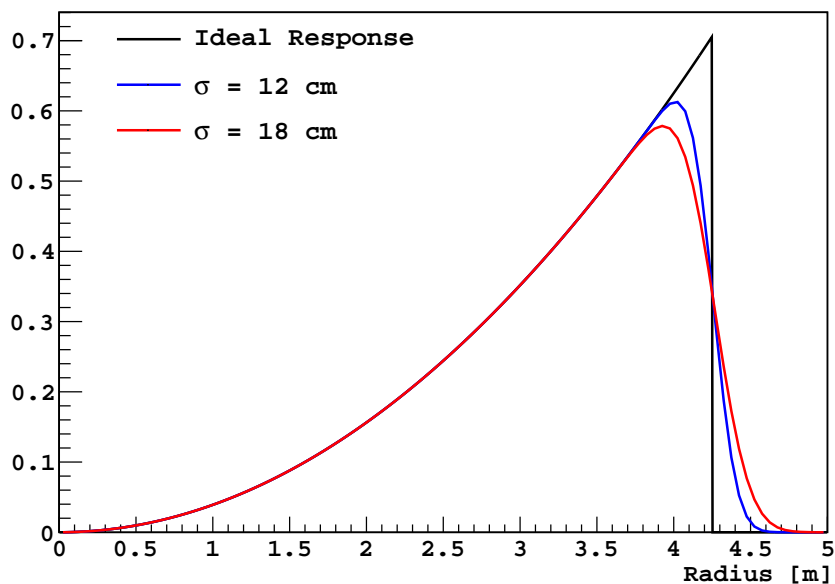
Figure 4.16: Simulated radial distribution of reconstructed positions for events uniformly distributed within a 4.25 m sphere (roughly the Inner Vessel radius). The black line indicates the distribution obtained for an ideal reconstruction with infinite precision, while the blue and red lines are simulated with fixed resolutions of 12 and 18 cm respectively.

4.4   Energy Reconstruction

There are two main methods used to estimate the energy of an event from the observed data: by calculating the number of PMT's hit during the event or by calculating the total charge recorded by the PMT's. The relationship between these energy estimators and the true energy will be discussed in detail in Chapter 5. In this section we will focus in how these values are computed. Once the start and end points of the cluster are identified, the calculation of the energy estimators is fairly straightforward, though there are some electronics-related issues such as channel re-triggering and noise that are described below.

4.4.1   npmts/nhits

First we sum up the number of hits with valid timing information that fall within the cluster. Then, based on the estimated noise rate in the trigger gate and the length

of the defined cluster, we subtract the predicted number of noise hits. Finally, in order to compare events across runs with different number of functional phototubes, we scale the number of hits by $2000/N_{live\_pmts}$. In the case that is most easily related to the energy of the event, we exclude multiple hits on the same channel. The sum then represents the total number of PMT's hit and will be referred to from here on as `npmts`. An alternative variable, including multiple hits on the same channel, is referred to as `nhits`.

4.4.2   npe

For every hit with valid timing charge information that falls within the cluster, we sum up the charge recorded for that hit. As in the case for `npmts` and `nhits`, we then subtract the predicted number of noise hits (assuming a single photoelectron for each noise hit) and scale the total charge by $2000/N_{good\_charge\_chans}$. This variable is referred to as `npe`. A related variable, npe_{avg}, is calculated by including all hits with valid timing within the cluster, irrespective of whether they have a valid charge value. For those hits without a valid charge readout, q_{avg} (described in Section 4.1.2) is used. We note that at the time of the ^{7}Be analysis, re-triggered hits were included in both of these variables. The latest version of *Mach4* includes additional variables that exclude multiple hits on the same channel.

4.5   Pulse Shape Discrimination

Due to the different ionization densities, the scintillation light produced by α and β particles have different time profiles. This difference in the emission time profiles allows us to discriminate between the two types of events and acts as a critical α background[2] reduction technique for the ^{7}Be analysis. The statistical technique used

---

[2]Radioactive β decays have the same emission time profile as electron recoils from neutrino interactions and hence cannot be distinguished from the signal

to distinguish particle types based on their emission time profiles is commonly known as the Gatti filter, after the author of the original paper [89].

4.5.1 Gatti Parameter Theory

In [89] a method is proposed to separate two classes of events with differing but known time profiles. For both α and β events, a normalized reference shape is created that represents the probability distribution, in time, for a photon to be emitted. The reference shapes are binned for ease of comparison with experimental data. If we denote the respective probability distributions as $P_\alpha(t)$ and $P_\beta(t)$ and the reference shapes as $r_\alpha[t_n]$ and $r_\beta[t_n]$ then, for an event occurring at time t_0, we have

$$r_\alpha[t_n] \equiv \int_{t_0+n\Delta t}^{t_0+(n+1)\Delta t} P_\alpha(t)dt \tag{4.16}$$

$$\sum_{n=0}^{\infty} r_\alpha[t_n] = \int_{t_0}^{\infty} P_\alpha(t)dt = 1 \tag{4.17}$$

where n is the bin number and Δt is the bin width (and similarly for βs).

The Gatti parameter for an event with a (binned and normalized) time profile $e[t_n]$ is then defined as:

$$g_e \equiv \sum_{n=0}^{\infty} e[t_n] \cdot w[t_n] \tag{4.18}$$

where the weight $w[t_n]$ is given by:

$$w[t_n] \equiv \frac{r_\alpha[t_n] - r_\beta[t_n]}{r_\alpha[t_n] + r_\beta[t_n]} \tag{4.19}$$

For time bins where both reference shapes are zero, the weight $w[t_n]$ is set to zero. If an event with N photoelectrons is drawn from the α (β) probability time distribution,

129

then the corresponding Gatti parameter also follows a probability distribution G_α (G_β). The mean and variance of this distribution are

$$\overline{G_\alpha} \equiv \sum_{n=0}^{\infty} r_\alpha[t_n] \cdot w[t_n] \tag{4.20}$$

$$var(G_\alpha) \equiv \frac{1}{N} \sum_{n=0}^{\infty} r_\alpha[t_n] \cdot w^2[t_n] - \left(\overline{G_\alpha}\right)^2 \tag{4.21}$$

and similarly for events drawn from the β probability time distribution. We note here that the absolute value for the means of the G_α and G_β distributions are the same (they differ in sign) and are independent of energy. The variance of the distributions are different and are energy dependent. The shapes of the probability distributions are not true Gaussians but should approach the normal distribution for large statistics.

A common figure of merit used to determine how well a discrimination parameter can separate two different classes of events is defined as:

$$D \equiv \frac{\overline{G_\alpha} - \overline{G_\beta}}{\sqrt{var(G_\alpha) + var(G_\beta)}} \tag{4.22}$$

This figure of merit is based on the fact that for well separated distributions, the difference in the values of the means (numerator) should be large compared to the sum, in quadrature, of the standard deviations of the individual distributions. It can be shown [89] that given two reference shapes, the Gatti parameter is the linear weighting of those reference shapes, that maximizes the figure of merit D.

4.5.2 Gatti Parameter Implementation

4.5.2.1 Reference Shapes

To obtain the reference shapes for α and β events, we use events tagged as ^{214}Bi-Po $\beta-$ α coincidences throughout the data taking period. To identify the ^{214}Bi-Po coincidences we place the following cuts on consecutive trigger events:

1. Both events must lie within a 4 m radius

2. The first event (^{214}Bi candidate) must have an energy in the range of 100 - 1750 $\texttt{npe}_{avg}$

3. The second event (^{214}Po candidate) must have an energy in the range of 300 - 500 $\texttt{npe}_{avg}$

4. The time difference between the two events must be in the range of 20 - 500 μs

5. The distance between the two events must be less than 0.6 m

The coincidence requirement ensures that we have a clean sample of events, relatively free from background. For each event in the detected coincidences, we generate a time-of–flight subtracted time profile by subtracting the transit time (assuming an index of refraction of dependent on energy) from the reconstructed position to the PMT. In order to align the different events in time, a peak-finding algorithm (using a kernel density estimation algorithm) is applied and the hits are translated in time such that the peak occurs at t = 0. The time-of-flight subtracted hits are then filled into the corresponding α or β histogram with a bin width of 2 ns and a time range of -50 ns to 950 ns relative to the peak. After all events are added, the histograms are normalized and used as the reference shapes for the Gatti filter. The binned reference shapes are shown in Figure 4.17 along with the corresponding weighting function $w[t]$.

For the reference shapes used in the *MOE97-Echidna12* code, the expected means and variances are

$$\overline{G_\alpha} = 0.0291457 \qquad\qquad \overline{G_\beta} = -0.0291457 \qquad (4.23)$$

$$var(G_\alpha) = \frac{3.574 \times 10^{-2}}{N} \qquad\qquad var(G_\beta) = \frac{2.085 \times 10^{-2}}{N} \qquad (4.24)$$
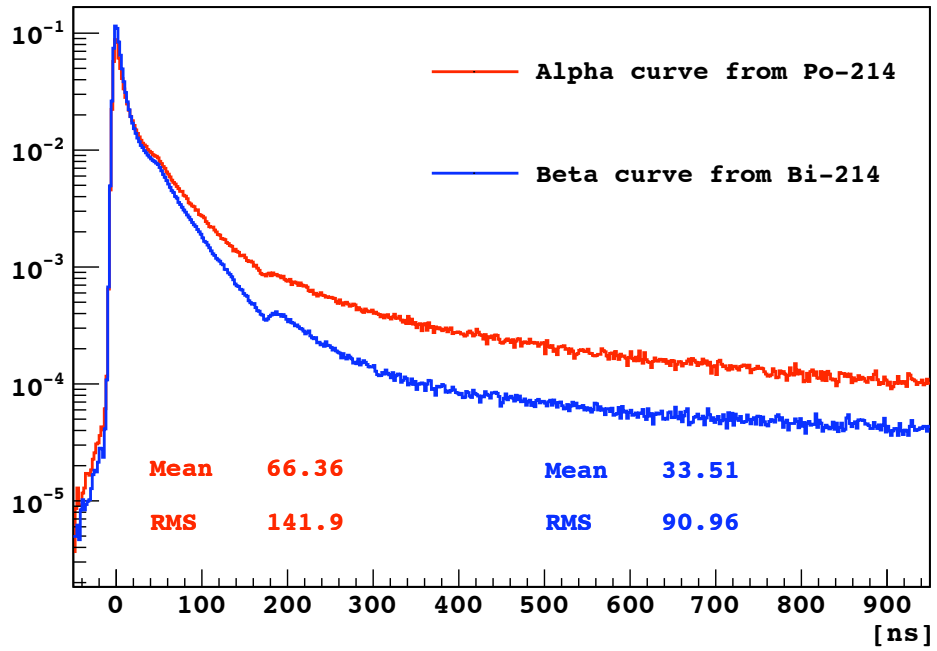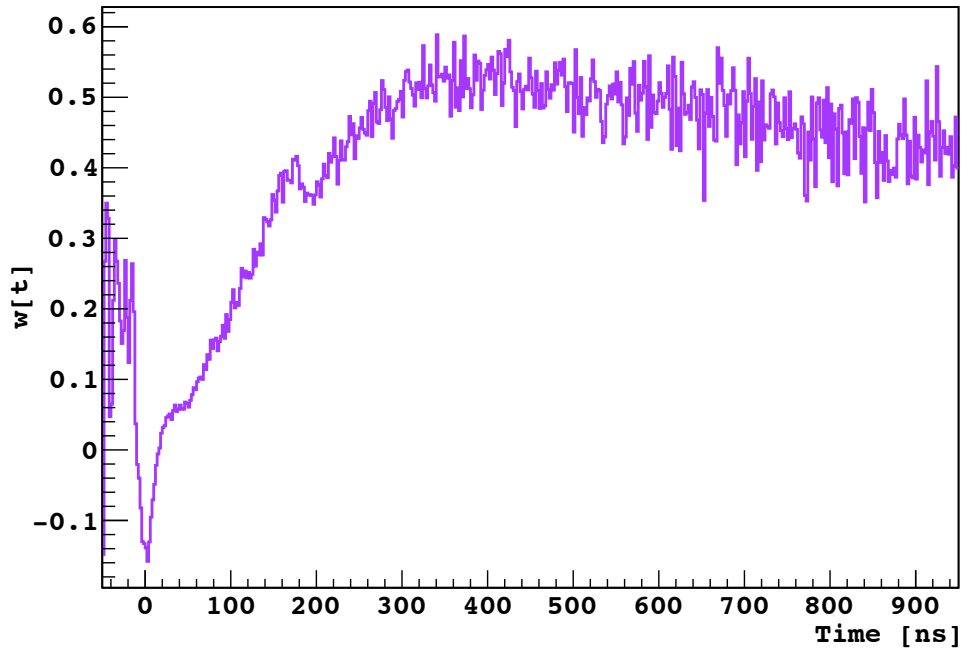
Figure 4.17: Top: Reference α and β emission time profiles used for the Gatti parameter calculation. The time profiles are obtained from the ^{214}Bi-^{214}Po $\beta-\alpha$ coincidences occurring throughout the regular data taking period. The cusp at around 50 ns is due to reflections off the SSS, while the kink at 180 ns is due to retriggering of channels following the enforced channel dead time. Bottom: Gatti parameter weighting $w[t]$ obtained from these reference time profiles

Using these values, we can calculate the figure of merit as

$$D = 0.245\sqrt{N} \qquad (4.25)$$

Under the ^{210}Po peak ($N \sim 210$), where discrimination is most important, the figure of merit $D \sim 3.55$. An example of the separation that can be achieved is illustrated in Figure 4.18 which shows the Gatti parameter distribution for ^{214}Bi-Po coincidences. We note that there are selection cuts excluding events with Gatti values beyond -0.02 and 0.02 for αs and βs respectively.

Gatti Parameter for ^{214}Bi-^{214}Po Coincidences
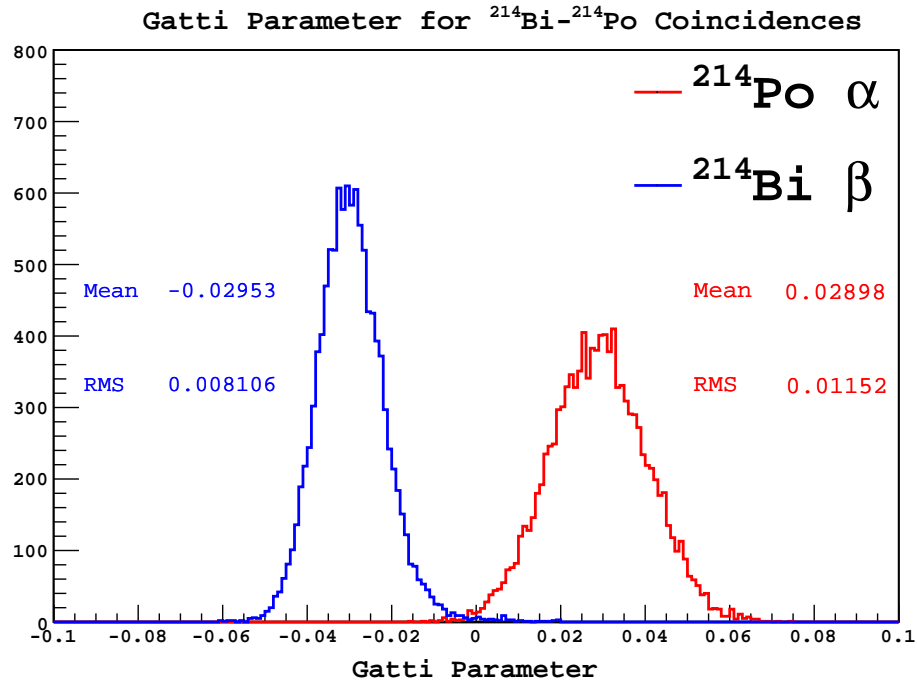
Figure 4.18: Gatti parameter distribution for α and β events tagged by the ^{214}Bi-Po coincidence. There are selection cuts excluding events with Gatti values beyond -0.02 and 0.02 for αs and βs respectively

4.5.2.2   Non-ideal behaviour

Reference Shape   The ^{214}Bi decay that is used to produce the β reference shape is not a pure β decay but rather a combination of a β decay and various γ emissions.

Since γ particles do not deposit all their energy at a single location, their emission time profile is different from single β decays (it is the superposition of several electron recoils occurring at different positions and times). Thus the reference shape currently being used does not accurately represent the emission time probability distribution of the electron recoil (or β decay) events we are trying to identify.

Energy Dependence The ^{214}Bi decay that is used to produce the β reference shape, is unfortunately peaked at a much higher energy (~ 1000 pe) than the region where the statistical subtraction is most needed - under the ^{210}Po peak (~ 200 pe). Since the Borexino electronics hardware only records the hit time of the first photoelectron on each channel and not each individual hit, the time profiles of high energy events can be significantly different from those at lower energies. Thus the reference shape used may not reflect the true probability distribution of β events under the ^{210}Po peak and the Gatti parameter distributions could have an extra energy dependence.

Position Dependence The above mentioned problem of the electronics also introduces a position dependence in the time-of-flight subtracted time profiles, since events closer to the Stainless Steel Sphere are more likely to have multiple hits on a single channel. Thus, identical events at different positions are likely to have different time profiles.

Another issue affecting the Gatti parameter implementation is the time-of-flight subtraction itself. It is known that there is a significant amount of scattering within the scintillator and buffer, however the time-of-flight subtraction only accounts for the straight line distance from the reconstructed position to the PMT. Since the probability to scatter depends on the path length, the Gatti parameter can differ for the same class of events at different positions.

Peak Determination   In order to make the reference shapes, and also to calculate the Gatti parameter for individual events, it is necessary to align them by some fixed reference point. Since the peak of the time profile has the largest statistics (by definition) and is therefore less subject to fluctuations, all events are aligned by setting the peak of the emission times as $t = 0$. The peak of the discrete hit times is found by creating a continuous function using a kernel density estimation[3] with a Gaussian kernel whose bandwidth is determined by minimizing the risk function for the ^{214}Bi emission time profile obtained from sources. The estimation of the peak strongly depends on the number of the hits and therefore the energy of the event. Fluctuations in the calculated peak location due to the low statistics (as in the ^{14}C region of the spectrum) can lead to a large spread in the Gatti parameter beyond the theoretical values calculated in Eq. 4.20.

The impact of the above-mentioned issues on the ability to separate α and β decays has been carefully studied and is further discussed (in relation to the ^{7}Be analysis) in Section 6.4.

4.5.2.3   Future Improvements

Several improvements have been made to the implementation of the Gatti parameter in the latest versions (cycle-98) of the *Mach4* and MOE code. Additional cuts to remove muons and electronics noise have been implemented in the selection of the ^{214}Bi-Po coincidences used for the reference shapes. The effect of the cuts has been to reduce the fraction of hits in the pre-pulse region (-50 to -20 ns) of the reference shapes to the level of 10^{-7} (compare to Figure 4.17). In order to deal with the non-ideal behavior of the Gatti parameter we have also created β reference shapes using only

---

[3]Each discrete hit is replaced with a continuous probability density function, referred to as a kernel, centered on the hit. The bandwidth is a free parameter of the kernel that determines the amount of smoothing. For a Gaussian kernel, the bandwidth is the standard deviation.

the low energy (< 700 p.e.) ^{214}Bi decays. While this reduces the statistics available for the reference shape, it has the advantage that these decays are almost purely β-like (decays with additional γs have higher energy) and are closer in energy to the region where $\alpha - \beta$ discrimination is most critical. Unfortunately these improvements were not well enough tested at the time to be used for the ^{7}Be analysis.

4.6 Muon Track Reconstruction

Accurate reconstruction of the track produced by through-going muons is extremely useful for the tagging of ^{11}C decays. While the neutron expelled from the ^{12}C nucleus can travel up to a few meters before thermalizing and being captured, the heavier ^{11}C atom remains close to the production site along the track. Previous experiments [70] suggest that the mean distance between the ^{11}C decay and the corresponding muon track is approximately 13 cm. Hence vetoing a cylindrical region around the muon track can allow one to remove a large fraction of ^{11}C decays without vetoing the entire detector.

4.6.1 Reconstruction Algorithm

The *Mach4* muon track reconstruction program is based on a likelihood method for detecting the earliest light. The reconstruction uses the fact that scintillation light produced inside the detector travels much slower than the muon. The group velocity of light in the scintillator used in Borexino has been measured to be $n_{scint} \sim 1.7$ at 425 nm. However, the average energy of muons at the Gran Sasso laboratory is around 270 GeV [76] implying that the through-going muons are traveling at very nearly the speed of light. This difference in speed means that for any of the photomultiplier detectors, there is a unique emission point along the muon track such that the light emitted from that point reaches the detector before any other light.
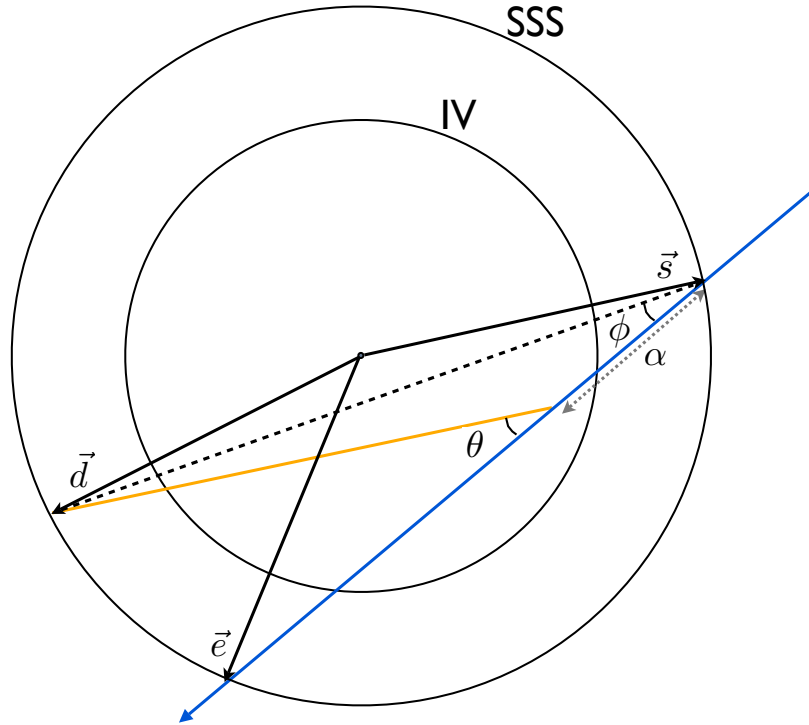
Figure 4.19: Schematic drawing of a muon track (blue line) passing through the detector with start and ending points at **s** and **e** respectively. A photomultiplier tube at **d** receives it first light from photons emitted a distance α along the track. The calculation of the distance α is discussed in the text.

Referring to Figure 4.19, consider a track with starting point vector **s**, ending point vector **e** and entrance time t_0 where the starting and ending points are defined as the intersection of the muon track with the Stainless Steel Sphere. Let **v** be the track vector, defined as $\mathbf{v} = \mathbf{e} - \mathbf{s}$. For a PMT at position **d**, light emitted at distance α along the track, arrives at time:

$$t = t_0 + \frac{\alpha}{c} + \frac{n_{scint}}{c}|\mathbf{d} - (\mathbf{s} + \alpha\hat{\mathbf{v}})| \tag{4.26}$$

To find the distance α that corresponds to the emission point of the earliest light to arrive at **d** we set $\frac{dt}{d\alpha} = 0$ to obtain:

$$\alpha_{min} = \max\left(l\cos\phi - \frac{l\sin\phi}{\sqrt{n_{scint}^2 - 1}}, 0\right) \tag{4.27}$$

137

where $\mathbf{l} = \mathbf{d} - \mathbf{s}$ and ϕ is as defined in Figure 4.19. Note that when $\alpha < 0$ this implies that the emission point lies outside the SSS, before the starting point. Since the SSS is light tight, the earliest emission point must be at the entrance ($\mathbf{s}$) and so we set $\alpha = 0$. More interestingly, and in hindsight obviously, one can calculate that the angle, θ, between the muon track and the line connecting the point of earliest emission to the photomultiplier tube (see Figure 4.19) to be:

$$\theta_{min} = \cos^{-1}(1/n_{scint}) = \theta_c \qquad (4.28)$$

which is just the angle of the Cherenkov cone. Thus the first photons detected in any direction, propagated outwards from the track at an angle θ_c. This fact is used as a first estimate of the track orientation - as outlined in the next section.

Plugging in α_{min} into Equation 4.26, we get the expected time to arrival of the first light at detector $\mathbf{d}$:

$$t_{exp} = t_0 + \frac{\alpha_{min}}{c} + \frac{n_{scint}^2 l \sin \phi}{c \sqrt{n_{scint}^2 - 1}} \qquad (4.29)$$

Using the log-likelihood method, for any arbitrary track $\mathbf{v}$ we calculate:

$$-\log(L) = \sum_{i=1}^{N} (t_{exp} - t_i)^2 \qquad (4.30)$$

where the sum is carried out over all hit channels with charge over 4 photoelectrons (to eliminate stray hits), and t_i is the time of the first hit on the ith channel. The form of the above log-likelihood function assumes that the true times of the hits will be normally distributed about the expected hit time and that width of the gaussian (the time resolution) is the same for all phototubes. The negative log-likelihood is calculated for various values of $\mathbf{s}, \mathbf{e}$ and t_0 and the track that minimizes the above sum is deemed the true muon track. If the minimization program, in our case MINUIT,

is unable to converge to a minimum, the track is not considered to be valid.

4.6.2   Parameterization and Initial Guess Values

The log-likelihood process requires that the minimization program move through the free parameters of the track in order to find a minimum. In our case we have chosen to parametrize the track by 5 independent parameters: the time of entry of the muon into the Stainless Steel Sphere, and two parameters each for the entrance and exit points describing the location of the intersection of the track with the SSS. In order to facilitate the exploration of the parameter space, we represented the surface of the sphere (r $\sim$ 6.85 m) using a stereographic projection. The stereographic projection was chosen so that the minimization program could move continuously over the surface of the sphere. The only discontinuity occurs at the point of projection. Since a large majority of the muons passing through the Borexino detector are downward-going muons, for the entrance of the track the point of projection was chosen to be the south pole while for the end of the track the projection point was shifted to the north pole.

Even with this transformation of coordinates, it was found that the convergence of the minimization program strongly depended on the starting values of the parameters used as an initial guess. To estimate the track orientation and position prior to fitting, all detected hits are first ordered in time. The guess for the starting point of the track (**s**) was simply picked to be the barycenter of the first ten detected hits that have a charge greater than 30% of the largest hit in the event. This is because, for most muons, the first hits are caused by scintillation light emitted (isotropically) in the buffer region at the entry point of the muon track. The guess for the ending point of the track is a little harder to estimate. In Figure 4.20 we show a schematic of the muon at four different positions as it passes through the detector. At each position the cone of light representing the scintillation wavefront, marked in yellow, is shown,

139

with the apex at the current position of the muon. One can see that the last detector to be hit ($\mathbf{d}_{last}$), sees first light when this cone becomes tangent to the SSS. Since the cone of propagation is tangent to the sphere at $\mathbf{d}_{last}$, the emission point of the light must also lie along the radial direction $\hat{\mathbf{d}}_{last}$. After some geometrical calculations one finds that the point of emission is:

$$\mathbf{p} = -\beta \mathbf{d}_{last} \tag{4.31}$$

$$\text{where } \beta = \cos\phi - \frac{\sin\phi}{\sqrt{n^2 - 1}} \tag{4.32}$$
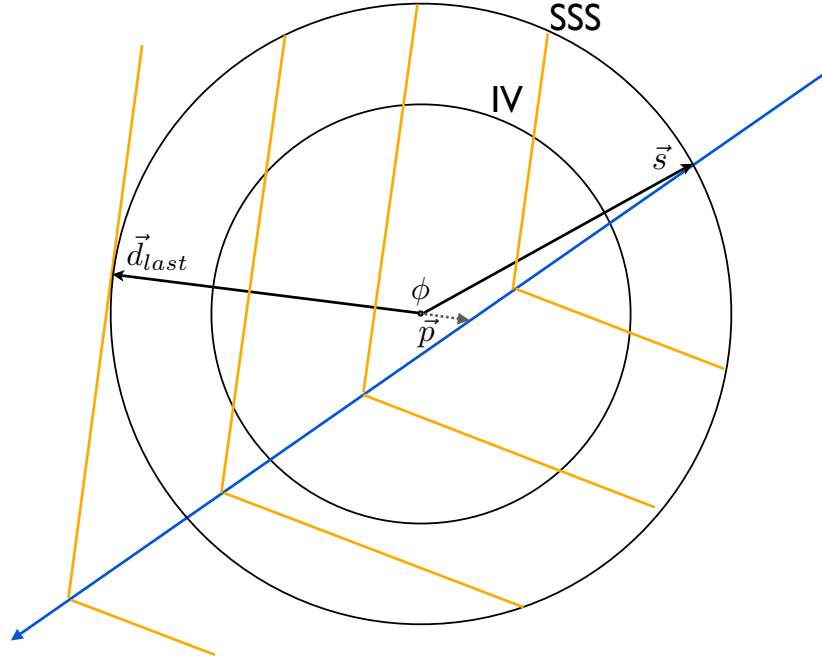
Figure 4.20: Schematic drawing of the propagation of the wavefront (yellow lines representing a cone with opening angle $\frac{\pi}{2} - \theta_c$) as the muon (blue line) passes through the detector. Details given in text.

Thus the initial guess value is calculated using (but not directly equal to) the last hits seen in the detector. As with the start point, $\mathbf{d}_{last}$ is estimated by taking the barycenter of the last ten hits with at least 30% of the charge of the largest hit.

4.6.3 Performance

An example of the reconstructed muon track is shown in Figure 4.21. The correlation between the reconstructed muon track and the positions of the following neutron captures and ^{11}C decays indicate that the reconstruction algorithm works well. The muon tracking has been found to be fairly reliable and is being used in the pep neutrino analysis currently being performed by the collaboration. A detailed analysis of the performance of the muon tracking algorithm can be found in [72] and will not be reproduced here. In addition to the tests performed in [72], a new external compact muon tracker [90] has been recently installed on the external surface of the Stainless Steel Sphere. The tracker consists of 192 drift tubes, arranged in four identical modules. The modules are stacked on top of each other with alternate modules rotated by 90 degrees, which allows for 3D reconstruction of the muon tracks. The external muon tracker is triggered independently from Borexino using a coincidence signal from plastic scintillators on the top and bottom of the tracker. At this time no comparison has yet been made between the *Mach4* muon track reconstruction and the external tracker, though we hope to conduct such tests in the near future.
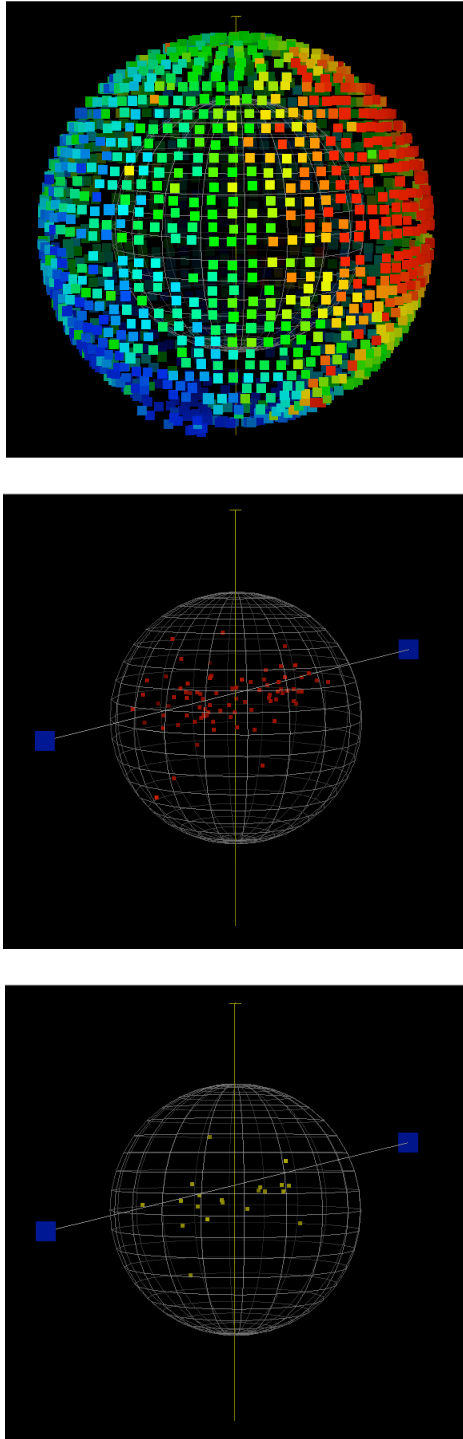
Figure 4.21: Top: *Mach4* event display depicting a muon event. Each colored square represents an inner detector PMT on the SSS with the color indicating the time of the hit (red for earlier hits, blue for later hits). Middle: Reconstructed muon track (white line with blue endpoints) passing through the inner vessel (gridded sphere). Red dots indicate position of neutron captures in the 2 ms following the muon. Bottom: Yellow dots indicate events in the ^{11}C energy region occurring within 2 hours of the muon.

4.7   Noise Reduction

4.7.1   Rack Noise
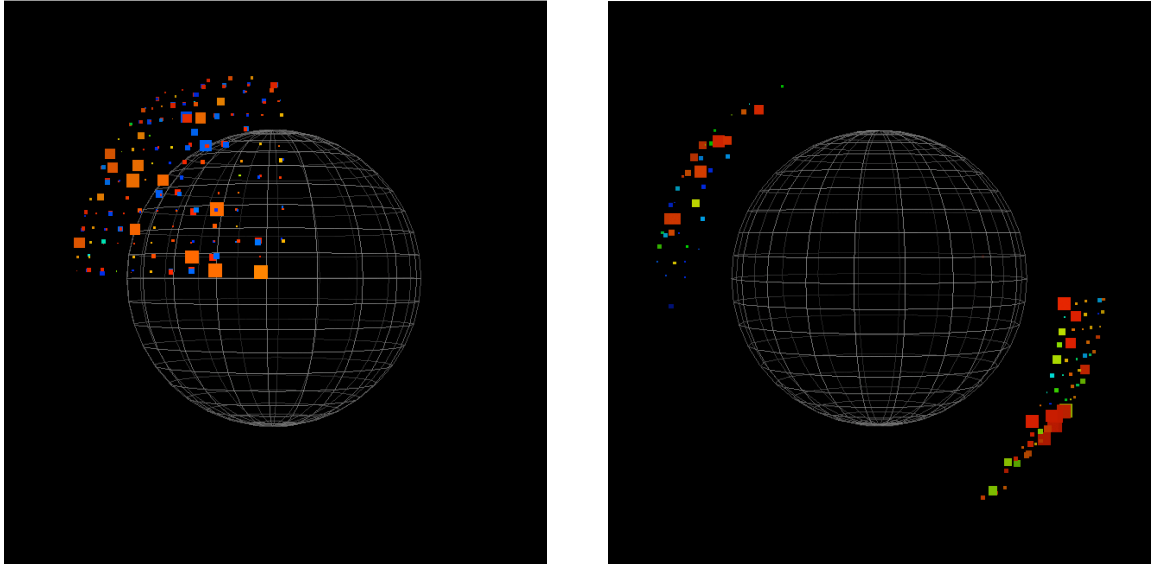
Figure 4.22: *Mach4* event display depicting rack noise events. Each colored square represents an inner detector PMT on the SSS with the color indicating the time of the hit (red for earlier hits, blue for later hits). The inner vessel is shown as a gridded sphere. In both of the above events, the hits are confined to a single rack whose corresponding PMT's are arranged in spherical lunes on the SSS.

Soon after the commencement of data-taking, it was noticed that there was a small population of events for which only PMT's cabled on a single electronics rack (160 channels) had triggered. These events can be easily visually identified using the *Mach4* event display since PMT's on a given rack are arranged in separated spherical lunes. Examples of such events are shown in Figure 4.22. Given the observed hit pattern with few, if any, hits detected outside a single rack, these events are evidently electronics noise. In order to identify and remove such events we have developed a specific set of software variables. For each event we calculate the fraction of hits recorded in each rack and record the fraction in the most active rack $f_{rack}(1)$. The distribution of $f_{rack}(1)$ is shown in Figure 4.23 for events from the source calibration campaigns. We have used data from all source types and locations (including those

lying outside the fiducial volume) though we require that the event reconstruct within 50 cm of the position given by the CCD cameras, in order to obtain a clean sample of source events. Evaluating the sacrifice of the rack noise cut, we find that the fraction of scintillation source events with $f_{rack}(1) > 0.75$ is less than 5×10^{-7}. Scintillation events are more likely to have all their hits concentrated within a narrow segment of the detector if they are near the edge of the fiducial volume. To study this effect we have also looked at the dependence of $f_{rack}(1)$ on the location of the source. Even at a radius of 4 m, the average value of f_{rack} for source events is < 0.2.

To illustrate the efficiency of this cut at separating rack noise from true scintillation
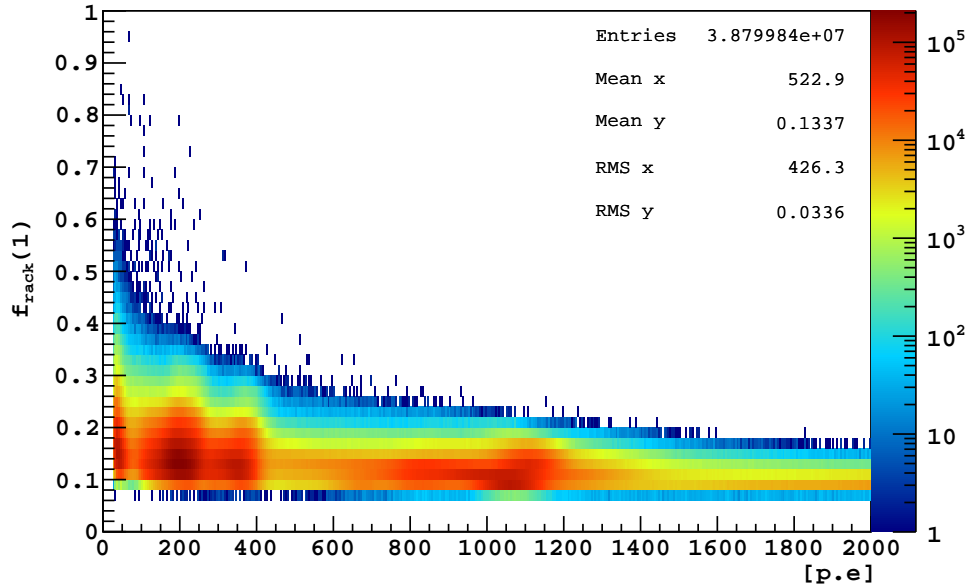
Figure 4.23: Distribution of $f_{rack}(1)$ versus energy for all source calibration data. Events are required to have reconstructed within 50 cm of their nominal position. For the ^{7}Be analysis, a cut is placed at $f_{rack}(1) > 0.75$, which corresponds to a sacrifice of $< 5 \times 10^{-7}$.

events, we have plotted (Figure 4.24) $f_{rack}(1)$ versus the recorded number of photoelectrons for events in the ^{7}Be analysis period. Only events that passed all other ^{7}Be analysis selection cuts (except the rack noise and geometrical uniformity cuts, see Section 6.2.2) are included. The examples shown in Figure 4.22 were taken from the selection of ~ 300 events with $f_{rack}(1) \sim 1$. The large separation between these

events and the rest gives us confidence that the fraction of rack noise events passing the $f_{rack} > 0.75$ cut is negligible.
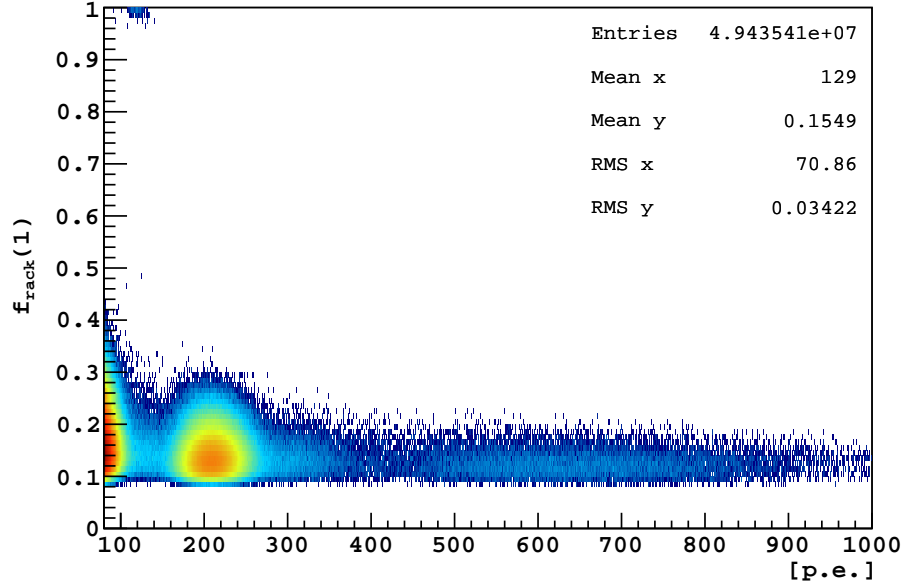
Figure 4.24: Distribution of $f_{rack}(1)$ versus energy for regular data. Only events that passed all other ⁷Be analysis selection cuts (except the rack noise and geometrical uniformity cuts) are shown. A cut is usually placed at $f_{rack}(1) > 0.75$. Examples of events with $f_{rack}(1) \sim 1$ are shown in Figure 4.22.

4.7.2 Isotropy

Most of the event reconstruction tools discussed above deal with the timing or charge information of the hits. Even the position reconstruction only uses the location of the hit PMTs to calculate the time of flight, no information about the spatial distribution of the hits (and their relation to one another) is used to determine the position. This can sometimes lead to events, as is shown in Figures 4.22 and 4.25, to have a perfectly valid position reconstruction even though the spatial distribution of hits around that position is non-physical. While it is easy to pick out these events visually, an algorithm was needed to accurately identify this type of event. What distinguishes these events from regular scintillation events is the non-uniform distribution of hits around the
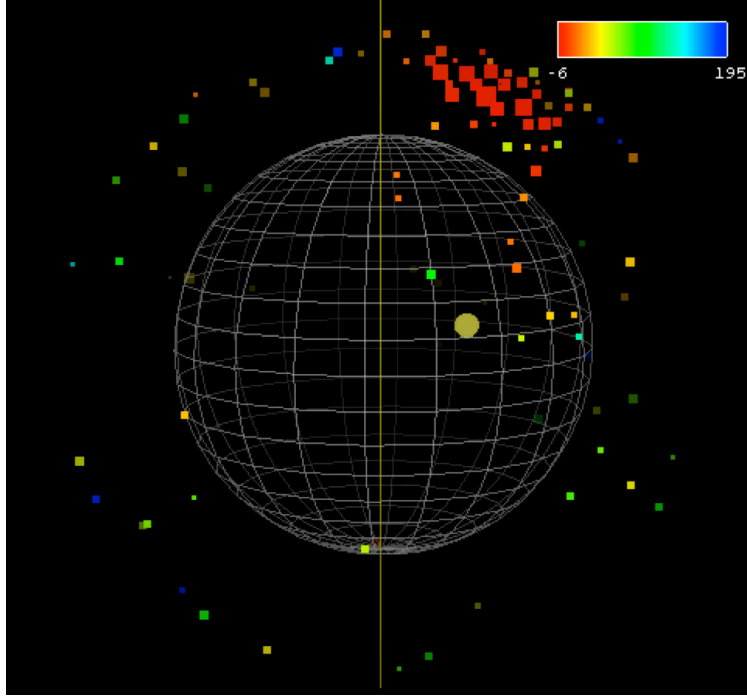
Figure 4.25: *Mach4* event display for an event whose hit distribution is anisotropic with respect to the reconstructed position. The position reconstruction algorithm converged so close to the center of the detector due to a single hit on a miscabled channel. For comparison to the source data in Figure 4.26, the charge of this event is $\mathtt{npe}_{avg} \sim 150$ p.e. and it has a β_1 value of ~ 0.3.

reconstructed position. Scintillation light is emitted isotropically from the point of excitation, and due to the spherical symmetry of the Borexino detector we expect the hit pattern to be similarly isotropic.

In order to quantify the isotropy, we have developed a parameter (inspired by a similar variable used by the SNO collaboration) that looks at the pattern of hits, from the perspective of the reconstructed position. For every pair of detected photoelectrons we calculate the angle subtended between their respective PMT's, with the reconstructed position at the origin. We then sum up the Legendre polynomials of these angles and normalize by the total number of photoelectron pairs:

$$\beta_l = \frac{1}{N(N+1)} \sum_{i=0}^{N} \sum_{j=i}^{N} P_l(\cos \theta_{ij}) \tag{4.33}$$

146

where θ_{ij} is the angle between the ith and j^{th} hit with respect to the reconstructed position of the event, P_l are the standard Legendre polynomials and the i and j indices run over the number of photoelectrons, N. Multiple photoelectrons on a single PMT are accounted for separately, such that a PMT with many more hits than its neighbors increases the anisotropy. We do not however include retriggered channels to avoid biases due to electronics noise. While we calculate the above isotropy variable for $l = 1, 2, 3$ and 4 we currently only use the $l = 1$ variable, β_1. For a perfectly isotropic emission in which the photoelectron positions are not quantized on individual PMT's, we would expect $\beta_1 \sim 0$. In order to determine the value at which to cut events, we have studied the distribution of β_1 for source calibration events. Since the nominal position of the source is known, we can select a very clean sample of events whose position reconstruction is known to be accurate. Figure 4.26 shows the distribution of the β_1 parameter versus the number of detected photoelectrons, for all source calibration events in which the reconstructed position was within 50 cm of the nominal position. As can be seen, there is a strong energy dependence, with low energy events having a much larger spread, as may be expected due to fewer statistics. By comparing the distribution for sources with a radius between 0 m and 1 m (top plot, Figure 4.26) with the corresponding distribution for sources between 3 m and 4 m (bottom plot), it can be seen that events at a larger radii have a greater mean value than those near the center. In order to have a cut with a uniform acceptance over the entire energy range, we calculated the 99.9% upper bound for every 10 photoelectron bin and fit the resulting data to the sum of two exponentials (shown as black lines in Figure 4.26). To be conservative we used the exponential parameterization of the 99.9% limit from the data between 3 and 4m for the ^{7}Be analysis:

$$\beta_1 > 0.02657 + e^{-1.306 - 0.01728q} + e^{-3.199 - 0.001738q} \tag{4.34}$$

where q is the *Mach4* charge variable $\mathtt{npe}_{avg}$. We note that while the above cut is designed to have a sacrifice probability of less than 0.1%, events such as those shown in Figures 4.22 and 4.25 have typical charge values of 100 p.e. $< \mathtt{npe}_{avg} < 200$ p.e. and β_1 values of ~ 0.3 (compare to data in Figure 4.26). The cut therefore serves as a good method to remove electronics noise and other mis-reconstructed events.
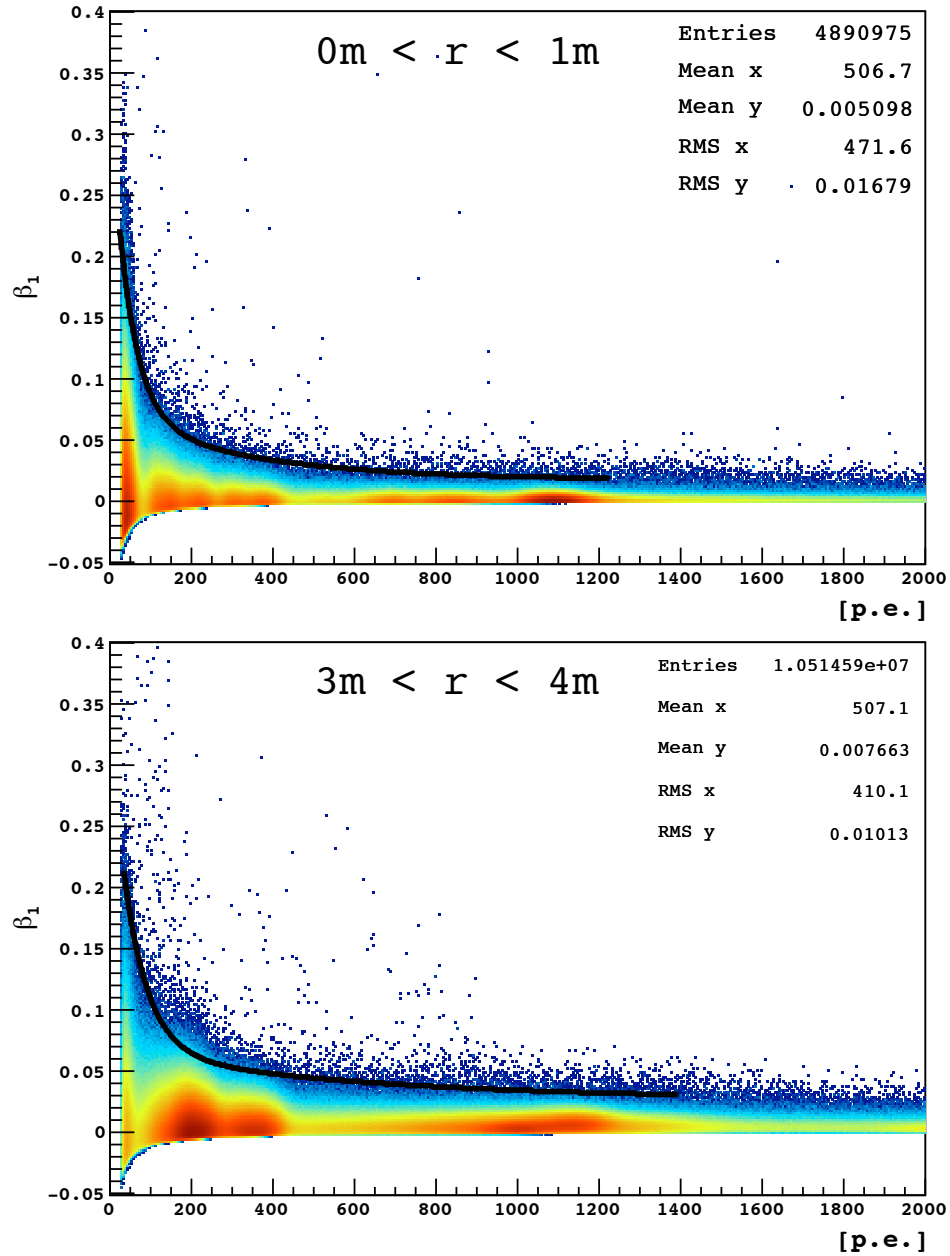
Figure 4.26: Distribution of β_1 (isotropy) parameter versus the number of detected photoelectrons for source calibration events with 0 m $< r <$ 1 m (top) and 3 m $< r <$ 4 m (bottom). The number of events are shown on a colored logarithmic scale, while the black line shows a double exponential fit to the 99.9% upper bound in each 10 p.e. bin.

Chapter 5

Energy Response

The determination of the rate of ^{7}Be neutrino interactions in Borexino is based on fitting the observed energy spectrum. In order to obtain a precise measurement of the neutrino rate, we need to have a very accurate understanding of the energy response of the detector. In this chapter we will discuss the analytical modeling of the energy scale as well as the response function, both of which play a critical role in the spectral fit.

The energy response of the detector can be defined as the response of the detector, in the observed energy estimator variables `nhits` and `npe`, to events with a given energy spectrum, spatial distribution and particle type. The transformation of the initial energy deposits into the final analysis variables `nhits` and `npe` can be broken down into several steps. First the deposited energy is converted into photons through the scintillation mechanism briefly described in Section 2.1.2.2. These photons then propagate outwards where some of them are converted into photoelectrons at a PMT photocathode. The initial photoelectron is then multiplied through the dynode chain and finally, the total output charge is integrated and rescaled into units of photoelectrons. The details of these transformations are discussed below:

5.1 Monoenergetic Localized Response Function

In this section we will develop an analytical model for the response of the detector to a monoenergetic electron with energy E located at position $\mathbf{r}$. The result can then be easily adapted to the case of a spectrum of events distributed throughout the detector, as is required for the spectral fit.

The need for a precise modeling of the energy response function is evident from the energy spectrum of the signals and backgrounds in Figure 3.1. The ^{210}Po background, sitting right above the ^{7}Be spectrum, and more than two orders of magnitude higher in rate, necessitates a detailed modeling of the tails of the distribution in order to fit the ^{7}Be spectrum. As an illustration of this, in Figure 5.1 we show a *g4bx* simulated spectrum of 1 million ^{210}Po α events (roughly the same number as in our data set) and a fit to the spectrum with a Gaussian. It can be seen that the Gaussian, the standard response function used in scintillation detectors, is a poor fit in the tail regions. We will therefore develop a different analytical model for the response function, going through the entire energy reconstruction process, step by step. We note that while the *g4bx* simulation includes all the known physics and electronics effects, the detector parameters such as attenuation lengths, reflectivity's, detection efficiencies, etc. have all been hard-coded into the simulation. If these parameters are not quite accurate, it can lead to difficulties in obtaining a good fit, as has been the case when attempting to fit the entire ^{210}Po peak with a *g4bx* simulated spectrum. The goal of the analytical approach is therefore to obtain a model of the shape and energy dependence of the response function (through it's central moments), while leaving the values of the parameters free in the final spectral fit.

Gaussian fit to MC simulation of ^{210}Po events at the center

Entries	999998
Mean	209.7
RMS	16.27
χ^2 / ndf	1350 / 147
Prob	0
Constant	2.459e+04 ± 3.000e+01
Mean	209.7 ± 0.0
Sigma	16.2 ± 0.0
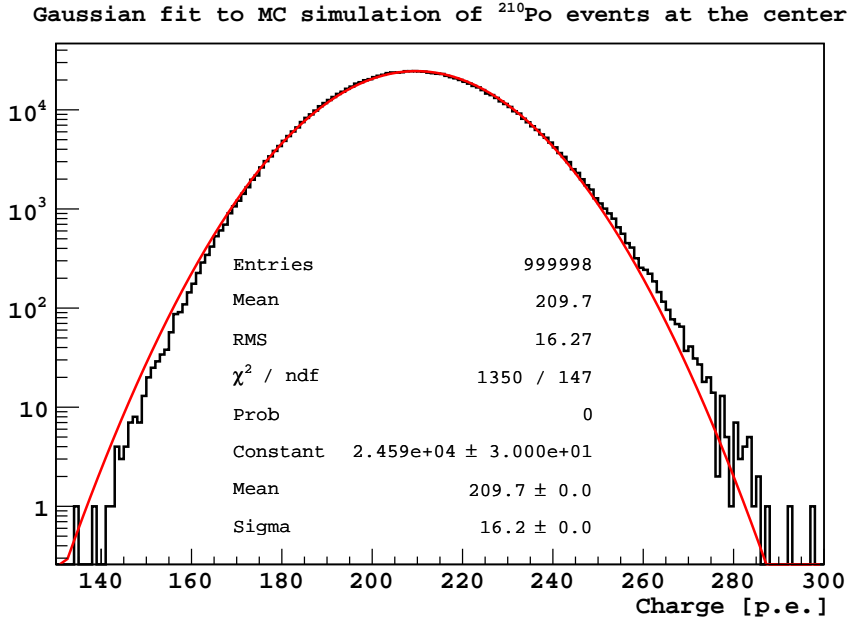
Figure 5.1: Fit of 1 million Monte Carlo generated ^{210}Po events with a Gaussian function. The poor quality of the fit is evidenced by the mismatch in the tails.

5.1.1 Photon Response Function

First, we consider the response of the detector in terms of the number of photons, f, produced. It is a common assumption [91], that the number of scintillation photons emitted by a monoenergetic source follows a Poisson distribution. This assumes a Fano factor of 1, which is considered to be accurate for most scintillators. We will denote the Poisson probability of producing f photons given a monoenergetic source as $\mathcal{P}(f|\mu'(E))$ where $\mu'(E)$ is the mean number of photons emitted:

$$P(f|E) = \mathcal{P}(f|\mu'(E)) \tag{5.1}$$

$$\equiv \frac{(\mu'(E))^f e^{-\mu'(E)}}{f!} \tag{5.2}$$

$$\mu'(E) = LY_{scint} \cdot Q(E) \cdot E \tag{5.3}$$

where $LY_{scint} \sim 10,000$ photons/MeV [45] is the scintillator lightyield and $Q(E)$ is the quenching factor. We defer the discussion regarding the energy response of the

152

scintillator to Section 5.2 on the energy scale. The mean number of photons emitted is assumed to be only a function of the energy of the electron and the scintillator used, neglecting any spatial effects (the density of the scintillator varies by less than 0.5% within the fiducial volume).

5.1.2 Photoelectron Response Function

Next, we consider the response of the detector in terms of photoelectrons, p. Let $c(\mathbf{r})$ denote the conversion probability, $i.e.$ the probability for a photon emitted at position $\mathbf{r}$ to be converted to a photoelectron. The conversion probability is determined by such things as the photon absorption length, the solid angle subtended by the working PMTs at position $\mathbf{r}$, PMT quantum and conversion efficiency, channel thresholds etc. We will assume that the conversion probability is independent of the energy of the event, (which is not strictly true at high energies due to the single channel dead time - see Section 5.1.5.5). Since each photon is emitted independently, the probability of obtaining p photoelectrons is given by the Binomial distribution, with the number of trials equal to the number of photons f, and the probability of a success given by $c(\mathbf{r})$. Combining this with the Poisson distribution of the number of photons, we get:

$$
\begin{aligned}
P(p|E,\mathbf{r}) &= \sum_{f=0}^{f=\infty} \mathcal{B}(p|f,c(\mathbf{r}))\mathcal{P}(f|\mu'(E)) \\
&= \sum_{f=0}^{f=\infty} \binom{f}{p} c(\mathbf{r})^p (1-c(\mathbf{r}))^{f-p} \cdot \frac{\mu'(E)^f e^{-\mu'(E)}}{f!} \\
&= \frac{\mu'(E)^p c(\mathbf{r})^p e^{-\mu'(E)}}{p!} \sum_{f=0}^{f=\infty} (1-c(\mathbf{r}))^{f-p} \cdot \frac{\mu'(E)^{f-p}}{(f-p)!}
\end{aligned}
$$

(5.4)

Rewriting the sum as an exponential (keeping in mind that the binomial distribution is 0 for $p > f$), we get :

$$P(p|E, \mathbf{r}) = \frac{[c(\mathbf{r})\mu'(E)]^p e^{-c(\mathbf{r})\mu'(E)}}{p!}$$

$$P(p|E, \mathbf{r}) = \mathcal{P}(p|\mu(E, \mathbf{r})) \tag{5.5}$$

Therefore the number of photoelectrons also follows a Poisson distribution with a modified mean:

$$\mu(E, \mathbf{r}) \equiv c(\mathbf{r})\mu'(E) \tag{5.6}$$

$$= c(\mathbf{r}) \cdot LY_{scint} \cdot Q(E) \cdot E \tag{5.7}$$

$$\equiv LY_{det}(\mathbf{r}) \cdot Q(E) \cdot E \tag{5.8}$$

where we have defined the position-dependent lightyield of the detector as $LY_{det}(\mathbf{r}) \equiv c(\mathbf{r}) \cdot LY_{scint}$

5.1.3   Individual PMT Photoelectron Response Function

If we label each of the photomultiplier tubes from 1 to N, then we can denote $c_i(\mathbf{r})$ as the probability that a photon will convert into a photoelectron on the ith PMT. For consistency we will also denote the probability of a photon not being converted on any PMT as $c_0(\mathbf{r})$. So we have:

$$c(\mathbf{r}) = \sum_{i=1}^{N} c_i(\mathbf{r}) = 1 - c_0(\mathbf{r}) \tag{5.9}$$

If we consider each phototube individually, we can use the same argument as in the previous subsection to conclude that the number of photoelectrons on each phototube

also follows a Poisson distribution with a modified mean:

$$\mu_i(E, \mathbf{r}) \equiv c_i(\mathbf{r})\mu'(E) \tag{5.10}$$

$$= c_i(\mathbf{r}) \cdot LY_{scint} \cdot Q(E) \cdot E \tag{5.11}$$

We will later need to sum the means and variances of the response function for each tube and so it is important to calculate the correlation between the different phototubes. If we let p_i be the number of photoelectrons on each tube (again with p_0 denoting the number of unconverted photons), then for a fixed number f of photons, the vector of created photoelectrons $\mathbf{p} = (p_0, ..., p_N)$ follows a multinomial distribution:

$$P(p_0, ..., p_N | f) = \frac{f!}{p_0! .... p_N!} c_0^{p_0} ... c_N^{p_N} \tag{5.12}$$

$$\text{where } f = \sum_{i=0}^{N} p_i \tag{5.13}$$

and the correlation between the number of photoelectrons observed on the ith and j^{th} PMT's is given by:

$$\rho(p_i, p_j) = -\sqrt{\frac{p_i p_j}{(1 - p_i)(1 - p_j)}} \tag{5.14}$$

In this case, for a fixed number of photons, the number of photoelectrons on a specific phototube is given by a binomial distribution and, as shown above, is negatively correlated with the number of photoelectrons on other tubes. However, we have assumed that the number of photons produced by a monoenergetic electron is not fixed, but rather follows a Poisson distribution. Therefore the probability of obtaining

a vector of created photoelectrons is given by:

$$P(p_0, ..., p_N | E, \mathbf{r}) = \frac{f!}{p_0! .... p_N!} c_0^{p_0} ... c_N^{p_N} \times \frac{\mu'^f e^{-\mu'}}{f!}$$

$$= \left(\frac{c_0^{p_0} \mu'^{p_0} e^{-c_0 \mu'}}{p_0!} \right) ... \left(\frac{c_N^{p_N} \mu'^{p_N} e^{-c_N \mu'}}{p_N!} \right)$$

$$= \mathcal{P}(p_0 | c_0 \mu') \cdot ... \cdot \mathcal{P}(p_N | c_N \mu') \tag{5.15}$$

$$\rho(p_i, p_j) = 0 \tag{5.16}$$

Since the probability can be written as simply the product of individual Poissonian terms we can consider the photoelectron distribution on each PMT to be **independent** Poisson distributions with appropriately scaled means. It should be stressed that other distributions for the total number of photoelectrons (say binomial) would not lead to independence among the PMT distributions.

To summarize, the assumption of a Poisson distributed number of photons implies not only that the total number of detected photoelectrons will also be Poisson distributed, but also that each PMT can be considered as an independent detector with a Poisson distribution of observed photoelectrons.

5.1.4 npmts Response Function

Since each PMT is independent of the others and the observed number of photoelectrons follows a Poisson distribution, the probability for the ith PMT to be hit (detect one or more photoelectrons) is given by:

$$h_i(E, \mathbf{r}) \equiv 1 - e^{-c_i(\mathbf{r})\mu'(E)} \tag{5.17}$$

$$= 1 - e^{-\mu_i(E, \mathbf{r})} \tag{5.18}$$

where, as before, $c_i(\mathbf{r})$ is the probability for a photon originating at $\mathbf{r}$ to be converted into a photoelectron on the ith PMT and $\mu'(E)$ is the mean number of photons

produced by an electron with energy E. We can study the hit probability $h_i(E, \mathbf{r})$ using the source calibration data. By summing all the hits on a given PMT, for a specific source, and dividing by the total number of events in the run we can obtain an estimate for $h_i(E, \mathbf{r})$.

Figure 5.2 shows the distribution of hit probabilities for a monoenergetic ^{214}Po source located at the center of the detector. With a monoenergetic source at the center, the only difference in the hit probabilities should come from the presence/absence of the light concentrators and differences in the individual efficiencies of the PMT's. As can be seen, the light concentrators make a large difference to the hit probability, though even amongst those with light concentrators, there is a fairly large spread in the conversion probability.
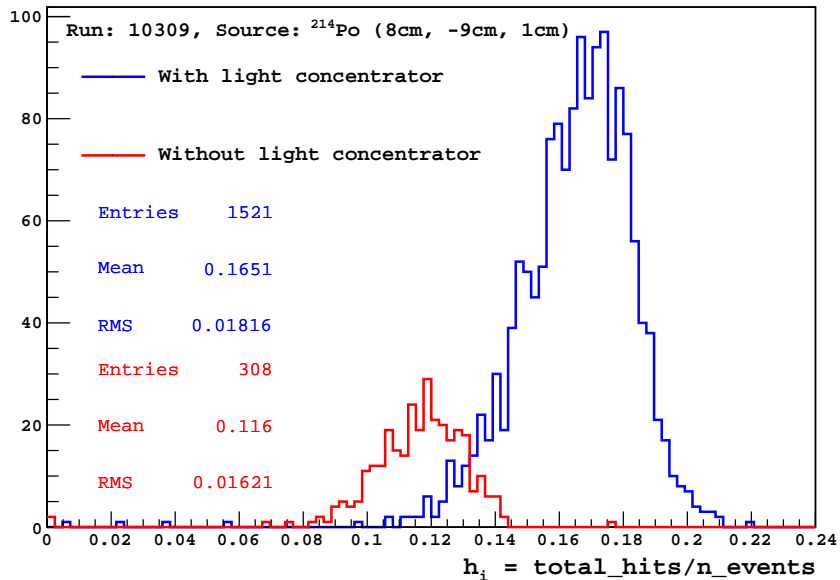
Figure 5.2: PMT hit probabilities measured using ^{214}Po source located at the center of the detector. In blue are the PMTs with light concentrators, while in red are PMTs without concentrators.

For sources located off-center, if you ignore scattering effects, one would expect that the probability for a photon to be converted to a photoelectron on a specific

PMT is directly proportional to the solid angle subtended by the PMT, *i.e.*

$$c_i(\mathbf{r}) \propto \Omega_{\mathbf{r},i} \tag{5.19}$$

$$\ln(1 - h_i(E, \mathbf{r})) \propto \Omega_{\mathbf{r},i} \tag{5.20}$$

where $\Omega_{\mathbf{r},i}$ is the solid angle subtended by the ith PMT from position $\mathbf{r}$. Figure 5.3 plots the relationship between $\ln(1 - h_i(E, \mathbf{r}))$ and $\Omega_{\mathbf{r},i}$ for a monoenergetic ^{214}Po source located off-center. As can be seen, the data indicates a proportional relationship as expected. We note here that a slightly better fit to the data is obtained if one assumes a linear relationship, with a small constant term, rather than direct proportionality. This is possibly due to scattering of light within the scintillator.
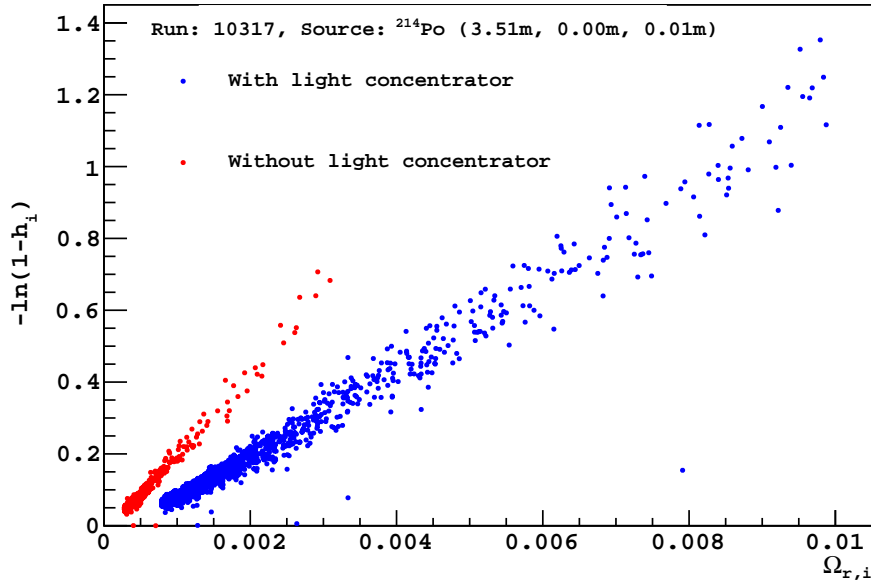
Figure 5.3: PMT hit probabilities versus the subtended solid angle measured using an off-center ^{214}Po source. In blue are the PMTs with light concentrators, while in red are PMTs without concentrators. The data shows a linear dependence as expected.

We can now use this information to study the detector response in the `npmts` variable - which is the total number of PMTs that are hit in a given event. For the

sake of conciseness we will use k to denote the value of the `npmts` variable. Since the means and variances of independent random variables simply add, we can calculate the mean and variance of k as :

$$\text{mean}(P(k|E,\mathbf{r})) = \sum_{i}^{N_T} h_i(E,\mathbf{r}) \tag{5.21}$$

$$= N_T \cdot \text{mean}(h_i) \tag{5.22}$$

$$\text{var}(P(k|E,\mathbf{r})) = \sum_{i}^{N_T} h_i(E,\mathbf{r})(1 - h_i(E,\mathbf{r})) \tag{5.23}$$

$$= N_T \cdot \text{mean}(h_i)\left(1 - \text{mean}(h_i) - \frac{\text{var}(h_i)}{\text{mean}(h_i)}\right) \tag{5.24}$$

where $N_T(= N_{live\_pmts})$ is the number of channels with working timing information and we have dropped the explicit dependence of h_i on energy and position. The number of triggered PMTs is usually normalized to 2000 working PMT's so that the variable can be used across runs with differing numbers of working channels. Defining the variable $k_N \equiv 2000/N_T \cdot k$, we obtain the first two moments of the normalized `npmts` variable:

$$\text{mean}(P(k_N|E,\mathbf{r})) = 2000 \cdot \text{mean}(h_i) \tag{5.25}$$

$$\text{var}(P(k_N|E,\mathbf{r})) = 2000 \cdot \text{mean}(h_i)\left(1 - \text{mean}(h_i) - \frac{\text{var}(h_i)}{\text{mean}(h_i)}\right) \tag{5.26}$$

In order to know the complete distribution of $P(k_N|E,\mathbf{r})$, one must know the details of the distribution of the hit probabilities $h_i(E,\mathbf{r})$. Unfortunately the $h_i(E,\mathbf{r})$ distribution, especially as a function of event position $\mathbf{r}$, is difficult to model analytically. It is primarily for this reason that we have chosen to use the charge energy variable `npe` instead of `npmts`.

5.1.4.1 Threshold Effects

In the above derivation we assumed that any channel that registers a photoelectron will be considered triggered. In practice this is not true. A PMT is considered triggered only if the integrated charge is larger that a certain threshold, q^{th}. Thus a channel recording multiple photoelectrons has a higher probability of triggering a PMT than if there is only a single photoelectron. Taking into consideration the effect of the threshold, the probability for a channel to trigger is modified from Eq. 5.18 to:

$$h_i(E, \mathbf{r}) = 1 - e^{-\mu_i(E, \mathbf{r})} \sum_{p=0}^{\infty} \left(\frac{\mu_i^p(E, \mathbf{r})}{p!} \int_0^{q^{th}} P_i(q'|p)dq' \right) \qquad (5.27)$$

where $P_i(q'|p)dq'$ is the probability of recording a charge value between $[q', q' + dq']$ given p photoelectrons. The hardware threshold is currently set at 0.2 times the mean charge of a photoelectron [45], and the fraction of the single photoelectron response below the threshold is typically 0.13 [92].

5.1.4.2 Estimates of the number of photoelectrons from `npmts`

It is sometimes needed to estimate the energy of a single event based on the number of triggered PMTs k. This is mostly necessary for tagging events in delayed coincidences such as identifying $^{85}\text{Kr} \rightarrow ^{85m}\text{Rb} \rightarrow ^{85}\text{Rb}$ decays. Consider the idealized case of an event at the center of the detector, and assume that all the PMT's are identical. In this situation, all the hit probabilities $h_i = \bar{h}$ are the same. Given that we observed k hits on N_T PMTs, the most likely estimate for the hit probability is: $\bar{h} = k/N_T$. The mean number of photoelectrons on each tube is then given by the Poisson distribution (Eq 5.18), and so we have:

$$\mu_i = \ln(1 - \bar{h}) = \ln\left(1 - \frac{k}{N_T}\right) \qquad (5.28)$$

Since the mean total number of photoelectrons $\mu(E)$ is just the sum of the means for each individual phototube, we have finally:

$$\mu(E) = -N_T \ln\left(1 - \frac{k}{N_T}\right) \tag{5.29}$$

For completeness, we will also consider the case where we have a fixed number of photoelectrons p. Then, in the same idealized conditions described above, the probability distribution for the number of detected hits is:

$$P(k|p, \mathbf{r} = \mathcal{O}) = \frac{k!}{N_T^p}\binom{N_T}{k}\left\{{p \atop k}\right\} \tag{5.30}$$

$$\text{mean}(P(k|p, \mathbf{r} = \mathcal{O})) = N_T\left[1 - \left(1 - \frac{1}{N_T}\right)^p\right] \tag{5.31}$$

where $\left\{{p \atop k}\right\}$ represents Stirling numbers of the second kind. Once again we can estimate the mean of the hit distribution as $mean(P(k|p, \mathbf{r} = \mathcal{O})) = k'$ which gives us:

$$p = \frac{1}{\ln\left(1 - \frac{1}{N}\right)}\ln\left(1 - \frac{k'}{N}\right) \equiv \mathtt{nhits\_corrected} \tag{5.32}$$

To summarize, we have derived two different estimates of the number of photo-electrons based on the observed number of triggered PMTs. Eq. 5.29, commonly used in *Echidna*, assumes a Poisson distribution of photoelectrons for an event of given energy, while Eq. 5.32 (previously used in *Mach4*) assumes a delta-function distribution for the number of photoelectrons. As mentioned at the start of this chapter, and will be verified later through comparison with data, the assumption of a Poissonian distribution of photoelectrons appears to be physically correct. We note that the formulas give very similar results for $N \gg 1$, which is the case for Borexino, with $N \sim 2000$ PMTs.

5.1.5   `npe` Response Function

In this section we will develop an analytical model for the response function of the `npe` variable, which is the total charge recorded during the event by all channels with working ADCs, normalized to 2000 working PMT's. In the previous sections we have seen that the number of photoelectrons (both the total and the number on each PMT) follows a Poissonian distribution. Here we study the response function of the PMTs to the photoelectron distribution and compare it with data and Monte Carlo simulations.

5.1.5.1   Individual PMT Charge Response Function

Let the single photoelectron charge response (SPE) function of the ith phototube be given by $P_i(q|p = 1) \equiv \psi_i(q)$. By rescaling the charge output of each PMT, we can set the mean of this distribution to 1 (to match the number of photoelectrons). We will denote the rescaled mean, variance and third central moment as:

$$\mu_i^{spe} \equiv 1 \tag{5.33}$$

$$v_i^{spe} \equiv \frac{\mathrm{var}(\psi_i)}{\mathrm{mean}^2(\psi_i)} \tag{5.34}$$

$$\kappa_i^{spe} \equiv \frac{\kappa(\psi_i)}{\mathrm{mean}^3(\psi_i)} \tag{5.35}$$

where κ denotes the third central moment, related to the skewness of the distribution. We note that it has been found that the single photoelectron response function for the Borexino PMT's is well fit by a Gaussian without any additional components. Both the Echidna and Mach4 code use a Gaussian to fit the laser calibration data and hence determine the single photoelectron mean. Since a Gaussian is symmetric, it has a vanishing third central moment, but we include it in the calculations for completeness, so that we may analyze the impact of any small skewness in the single photoelectron response.

We will consider the response of the phototubes to be perfectly linear. The charge response to p photoelectrons is then simply the convolution of p single photoelectron responses:

$$P_i(q|p) = \psi_i(q) \otimes ...(\text{p convolutions})... \otimes \psi_i(q) \tag{5.36}$$

Since the first three centralized moments add for convolutions, we have:

$$\text{mean}(P_i(q|p)) = p \tag{5.37}$$

$$\text{var}(P_i(q|p)) = p \cdot v_i^{spe} \tag{5.38}$$

$$\kappa(P_i(q|p)) = p \cdot \kappa_i^{spe} \tag{5.39}$$

For a Poisson distributed number of photoelectrons (as obtained from a monoenergetic electron) we therefore have:

$$P_i(q|E,\mathbf{r}) = \sum_{p=0}^{\infty} P_i(q|p) \cdot P_i(p|E,\mathbf{r}) \tag{5.40}$$

$$= \sum_{p=0}^{\infty} P_i(q|p) \cdot \frac{\mu_i^p(E,\mathbf{r})e^{-\mu_i(E,\mathbf{r})}}{p!} \tag{5.41}$$

A fairly straightforward calculation yields the first three centralized moments:

$$\text{mean}(P_i(q|E,\mathbf{r})) = \mu_i(E,\mathbf{r}) \tag{5.42}$$

$$\text{var}(P_i(q|E,\mathbf{r})) = \mu_i(E,\mathbf{r}) \cdot (1 + v_i^{spe}) \tag{5.43}$$

$$\kappa(P_i(q|E,\mathbf{r})) = \mu_i(E,\mathbf{r}) \cdot (1 + 3v_i^{spe} + \kappa_i^{spe}) \tag{5.44}$$

Note that we have not specified any functional form for the phototube single photoelectron charge response $\psi_i(q)$, just the first three moments.

5.1.5.2 Combined PMT Charge Response Function

The charge signal from each of the PMTs is then summed to obtain the combined energy response function. Since we have shown previously that each PMT can be regarded as an independent detector, the combined response function is the convolution of the individual ones and the first three centralized moments of the individual response functions simply add:

$$P(q|E,\mathbf{r}) = P_1(q|E,\mathbf{r}) \otimes ... \otimes P_N(q|E,\mathbf{r}) \tag{5.45}$$

$$\text{mean}(P(q|E,\mathbf{r})) = \sum_i \mu_i(E,\mathbf{r}) = \mu(E,\mathbf{r}) \tag{5.46}$$

$$\text{var}(P(q|E,\mathbf{r})) = \sum_i \mu_i(E,\mathbf{r}) \cdot (1 + v_i^{spe}) \tag{5.47}$$

$$\kappa(P(q|E,\mathbf{r})) = \sum_i \mu_i(E,\mathbf{r}) \cdot (1 + 3v_i^{spe} + \kappa_i^{spe}) \tag{5.48}$$

If we consider all the phototube SPE response functions to have the same or similar variance and third moments, then we can simplify the formulas to:

$$\text{var}(P(q|E,\mathbf{r})) = \mu(E,\mathbf{r}) \cdot (1 + \overline{v}^{spe}) \tag{5.49}$$

$$\kappa(P(q|E,\mathbf{r})) = \mu(E,\mathbf{r}) \cdot (1 + 3\overline{v}^{spe} + \overline{\kappa}^{spe}) \tag{5.50}$$

where $\overline{v}^{spe}$ and $\overline{\kappa}^{spe}$ are the average variance and third moment of the PMT's SPE response.

5.1.5.3 Normalized Charge Response Function

In order to combine data from different runs, the charge recorded for each event is scaled to a fixed number of PMT with valid charge readout ($N_C = N_{good\_charge\_chans}$).

This scaling parameter, denoted by η, is defined as:

$$\eta \equiv \frac{2000}{N_C} \tag{5.51}$$

Since we are not currently studying variations of the response function in time, for now we will consider the parameter to be a constant. This simply scales the charge response function and all its moments:

$$\text{mean}(P(q_N|E,\mathbf{r})) = \eta \cdot \mu(E,\mathbf{r}) \tag{5.52}$$

$$\text{var}(P(q_N|E,\mathbf{r})) = \eta^2 \cdot \mu(E,\mathbf{r}) \cdot (1 + \overline{v}^{spe}) \tag{5.53}$$

$$\kappa(P(q_N|E,\mathbf{r})) = \eta^3 \cdot \mu(E,\mathbf{r}) \cdot (1 + 3\overline{v}^{spe} + \overline{\kappa}^{spe}) \tag{5.54}$$

5.1.5.4 Final Localized Charge Response Function

We have finally arrived at the charge response function for monoenergetic electrons at a given location in the detector $P(q_N|E,\mathbf{r})$. As described in Eqns 5.52, 5.53 and 5.54 the mean of the response function is simply equal to the (normalized) mean number of photoelectrons produced at the given energy and position. The variance and third moment of the response function are both proportional to the mean number of photoelectrons produced, with the proportionality constants related to the central moments of the single photoelectron response of the photomultipliers.

The complete functional form of $P(q_N|E,\mathbf{r})$ depends on the SPE response of individual phototubes, $\psi_i(q)$. In the case that the SPE response is taken to be a

Gaussian, we can make some important simplifications:

$$P_i(q|p) = \mathcal{N}(q|1, v^{spe}) \otimes ...(\text{p convolutions})... \otimes \mathcal{N}(q|1, v^{spe}) \tag{5.55}$$

$$= \mathcal{N}(q|p, pv^{spe}) \tag{5.56}$$

$$P_i(q|E, \mathbf{r}) = \sum_{p=0}^{\infty} \mathcal{N}(q|p, pv^{spe}) \cdot \mathcal{P}(p|\mu_i(E, \mathbf{r})) \tag{5.57}$$

$$P(q|E, \mathbf{r}) = P_1(q|E, \mathbf{r}) \otimes ... \otimes P_N(q|E, \mathbf{r}) \tag{5.58}$$

where $\mathcal{N}(x|\mu, \sigma^2)$ is a Gaussian distribution on x with mean μ and variance σ^2 and $\mathcal{P}(k|\mu)$ is a Poisson distribution on k with mean μ.

Since we have considered the PMTs to be identical and linear, we can write the final response function as:

$$P(q_N|E, \mathbf{r}) = \sum_{p=0}^{\infty} \mathcal{N}(q_N|\eta p, \eta^2 pv^{spe}) \cdot \mathcal{P}(p|\mu(E, \mathbf{r})) \tag{5.59}$$

The channel normalization factor is known precisely for each run, so there are only two free parameters in the response function: the mean number of photoelectrons produced ($\mu(E, \mathbf{r})$) and the variance of the single photoelectron response (v^{spe}). Of course the general equations for the moments described in Eqns 5.52, 5.53 and 5.54 still hold, with $\overline{\kappa}_i^{spe} = 0$.

5.1.5.5 Electronics Complications

In the analytical model discussed above, the behavior of the electronics is considered to be ideal. In the section we discuss some of the issues with the electronics and their possible effects on the response function.

Channel Threshold In Section 5.1.5.1, we assumed that the charge from all photoelectrons is recorded. In reality, as mentioned in Section 2.2, a PMT is considered

to be hit only if the charge output exceeds a certain threshold q^{th}. Thus the combined charge response of all the PMTs, Eq. 5.45, should be modified to (dropping the explicit dependence on E and $\mathbf{r}$):

$$P(q) = P_1^{th}(q) \otimes ... \otimes P_N^{th}(q) \tag{5.60}$$

$$\text{where } P_i^{th}(q) = \Theta(q - q^{th})P_i(q) + \delta(q) \int_0^{q^{th}} P_i(q')dq' \tag{5.61}$$

Without any explicit calculation, it is clear that the effective PMT response $P_i^{th}(q)$, taking into account the threshold, has a lower mean and higher variance than that of PMT response without the threshold $P_i(q)$.

The size of this effect depends on the value of the threshold. The discriminator threshold, q^{th}, is currently set to approximately 0.2 times the mean charge of a single photoelectron [45] and for a single photoelectron response, the fraction of the distribution below the threshold is approximately 0.13 [92]. For two or more photoelectrons on the same PMT, the threshold effect is negligible.

Channel Dead Time   The charge output of the PMT is integrated for a period of 80 ns, starting from the time of the first detected photoelectron. However, following each photoelectron, the discriminator on the channel is disabled for 140 ns (see Section 2.2). In addition to this hardware dead time, there is an additional software cut that rejects any hits occurring within 180 ns. Thus, if a photoelectron is produced between 80 and 180 ns from the first photoelectron on the channel, it will neither record a hit nor be included in the charge output. This effect is both position and energy dependent since the probability of getting two photoelectrons on a single channel depends on the total number of photoelectrons and the solid angle subtended by the PMT. At 200 p.e., at the center of Borexino, the effect is estimated to be < 1%, while for an event with 1000 p.e., the effect is estimated to be $\sim 2.5\%$.

Non-Ideal Normalization   It is possible that the rescaling of the single photoelectron response is slightly inaccurate due to the misidentification of the mean during the precalibration process. We can define an accuracy parameter:

$$l_i \equiv \frac{\text{mean}(\psi_i)}{\text{mean}'(\psi_i)} \tag{5.62}$$

where $\text{mean}'(\psi_i)$ is the possibly inaccurate mean from calibration. The rescaled moments given by Eqns 5.33 should then be replaced by:

$$\mu_i'^{spe} = l_i \cdot \mu_i^{spe} = l_i \tag{5.63}$$

$$v_i'^{spe} = l_i^2 \cdot v_i^{spe} \tag{5.64}$$

$$\kappa_i'^{spe} = l_i^3 \cdot \kappa_i^{spe} \tag{5.65}$$

The final moments for the localized charge response function would then be changed from Eqns 5.52, 5.53, 5.54 to:

$$\text{mean}(P(q_N|E,\mathbf{r})) = \eta \cdot \bar{l} \cdot \mu(E,\mathbf{r}) \tag{5.66}$$

$$\text{var}(P(q_N|E,\mathbf{r})) = \eta^2 \cdot \overline{l^2} \cdot (1 + \overline{v}^{spe}) \cdot \mu(E,\mathbf{r}) \tag{5.67}$$

$$\kappa(P(q_N|E,\mathbf{r})) = \eta^3 \cdot \overline{l^3} \cdot (1 + 3\overline{v}^{spe} + \overline{\kappa}^{spe}) \cdot \mu(E,\mathbf{r}) \tag{5.68}$$

Effective Central Moments   The sum total of these effects should be small on the overall shape of the response function and should not greatly affect the energy dependence of the parameters. Changes to the mean value of the response function can be absorbed into the energy-dependent quenching term, $Q(E)$. We will assume that the variance and third central moment will remain proportional to this effective mean such that we can write the first three central moments as:

$$\text{mean}(P(q_N|E, \mathbf{r})) = \eta \cdot LY_{det} \cdot Q_{\text{eff}}(E) \cdot E \qquad (5.69)$$

$$\equiv \mu_{\text{eff}}(E, \mathbf{r})$$

$$\text{var}(P(q_N|E, \mathbf{r})) = g_1 \cdot \mu_{\text{eff}}(E, \mathbf{r}) \qquad (5.70)$$

$$\kappa(P(q_N|E, \mathbf{r})) = g_2 \cdot \mu_{\text{eff}}(E, \mathbf{r}) \qquad (5.71)$$

where we describe, in detail, the effective quenching function Q_{eff} in Section 5.2. We have defined energy independent parameters g_1 and g_2 to denote the proportionality constants between the mean and the variance and third central moment respectively. In the ideal case where the above-mentioned electronics effects are negligible, these constants are given by

$$g_1 \sim \eta \cdot (1 + \overline{v}^{spe}) \qquad (5.72)$$

$$g_2 \sim \eta^2 \cdot (1 + 3\overline{v}^{spe} + \overline{\kappa}^{spe})$$

Some of these assumptions will be tested with data and MonteCarlo in Sections 5.1.5.7 and 5.1.5.8.

5.1.5.6 Approximation of Localized Charge Response Function

There are two main reasons why we have not directly adopted Eqn 5.59 as our localized charge response function. The first is practical: since Eqn 5.59 cannot be expressed in closed analytical form, but rather is an infinite series, the fit with such a model is many times slower than a typical analytical fit. The second reason involves modeling the details of the electronics listed in Section 5.1.5.5, which are difficult to account for in the analytical model. While these effects are small compared to the overall width and shape of the response function, the analytical relationships be-

tween the central moments may no longer be strictly true. Thus we would like to use a model that has the general shape and energy properties of the analytical model (see Eqns. 5.69, 5.70, 5.71) but with an extra parameter to fit the the details that have been left unaccounted for.

It is for these reasons that we have decided to use an empirical function to approximate the model when fitting the energy spectra. The empirical analytical function we have adopted to approximate the model for the localized charge response function (Eqn 5.59) is given by :

$$P_{emp}(q_N|\lambda, a, b) = \frac{1}{\sqrt{2\pi}\sqrt{a + b \cdot q_N}} \exp\left(-\frac{(q_N - \lambda)^2}{2(a + b \cdot q_N)}\right) \tag{5.73}$$

This function, from now onwards referred to as a modified Gaussian, is an empirical function that was chosen because it closely matches the shape of the model given by Eqn 5.59.

In order to determine the energy dependence of the parameters of the modified Gaussian (*i.e* λ, a and b) we calculated the first three moments. Unfortunately, one cannot calculate the moments analytically, but to very good approximation for the range of parameters relevant to our model, they are:

$$\text{mean} = \lambda + b \tag{5.74}$$

$$\text{var} = a + b\lambda + 2b^2$$

$$= a + b^2 + b \cdot \text{mean} \tag{5.75}$$

$$\kappa = 3ab + 3b^2\lambda + 8b^3$$

$$= 3b \cdot \text{var} + \mathcal{O}[b^3] \tag{5.76}$$

We can match these moments with those of the model given in Eqns. 5.69, 5.70

and 5.71 to obtain the energy dependence of the parameters:

$$b = \frac{g_2}{3g_1} \tag{5.77}$$

$$\lambda = \mu_{\text{eff}}(E, \mathbf{r}) - \frac{g_2}{3g_1} \tag{5.78}$$

$$a = \left(g_1 - \frac{g_2}{3g_1}\right)\mu_{\text{eff}}(E, \mathbf{r}) - \left(\frac{g_2}{3g_1}\right)^2 \tag{5.79}$$

We recall that the parameters g_1 and g_2 are the constants of proportionality relating the variance and third central moment to the mean number of photoelectrons (Eqn 5.72).

Thus for the empirical localized response function of the detector, we expect b to be an energy independent constant, λ to be shifted from the normalized mean number of photoelectrons by b and a to be a constant fraction of the normalized mean minus a small constant offset, b^2. The energy dependence of these relationships have been tested with Monte Carlo and are described later in Section 5.1.5.8.

One will notice that while our analytical model had only two free parameters (the mean number of photoelectrons and the variance of the single photoelectron), the empirical approximation uses three free parameters $(\mu_N(E, \mathbf{r}), g_1, g_2)$. While we could place the additional constraint that the single photoelectron response be symmetric (κ^{spe}) and rewrite the parameters g_1 and g_2 in terms of a single parameter v^{spe}, we have decided to only enforce the general energy dependence of the mean and variance, to allow for some of the details of the electronics that were not modeled (see Section 5.1.5.5 for details). We have found that the additional free parameter accounts for broadening of the detector response without slowing down the spectral fit significantly.
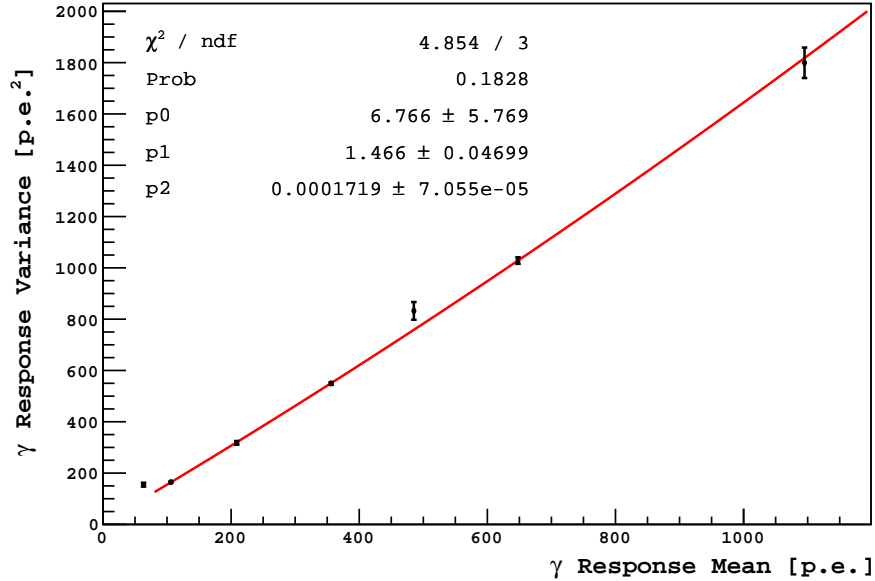
Figure 5.4: Dependence of the variance of the response function of a localized source on the mean number of detected p.e.

5.1.5.7 Tests of Localized Charge Response Function with Data

We can test the energy dependence of the variance of $P(q_N|E, \mathbf{r})$, Eqn 5.53, by looking at γ source calibration runs at the centre of the detector. For each of the γ sources, we plot the charge response in a histogram and fit the peak ($\pm 2\sigma$) to a Gaussian. The mean of the Gaussian is taken as the estimate of the parameter $\text{mean}(P(q_N|E, \mathbf{r}))$ and the variance of the Gaussian is taken as the estimate of the parameter $\text{var}(P(q_N|E, \mathbf{r}))$. From our analytical model (see Eqns 5.69, 5.70), we expect the variance to be directly proportional to the mean. While we do not expect the shape of the response function to be perfectly Gaussian, we have used a Gaussian to estimate the mean and variance by fitting around the peak, so as to reduce the effect of backgrounds, while not making any too many assumptions about the true shape of the response function. Figure 5.4 shows the variance of the Gaussian versus the mean for the different γ sources. The dependence is then fit to the function $variance = p_0 + p_1 \cdot mean + p_2 \cdot mean^2$ where p_0, p_1 and p_2 are left as free parameters as shown in Figure 5.4. We note that

172

we have excluded the lowest energy ^{139}Ce source from the fit as it does not seem to follow the same trend as the others. The cause of this difference is not currently known, but since the energy of the source (165 keV) is well below the energy threshold being fit, we can safely ignore it. As we expect from Eqn 5.53, the parameter p_0 fits to a value consistent (at 1.2 σ) with zero. The value for p_1 corresponds to a value of $g_1 = 1.47 \pm 0.05$. It is important to note that due to the multiple Compton scattering of γ's and the non-linear quenching of the scattered electrons, we expect an additional variance for monoenergetic γ sources as compared to monoenergetic βs. Interestingly the best fit value for p_3 indicates (at $\sim 2.4\ \sigma$) a non-zero quadratic term. If physical, it is possible that it arises from one of the electronics effects mentioned in Section 5.1.5.5. The introduction of a quadratic term in the response function will be discussed in Section 5.3. We note that even if the best-fit parameters for p_0 and p_2 represent a physical broadening of the response function, they are extremely small compared to the dominant width represented by the linear term p_1. For example, at the highest energy range normally used for the ^{7}Be analysis, 800 p.e., the increase in the standard deviation of the response function due to the constant and quadratic term is ~ 1.7 photoelectrons, compared to the predicted standard deviation of 34 photoelectrons. Given that the standard bin width for histogramming the data is 5 photoelectrons, such an increase is not noticeable.

Unfortunately, the presence of backgrounds in the source calibration data make it very difficult to evaluate the overall shape of the response function to the accuracy required to fit the high statistics regions of the spectrum - namely the ^{210}Po and the ^{14}C spectra. For testing the overall shape we have had to rely on comparisons with the g4bx Monte Carlo program, as described in the next section.

Analytical Model fit to MC simulation of 0.46 MeV electrons at center

Entries	999998
Mean	212.1
RMS	16.27
Skewness	0.07991
χ^2 / ndf	170.6 / 159
Prob	0.2502
Pois_Mean	201.3 ± 0.0
SPE_Var	0.1839 ± 0.0017
Amplitude	9.49e+05 ± 9.60e+02
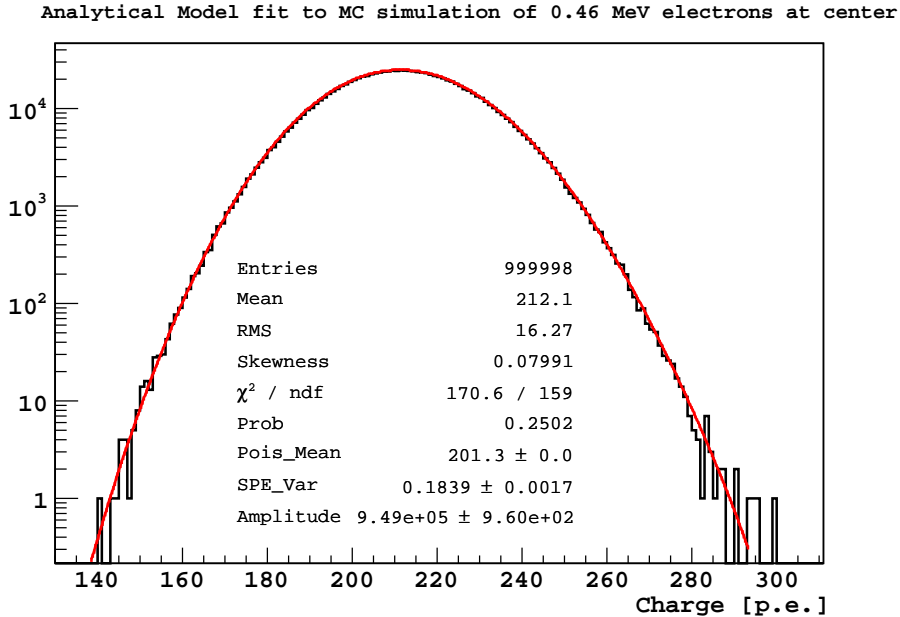
Figure 5.5: Fit of 1 million Monte Carlo generated βs with the analytical model given by Eqn 5.59.

5.1.5.8 Tests of Localized Charge Response Function with Monte Carlo

Since we did not have enough background-free data to sufficiently test the model, we ran a series of tests using the *g4bx* Monte Carlo program. We note that in addition to simulating the physical processes occurring during energy deposition, scintillation and light propagation, there is a dedicated electronics package that simulates the Borexino data acquisition system. Thus, the effect of many of the details of the electronics that were not directly included in the model (see Section 5.1.5.5) are included in the Monte Carlo output. The comparison with Monte Carlo output is therefore a good test of the flexibility of the analytical and empirical models to account for non-ideal behavior. To compare the model with the g4bx Monte Carlo output, we generated 1 million events at the centre of the detector, for both αs and βs, with a mean charge of ~ 210 p.e., approximately the charge of the ^{210}Po peak. The number of valid charge channels, N_C, used for the simulation was 1898.

We first fit the simulated spectrum to the analytical model given by Eqn. 5.59

174

	Mean	Variance	Skewness
MonteCarlo	212.10	264.51	0.0799*
Fitted Analytical Model	212.11 ± 0.02	264.5 ± 0.4	0.0849 ± 0.0001
Fitted Empirical Approximation	212.11 ± 0.02	264.6 ± 0.4	0.0797 ± 0.002

Table 5.1: This table presents the central moments of the Monte Carlo data as compared to the fit shown in Figure 5.5 with the model given by Eqn 5.59. *The value of the skewness of the Monte Carlo data is approximate due to the binning of the data.

with the mean number of photoelectrons and the variance of the single photoelectron responce (v^{spe}) left as free parameters. The resulting fit for electrons is shown in Figure 5.5. As can be seen, the fit shows extremely good agreement with the model over the entire range (the fit is done over a range of $\pm 5\sigma$). Table 5.1 compares the first three moments of the model with the MonteCarlo output.
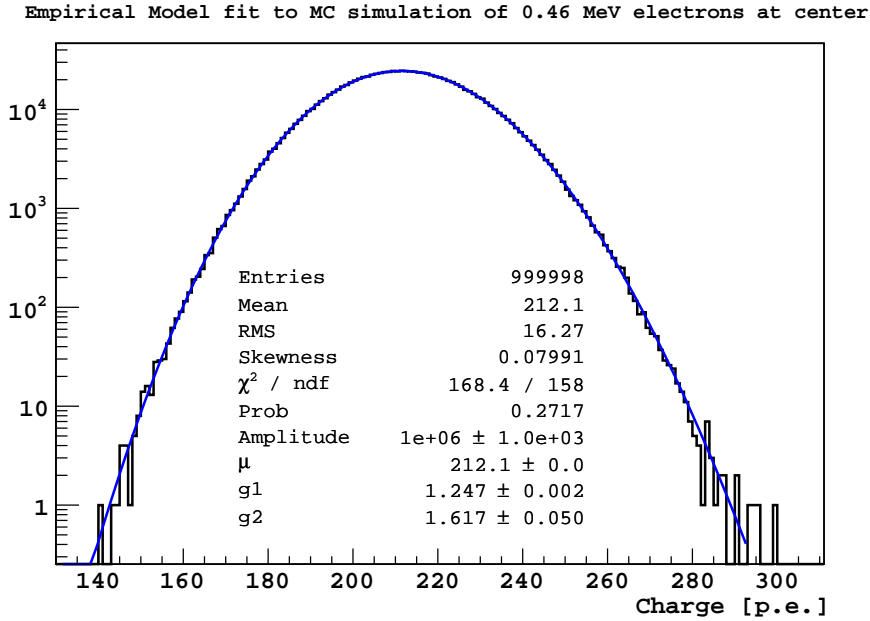
Figure 5.6: Fit of 1 million Monte Carlo generated βs with the empirical model given by Eqn 5.73.

We then fit the same Monte Carlo spectrum using the empirical model given by Eqn. 5.73, written in terms of the parameters $\mu_N(E, \mathbf{r})$, g_1 and g_2 (Eqns 5.77, 5.78 and 5.79). The fit, shown in Figure 5.6, also shows very good agreement with the data all the way out to the tails. The corresponding moments of the fitted distribution are

compared in Table 5.1.

To summarize, we have obtained an empirical approximation to our analytical model for the localized charge response function that agrees extremely well in both energy dependence and shape with the available data and Monte Carlo output.

5.2 Energy Scale

5.2.1 β Photoelectron Scale

In this section we shall discuss the energy response of the scintillator for electrons. We shall motivate the expression used in Eqn. 5.3 for the mean number of emitted scintillation photons from an electron of energy E

$$F(E) \equiv \mu'_\beta(E) = LY_{scint} \cdot Q_\beta(E) \cdot E \tag{5.80}$$

and explicitly model the energy-dependent quenching factor for electrons $Q_\beta(E)$.

5.2.1.1 Scintillation Light

In an ideal scintillator, the light output would be directly proportional to the amount of energy deposited such that

$$F(E) = LY_{scint} \cdot E \tag{5.81}$$

where the proportionality constant LY_{scint} is commonly referred to as the lightyield of the scintillator and expressed in units of photons/MeV. We note that here we are only concerned with the mean number of scintillation photons emitted, not the details of the distribution (which was discussed in Section 5.1). It has been noticed that while this ideal relationship holds true at high energies, at lower energies there is a non-linear dependence. In order to describe this behavior a simple model was proposed

176

by Birks [93]. This model is based on the exciton theory in which the electronic energy excited by the incident ionizing particle is transferred between the molecules of the scintillator until it is captured by a single molecule which either fluoresces, or is quenched. The number of excitons produced per unit path length is proportional to the energy loss per unit path length dE/dx, or stopping power, of the initial particle. In the absence of quenching, some fixed fraction of these will fluoresce, leading to a light output that is proportional to the number of excitons produced:

$$\frac{dF}{dx} = L\frac{dE}{dx} \text{ (no quenching)} \tag{5.82}$$

where dF/dx is the light output per unit track length and L is the proportionality constant. However, the ionizing particle also creates a local concentration of "damaged" molecules which quench the light. The concentration of these damaged particles is also proportional to the stopping power. If we denote the concentration of damaged particles as $B \cdot dE/dx$ and the probability for an exciton to capture on a damaged particle relative to an undamaged particle as k, then the light output per unit length becomes:

$$\frac{dF}{dx} = \frac{L\dfrac{dE}{dx}}{1 + kB\dfrac{dE}{dx}} \tag{5.83}$$

which we can rewrite in terms of the total scintillation light output as

$$F = L \cdot E \cdot \frac{1}{E} \int_0^E \frac{dE'}{1 + kB\frac{dE}{dx}} \tag{5.84}$$

$$\equiv L \cdot E \cdot Q_\beta(E) \tag{5.85}$$

where we have pulled out a factor of E (the initial kinetic energy of the particle) such that the final term, referred to as the ionization quenching function, goes to

1 for sufficiently small values of the stopping power. We have thus obtained the functional form used in Eqn. 5.3, where $LY_{scint} \equiv L$ is referred to as the lightyield of the scintillator. The rest of this section will be devoted to characterizing the energy dependence of the quenching function:

$$Q_\beta(E) = \frac{1}{E} \int_0^E \frac{dE'}{1 + kB\frac{dE}{dx}} \tag{5.86}$$

In order to calculate the quenching as a function of energy, one must know the values of the parameters k and B as well as the stopping power as a function of energy.

The stopping power for electrons in the scintillator can be calculated using the known composition and density. Figure 5.7 shows the stopping power for electrons in pseudocumene (C_9H_{12}, $\rho = 0.88$ g/cm^3) as a function of energy [94]. As can be seen in the figure, the stopping power at low energies is dominated by collisional losses and decreases monotonically until ~ 1.5 MeV after which it begins to increase due to the increasing effect of radiative losses. For reference, the stopping power and range for a 1 MeV electron in pseudocumene ($\rho = 0.88$ g/cm^3) is ~ 1.64 MeV/cm and 0.38 cm respectively.

Unfortunately, the parameters k and B, like the scintillator lightyield, cannot be predicted theoretically but must be experimentally measured for each scintillator individually. Since the parameters only appear together as a product, they can be regarded as a single parameter kB (which has a typical value of 0.01 cm/MeV for organic scintillators).

From Section 5.1.2 we know that the mean number of scintillation photoelectrons produced is related to the mean number of scintillation photons produced through the conversion probability, so we can write (Eq. 5.8):

$$\mu_\beta(E, \mathcal{O})_{scint} = LY_{det}(\mathcal{O}) \cdot Q_\beta(E, kB) \cdot E \tag{5.87}$$
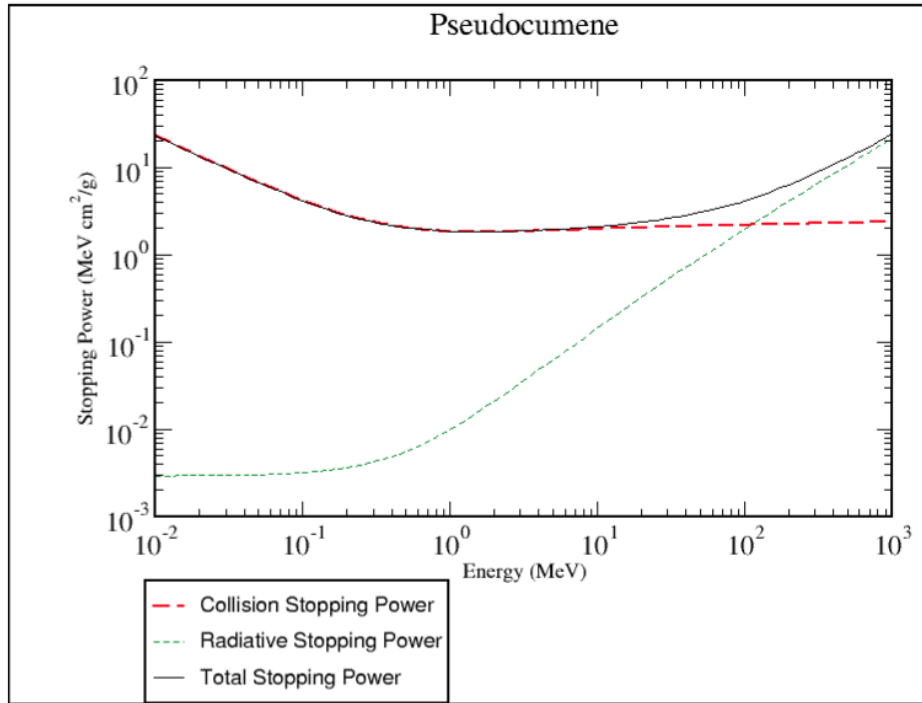
Figure 5.7: Electron stopping power in pseudocumene (C_9H_{12}) at a density of 0.88 g/cm^3. Figure taken from [94].

where we have explicitly noted the dependence of the quenching on the unknown parameter kB.

5.2.1.2 Cherenkov Radiation

So far we have only considered the emission of scintillation photons. Electrons moving through the scintillator can also produce Cherenkov radiation in addition to the excitation of the scintillator molecules. Even though the Cherenkov spectrum is weighted towards shorter wavelengths, it can be shifted to higher wavelengths (that better matches the PMT sensitivity) by the PPO dissolved in the scintillator. Of course electrons can only produce Cherenkov radiation if they are moving faster than the phase velocity of light in the scintillator. At the peak absorption wavelength of PPO ($\sim$ 300 nm [95]) the refractive index related to the phase velocity of the scintillator is $\sim$ 1.58, which leads to a Cherenkov energy threshold of 149 keV. Using

the *g4bx* Monte Carlo program it is estimated that a 1 MeV electron produces roughly 3 Cherenkov photoelectrons (see Figure 5.8), which is less than 0.75% of the total number of scintillation photoelectrons produced. Since the contribution is small, we do not expect it to affect the Poisson statistics of the scintillation light and simply include the effect in the energy scale as:

$$\mu_\beta(E, \mathcal{O}) = LY_{det}(\mathcal{O}) \cdot Q_\beta(E, kB) \cdot E + \mu_\beta(E, \mathcal{O})_{Ch} \tag{5.88}$$

where $\mu_\beta(E, \mathcal{O})_{Ch}$ is the mean number of Cherenkov photoelectrons produced by an electron with energy E at the center, as estimated using *g4bx* (see Figure 5.8).
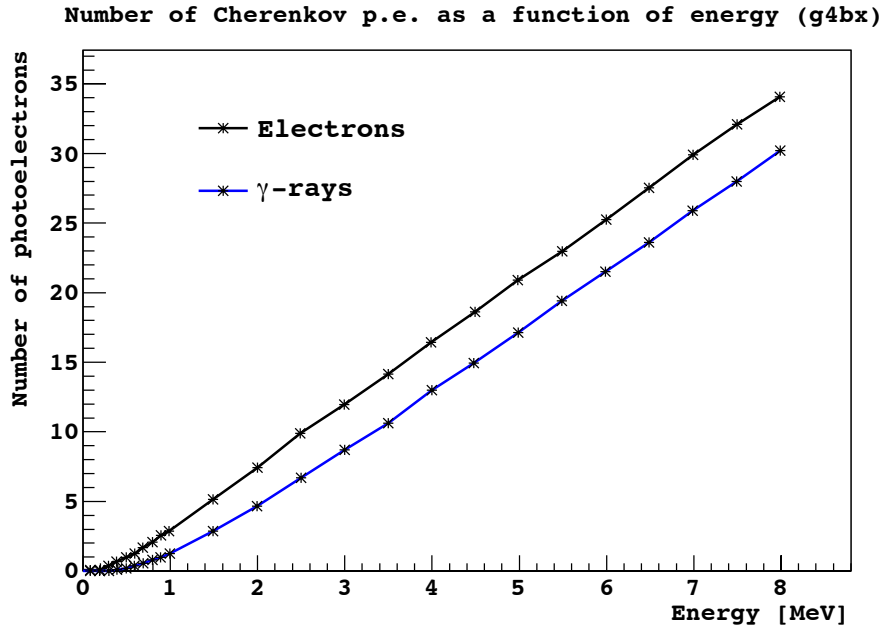
Figure 5.8: Mean number of Cherenkov photoelectrons produced by electrons (black) and γ rays (blue) at the center of the detector, as a function of energy. Data obtained using *g4bx* Monte Carlo simulation. Figure adapted from [96]

.

Suppose we had a set of monoenergetic electron sources of different energies, located at the center of the detector. For each source run we could measure the individual PMT hit probabilities, h_i, as the fraction of source events for which the PMT

was triggered. Then, using Eq. 5.18, (neglecting threshold effects) we could calculate the mean number of photoelectrons produced as:

$$\mu(E, \mathcal{O})_{data} = \sum_{i=1}^{N} \mu_i(E, \mathcal{O}) \tag{5.89}$$

$$= -\sum_{i=1}^{N} \ln(1 - h_i(E, \mathcal{O})) \tag{5.90}$$

By plotting the experimentally measured quantity, Eq. 5.90, versus energy, we could then fit the data using Eq. 5.88 to obtain $LY_{det}(\mathcal{O})$ and kB. Unfortunately we did not use any monoenergetic electron sources during the calibration campaigns and thus had to rely on γ sources. The description of the calibration of the energy scale with the γ sources is described in the next section.

5.2.2 γ Photoelectron Scale

The calibration of the energy scale with γ sources follows the same procedure outlined above for the hypothetical monoenergetic electron sources except for one important detail: γ rays do not deposit all their energy at a single position, but rather undergo multiple interactions. Given the γ source energies used and the composition of the Borexino scintillator, these interactions are dominated by Compton scattering and produce multiple recoiling electrons. Each one of these recoil electrons then produces light as described above in Section 5.2.1.

Consider a single γ ray with energy E_γ that undergoes a series of interactions within the scintillator that produces m secondary electrons with energies $\{E_1, ..., E_m\}$. The mean number of photons produced is the sum of the photons produced by each individual electron, and since the sum of Poisson random variables also follows a Poisson distribution, the assumptions used to derive Eq. 5.90 still hold. We note that since the interactions occur at spatially separated locations, the conversion probability

could be different for different interaction points. However, since the conversion probability roughly scales as the solid angle subtended by the PMTs and the γ mean free path (25 cm for $E_\gamma \sim 2.2$ MeV [80]) is small compared to the distance between the PMTs and the center of the detector, we can ignore this effect. The number of photoelectrons produced is therefore given by:

$$p_\gamma(E_\gamma, \mathcal{O}) = LY_{det}(\mathcal{O}) \cdot \sum_{j=1}^{m} Q_\beta(E_j, kB) \cdot E_j + \sum_{j=1}^{m} \mu_\beta(E_j, \mathcal{O})_{Ch} \qquad (5.91)$$

If we calculate the above for not just one, but thousands of γ rays, using the energy deposit information from *g4bx* and calculating the quenching to the individual secondary electrons using the `kB` program [97], then we can define the average number of photoelectrons produced by γ rays as:

$$\mu_\gamma(E_\gamma, \mathcal{O}) \equiv LY_{det}(\mathcal{O}) \cdot Q_\gamma(E_\gamma, kB) \cdot E_\gamma + \mu_\gamma(E_\gamma, \mathcal{O})_{Ch} \qquad (5.92)$$

where we have defined effective quenching and Cherenkov functions for γ rays as:

$$Q_\gamma(E_\gamma, kB) \equiv \frac{1}{E_\gamma} \left\langle \sum_{j=1}^{m} Q_\beta(E_j, kB) \cdot E_j \right\rangle_{MC} \qquad (5.93)$$

$$\mu_\gamma(E_\gamma, \mathcal{O})_{Ch} \equiv \left\langle \sum_{j=1}^{m} \mu_\beta(E_j, \mathcal{O})_{Ch} \right\rangle_{MC} \qquad (5.94)$$

where $\langle \rangle_{MC}$ indicates that the quantity was averaged over many MonteCarlo simulations. The function $\mu(E_\gamma, \mathcal{O})_{\gamma, Ch}$ is shown in Figure 5.8.

We are now finally in a position to calculate the parameters kB and the lightyield of the detector at the center. First, using the source calibration data, we plot Eq. 5.90 versus E_γ for each source. For the ^{7}Be analysis we used the following γ sources (in order of increasing energy): ^{203}Hg, ^{85}Sr, ^{54}Mn, ^{65}Zn, ^{40}K, and the 2.2 MeV γ ray from neutron captures on hydrogen . These sources span the entire energy range of

the spectral fit for the analysis. We then fit the data using the model described by Eq. 5.92, leaving kB and $LY_{det}(\mathcal{O})$ free. Figure 5.9 shows the data and the fitted model, where we have divided both by E_γ to emphasize the non-linear quenching. The best fit values we obtained were $kB = 0.0115 \pm 0.0007$ cm/MeV and $LY_{det}(\mathcal{O}) = 488.5 \pm 1.6$ p.e./MeV. For details regarding the uncertainties and systematics of the procedure, refer to [98].
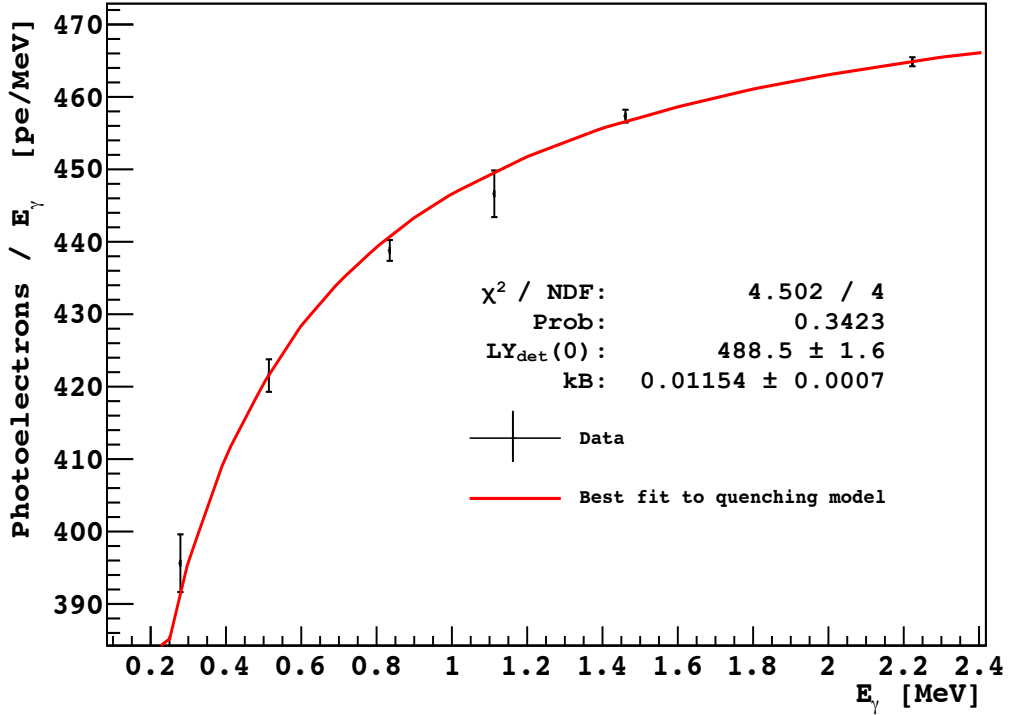
Figure 5.9: Mean number of photoelectrons per MeV as a function of energy for six γ ray sources located at the centre of the detector. Red line shows the best fit to the data with a quenching model that includes both scintillation and Cherenkov light. The free parameters in the model are the detector lightyield at the center and Birk's quenching parameter kB.

5.2.3 Charge Scale

Given the values of the kB and $LY_{det}(\mathcal{O})$ parameters, and the number of Cherenkov photoelectrons produced as a function of energy, we can use Eq. 5.88 and Eq. 5.92 to determine the number of photoelectrons produced for an electron and γ-ray of any energy at the center of the detector. We recall that in using Eq. 5.90, we have

used the `npmts` variable to estimate the number of photoelectrons. This is because at the center of the detector it is an analytically easier variable to use, as it does not suffer from most electronics effects. To compare the mean number of photoelectrons obtained from `npmts`, $\mu(E, \mathcal{O})_{data}$ in Eq. 5.90, to the value obtained from the charge variable, $\text{mean}(P(q|E, \mathcal{O}))$, the two values were compared for the same six γ ray sources used to determine kB. The data was then fit to the function:

$$\text{mean}(P(q|E, \mathcal{O})) = (1 + a) \cdot \mu(E, \mathcal{O})_{data} + b \cdot \mu^2(E, \mathcal{O})_{data} \qquad (5.95)$$

For an ideal charge variable with no electronics issues, both a and b would be zero. However the best fit values obtained gave $a = 0.05$ and $b = -1.25 \times 10^{-5}$. These non-zero values can arise from a combination of the various issues mentioned in Section 5.1.5.5, a further discussion of which can be found in [98]. The effect of the non-linear term, b, on the energy scale of the spectrum is studied in Section 6.8.3.2.

5.2.3.1 β Charge Scale

In theory we are already done: using the calculated values for $a, b, kB, LY_{det}(\mathcal{O})$, $\mu_\beta(E, \mathcal{O})_{Ch}$ and Eq. 5.88, we could determine the energy dependence of the mean of the charge variable for electrons at the center of the detector:

$$\mu_{\beta\text{eff}}(E, \mathcal{O}) \equiv (1 + a) \cdot \mu_\beta(E, \mathcal{O}) + b \cdot \mu_\beta^2(E, \mathcal{O}) \qquad (5.96)$$

However, computing the integral within the quenching function is very slow. We have therefore chosen to parameterize the charge variable energy dependence using

A_1	A_2	A_3	A_4	A_5
1.01935	0.127233	6.06714×10^{-5}	0.116877	0.0074905

Table 5.2: Parameters to model the energy response of the `npe` variable using Equation 5.98, with E in units of MeV. This model includes the kB parameter from the best fit to the scintillation and Cherenkov light as well as the best fit to the non-linear relationship between charge and the number of photoelectrons.

the model described in [99]:

$$\mu_{\beta\text{eff}}(E, \mathcal{O}) \equiv LY_{det}(\mathcal{O}) \cdot Q_{\beta\text{eff}}(E) \cdot E \tag{5.97}$$

$$\text{where } Q_{\beta\text{eff}}(E) \equiv \frac{A_1 + A_2 \ln(E) + A_3 \ln^2(E)}{1 + A_4 \ln(E) + A_5 \ln^2(E)} \tag{5.98}$$

The values of the A_i parameters are given in Table 5.2 (for E in units of MeV) and the function is depicted in Figure 5.10. These parameter values include the scintillator quenching as well as the effects of Cherenkov radiation and the non-ideal response of the charge variable. The parameters are for the normalized charge variable, such that they do not need to be modified when applied to different runs. We note that above ~ 300 keV the value of the quenching function is slightly larger than 1. This is because this is an effective quenching function defined relative to the number of photoelectrons obtained by the total number of hits, and therefore can be greater than unity.

5.2.3.2 γ Charge Scale

In addition to determining the energy scale parameters for electrons, we also need to set the scale for the γ-rays that are present in the energy spectrum for the ^{7}Be analysis. As was done in the case for electrons, we can define the effective mean charge for γ-rays at the center of the detector:

$$\mu_{\gamma\text{eff}}(E, \mathcal{O}) \equiv (1 + a) \cdot \mu_\gamma(E, \mathcal{O}) + b \cdot \mu_\gamma^2(E, \mathcal{O}) \tag{5.99}$$
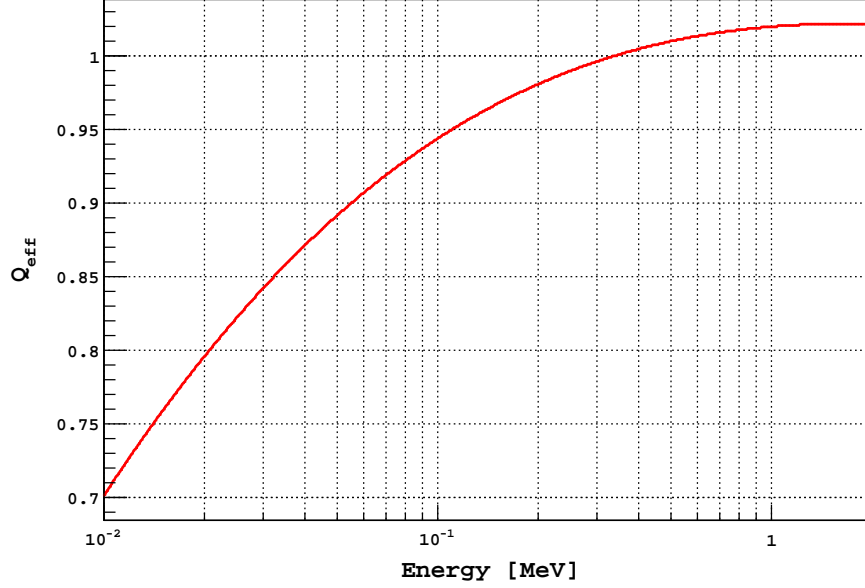
Figure 5.10: Effective electron quenching function for the charge variable. This model includes the kB parameter from the best fit to the scintillation and Cherenkov light as well as the best fit to the non-linear relationship between charge and the number of photoelectrons.

using the calculated values for a, b, kB, $LY_{det}(\mathcal{O})$, $\mu_\beta(E, \mathcal{O})_{Ch}$ and Eq. 5.92. We can also similarly define an effective quenching parameter for γ rays:

$$\mu_{\gamma\text{eff}}(E, \mathcal{O}) \equiv LY_{det}(\mathcal{O}) \cdot Q_{\gamma\text{eff}}(E) \cdot E \qquad (5.100)$$

$$\text{where } Q_{\gamma\text{eff}}(E) \equiv \frac{(1 + a) \cdot \mu_\gamma(E, \mathcal{O}) + b \cdot \mu_\gamma^2(E, \mathcal{O})}{LY_{det}(\mathcal{O}) \cdot E} \qquad (5.101)$$

Unlike the case for the electrons, we do not have a convenient parameterization for effective quenching parameter $Q_{\gamma\text{eff}}(E)$ and it must be calculated independently for each energy. Table 5.3 gives the values of $Q_{\gamma\text{eff}}(E)$ for γs that are relevant to the ^{7}Be analysis. Most of the γ decays originate from backgrounds that are sub-dominant in the spectrum such that the exact quenching values do not affect the fit For the critical quenching of the 2×0.511 MeV ^{11}C γ rays we have included an uncertainty based on the fitted kB value (see Figure 5.9). A detailed study of its effect on the fit is given in Section 6.8.3.2.

Source	E_γ [MeV]	$Q_{\gamma\mathrm{eff}}(E_\gamma)$
^{11}C	2×0.511	0.9011 ± 0.0061
^{214}Pb	0.888	0.9476
	0.839	0.9428
	0.801	0.9406
	0.534	0.9074
	0.352	0.8660
	0.295	0.8477
^{40}K	1.460	0.9738
^{7}Be	0.478	0.8970
^{10}C	$2 \times 0.511 + 0.718$	0.9102
n capture on H	2.223	0.9867

Table 5.3: Effective quenching values for γ rays relevant to the ^{7}Be analysis. The uncertainty in the ^{11}C quenching value was obtained from the uncertainty of the fitted kB value (see Figure 5.9)

5.2.4 α Charge Scale

Though most α decays produce particles with kinetic energies above 4 MeV (well above the energy range of interest for the ^{7}Be analysis), the large amount of ionization produced by these particles in the scintillator leads them to be severely quenched with respect to electrons of similar energies. Comparing the stopping power for αs, shown in Figure 5.11 for toluene (which has a similar structure and composition to pseudocumene), to the electron stopping power shown in Figure 5.7, we can see that the α stopping power is more than an order of magnitude greater than that for electrons. This relative quenching factor (which is roughly 10 for most organic scintillators) unfortunately leads to α backgrounds in the critical energy window (300 - 1000 keV) for the ^{7}Be analysis. In order to include these species in the fit, it is important to determine the α energy scale.

The dominant α background in Borexino is by far ^{210}Po which has an average rate of ~ 2000 cpd/100 tons. Due to the high rate, the ^{210}Po α peak is prominent in the energy spectrum and its position can be easily determined using the data itself. In most circumstances we therefore leave the position free in the fit instead of tying
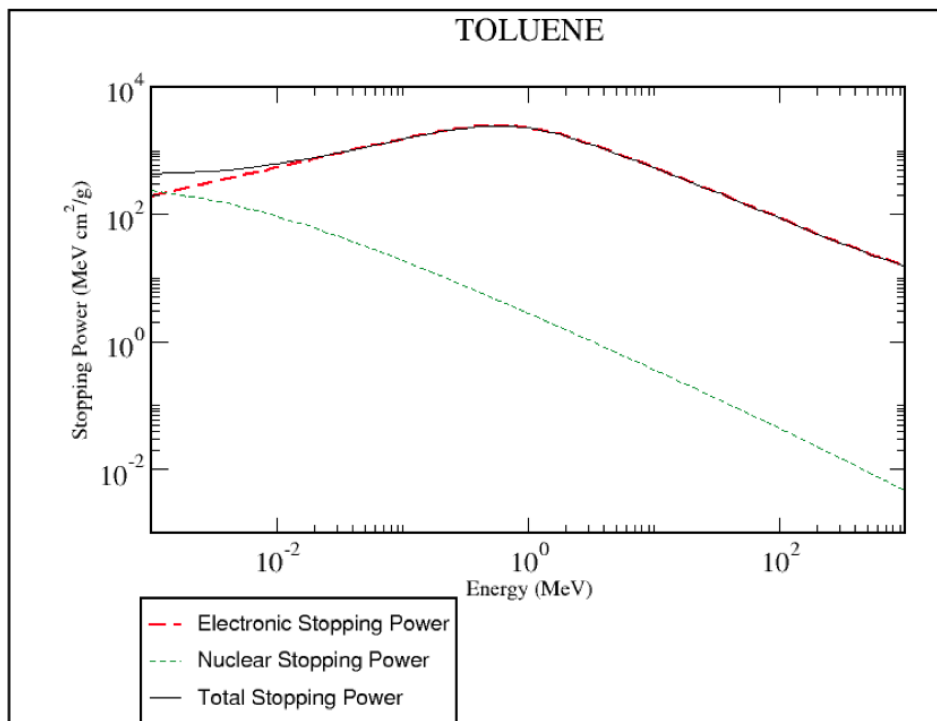
Figure 5.11: α stopping power in toluene (C_7H_8) at a density of 0.87 g/cm^3. Figure taken from [94].

it to some predetermined α energy scale. There are other α backgrounds however, most notably ^{222}Rn and ^{218}Po, with a much lower rate of decay. For these species, the decay rate is lower than the other species at the same electron-equivalent energy and thus no peak is visible. While the characteristic monoenergetic α peak is not visible above the other backgrounds, they can still contribute significantly to the count rate, and thus it is critical to know their positions in the spectrum such that they may be fixed in the fit. Since we only need to calibrate the α energy scale at a few individual points, rather than determining a continuous function as was done in the case of the electron energy scale, we can simply convert the peak positions to the charge variable and not bother with calculating the corresponding kB parameter.

For this analysis we considered the α decays of ^{210}Po, ^{212}Po, ^{214}Po, ^{216}Po and ^{220}Rn. We can also use the high rate of ^{214}Po, ^{222}Rn and ^{218}Po in the Rn source calibration runs to estimate the energy conversion, keeping in mind that the α quenching in

the scintillator used during the source calibration campaign is significantly different from the Borexino scintillator. The method for tagging the relevant α decays and determining the mean and variance of their energies in the charge scale is described briefly in the sections below.

^{210}Po The rate of ^{210}Po is sufficiently high ($\sim$ 2000 cpd/100 tons) such that one can fit the energy peak directly from the energy spectrum. Using the standard fiducial volume (r < 3m and $|z|$ < 1.67m), but before applying any pulse-shape discrimination cuts, the energy region between 170 and 250 photoelectrons was fit with a Gaussian.

^{212}Po ^{212}Po events are tagged through the fast coincidence with ^{212}Bi in the ^{232}Th decay chain. The parameters for the coincidence search are given in Table 5.4. Due to the very low levels of ^{232}Th contamination in the scintillator ($\sim 6 \times 10^{-18}$ g/g) only 31 candidate coincidences passed all the cuts. Since there were too few events to fit, the peak energy was simply taken as the mean, and the uncertainty was determined to be the standard deviation of the mean.

^{214}Po ^{214}Po events are tagged through the fast coincidence with ^{214}Bi in the ^{222}Rn decay chain. The parameters for the coincidence search are given in Table 5.4. The energy spectrum of the ^{214}Po candidates is then fit with a Gaussian.

^{214}Po within source calibration runs Using the ^{222}Rn source calibration run located at the centre of the detector (Run 10309), ^{214}Po events are tagged through the fast coincidence with ^{214}Bi using the same parameters as above. The energy spectrum of the ^{214}Po candidates is then fit with a Gaussian. As noted before, the αs from the source calibration runs have a different quenching factor when compared to those observed during regular data runs due to the different scintillators used and also possibly due to shadowing effects of the source insertion system. One should also

consider that the source calibration run used had the source localized at the centre of the detector, and not distributed within the Fiducial Volume as during regular runs. In order to account for these differences, we calculated a linear scaling factor between the source and regular runs by comparing the peak position of the ^{214}Po αs in the source $(357.3 \pm 0.2$ p.e.$)$ and regular runs $(422.1 \pm 1.0$ p.e.$)$. This factor is then used to scale the ^{222}Rn-^{218}Po α peak positions from source calibration runs. A linear scaling assumes that the decrease in light during the source calibration runs is roughly constant and that the α quenching is not significantly different over the range of α energies measured.

^{220}Rn-^{216}Po The parameters for the ^{220}Rn-^{216}Po coincidence search in the ^{232}Th chain are given in Table 5.4. Due to the very low levels of ^{232}Th contamination in the scintillator $(\sim 6 \times 10^{-18}$ g/g$)$ only 32 candidate coincidences passed all the cuts. Since there were too few events to fit, the peak energy was simply taken as the mean, and the uncertainty was determined to be the standard error of the mean.

Coinc.	1st Event		2nd Event		Δt	FV
	Energy	Gatti	Energy	Gatti		
	[p.e.]		[p.e.]		[μs]	[m]
^{212}Bi-Po	[100, 1250]	[-0.1, 0.02]	[500, 650]	[-0.02, 0.1]	< 1	$r < 3$
^{214}Bi-Po	[100, 1700]	[-0.1, 0.02]	[300, 600]	[-0.02, 0.1]	> 1.5	$r < 3$
					$< 10^3$	$|z| < 1.7$
^{220}Rn-^{216}Po	[240, 340]	[-0.02, 0.1]	[260, 400]	[-0.02, 0.1]	< 0.3	$r < 3$

Table 5.4: Search parameters for tagging α decays in data and source runs. Δt is the time interval between the first and second event and FV is the fiducial volume that was used. All coincidence searches required that the two events have a spatial separation of less than 1 m between their reconstructed positions.

^{222}Rn-^{218}Po within source calibration runs Using the ^{222}Rn source calibration run located at the centre of the detector (Run 10309), events that reconstructed within 0.5m of the centre, with charge less than 600 pe and a Gatti parameter above

190

0.015 were selected. The selected events contained ^{222}Rn, ^{218}Po and ^{214}Po α decays, with the ^{222}Rn and ^{218}Po too close in energy to distinguish separate peaks. The energy spectrum of these events below 270 p.e. (excluding the ^{214}Po peak) was fit to two Gaussians used to represent the ^{222}Rn and ^{218}Po spectra. The amplitudes of the Gaussians were forced to have the same value and the standard deviations were also tied together by setting them to be $\sigma_i = k \cdot \sqrt{\mu_i}$ where μ_i is the mean value of the corresponding Gaussian and k is a fixed constant for both.
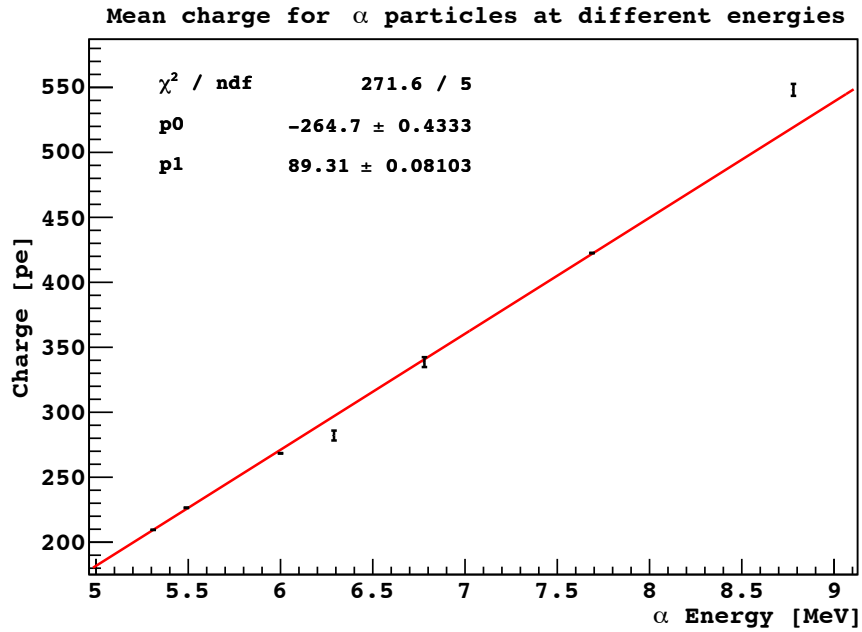
Figure 5.12: Mean charge values for α decays versus the kinetic energy of the α particle. Red line shows best linear fit $(y = p_0 + p_1 x)$ to data.

Plotting the observed energy of the αs, in photoelectrons, versus the decay energy, we find that the data follows a roughly linear pattern as shown in Figure 5.12. We have fit a straight line to the data points and though the fit is not good, it does represent the general trend. With the exception of ^{220}Rn and ^{212}Po the fit agrees with the data to within 3 p.e. (see Table 5.5). The best fit parameters give the

α Decay	E_α [MeV]	Data Set	Mean Data [pe]	Mean Pred. [pe]	σ Data [pe]	$Q_\alpha(E_\alpha)$ Data
^{210}Po	5.31	Entire	209.5 $\pm$ 0.02	209.5	18.19 $\pm$ 0.02	0.0789
^{222}Rn	5.49	Source	226.5* $\pm$ 0.2	225.6	20.61* $\pm$ 0.2	0.0825
^{218}Po	6.00	Source	268.4* $\pm$ 0.2	271.2	22.44* $\pm$ 0.2	0.0895
^{220}Rn	6.29	Entire	282.1 $\pm$ 3.8	297.1	21.3 $\pm$ 3	0.0897
^{216}Po	6.78	Entire	338.6 $\pm$ 3.8	340.8	21.5 $\pm$ 3	0.0999
^{214}Po	7.69	Entire	422.1 $\pm$ 1.0	422.1	24.86 $\pm$ 0.82	0.1098
^{214}Po	7.69	Source	422.1* $\pm$ 0.2	422.1	30.12* $\pm$ 0.12	0.1098
^{212}Po	8.78	Entire	548.1 $\pm$ 4.6	519.4	25.7 $\pm$ 3.3	0.1249

Table 5.5: Observed energies of α decays in photoelectrons. Second to last column gives the predicted peak position based on the linear fit shown in Figure 5.12. *Source run data has been rescaled upwards by a factor of ~ 1.18 such that the ^{214}Po peak from source and regular data runs match.

following relationship between the measured charge and α particle kinetic energy:

$$\text{mean}(q_N) = 89.31 \cdot E_\alpha[\text{MeV}] - 264.7 \tag{5.102}$$

Assuming a fiducial-volume-averaged electron lightyield of $LY_{det} = 500$ p.e./MeV and noting that the electron quenching factor is negligible above 5 MeV, we can define an effective quenching function for α particles as:

$$\text{mean}(q_N) = \mu_{\alpha\text{eff}}(E_\alpha) \tag{5.103}$$

$$\equiv LY_{det} \cdot Q_{\alpha\text{eff}}(E_\alpha) \cdot E_\alpha \tag{5.104}$$

$$Q_{\alpha\text{eff}}(E_\alpha) \equiv 0.179 - \frac{0.529}{E_\alpha[\text{MeV}]} \tag{5.105}$$

It should be noted that the linear fit returns an unphysical negative y-intercept indicating that the linear model is not a good approximation at low energies. Thus the above formulas are only valid in the fitted range (5 - 9 MeV). In Table 5.5 we have listed the mean and standard deviation values from the data as well as the predicted mean value from the linear fit and the effective quenching value. The quenching values agree with the general trend found in the CTF data [100] [43], though the CTF

scintillator exhibited larger α quenching (smaller values of $Q_{\alpha\mathrm{eff}}(E_\alpha)$).

5.3 Charge Response Function for a Distributed Source

Neither the background nor signal events in Borexino are located at a single position, but rather are distributed within the Inner Vessel. In this section we will consider the the charge response function of the detector for a monoenergetic electron distributed within the Fiducial Volume with a normalized probability density $\rho(\mathbf{r})$.

The response function for such a source is simply the volume-averaged response function for a localized source:

$$P(q_N|E) = \int_{FV} P(q_N|E, \mathbf{r})\rho(\mathbf{r})d\mathbf{r} \qquad (5.106)$$

We can calculate the mean of this distribution:

$$\mathrm{mean}(P(q_N|E)) = \int_{FV} \rho(\mathbf{r})\mu_{\mathrm{eff}}(E, \mathbf{r})d\mathbf{r} \qquad (5.107)$$

$$= \eta \cdot LY_{scint} \cdot Q_{\mathrm{eff}}(E) \cdot E \int_{FV} \rho(\mathbf{r})c(\mathbf{r})d\mathbf{r} \qquad (5.108)$$

where, as before, $c(\mathbf{r})$ is the position-dependent photon to photoelectron conversion probability. We recall that we have calibrated the electron energy scale using γ sources at the center of the detector (see Sections 5.2.1 and 5.2.2). In order to make use of that information, we define a relative conversion probability as a fraction of the conversion probability at the center of the detector:

$$c'(\mathbf{r}) \equiv \frac{c(\mathbf{r})}{c(\mathcal{O})} \qquad (5.109)$$

Then we can write the mean of the response function as:

$$\text{mean}(P(q_N|E)) = \mu_{\text{eff}}(E, \mathcal{O}) \int_{FV} \rho(\mathbf{r})c'(\mathbf{r})d\mathbf{r} \tag{5.110}$$

$$\equiv \mu_{\text{eff}}(E, \mathcal{O}) \cdot \langle c' \rangle_{FV} \tag{5.111}$$

$$\equiv \eta \cdot LY_{det} \cdot Q_{\text{eff}}(E) \cdot E \tag{5.112}$$

$$\equiv \mu_{\text{eff}}(E) \tag{5.113}$$

where $\langle c' \rangle_{FV}$ is the fiducial-volume-averaged relative conversion probability and we have defined $LY_{det} \equiv LY_{scint} \cdot c(\mathcal{O}) \cdot \langle c' \rangle_{FV}$ as the fiducial-volume-averaged lightyield of the detector. $\langle c' \rangle_{FV}$ is simply a constant, which for a perfectly uniform detector (in terms of light collection) is 1. Consistent with the previous notation, $\mu_{\text{eff}}(E, \mathcal{O})$ is the effective mean number of photoelectrons for the charge variable, produced by a monoenergetic event with energy E at the centre of the detector.

Similarly the variance and third centralized moment of the mixture distribution of response functions at different locations is given by:

$$\text{var}(P(q_N|E)) = g_1 \cdot \mu_{\text{eff}}(E) + g'_3 \cdot \mu^2_{\text{eff}}(E)$$

$$\kappa(P(q_N|E)) = g_2 \cdot \mu_{\text{eff}}(E) + 3g_1 g'_3 \cdot \mu^2_{\text{eff}}(E) + g'_4 \cdot \mu^3_{\text{eff}}(E) \tag{5.114}$$

where we have defined additional, energy-independent, parameters related to the moments of the conversion probability distribution:

$$g'_3 \equiv \frac{\text{var}(c')_{FV}}{\langle c' \rangle^2_{FV}} \tag{5.115}$$

$$g'_4 \equiv \frac{\kappa(c')_{FV}}{\langle c' \rangle^3_{FV}} \tag{5.116}$$

In both of the above equations for the centralized moments, the first term comes from the intrinsic variance and third moment of the localized response function, cal-

culated in Section 5.1.5.5, averaged over all positions in the detector. The subsequent terms arise from possible higher moments of the spatial distribution of the conversion probability.

We can study the photon to photoelectron conversion probability as a function of position within the detector using the ^{214}Po peak from the ^{222}Rn source calibration as well as the ^{210}Po peak during regular data-taking. Figure 5.13 show the conversion probability in the x-z plane of the detector obtained by identifying the ^{214}Po peak for each source location and interpolating between positions. Due to sparseness of available data, we assumed the conversion probability to be uniform in the ϕ direction. It can be seen that the Inner Vessel is fairly uniform in terms of light collection with a maximum variation of $\sim 20\%$ within the innermost 3.5m. This is due to the spherical symmetry of the detector and the large buffer region between the PMTs and the active volume. We can also see that the conversion probability decreases as one moves from the center towards the bottom due to a greater number of non-functional phototubes at the bottom. Though they both show the same general trends there is a slight difference between the two maps in Figure 5.13 which come from the Jan-Feb 2009 and June 2009 calibration campaigns. This indicates that there is some time-dependence in the light collection efficiency that is partly due to the changing number of functional PMT's but also possibly due to the purification and refilling operations performed on the buffer and scintillator that could have changed some of the optical properties. However, as shown in Table 5.6, these differences are negligible within the ^{7}Be analysis fiducial volume.

One can also use the ^{210}Po peak from within the data set to estimate the spatial dependence of the conversion probability (Figure 5.14). In this case, due to the large ^{210}Po contamination levels, we did not have to assume azimuthal symmetry. The advantage of using the ^{210}Po source is that because it is present in the entire data set, it gives us an idea of the time-averaged conversion probability. Comparing
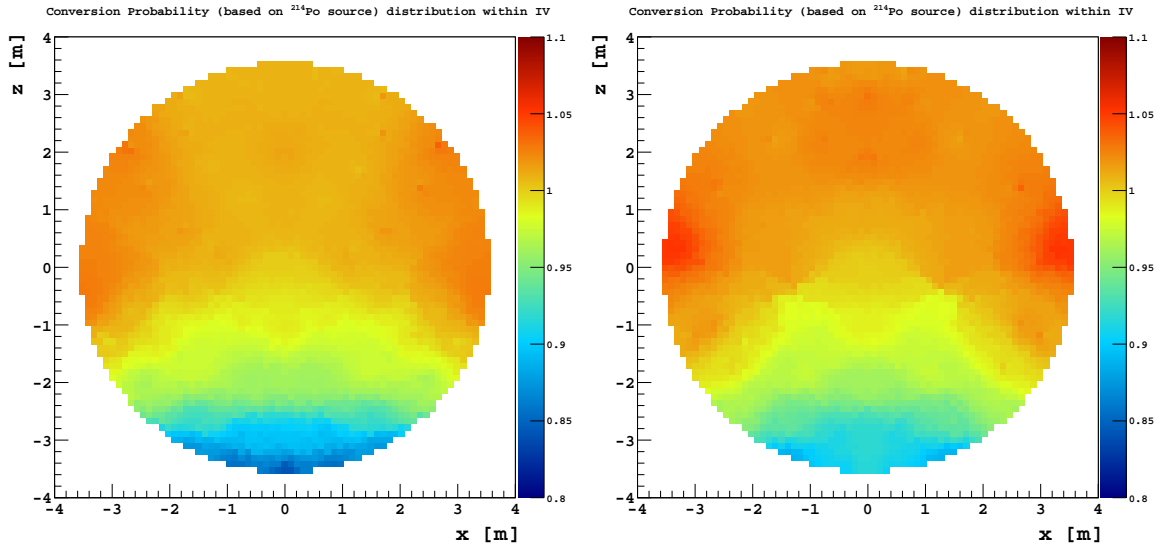
Figure 5.13: Variation of the photon conversion probability within the Inner Vessel, as determined from the ^{214}Po peak position in source calibration data. Values between source positions are determined using an inverse-distance weighted interpolation assuming azimuthal symmetry. Left:Jan-Feb 2009 calibration campaign (Runs 9458 - 9615). Right: June 2009 calibration campaign (Runs 10301 - 10391).

Figures 5.13 to 5.14 one finds that the ^{210}Po indicates a larger decrease of light collection at the top than the ^{214}Po source. In Figure 5.15 we compare the values of the conversion probability along the z-axis for the ^{214}Po sources and ^{210}Po. In this comparison we also include data from ^{214}Po decays occurring after the water extraction in 2010, tagged through the ^{214}Bi-Po coincidence. One can see that the trend for ^{214}Po, from both the source and regular data is consistent, while ^{210}Po shows a relatively large decrease in the conversion probability at the top. The reason for this discrepancy needs further investigation, but is thought to be related to the filling of pure PC (without the wavelength shifter, PPO) from the top of the inner vessel in March 2010. Within the ^{7}Be fiducial volume however, these differences are small (see Table 5.6).

Using this same information, we can estimate the first three central moments of the conversion probability spatial distribution. Table 5.6 lists the relevant values for a uniform source distribution based on the conversion probabilities calculated

196
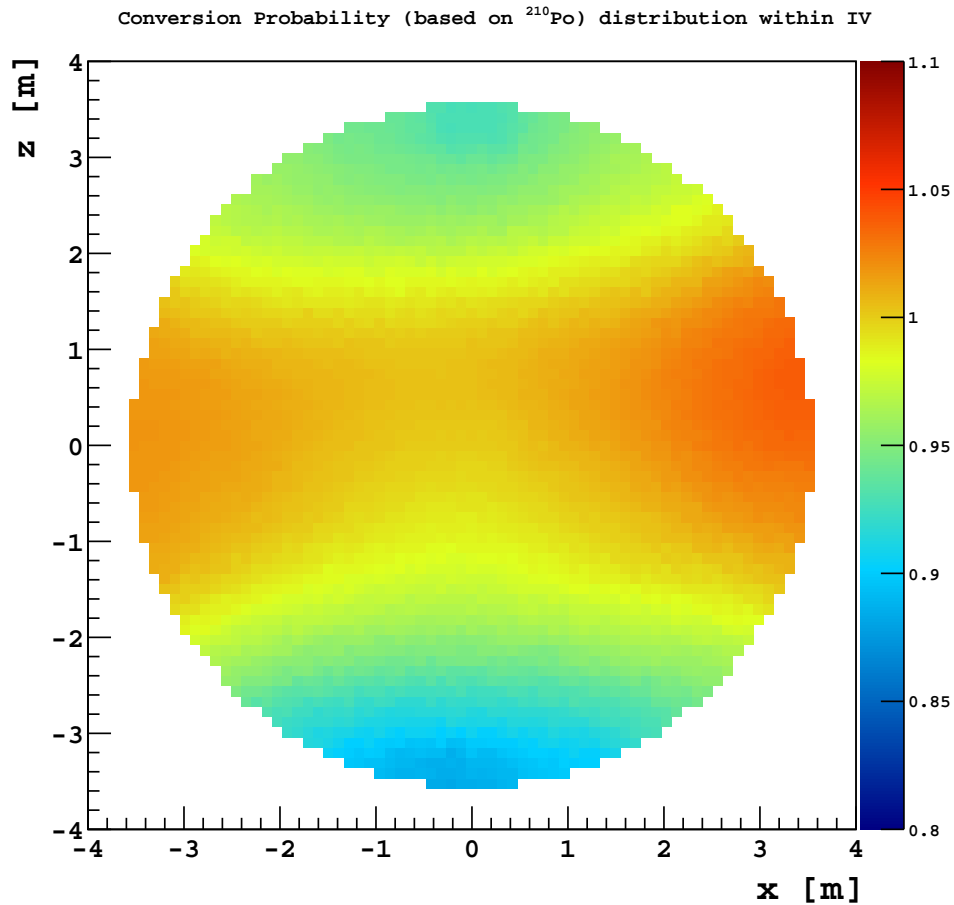
Figure 5.14: Variation of the photon conversion probability within the Inner Vessel, as determined from the ^{210}Po peak position in data.

from the two ^{214}Po source calibrations and the internal ^{210}Po background. We note that these values are only relevant for uniformly distributed sources such as neutrino events and most internal backgrounds (for eg. ^{85}Kr and ^{11}C). For ^{210}Po, whose spatial distribution is non-uniform due to contaminations from scintillator refilling operations, these values vary by about 0.5% [98] over the data-taking period and these effects will be neglected. However for external backgrounds, whose radial profile is roughly exponential, the average conversion probability is significantly higher due to the larger fraction of events near the outer edge of the fiducial volume. It is partly for this reason that the external backgrounds are typically not included in the standard analytical fit. When they are included, different response function parameters are
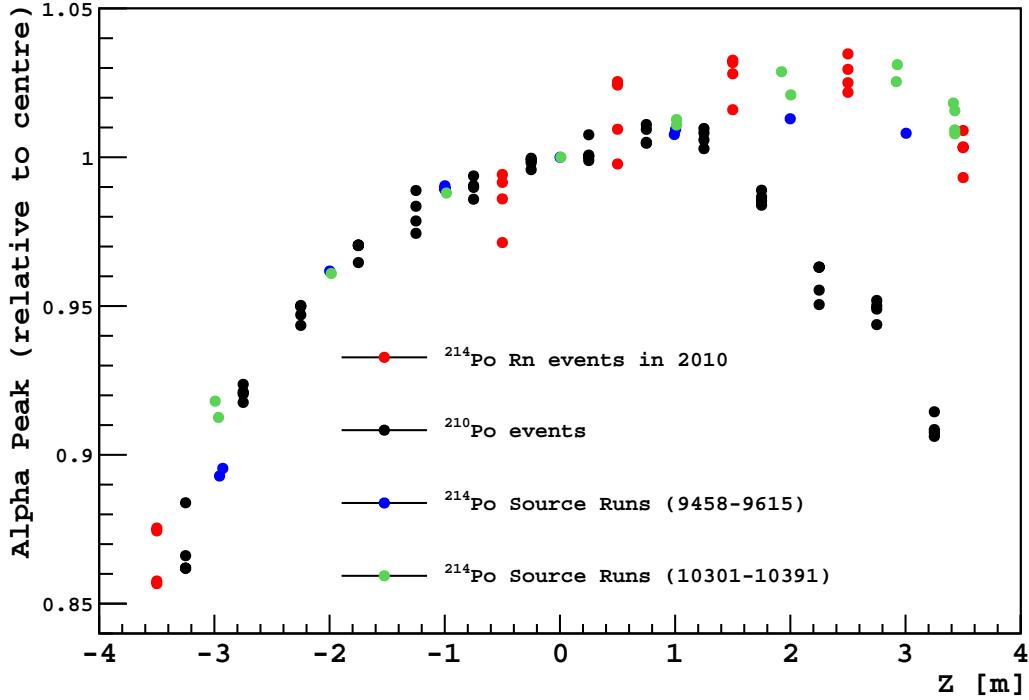
Figure 5.15: Comparison of α peak values at different z positions, relative to the centre, for different α sources. Multiple entries at a given z position indicate the spread in the $x - y$ plane. Values obtained using the ^{214}Po data (both from the source calibration and regular data) are consistent, while the ^{210}Po data indicates a large decrease in the conversion probability towards high z values.

Source	$\langle c' \rangle_{FV}$	$\text{var}(c')_{FV}$	$\kappa(c')_{FV}$
^{214}Po (Runs 9458 - 9615)	1.006	1.82×10^{-4}	-2.26×10^{-6}
^{214}Po (Runs 10301 - 10391)	1.011	2.26×10^{-4}	-2.88×10^{-6}
^{210}Po (Entire Exposure)	1.008	1.68×10^{-4}	-7.46×10^{-7}

Table 5.6: Central moments of the conversion probability for a uniform distribution of events in the Fiducial Volume ($r < 3.021$m, $|z| < 1.67$ m), as calculated from the ^{214}Po source calibration and ^{210}Po data. The values obtained from the ^{214}Po source calibration data use an interpolation between the different source positions and assume azimuthal symmetry.

used, as compared to those for the rest of the backgrounds.

Given the excellent uniformity in light collection within the Fiducial Volume, evidenced by the small values of $\text{var}(c'_{FV})$ in Table 5.6, the higher moments of the conversion probability contribute a small fraction to the overall variance of the response function. For example, at the ^{210}Po energy (~ 210 p.e.), where we are most

Source	$\langle c' \rangle_{FV,T}$	$\mathrm{var}(\langle c' \rangle_{FV})_T$	$\kappa(\langle c' \rangle_{FV})_T$
^{210}Po (Entire Exposure)	$\equiv 1$	1.17×10^{-4}	6.60×10^{-7}

Table 5.7: This table presents the central moments of the conversion probability distribution as a function of time, as calculated from the ^{210}Po peak position depicted in Figure 5.16. The values are only approximate since the data is not weighted by the length of the run and runs with too few events to estimate the ^{210}Po peak are excluded. Due to the limited statistics in each run, there is also some uncertainty in determining the peak.

sensitive to the shape of the response function, assuming a value of $g_1 = 1.25$, the term related to the variance of the conversion probability distribution changes the standard deviation by $\sim 2\%$ (0.3 p.e.). At the high energy limit of the spectral fit (800 p.e.) this number increases to about 7% (2 p.e.).

5.4   Time Averaged Charge Response Function

In the previous sections we have assumed that the photon to photoelectron conversion probability was dependent only on position. However, due to the changing number of working PMTs and various refilling operations, the light collection does in fact vary slightly with time. In Figure 5.16 we plot the position of the ^{210}Po peak for different runs in the data set. Only runs with enough events to accurately determine the ^{210}Po peak position (using a Gaussian fit) were included. From the figure it is clear that there are non-statistical variations in the peak position during different periods. Normalizing to the mean value, we can estimate the central moments of the distribution, in time, of the fiducial-volume-averaged conversion probability (see Table 5.7). Note that these are only approximate values due to the low statistics available in each run and the fact that the data is not weighted for the run length. Using the same method as previously to calculate the central moments of a mixture of distributions, we can calculate the time-averaged mean and variance as:
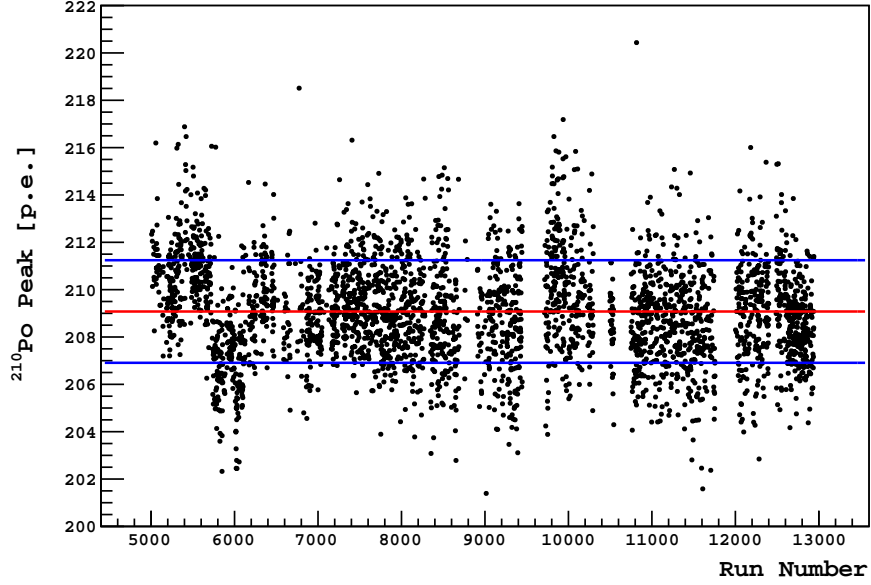
Figure 5.16: Position of ^{210}Po peak for valid runs in the data set. Only runs with enough statistics to determine the location of the ^{210}Po peak (using a Gaussian fit) were included. The red line indicates the mean and the blue line indicates the $\pm 1\sigma$ spread.

$$\text{mean}(P(q_N|E))_T = LY_{scint} \cdot Q_{\text{eff}}(E) \cdot E \cdot \frac{1}{T} \int_T \langle c'(t) \rangle_{FV} \, dt \tag{5.117}$$

$$\equiv LY_{det,T} \cdot Q_{\text{eff}}(E) \cdot E \tag{5.118}$$

$$\equiv \mu_T(E) \tag{5.119}$$

$$\text{var}(P(q_N|E))_T \sim g_1 \cdot \mu_T(E) + g_3 \cdot \mu_T^2(E) \tag{5.120}$$

where $LY_{det,T}$ is the time-averaged lightyield of the detector. For the calculation of the variance we have used the approximation $g_3' \ll 1$ (see Eq. 5.115 and Table 5.6) and have introduced the energy independent term:

$$g_3 \equiv \frac{\text{var}(c')_{FV}}{\langle c' \rangle_{FV}^2} + \frac{\text{var}(\langle c' \rangle_{FV})_T}{\langle c' \rangle_{FV,T}^2} \tag{5.121}$$

200

The third central moment can be reasonably estimated as:

$$\kappa(P(q_N|E))_T \sim g_2 \cdot \mu_T(E) + 3g_1 g_3 \cdot \mu_T^2(E) + g_4 \cdot \mu_T^3(E)$$

$$\text{with } g_4 \equiv \frac{\kappa(c')_{FV}}{\langle c' \rangle_{FV}^3} + \frac{\kappa(\langle c' \rangle_{FV})_T}{\langle c' \rangle_{FV,T}^3} \tag{5.122}$$

5.5 Final Response Function

Combining the model and effects discussed in the previous sections of this chapter, we define the final response function that will be used in the analytical fit of the energy spectrum in the charge variable:

$$P(q_N|E) = \frac{1}{\sqrt{2\pi}\sqrt{a + b \cdot q_N}} \exp\left(-\frac{(q_N - \lambda)^2}{2(a + b \cdot q_N)}\right) \tag{5.123}$$

We obtain the energy dependence of the a, b and λ parameters by matching the moments with the analytical model:

$$b = \frac{g_2 + 3g_1 g_3 \cdot \mu_T(E) + g_4 \cdot \mu_T^2(E)}{3(g_1 + g_3 \cdot \mu_T(E))} \tag{5.124}$$

$$\lambda = \mu_T(E) - b \tag{5.125}$$

$$a = -b^2 + (g_1 - b) \cdot \mu_T(E) + g_3 \cdot \mu_T^2(E) \tag{5.126}$$

where g_i are energy-independent parameters and $\mu_T(E)$ is the time-averaged mean number of photoelectrons produced by a uniformly distributed source of energy E. We can express $\mu_T(E)$ as:

$$\mu_T(E) = LY_{det,\ T} \cdot Q_{\text{eff}}(E) \cdot E \tag{5.127}$$

where $LY_{det,T}$ is the time and fiducial-volume-averaged lightyield of the detector (usually left as a free parameter of the fit) and Q_{eff} is given by Equation 5.98, 5.100,

or 5.105 for electrons, γ-rays and αs respectively.

For events that have simultaneous emissions of different types of particles, we have to add the contribution of each. For example, for a ^{11}C decay that produces a positron with kinetic energy E, the light from the two annihilation γs ($E_\gamma = 0.511$ MeV) are detected simultaneously with the positron scintillation light and so:

$$\mu_T(E) = LY_{det,\ T} \cdot (Q_{\beta\text{eff}}(E) \cdot E\ +\ 2 \cdot Q_{\gamma\text{eff}}(E_\gamma + E_\gamma) \cdot E_\gamma) \tag{5.128}$$

We note that since the relationship between charge and the true number of photoelectrons is not linear, we should first calculate the total number of photoelectrons and then apply the same scaling as in Eq. 5.95, rather than adding up the charge values as given by the equation above. However, we have noticed that due to the small value of the non-linear term b, this makes very little difference in the fit. The effect of the value of b on the fit result is studied in Section 6.8.3.2.

The parameters g_i are related to the energy dependence of the central moments of the response function:

$$\text{mean}(P(q_N|E)) \equiv \mu_T(E) \tag{5.129}$$

$$\text{var}(P(q_N|E)) \sim g_1 \cdot \mu_T(E) + g_3 \cdot \mu_T^2(E) \tag{5.130}$$

$$\kappa(P(q_N|E))_T \sim g_2 \cdot \mu_T(E) + 3g_1g_3 \cdot \mu_T^2(E) + g_4 \cdot \mu_T^3(E) \tag{5.131}$$

The relative energy resolution of the detector is given by:

$$\sqrt{\frac{\text{var}(P(q_N|E))}{\text{mean}^2(P(q_N|E))}} = \sqrt{\frac{g_1}{\mu_T(E)} + g_3} \tag{5.132}$$

$$= \sqrt{\frac{g_1}{LY_{det,\ T} \cdot Q_{\text{eff}}(E) \cdot E} + g_3} \tag{5.133}$$

In the ideal case where we can ignore electronics effects, the parameters g_i can be

Parameter	η	$\overline{v}^{spe}$	$\overline{\kappa}^{spe}$	$\frac{\text{var}(c')_{FV}}{\langle c' \rangle_{FV}^2}$	$\frac{\text{var}(\langle c' \rangle_{FV})_T}{\langle c' \rangle_{FV,T}^2}$	$\frac{\kappa(c')_{FV}}{\langle c' \rangle_{FV}^3}$	$\frac{\kappa(\langle c' \rangle_{FV})_T}{\langle c' \rangle_{FV,T}^3}$
Approx. Value	1.08	0.3	0	2×10^{-4}	1×10^{-4}	-4×10^{-7}	7×10^{-7}

Table 5.8: Approximate values for the physical parameters of the detector related to the energy response function.

obtained from the physical parameters of the detector using:

$$g_1 \sim \quad \eta \cdot (1 + \overline{v}^{spe}) \quad = \quad 1.40 \quad (5.134)$$

$$g_2 \sim \quad \eta^2 \cdot (1 + 3\overline{v}^{spe} + \overline{\kappa}^{spe}) \quad = \quad 2.22 \quad (5.135)$$

$$g_3 \sim \quad \frac{\text{var}(c')_{FV}}{\langle c' \rangle_{FV}^2} + \frac{\text{var}(\langle c' \rangle_{FV})_T}{\langle c' \rangle_{FV,T}^2} \quad = \quad 3 \times 10^{-4} \quad (5.136)$$

$$g_4 \sim \quad \frac{\kappa(c')_{FV}}{\langle c' \rangle_{FV}^3} + \frac{\kappa(\langle c' \rangle_{FV})_T}{\langle c' \rangle_{FV,T}^3} \quad = \quad 3 \times 10^{-7} \quad (5.137)$$

where we have used approximate values of the physical parameters, estimated through both regular and source calibration data, as well as Monte Carlo simulations (summarized in Table 5.8).

The parameters g_1, g_2 and g_3 are usually left free in the fit, while the contribution of g_4 is usually ignored due to computational constraints. Anticipating the results of the spectral fits in Chapter 6, we obtain a value for the overall detector light yield of ~ 502 p.e./MeV and values for the g_i parameters of $g_1 \sim 1.55$, $g_2 \sim 3.07$ and g_3 consistent with zero. The reason these values differ from the estimated values above is most probably due to the non-ideal electronics effects mention in Section 5.1.5.5. Plugging these values into Eq. 5.133 we get a relative detector resolution of:

$$\sqrt{\frac{\text{var}(P(q_N|E))}{\text{mean}^2(P(q_N|E))}} = \frac{0.0556}{\sqrt{Q_{\text{eff}}(E) \cdot E}} \quad (5.138)$$

where E is the energy in units of MeV. At 1 MeV, the relative resolution for electrons is 5.5%.

Chapter 6

^{7}Be Analysis

6.1 Data Selection

The period selected for this analysis extends over nearly three years, from the start of data-taking, 16 May 2007, up until 30th Jan 2010 (991 total days). This interval was divided into 9 sub-periods for purposes of cross-comparisons between the different analysis groups and consistency checks. These sub-periods are listed in Table 6.1 along with the corresponding livetimes. Only runs that fell within the given time periods and passed the standard validation checks were included in the analysis. During the establishment of the standard cuts (detailed in Section 6.2), a few more problematic runs (listed in Table 6.2) were identified and excluded from the data set. The final data set contains 3568 runs, with a total livetime of 689.35 days before any selection cuts.

We note that for the analysis presented in [86] an additional 68.5 days of livetime was included after period 7. This period was excluded for the current analysis, due to electronics instabilities, discussed in more detail in Section 6.8.1.1.

Period	Start Week	End Week	Run Start	Run End	Livetime (days)
1	13 May 2007	09 Dec 2007	5003	6562	136.718
1a	16 Dec 2007	06 Jan 2008	6578	6897	12.819
2	13 Jan 2008	01 Jun 2008	6898	7937	127.292
3	08 Jun 2008	05 Oct 2008	7938	8791	99.082
4	05 Oct 2008	11 Jan 2009	8910	9451	73.728
5	08 Feb 2009	14 Jun 2009	9713	10297	84.041
5a	28 Jun 2009	12 Jul 2009	10497	10545	9.017
6	26 Jul 2009	25 Oct 2009	10750	11517	74.005
7	01 Nov 2009	24 Jan 2010	11518	12400	72.648
TOTAL	13 May 2007	24 Jan 2010	5003	12400	689.350

Table 6.1: Data set used for ^{7}Be analysis. The data was broken up into 9 different periods for the purpose of comparisons and checks. The livetime listed in the last column is before any analysis cuts.

6.1.1 Annual Variation

Due to the slight eccentricity of the Earth's orbit around the Sun ($\epsilon \sim 0.01671$), the flux of solar neutrinos at the Earth is time dependent:

$$\Phi_E(t) = \frac{R_S^\nu}{4\pi r^2(t)} \tag{6.1}$$

where R_S^ν is the production rate of neutrinos in the Sun, Φ_E is the solar neutrino flux at the Earth, and $r(t)$ is the time-varying Earth-Sun distance. The peak-to-peak annual variation, defined to be the ratio of the flux at perihelion to aphelion, is given by:

$$\frac{\Phi_E(t_{per})}{\Phi_E(t_{aph})} = \frac{r^2(t_{aph})}{r^2(t_{per})} = \left(\frac{1+\epsilon}{1-\epsilon}\right)^2 \sim 1.069 \tag{6.2}$$

Since our data-taking period is not uniformly distributed throughout the year, we must take into account these variations in order to calculate the average annual flux of solar neutrinos.

We know from Kepler's Second Law (or equivalently, conservation of angular mo-

Run	Reason for Exclusion
5003, 6578, 6692 - 6704, 6825, 6826	Low rate ($< 10\sigma$ below average) of events passing standard cuts
5744, 7835	High rate ($> 10\sigma$ above average) of events passing standard cuts
7584, 9721, 9722, 9734, 12575	MOE file missing
5433, 5435, 5437, 5439, 5445, 6562, 8694 - 8723, 8812, 8856, 8858, 8869, 11656, 12779, 12901	High muon-tagging rate ($> 10\sigma$ above average)
5743, 7702, 7708, 10068, 10134, 10996, 11000, 11002, 11005, 11023, 11025, 12614, 12667	Bug in MOE live channels readout

Table 6.2: List of excluded validated runs

mentum) that the Earth sweeps out equal areas in equal times, *i.e.,*

$$r^2\dot{\theta} = \text{constant} \equiv h \tag{6.3}$$

where θ is the azimuthal angle within the orbital plane and h is the specific relative angular momentum. The mean flux of solar neutrinos over any data-taking period $[t_0, t_0 + \Delta t]$ is then

$$\frac{1}{\Delta t} \int_{t_0}^{t_0+\Delta t} \Phi_E(t) dt = \frac{R_S^\nu}{4\pi\Delta t} \int_{t_0}^{t_0+\Delta t} \frac{1}{r^2(t)} dt \tag{6.4}$$

$$= \frac{R_S^\nu}{4\pi h \Delta t} \int_{t_0}^{t_0+\Delta t} \dot{\theta} dt \tag{6.5}$$

$$= \frac{R_S^\nu}{4\pi h \Delta t} (\theta(t_0 + \Delta t) - \theta(t_0)) \tag{6.6}$$

For one complete orbit, we have:

$$\langle \Phi_E(t) \rangle_{yr} \equiv \int_{t_0}^{t_0+1} \Phi_E(t) dt = \frac{R_S^\nu}{2h} \tag{6.7}$$

where $\langle\rangle_{yr}$ indicates the time-average over an entire year and time t is measured in units of years. To relate the yearly-averaged solar neutrino flux (Eq. 6.7) to the average measured flux over the data period (Eq. 6.6) one therefore needs to know the angular position of the Earth as a function of time, $\theta(t)$:

$$\langle\Phi_E(t)\rangle_T \equiv \langle\Phi_E(t)\rangle_{yr} \cdot \frac{\theta(t_0 + \Delta t) - \theta(t_0)}{2\pi\Delta t} \tag{6.8}$$

where $\langle\rangle_T$ indicates the time-average over the data taking period $[t_0, t_0 + \Delta t]$. Unfortunately the equation relating the polar coordinates of an orbiting body (r, θ) to the time elapsed from a given initial point (known as Kepler's Equation) is transcendental and cannot be solved algebraically.
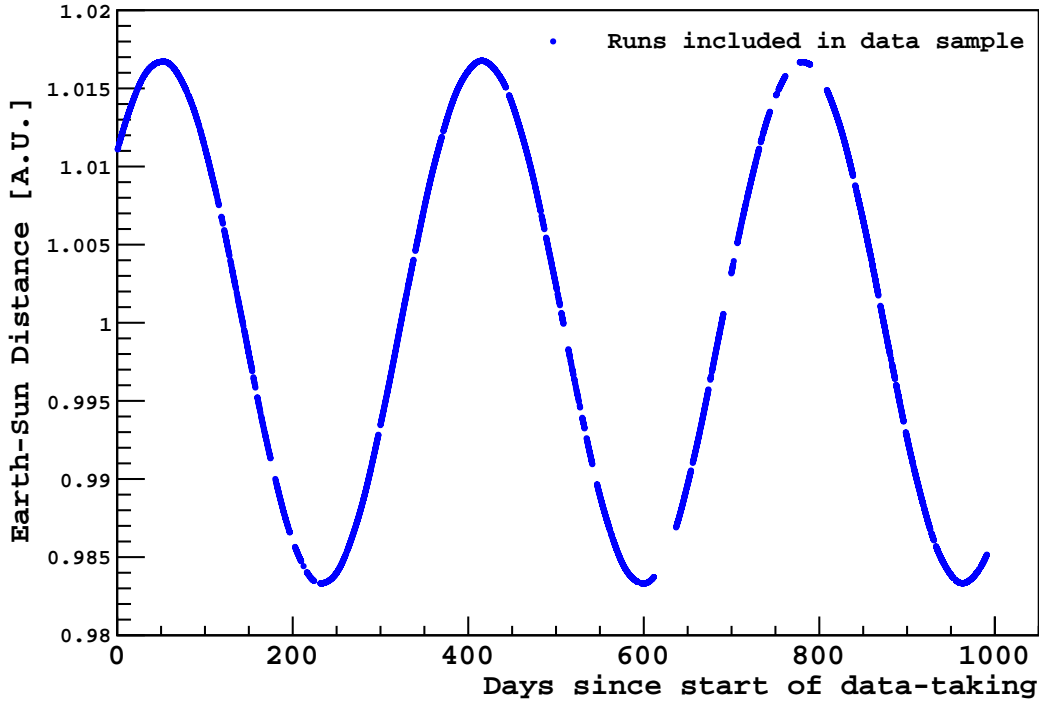
Figure 6.1: Distance between the Earth and Sun [101] at the midpoint of each run in the data set as a function of time since the start of data-taking. Table 6.3 lists the causes of the observed interruptions in the runs.

In order to estimate the effect of the annual variation, we calculated the length and

mid-point, in time, of each run in the data set. Using data available from the NASA Jet Propulsion Laboratory HORIZONS Web-Interface [101], we also obtained the Earth-Sun distance at midnight of each day within the data period. The Earth-Sun distance was then estimated at the mid-point of each run, using a linear interpolation in time. Since the change in distance during one day is at most 0.03%, a linear interpolation was considered sufficient. It should be noted that while the NASA database uses UTC time, the Borexino database has chosen Central European Time as its standard. Thus, due to changes in CET for daylight savings, there is a possible 1 hour shift in the distance estimation. This difference (at most 0.0013%) was also considered negligible and left unaccounted. Figure 6.1 shows the Earth-Sun distance versus time for each run in the final data set. The annual variation is clearly visible, along with gaps due to interruptions in data acquisition. A list of major interruptions in the data-taking period is given in Table 6.3.

Cause of Interruption	Start Date	End Date
1st Source Calibration	4th Oct 2008 (Day 507)	10th Oct 2008 (Day 513)
2nd Source Calibration	16th Jan 2009 (Day 611)	6th Feb 2009 (Day 632)
Earthquake	6th Apr 2009 (Day 691)	14th Apr 2009 (Day 699)
3rd Source Calibration	15th Jun 2009 (Day 761)	29th Jun 2009 (Day 775)
4th Source Calibration	13th Jul 2009 (Day 789)	29th July 2009 (Day 805)
New Elec. Firmware	30th Jan 2010 (Day 990)	14th Feb 2010 (Day 1005)

Table 6.3: List of major interruptions, with days since the start of data-taking in parenthesis.

Since we are interested in the average neutrino flux, we can write:

$$\langle \Phi_E \rangle_{yr} \equiv \frac{R_S^\nu}{4\pi \cdot r_0^2} \tag{6.9}$$

$$= \langle \Phi_E \rangle_T \cdot \frac{1}{\left\langle (r_0/r)^2 \right\rangle_T} \tag{6.10}$$

where $r_0 \equiv 1$ astronomical unit (A.U.). Figure 6.2 shows the distribution of the inverse squared of the Earth-Sun distance for each run in the data set, weighted by

the length of the run. The mean value predicts a multiplicative correction of 1/0.9997 = 1.0003 to the measured neutrino flux during the selected data period, in order to obtain an average annual flux.
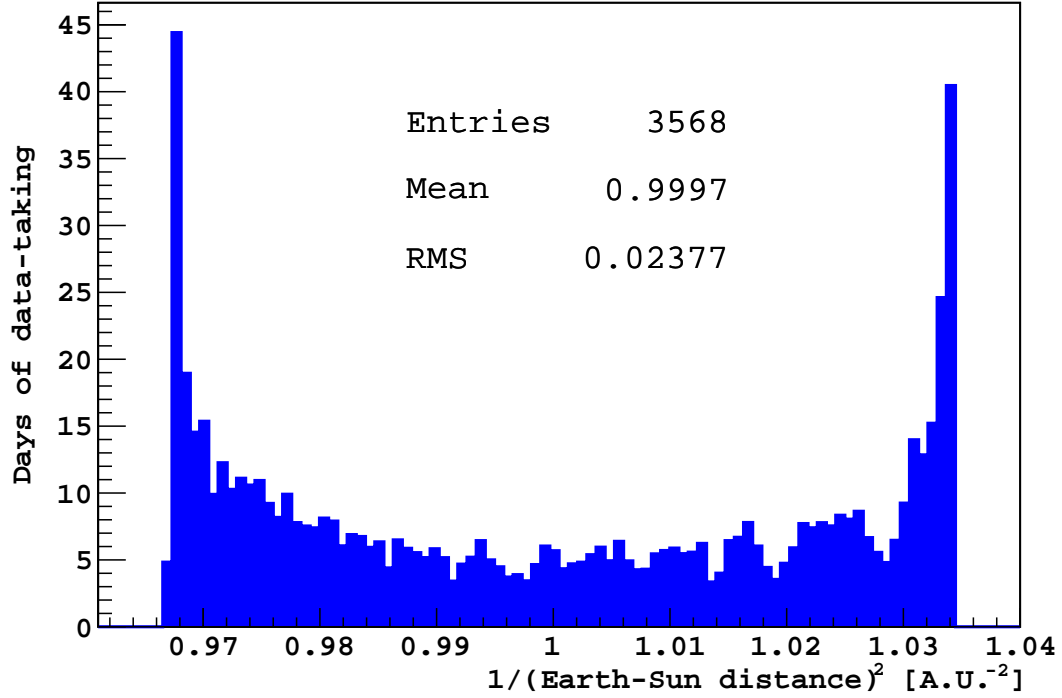
Figure 6.2: Inverse-squared distance between the Earth and Sun [101] at the midpoint of each run in the data set, weighted by the length of the run. The mean value indicates the inverse multiplicative correction factor that needs to be applied to the final ^{7}Be neutrino flux in order to obtain an average annual flux.

6.2 Event Selection

Due to the presence of various backgrounds, we cannot obtain the rate of ^{7}Be neutrinos by simple counting, but we must instead rely on a fit of the energy spectrum. Before performing the fit we first reduce the number of background events (such as radiogenic and cosmogenic events), as well as electronic noise in the spectrum through a sequence of selection cuts. In this section we describe the criteria used to select events used to create the final spectrum to be fit.

6.2.1 DST Creation

During the 689.35 days of livetime used for this analysis, approximately 1.5 billion triggers were recorded. More than 85% of these are low energy (< 75 p.e.) events due to ^{14}C decays. In order to make the data set more manageable, a set of initial cuts are applied to reduce the number of events by removing events in the low energy part of the spectrum that is not used in the spectral fit. These cuts are implemented in three successive steps with special care to keep all categories of events that will be useful later. For example, in order to tag muons we must keep all outer detector triggers as well as inner detector events that pass the muon selection criteria, while to tag ^{214}Bi-Po coincidences we must keep all events occurring in temporal coincidence with another event. The cuts are listed below:

- Cut I

  In order to pass this cut, events must have at least one identified cluster in the trigger gate, or occur in a trigger where the outer detector was triggered.

- Cut II

  Only events that occur in standard inner detector or outer detector or neutron triggers (trigger type = 1 or 2 or 128) are kept.

- Cut III

  In order to pass the final cut, an event must pass at least one of the following conditions:

  - Either a recorded charge of more than 75 p.e., or more than 75 hit PMTs

  - Have more than one identified cluster in the trigger window

  - Be tagged as a muon, or occur less than 300 ms after a muon.

  - Occur within 2 ms of another event

The criteria used to tag muons are listed in Appendix B. The total number of events passing all these cuts is approximately 250 million, and they are stored in separate files, known as DSTs, for the subsequent analysis.

6.2.2 Energy Spectrum Creation

Below, we briefly describe the selection cuts we have applied to remove noise and background events from the spectrum. The exact definitions of the cuts along with the parameter values used are given in Appendix A

1. Muons, Cosmogenics and Post-Muon Noise

   Muons

   We will briefly describe the selection criteria used to identify (and remove) muons within the data set below, referring the reader to a more complete description in [44]. Muons passing through Borexino are identified using both the instrumented outer detector (OD) water tank and the data from the inner detector (ID).

   The outer detector, which detects the Cherenkov light produced by the muons as they traverse the water, has a trigger threshold (MTF) set at 6 PMTs firing within a 150 ns window. Since data from both the inner and outer detector are saved for each trigger, events in the ID that were below the OD trigger threshold can also be tagged as a muon through a second, software-based muon flag (MCF). The MCF uses a lower threshold than the OD trigger by also taking into consideration the spatial information of the OD PMT hits.

   The inner detector flag (IDF) uses the timing profile of the event pulse shape to distinguish point-like interactions in the scintillator (neutrino interactions or radioactive decays) from the extended emission of a through-going muon.

   The parameters used for each flag in this analysis are listed in Appendix B. The combined overall efficiency of all three flags (MTF, MCF and IDF) is estimated

to be $(99.972 - 99.992)\%$ for muons passing through the inner detector [44].

Post-Muon Veto

If a muon is determined to have passed through the inner detector, all events occurring within the next 300 ms are rejected. Muons passing through the scintillator can deposit hundreds of MeV of energy and produce large amounts of light that saturate the inner detector electronics. The saturation of the electronics produces large amounts of noise that follows these muons (see Figure 4.6). It was noticed [102] that trigger gates immediately following a muon (excluding the forced neutron trigger) contain a large amount of noise (~ 2 hits/100 ns). This is due to an issue with the memory buffer, which causes the subsequent trigger to contain many extra hits, even hundreds of milliseconds after the muon. In order to remove these triggers from the data sample, while keeping a fixed veto time for the purposes of livetime estimations, a 300 ms veto was adopted. Given the average trigger rate of 26.2 Hz, a 300 ms veto rejects about 99.96% of noisy, post-muon triggers. The rate of muons passing through the inner detector is ~ 4250/day, which corresponds to about 2 noisy triggers per day passing the post-muon veto. This is a conservative estimate since not all muons passing through the inner detector saturate the electronics. We note that during the early data-taking period (Runs 5003 - 6562, 137 days) the average trigger rate was only 14.6 Hz. This implies a rejection fraction of 98.75% and a leakage rate of 53/day. Luckily more than 95% of the triggers during this period were due to low energy ^{14}C decays that fall below the threshold for the ^{7}Be analysis. For future analysis, it is suggested to use a longer veto during the early periods.

If the muon passes only through the outer detector, then a shorter 2 ms veto is applied. Fast neutrons produced by the muon can pass through the Stainless Steel Sphere, so the 2ms veto is used to reject both the proton recoils from neutron scattering and the capture γs ($\tau_{capture} = 254.5 \pm 1.8$ μs [44]). The pro-

duction rate of cosmogenics within the fiducial volume from these fast neutrons is expected to be negligible.

2. Trigger Types, Empty Triggers and Clustering Consistency

Only regular inner detector triggers are kept. Outer detector, neutron and laser service triggers are removed.

Trigger gates which contain no identified clusters are excluded. These triggers were only kept within the DSTs because they may be associated with a muon passing through the outer detector.

We also remove events which have a different number of clusters identified by the *Mach4* and *Echidna* clustering algorithms which mostly occurs for pileup and noise events.

3. Fast Coincidences and Multiple Clusters

All events that occur within 2 ms and a 1.5 m radius of another event are removed. The main purpose of this cut is to exclude ^{214}Bi-Po coincidences ($\tau_{^{214}\mathrm{Po}} = 236 \ \mu s$) from the data sample. It should be noted that it was found that the large size of the veto radius (1.5 m) used causes a lot of accidental coincidences to be tagged and removed (see Section 6.2.4). Since 98% of ^{214}Bi-Po coincidences have a separation of less than 0.7 m, a 1.0 m radius is more than sufficient and should be adopted for future analyses.

All triggers with more than one identified cluster are also removed.

4. Start time of cluster

If the position of the first cluster in a trigger is not as expected, we discard the event. This cut is mainly to remove laser service triggers with an incorrect trigger type, as they have a different delay with respect to the start of the trigger gate.

5. Exclude Rack noise

In order to remove events caused by noisy electronics racks (see Section 4.7.1), events which have more than 75% of their hits in a single rack are removed.

6. Fiducial Volume Cut

   To exclude backgrounds from external γs (see Section 3.2.11), only events within a radius of 3.021 m were included in the analysis.

   In addition to the radial cut, a further cut was placed along the vertical (z) axis excluding events that had a reconstructed vertical position of $|z| > 1.67$. This cut removes events originating from the end-caps and excludes regions near the bottom of the detector with poor light conversion (see Section 5.3).

   The fiducial region chosen has a volume of 86.0084 m^3, which corresponds to a mass of 75.7046 tons.

7. Geometrical uniformity

   We expect scintillation light to be emitted isotropically and can remove events whose hit patterns indicate a non spherically symmetric emission. This cut is implemented in two independent ways. The first uses the *Mach4* isotropy parameter (described in Section 4.7.2) while the second uses the *Echidna* `sh_power` parameter, which calculates an effective spherical harmonic decomposition of the PMT hit pattern.

8. Pileup Cut

   Events that have more than one peak in the observed hit time profile are removed. This cut is used to reduce the contamination of pileup events in the spectrum.

9. Comparison of charge and hits

   It was noticed early in the data-taking that there was a class of events with very little integrated charge compared to the number of PMT's that recorded hits. While the source of these events is not clear (they are some form of electronics

noise that cause the channels to trigger in the absence of photoelectrons), we eliminate these events by comparing the output of the charge variable to what we would expect given the number of triggered PMTs.

The effect of the selection cuts on the energy spectrum is shown in Figure 6.3, with the largest number of events removed by the muon and fiducial volume cuts.
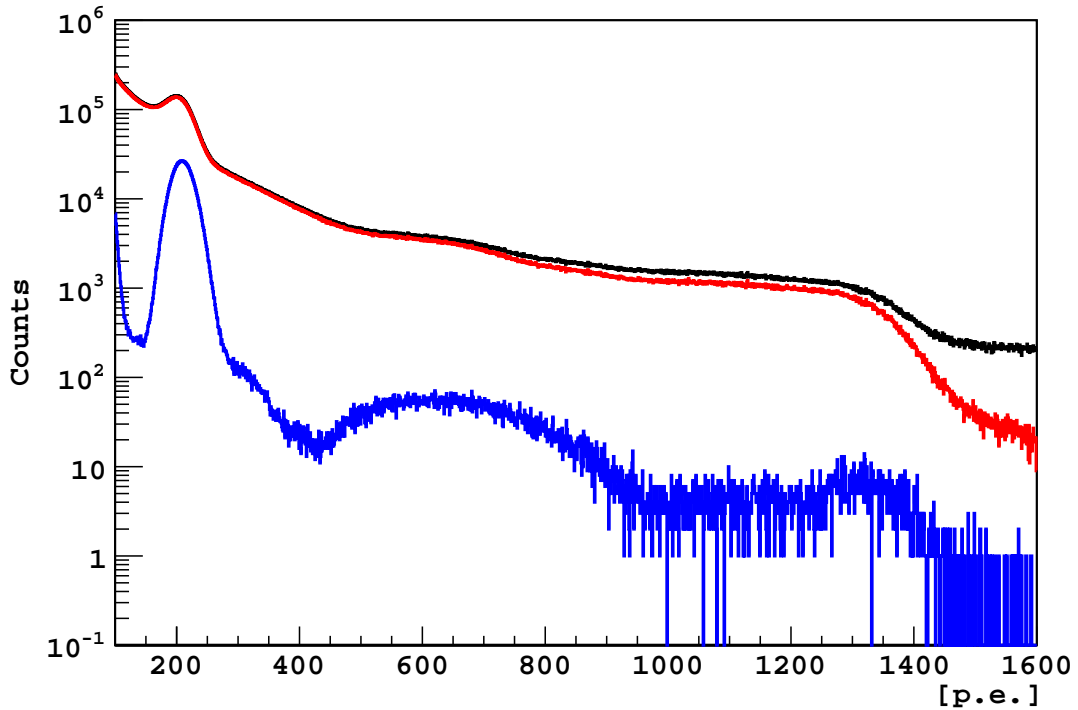
Figure 6.3: Effect of the selection cuts on the energy spectrum. The black histogram shows the original spectrum of all events before any cuts. The y-axis is the number of counts in 1 p.e. bins. The red histogram shows the spectrum after the muon cut, while in blue is the final spectrum after all the cuts. The difference between the red and blue histograms is mostly due to the fiducial volume cut.

6.2.3 Cut Performance

We have studied the performance of the selection cuts by evaluating the sacrifice probability (the probability that a "good" scintillation event is removed by the cuts) using the γ source calibration data, and estimating the residual number of background

events.

6.2.3.1 Cut Sacrifice

Since the energy and position of the γ sources is well known, we can select, with high purity, events that are known to be scintillation events. Using this sample, we can then evaluate what fraction of these "good" events are removed by the selection cuts in the previous section. Table 6.4 shows the overall sacrifice probability for five different γ sources at different energies. Three different source positions were compared to study the radial dependence of the cuts. The 68% confidence interval for the sacrifice probability was calculated using the Agresti-Coull interval as recommended in [103]. As can be seen from the table, the sacrifice probability is mostly independent of position and energy. Taking all the data together, the sacrifice probability is $(4.0 \pm 0.3) \times 10^{-4}$. In order to account for the small energy dependence, we have chosen to use $(4.0 \pm 2.0) \times 10^{-4}$ as our final uncertainty estimate such that the central values for the two sources that overlap the ^{7}Be spectrum, ^{85}Sr (6×10^{-4}) and ^{54}Mn (2×10^{-4}), are covered.

Unfortunately, due to the nature of the source calibration data, it is not possible to evaluate the sacrifice probability for all of the cuts. The cuts that were not included in the evaluation with the source calibration data are listed below:

- Triggering Efficiency

  The activity of the sources was measured using a Germanium counter, but the precision of the measurement was limited to 2%. In order to determine the trigger efficiency with greater precision, a dedicated study was made with the timing laser used to synchronize the PMTs. By pulsing the laser at a known frequency for a given amount of time, the fraction of triggers that were detected was measured. It was found that for a trigger threshold of 25 hits (the default value used for most runs in this analysis), the trigger efficiency is greater than

Isotope	Energy [keV]	(x, y, z) [m]	Fraction of Events Removed	Probability [68% CI] ($\times 10^{-4}$)
^{203}Hg	279	(0,0,0)	28 / 69497	$[3.33 - 4.86]$
		(0,0,3)	11 / 18822	$[4.32 - 7.90]$
		(0,0,-3)	9 / 17145	$[3.75 - 7.32]$
^{85}Sr	514	(0,0,0)	7 / 23778	$[2.01 - 4.30]$
		(0,0,3)	9 / 8366	$[7.69 - 15.01]$
		(0,0,-3)	9 / 8023	$[8.02 - 15.65]$
^{54}Mn	834	(0,0,0)	17 / 103193	$[1.29 - 2.10]$
		(0,0,3)	5 / 32959	$[0.96 - 2.37]$
		(0,0,-3)	14 / 35792	$[2.99 - 5.11]$
^{65}Zn	1115	(0,0,0)	5 / 13197	$[2.40 - 5.93]$
		(0,0,3)	1 / 4736	$[0.59 - 5.72]$
		(0,0,-3)	9 / 4805	$[13.38 - 26.13]$
^{40}K	1460	(0,0,0)	14 / 74107	$[1.45 - 2.47]$
		(0,0,3)	9 / 23542	$[2.73 - 5.33]$
		(0,0,-3)	40 / 25920	$[13.18 - 18.06]$
TOTAL			187 / 463882	$[3.75 - 4.34]$

Table 6.4: The fraction of γ–source events thrown away by the selection cuts. The second column lists the energy of the γ ray and the third column gives the source position within the detector. The 68% confidence interval (last column) is calculated using the Agresti-Coull method [103].

99.9% above 55 hits (the standard starting point for the spectral fit is ~ 145 hits). Further details can be found in [104].

- Fast Coincidences

  Since the source has a high rate and is localized in space, it is not possible to evaluate the sacrifice of these cuts using the calibration data. The sacrifice of these cuts are estimated as part of the livetime systematics in Section 6.2.4.

- Fiducial Volume Cut

  The systematics related to determining the true size of the fiducial volume was part of a dedicated study that is summarized in Section 4.3.1.1.

6.2.3.2 Residual Muons and Cosmogenics

While the muon selection criteria described in 6.2.2 have a very good overall efficiency for muons passing through the inner detector (between 99.972% and 99.992%), the tagging efficiency for muons that produce 110 - 500 hits (roughly the energy range for the ^{7}Be analysis) is only in the range of $99.5\% - 99.8\%$ [44]. The fraction of the total number of muons that deposit energy in the 110 - 500 hits range is $\sim 2.4\%$, which given a total muon rate of ~ 4250/day, implies that there are approximately 0.2 - 0.5 c/day of untagged muons in the ^{7}Be fit range. However, because muons do not have the point-like scintillation characteristics of regular events, some fraction of untagged muons are removed from the spectrum due to other cuts. Over the entire exposure of 689 days ($\sim 3 \times 10^6$ muons), only 641 events that were tagged by the outer detector (OD), were not also removed by the other selection cuts. Assuming that the OD is independent of the other selection cuts (which only use data from the inner detector), we obtain an efficiency of 99.98% for the selection cuts, relative to the OD. Combining this with the muon rejection efficiency of the OD ($\sim 99\%$), we estimate that the total muon rejection inefficiency is 2×10^{-6}, corresponding to ~ 6

muons in the final spectrum. If we conservatively assume that all residual muons will be fitted as ^{7}Be neutrinos (very unlikely given the different shapes of the spectrum) we obtain an uncertainty of ~ 0.01 cpd/100 tons.

Part of the purpose of the $T_V = 300$ ms veto after every tagged muon is to reduce the contribution of short-lived cosmogenic isotopes. However, if a muon is untagged, (even if the muon itself is later removed by another selection cut) then no veto is applied and the decay of the cosmogenic isotope may be included in the spectrum. For the sake of simplicity, we will assume that untagged muons have the same impact parameter and energy distribution as tagged muons. Given a muon tagging efficiency of $\epsilon = 0.99982$, the residual rate R_{res} of a cosmogenic isotope, after the muon veto, is then given by:

$$R_{res} = \left(\epsilon \cdot \exp\left(-\frac{T_V}{\tau} \right) + 1 - \epsilon \right) \cdot R \tag{6.11}$$

where R is the production rate of the isotope and τ is the mean life.

For the known cosmogenic isotopes produced in organic scintillators, we have estimated the production rates from [77] when available, or otherwise calculated them directly from the results of the KamLAND Collaboration [71] using the data if present or otherwise the given FLUKA calculations. Table 6.5 lists the cosmogenic isotopes and their residual rates. We note that because of the presence of the fast coincidences cut, cosmogenic isotopes that have neutrons as one of their decay products (^{8}He and ^{9}Li) will be further reduced due to the coincidence with the neutron capture γ.

6.2.4 Livetime Corrections and Systematics

The livetime for each run is calculated by taking the difference in time between the first and last valid trigger. The time of each trigger is obtained from a GPS clock and care is taken to avoid problems with changes due to daylight savings. The total

Isotope	Mean Life	Energy [MeV]	Production Rate [cpd/100 tons]	Residual Rate [cpd/100 tons]
^{12}N	15.9 ms	17.3 (β^+)	0.058 ± 0.013	$(1.04 \pm 0.23) \times 10^{-5}$
^{12}B	29.1 ms	13.4 (β^-)	1.41 ± 0.04	$(3.00 \pm 0.09) \times 10^{-4}$
^{8}He	171.7 ms	10.7 $(\beta^- \gamma n)$	0.026 ± 0.012	$(4.5 \pm 2.1) \times 10^{-3}$ [†]
^{9}C	182.5 ms	16.5 (β^+)	0.096 ± 0.031	0.019 ± 0.006
^{9}Li	257.2 ms	13.6 $(\beta^- \gamma n)$	0.071 ± 0.005	0.022 ± 0.002 [†]
^{8}B	1.11 s	18.0 $(\beta^+ \alpha)$	0.273 ± 0.062	0.21 ± 0.05
^{6}He	1.16 s	3.51 (β^-)	0.395 ± 0.027	0.31 ± 0.02
^{8}Li	1.21 s	16.0 $(\beta^- \alpha)$	0.40 ± 0.07	0.31 ± 0.05
^{11}Be	19.9 s	11.5 (β^-)	0.035 ± 0.006	0.034 ± 0.006
^{10}C	27.8 s	3.65 $(\beta^+ \gamma)$	0.54 ± 0.04	0.53 ± 0.04
^{11}C	29.4 min	1.98 (β^+)	27.65 ± 4.45	27.6 ± 4.5
^{7}Be	76.9 days	0.478 $(EC\ \gamma)$	3.35 ± 0.22	0.35 ± 0.02 [††]

Table 6.5: Cosmogenic isotopes in Borexino. Production rates are obtained from [77] when available, otherwise calculated directly from [71] using data if present or otherwise FLUKA calculations. Residual rates are estimated based on the muon tagging efficiency and post-muon veto (see Eq. 6.11). [†]Residual rate is further reduced by fast coincidence cut. [††]Residual rate includes 10.5% branching ratio for γ.

livetime of the data taking period before any event selection cuts is 689.35 days. The uncertainty of the GPS clock compared to the total length of the data taking period is negligible. There are however other sources of systematics related to the evaluation of the livetime such as the trigger dead time and the DAQ software feature known as the "6:25 am Bug". In addition to this, a few of the cuts involve vetoing sections of the detector for varying periods of time, which reduces the effective livetime of the detector. The uncertainty associated with each of these features is discussed below. Relevant numbers required for the estimation of these uncertainties are summarized in Table 6.6.

Runs	Livetime [days]	Trigger Gate [μs]	Dead Time [μs]	# of Triggers	Avg. Rate [Hz]
5003 - 6562	136.72	6.9	6.1	172,356,911	14.59
6578 - 12400	552.63	16.5	2.5	1,387,014,886	29.05
5003 - 12400	689.35			1,559,371,797	26.18

Table 6.6: Details of Trigger Gate

6.2.4.1 Cosmogenic Veto

Following each event identified as a muon, all events within 300 ms are rejected. This 300 ms veto of the entire detector results in a significant dead time and is estimated based on the number of muon vetos (overlapping vetos are also accounted for). The loss in livetime is 11.25 ± 0.36 days ($1.63 \pm 0.05\%$). The uncertainty arises from the different estimations of the various analysis groups.

6.2.4.2 Trigger Dead Time

Following each hardware trigger, the detector is dead for a certain period of time as the DAQ system resets itself. The length of this dead period was changed during the exposure, from 6.1 μs to 2.5 μs (see Table 6.6) . In order to calculate the dead time due to this effect we simply multiply the number of triggers by the corresponding trigger dead time. This gives a dead time of 0.052 days. Since a fraction of these triggers are already excluded by the above mentioned cosmogenic veto we scale this number down by 1.63% to obtain a dead time of 0.052 days. The uncertainty in the length of the trigger dead time is approximately ±100ns which gives a systematic uncertainty of 0.002 days.

6.2.4.3 6:25 am bug

During the early periods it was found that the data acquisition system (DAQ) would regularly crash at 6:25 am each day. Many possible causes were investigated but the origin of the problem could not be identified. As a temporary work-around, the DAQ was temporarily paused just before 6:25 am and restarted approximately 40 seconds later. By studying the time difference between consecutive events (with an average trigger rate of 26.2Hz we expect a trigger every 38 ms) we have found that the 40 second delay occurs about 403 times in our data set. This amounts to a total dead time of 0.187 days with an uncertainty of 0.005 days. The cause of the DAQ crashes

has recently been identified as being due to the running of automated scripts at 6:25 each morning.

6.2.4.4 Trigger-less Dead Time

During the period between runs 5515 and 7620 there were 17 runs containing multiple periods during which no triggers were recorded for approximately 2 seconds. Since this is statistically very unlikely ($< 1 \times 10^{-23}$), this is probably caused by the DAQ system temporarily freezing. The sum of these trigger-less periods corresponds to a total dead time of 0.02 days. Since the cause of these freezes is currently unknown, it is difficult to estimate the uncertainty. We conservatively estimate the uncertainty as ± 0.02 days.

6.2.4.5 Fast Coincidence Cut

All events that fall within $T = 2$ms and 1.5m of another event are removed from the spectrum. We need to estimate the rate of good events lost to this cut due to accidental coincidences. The trigger rate within the entire Inner Vessel is ~ 26.2Hz. As a simple first approximation, if we assume that this rate is uniform within the entire Inner Vessel then the rate of events within any sphere of 1.5m radius is $\lambda \sim 26.2 \cdot (\frac{1.5}{4.25})^3 = 26.2 \cdot 0.04396 = 1.152$ Hz. Using this value we would then estimate the fractional dead time due to this cut is $(1 - e^{-2\lambda T}) = 0.460\%$. There are two caveats to this estimation. Firstly, events within the Inner Vessel are non-uniformly reconstructed, with ^{14}C events reconstructing slightly inwards and external γs having a much higher rate near the nylon vessel. Secondly, there is a small geometric correction needed to account for the fact that there are points within the Fiducial Volume that are less than 1.5m from the edge of the nylon vessel. In order to account for these effects, a simple Monte Carlo was written to estimate the average fraction of IV events contained in a 1.5m sphere centered on a random point within the Fiducial

Volume (we are only concerned about losing events that lie within the Fiducial Volume). In the Monte Carlo, we used different radial distributions of events obtained from 4 different periods of data-taking (Runs: 5550 - 5560, 7600 - 7609, 9210 - 9219, 11400 - 11409) as estimated by *Mach4*. The final value obtained from the Monte Carlo, taking the average and standard deviation over the 4 different periods, was 0.0452 ± 0.0006, to be compared with the 0.04396 from the first approximation above. Thus the fractional dead time due to this cut is $(1 - e^{-2\lambda T}) = 0.473 \pm 0.006\%$ where $\lambda = 26.2 \cdot 0.0452$. We note that from the data itself, the fraction of events within the Fiducial Volume that are removed by this cut is 0.53% of which $\sim 0.07\%$ should be ^{214}Bi-Po coincidences, roughly consistent with the MC estimation. Evaluating this as a fraction of the livetime after the above corrections (677.84 days) we get a dead time of 3.20 days with an uncertainty of ~ 0.04 days.

6.2.4.6 Multi-Cluster Cut

If a trigger gate includes more than one cluster, all of the clusters in that gate are discarded. As before, we need to estimate the rate of good events lost to this cut due to accidental coincidences. Any given cluster can only make it into the final spectrum if there are no other clusters within the same trigger gate. To begin with, we will only consider "other" clusters above the trigger threshold. If the rate of clusters above trigger threshold is λ, then the probability that there is no other cluster within $\pm T$ of the original cluster is simply $e^{-2\lambda T}$. If we neglect the short pre-trigger time of the gate (the trigger normally falls in the first 1.2 μs of the gate), then for T equal to the trigger gate length, this is also the probability of not having any other cluster in the same trigger gate. Given that we have two different trigger gate lengths and trigger rates during our data sample, we can write the probability for the original cluster to

pass this cut as

$$P_{above\ thresh} = \frac{L_1}{L}e^{-2\lambda_1 T_1} + \frac{L_2}{L}e^{-2\lambda_2 T_2} \tag{6.12}$$

$$= 1 - 8.08 \times 10^{-4} \tag{6.13}$$

where L_i, λ_i and T_i are the livetime, average rate and trigger gate length during each of the two periods listed in Table 6.6.

We must also consider events that are below the trigger threshold but above the clustering threshold. These events can not open a trigger gate by themselves, but once the gate is open can form a cluster, causing the original event to be discarded. By studying the rate of clustered events in random trigger gates we estimate that the rate of events below the trigger threshold but above the clustering threshold is $\lambda_C \sim 48 \pm 1$ Hz. If the trigger gate length is T, then the probability that there is no other event within $+T$ of the original event is simply $e^{-\lambda_C T}$. So we have:

$$P_{below\ thresh} = \frac{L_1}{L}e^{-\lambda_C T_1} + \frac{L_2}{L}e^{-\lambda_C T_2} \tag{6.14}$$

$$= 1 - 7.00 \times 10^{-4} \tag{6.15}$$

Combining the two probabilities, we find that the probability for an event to fail the multi-cluster cut is $1 - P_{above\ thresh} \cdot P_{below\ thresh} = 0.151\%$. Evaluating this as a fraction of the livetime after all the above corrections (674.64 days) we get a dead time of 1.02 days with an uncertainty of ~ 0.01 days.

6.2.4.7 Final Livetime

The livetime corrections and uncertainties are summarized in Table 6.7. The final value for the livetime of the data-set used for the ^{7}Be analysis is 673.62 ± 0.36 days.

Source	Correction [days]	Systematic Uncertainty (% of final livetime)
Livetime before cuts	689.35	-
Cosmogenic Veto	-11.25 ± 0.36	0.053
Trigger Dead Time	-0.052 ± 0.002	$< 3 \times 10^{-4}$
6:25 am Bug	-0.187 ± 0.005	$< 8 \times 10^{-4}$
Trigger-less Dead Time	-0.02 ± 0.02	0.003
Fast Coincidence Cut	-3.20 ± 0.04	0.006
Multi-Cluster Cut	-1.02 ± 0.01	0.001
TOTAL	673.62 ± 0.36	0.054

Table 6.7: Summary of livetime corrections. The first row lists the total livetime of the data set before any cuts.

6.3   Radon Tagging

In this section we estimate the rate of radioactive backgrounds in the heavy element decay chains (Section 3.2.6) through the tagging of delayed coincidences. While the events in the coincidences can be individually tagged and removed, the rate of the other decays is large enough to have a significant effect on the fit results but too small for the rate or energy to be determined by the fit itself. Therefore, to include these events in the fit, we must independently determine their rate and energy in photoelectrons. In the following section we will determine the rates while their energies were calculated in Section 5.2.4.

6.3.1 ^{222}Rn

The ^{222}Rn decay chain (shown in Figure 3.9) includes the ^{222}Rn and ^{218}Po α emissions, followed by the ^{214}Pb β decay, the ^{214}Bi-Po $\beta - \alpha$ coincidence and finally ^{210}Pb which has a 22 year half-life.

6.3.1.1 ^{214}Bi-Po Coincidence

We will assume that the decay rates of all the ^{222}Rn daughters, up until ^{210}Pb, are in secular equilibrium. The decay rate can be easily determined by searching for the

^{214}Bi-Po coincidence. The short mean-life of ^{214}Po, combined with the fact that the energy of ^{214}Po is above the dominant ^{210}Po α energy, allows us to obtain a very clean sample of ^{214}Bi-Po candidates. The cuts used to tag the candidates are given below:

- Not tagged as a muon

- Single-cluster trigger

- 200 p.e. $< {}^{214}$Po charge < 500 p.e.

- 90 p.e. $< {}^{214}$Bi charge < 1800 p.e.

- 20 μs $< \Delta$t < 1.888 ms

- Δs < 1m

The efficiency of the above cuts for tagging the ^{214}Bi-Po coincidence events is estimated to be 0.89. The largest factor in the 11% inefficiency is the minimum Δt cut at 20 μs. The lower limit is set to avoid complications due to the electronics dead time following each trigger. This single cut corresponds to an inefficiency of 8%.

Using the selection cuts, 735 coincidence candidates were identified within the data set (673.6 days, 75.70 tons). This corresponds to an average coincidence rate, including the inefficiency in the selection cuts, of 1.62 ± 0.06 cpd/100 tons. Since we are assuming secular equilibrium, this is also the average decay rate of the isotopes from ^{222}Rn to ^{214}Pb.

As mentioned in Section 3.2.6.1, the distribution of ^{214}Bi-Po coincidences in time indicates that a large fraction of the decays come from a contamination of the scintillator with ^{222}Rn in the air during periodic detector operations and not from an intrinsic ^{238}U contamination. By studying the rate of ^{214}Bi-Po coincidences far from any detector procedures, the equilibrium rate was found to be 0.57 ± 0.05 cpd/100 tons [73]. The corresponding contamination for ^{238}U in the scintillator is $(5.3 \pm 0.5) \times 10^{-18}$

g/g. The level of ^{238}U contamination, as determined from the spectral fits, is further discussed in Section 6.7.

We note that among the standard cuts for the ^{7}Be analysis is a cut to remove all pairs of events that occur within 2 ms and 1.5 m of each other, regardless of their energy. Since 2 ms is more than eight times the ^{214}Po mean-life and $\sim 98\%$ of ^{214}Bi-Po coincidences have a separation below 0.7 m, the number of ^{214}Bi and ^{214}Po events remaining in the spectrum is negligible.

6.3.2 ^{220}Rn

The ^{220}Rn decay chain (shown in Figure 3.13) includes the ^{222}Rn and ^{216}Po α emissions, followed by the ^{212}Pb β decay, the ^{212}Bi-Po $\beta - \alpha$ coincidence and finally ^{208}Pb which is stable. ^{212}Bi also has an α emitting branch (Branching Ratio: 36%) to ^{208}Tl which is one of the largest contributors to the external background rate due to the production of a 2.6 MeV γ ray.

6.3.2.1 ^{212}Bi-Po Coincidence

Due to their short half-lives, we will assume that the decay rates of all the ^{220}Rn daughters are in secular equilibrium. There are multiple short lived isotopes in the chain that allow for coincidence tagging, such as ^{220}Rn ($\tau_{1/2} = 56$ s), ^{206}Po ($\tau_{1/2} = 145$ ms) and ^{208}Tl ($\tau_{1/2} = 3.1$ min). However the extremely short mean-life of ^{212}Po ($\tau_{1/2} = 299$ ns), combined with the high energy of the α decay, makes it easiest to identify ^{212}Bi-Po candidates. We will therefore only discuss tagging with ^{212}Bi-Po, though preliminary studies of the other coincidences yield similar results. The cuts used to tag the candidates are given below:

- Not tagged as a muon

- Single-cluster trigger

- 450 p.e. $< ^{212}$Po charge < 650 p.e.

- 0 p.e. $< ^{212}$Bi charge < 1200 p.e.

- 400 ns $< \Delta$t < 1732 ns

- Δs < 1m

The efficiency of the above cuts for tagging the ^{212}Bi coincidence events is estimated to be 0.34. The largest factor in the 66% inefficiency is the minimum Δt cut at 400 ns. The lower limit is set to ensure that the inefficiency of the clustering algorithm to separate two events is minimal (see Section 4.2.1). This single cut corresponds to an inefficiency of 60%.

In order to estimate the equilibrium contamination rate within the scintillator (for determining the efficacy of the purification techniques), only events occurring far from any detector operations (611 days of livetime) and within a 3.3 m sphere (132.5 tons) were included. The average coincidence rate, including the inefficiency in the selection cuts, was found to be 0.13 ± 0.03 cpd/100 tons [73]. If we assume secular equilibrium, this is also the average decay rate of the isotopes from ^{228}Th to ^{208}Pb. The corresponding contamination for ^{232}Th in the scintillator is $(3.8 \pm 0.8) \times 10^{-18}$ g/g. The level of ^{232}Th contamination, as determined from the spectral fits, is further discussed in Section 6.7.

As with the ^{214}Bi-Po coincidences, the cut to remove all pairs of events that occur within 2 ms and 1.5 m of each other, regardless of their energy ensures that the number of ^{212}Bi and ^{212}Po events remaining in the spectrum is negligible.

6.4 Alpha/Beta Statistical Subtraction

The top plot in Figure 6.4 shows the energy spectrum after all the standard event selection cuts are applied. As can be seen, the ^{210}Po α peak is more than two orders
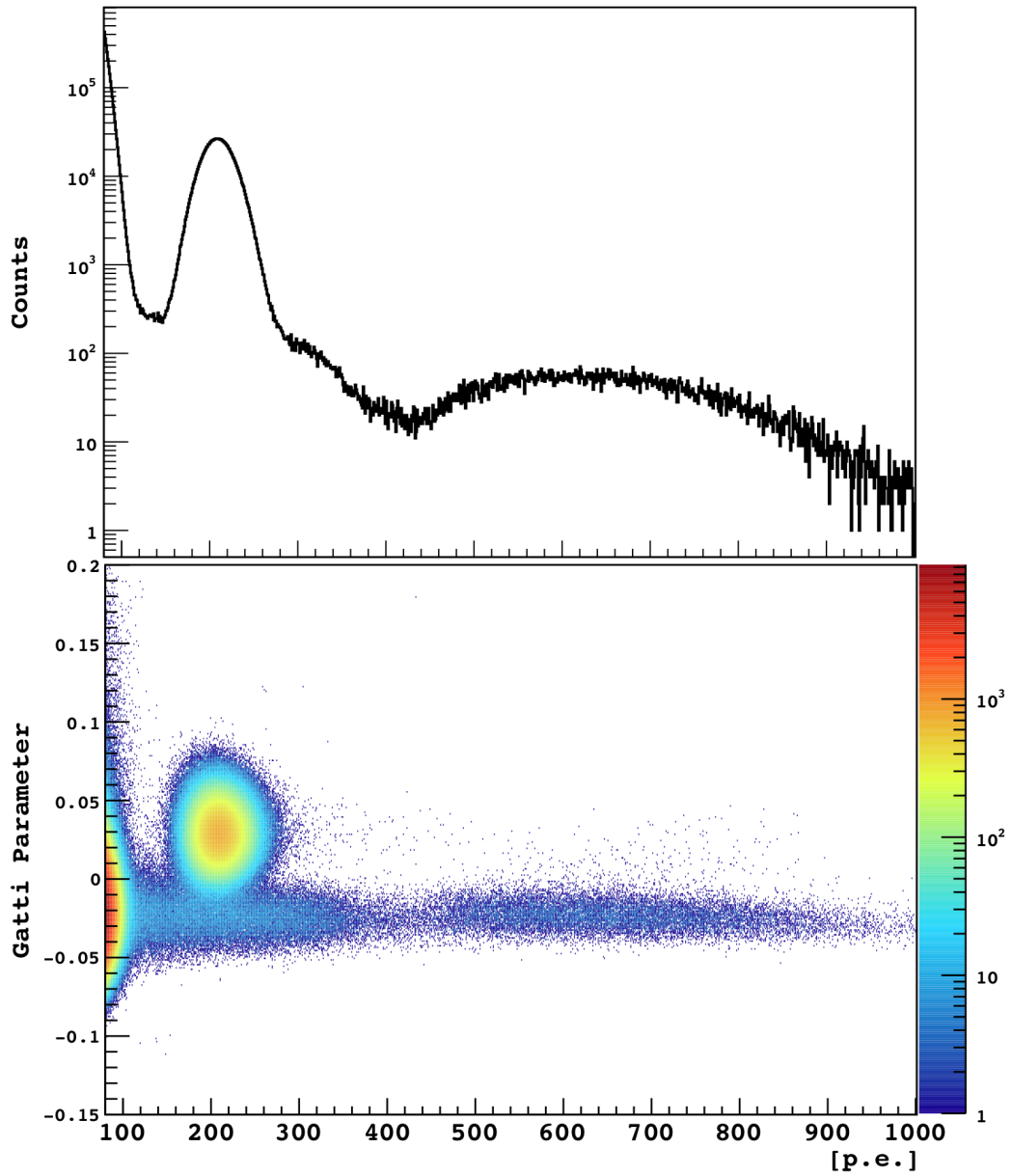
Figure 6.4: Top: Energy spectra of all events passing the standard selection cuts. Bottom: Same set of events as top figure, with the corresponding Gatti parameter plotted along the y-axis. Number of events is indicated by colored-logarithmic scale.

of magnitude higher than the ^{7}Be shoulder. In order to determine the ^{7}Be rate with high precision, one must either model the ^{210}Po line shape, including the tails, to high

accuracy (see Chapter 5) or somehow reduce the ^{210}Po contribution. Fortunately, there is additional information in the emission time profiles of each event that allows us to discriminate between αs and βs using the Gatti parameter (see Section 4.5 for the definition and implementation). The bottom plot of Figure 6.4 shows the same events in a two dimensional histogram with the Gatti parameter along the y-axis and the color indicating the number of events in each bin, in logarithmic scale. It can be seen that the the bulk of ^{210}Po events have a positive Gatti parameter value and are separated from the rest of the spectrum. Unfortunately, due to the high rate of ^{210}Po, the tails of the distribution extend into the negative Gatti parameter region and overlap with β-like events. Since we cannot individually identify α events in the region of overlap, we cannot place a simple cut to remove all ^{210}Po events. However, we can use the known shape of the the Gatti parameter distribution to statistically determine the number of αs and subtract them, as described in the following sections.

In order to carry out the statistical subtraction, we first produce an energy spectrum with a binning of 5 photoelectrons. For each bin, we histogram (bin width 0.002) the Gatti parameter of all the events that fall within that bin. The statistical subtraction is then performed in three steps:

6.4.0.2   Step I

The Gatti parameter histogram for each bin is fit to two normalized Gaussians. All parameters are left free though they are constrained to reasonable ranges. The fit results for each bin, examples of which are shown in Figure 6.5, are saved for use in Step 2. Additionally, a graph of the energy dependence of the means of each Gaussian is created, as depicted in Figure 6.6. Since the fitting of two Gaussians was found to be biased (see Section 6.4.1.2), a further two steps were introduced to reduce the bias in the subtraction.
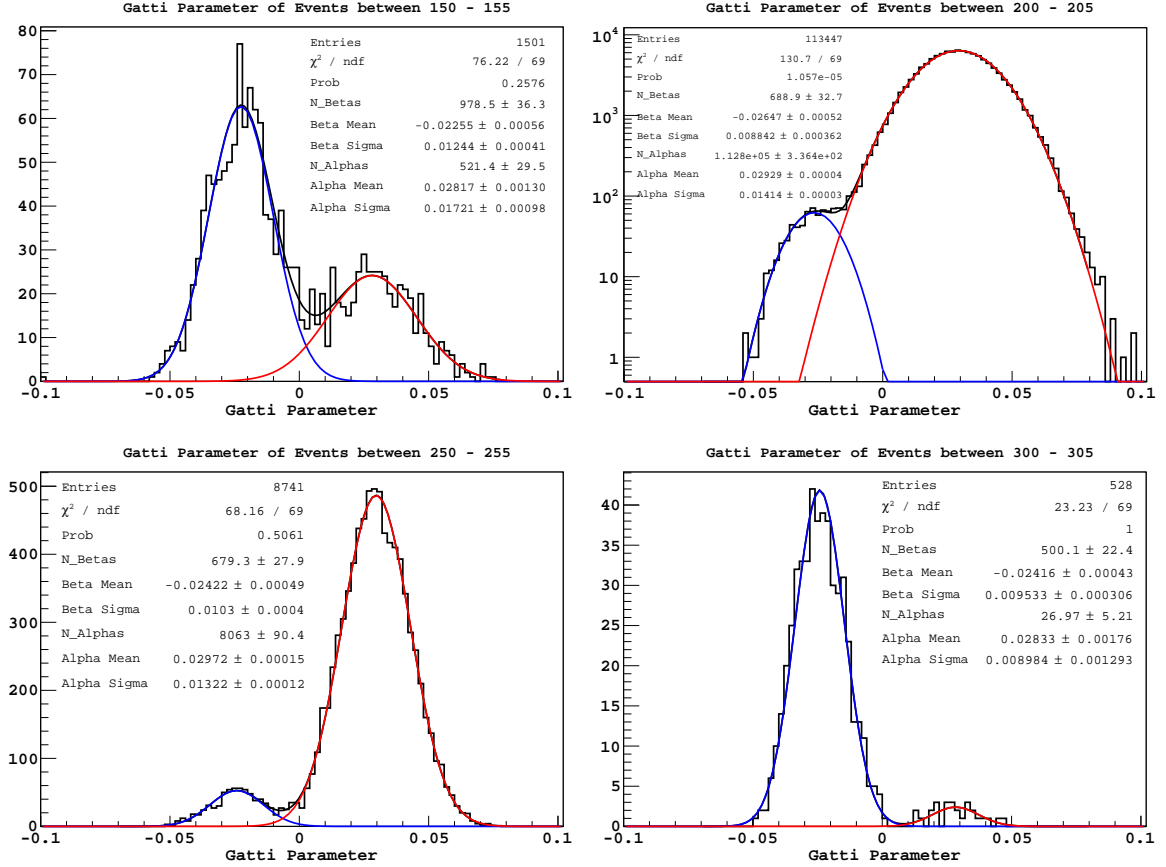
Figure 6.5: Gatti parameter distributions for events in individual energy bins. The Gaussian fit to the individual populations is shown (Blue: βs, Red: αs) as well as the total (Black). Top Left: 150 - 155 p.e., Top Right: 200 - 205 p.e. (in logarithmic scale), Bottom Left: 250 - 255 p.e., Bottom Right: 300 - 305 p.e.

6.4.0.3 Step II

From Figure 6.6, we see that the means of the Gaussians exhibit a roughly linear trend with energy above 100 p.e. As mentioned before, theoretically they should be independent of energy but due to the various non-ideal components of the implementation, they vary with energy. There are two distinct kinks in the Gatti distribution mean for βs (shown in blue in Figure 6.6). The first is the dip in the mean value at around 200 p.e. This is due to the bias in the fitting procedure caused by large number of ^{210}Po αs. In Section 6.4.1.2 it is shown that both the fitted number of βs and the mean value of the distribution are biased when the ratio of $\alpha : \beta$ events is
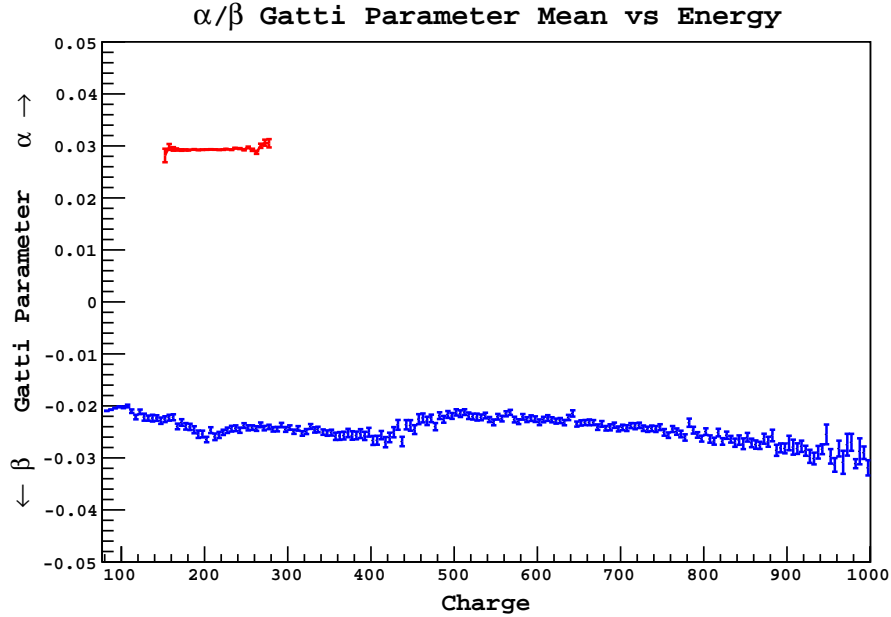
Figure 6.6: Energy dependence of the fitted means of the Gatti distribution for αs and βs. For the αs only the region under the ^{210}Po peak is shown due to the poor statistics in other regions.

greatly skewed.

As is discussed in the same section, the bias in the fitting of two Gaussians is reduced if the means of the Gaussians are fixed. Since the fitted means seem to be reliable when the fraction of the smaller class of events is larger than 0.3 (again, see Section 6.4.1.2) we fit only those regions to a straight line, thereby excluding the region under the ^{210}Po peak. The fits to the means of both the α and β distributions are shown in Figure 6.7.

There is a second distinct kink in the means of the β distribution starting at ~ 420 photoelectrons, after which a liner trend resumes. It is likely that this discontinuity arises from the fact that in that energy region, a majority of those events are 511 keV γ rays with very low energy βs coming from ^{11}C positron emission. The emitted positron sometimes ($\sim 51\%$ [105]) forms ortho-positronium which has a mean life of 3.1 ns [105], altering the scintillation emission time profile and thereby changing the calculated Gatti parameter. On annihilation, two back-to-back 511 keV γ rays
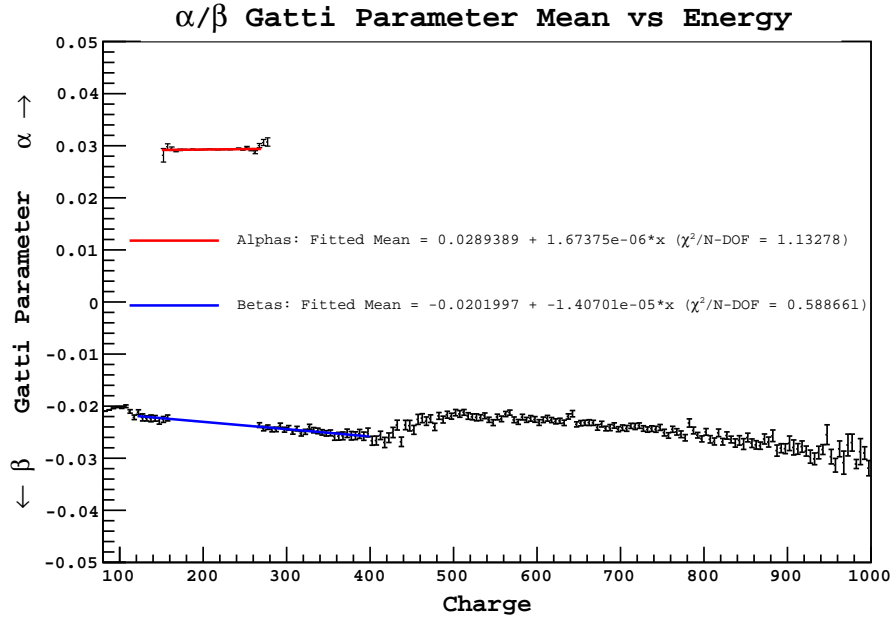
Figure 6.7: Fit to the energy dependence of the fitted means of the Gatti distribution for αs and βs in the selected region. See text for details.

are created which also produce scintillation light that differs from regular point-like events[1]. For this reason, we only fit the β means below 400 p.e.

In the same energy regions that the means are fitted, we also fit the energy dependence of the standard deviations of the two Gaussians. Unfortunately the dependence of the β distribution standard deviation is not very clear and we therefore only use the interpolation for the bias estimates in Step III, not for the refitting done in this step.

Once the means are fitted, we redo the fits done in Step I, this time constraining the means of the Gaussians (only below the ^{11}C starting point for βs), to the obtained linear dependence (i.e. the means are constrained to lie within 1σ of the fitted line). The variances of the Gaussians are left free. The resulting integral of the fitted Gaussians are then used as the corresponding α and β populations in that bin.

---

[1]These differences in the emission time profile between βs and positrons is exploited in the ongoing *pep* neutrino analysis to supress the background due to ^{11}C

6.4.0.4 Step III

In this step we correct for the bias, described in Section 6.4.1.2, while fitting energy regions with small fractions of βs. We take the linear fits to the means and standard deviations of the Gaussians in Step II as the true energy-dependent values of the distributions. For each bin we then simulate events according to those parameters. The number of events simulated in each category is obtained from the fit results for the number of βs and αs obtained in Step II. These numbers are not the true numbers (which is why we are trying to correct the bias) but the dependence of the bias correction on the true fraction is small compared to the bias correction itself (see Figure 6.12) and is currently neglected. The simulation for each bin is carried out 1000 times (for details see Section 6.4.1.2) and the mean bias is calculated. The error on this bias correction is estimated by the standard error on the mean. The value of βs in each bin is then corrected by the mean bias.

6.4.0.5 Statistical Errors

The error associated with each bin after the subtraction is obtained from the error on the fitted number of βs returned by the fit in Step II, combined with the error on the bias calculated in Step III.

The results of the individual steps of $\alpha - \beta$ statistical subtraction listed above are shown in Figure 6.8. The final α and β spectra are shown overlaid in Figure 6.9.

6.4.1 Bias in the Statistical Separation

6.4.1.1 Non-Gaussian Shapes

As mentioned earlier, the theoretical Gatti parameter distributions are not true Gaussians. Besides the theoretical shapes, due to the position dependence mentioned in
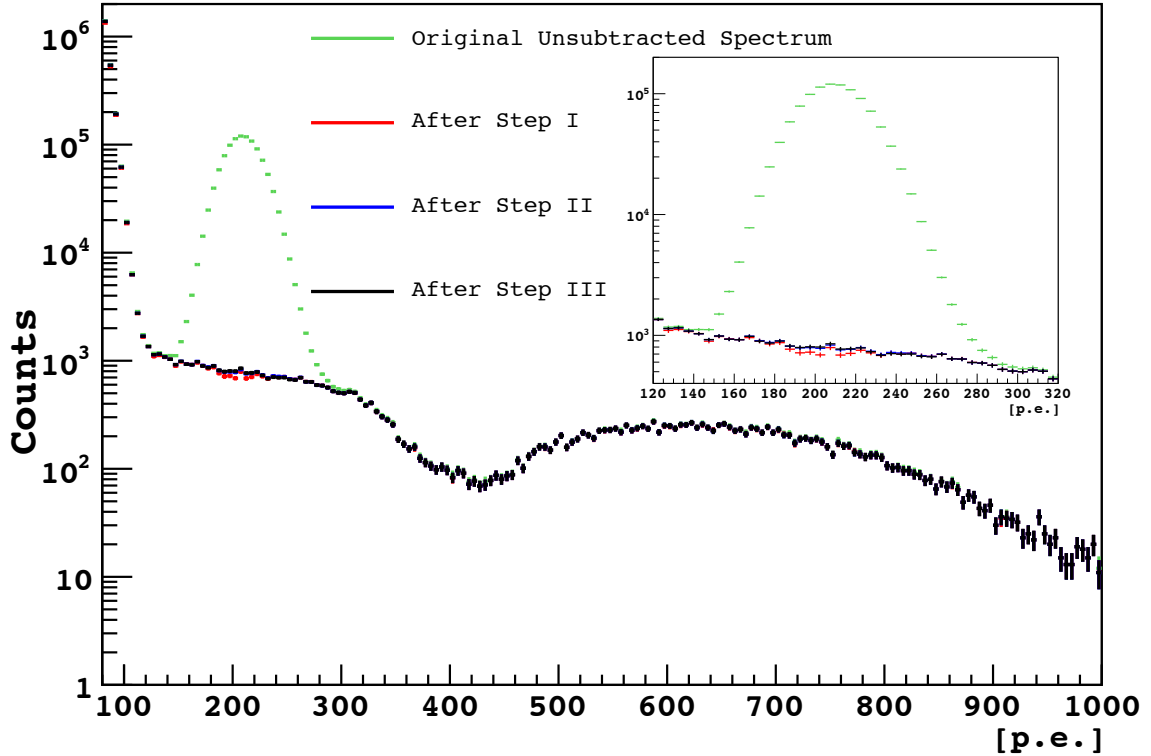
Figure 6.8: Results of the each step of the $\alpha - \beta$ statistical subtraction over the entire energy region. Inset: Expanded view of ^{210}Po energy region.

Section 4.5.2.2, the Gatti parameter distributions differ at different locations within the detector, Thus, the FV-averaged distribution is the combination of events drawn from many different distributions and may no longer resemble either a Gaussian or the true theoretical distribution.

In order to study this effect, we used ^{214}Bi-^{214}Po coincidences from the source calibration runs during the Jan 2009 calibration campaign. The coincidence allows us to obtain a relatively clean sample of αs and β's, though there is some contamination due to the high rate of ^{222}Rn decays. The source calibration data from the June 2009 campaign were excluded due to the large number of accidental coincidences caused by the high activity ^{222}Rn source used.

In Figure 6.10 we show the α and β distributions at two different positions within
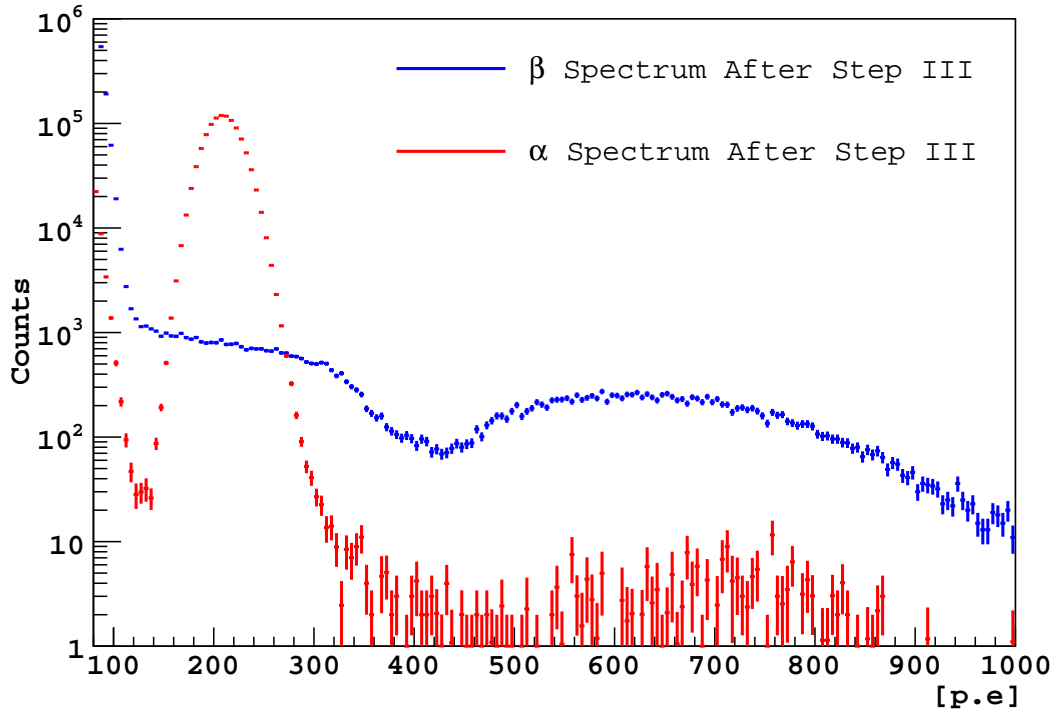
Figure 6.9: Final spectra for βs (blue) and αs (red) after statistical subtraction.

the detector as well as the combined distributions for all source positions. Note that the distributions are shifted with respect to each other for the different source positions. In each case a fit to a Gaussian is performed. As can be seen by the quality of the fit, the distributions differ visibly from a Gaussian. Despite the non-Gaussian shapes, for all these distributions the Gaussian fit returns a normalization value that is within 0.05% of the true number.

We note that the excess of events below -0.01 in the ^{214}Po and above 0.01 in the ^{214}Bi Gatti distributions has been investigated and found to be mostly due to accidental coincidences. For these coincidences, the time separation between the first and second events follows a flat distribution rather than the exponential distribution we expect.

The question of interest to us, however, is how well a Gaussian fit is able to separate these two species given their non-Gaussian shapes. In Figure 6.11 we combine the
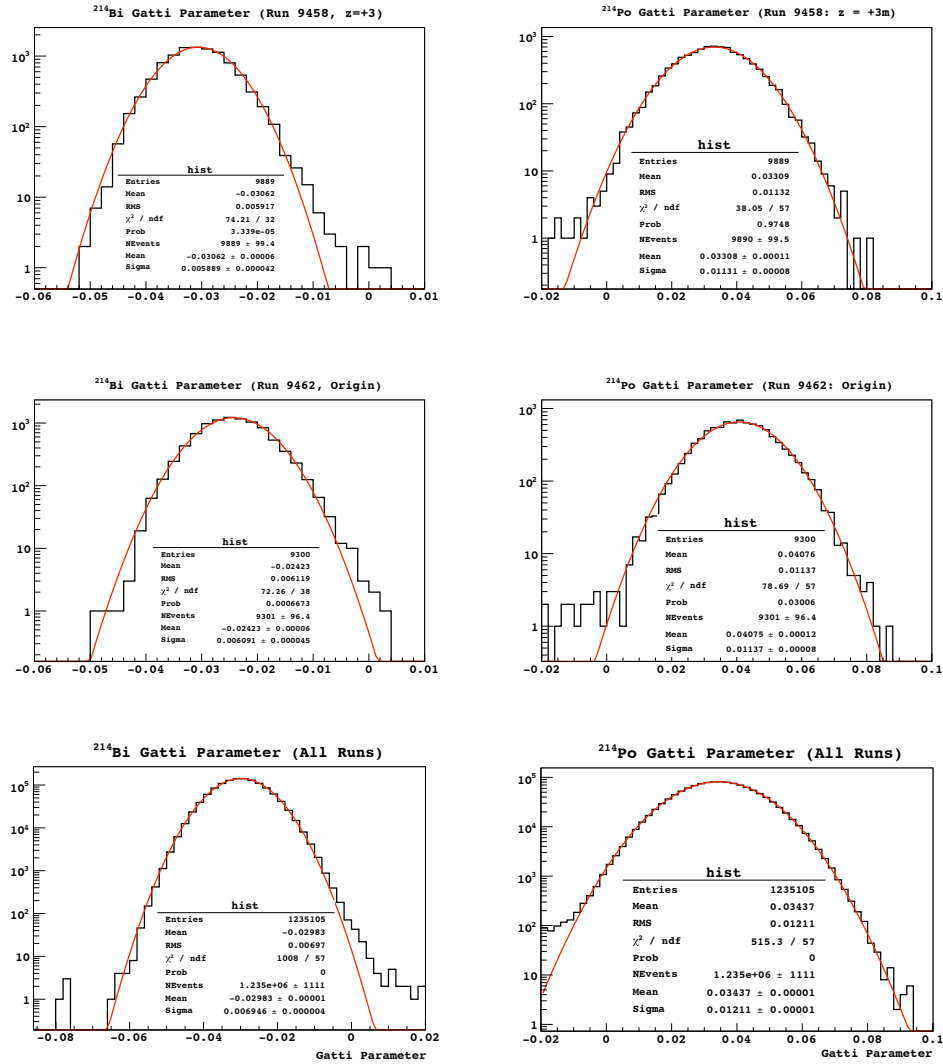
Figure 6.10: Gatti parameter distributions for individual calibration runs (top and center) and all runs combined (bottom). The distributions have different shapes and locations for different source positions. The red line is a fit to a Gaussian distribution. The estimates for the total number of events are all within 0.05% of the true value.

α and β histograms in ratios of α:β = 1:1 (all events included), 0.1:1 (using all β events) and 1:0.1 (using all α events). A wider range of ratios was not used, since at the level of a few percent, the tails due to random coincidences becomes significant and distort the results.

Since no bias related to non-Gaussian shapes was observed using the statistics available, there is currently no correction performed to the Gaussian fits done in
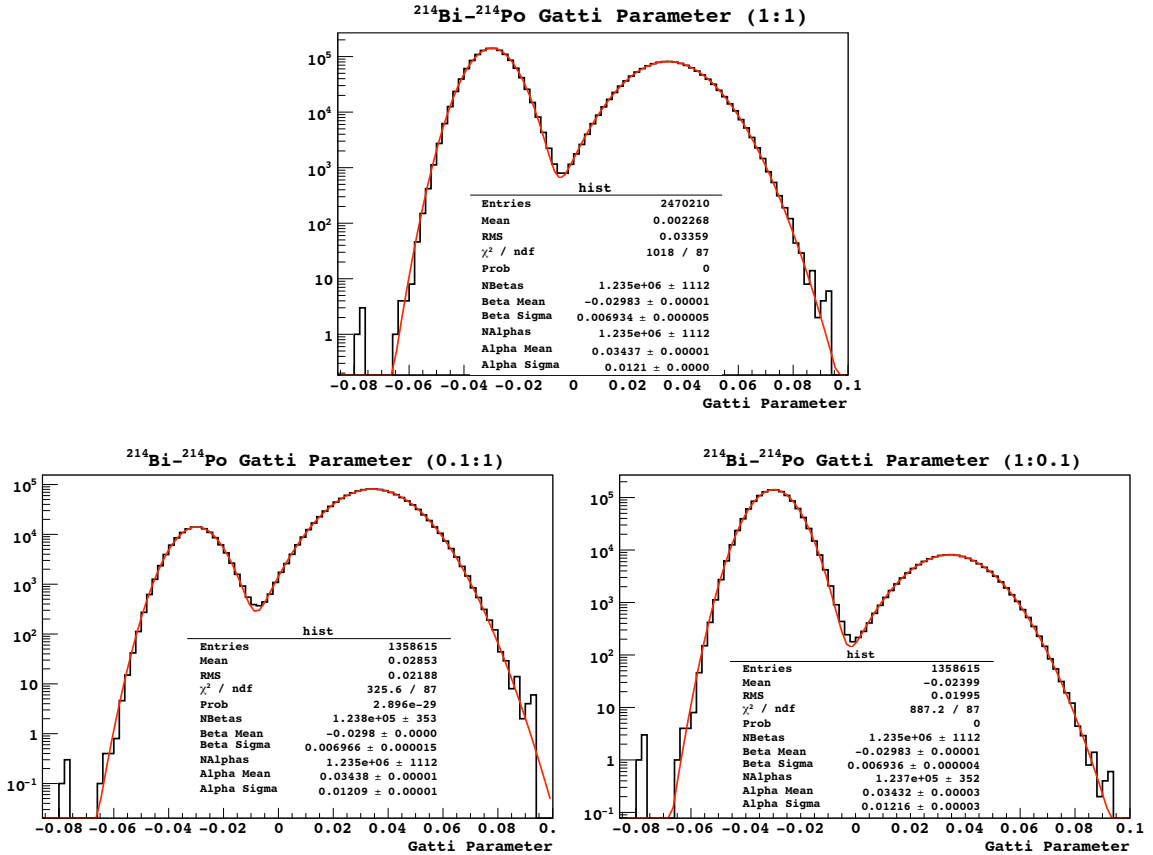
Figure 6.11: Combined Gatti parameter distribution for ^{214}Bi and ^{214}Po in all calibration runs. The ratio between the two populations was varied. The red line is a fit to a double Gaussian distribution. Note that the estimate for the total number of βs and αs is always within 0.3% of the true numbers.

Step I and II. A cleaner sample of α and β events is required in order to make a more detailed study of the shape of the Gatti distribution and also to look for biased results when the α and β shapes are not as well separated.

6.4.1.2 Bias in the Gaussian fits

Even if we assume that the Gatti parameter distributions are Gaussian, it is possible that the fit is biased due to the large overlap of distributions and the huge variation in the ratio of α and β events under the ^{210}Po peak. To study this issue, we simulated Gaussians with parameters similar to the α and β distributions we find within the data, combine them in different ratios and determine how well the fit can separate

the two components.

To estimate the worst possible bias, we use the data to determine the parameters under the ^{210}Po peak that make it most difficult to separate:

$$\overline{G_\alpha} = 0.029 \hspace{4cm} \overline{G_\beta} = -0.022 \hspace{2cm} (6.16)$$

$$var(G_\alpha) = 2.25 \times 10^{-4} \hspace{2.5cm} var(G_\beta) = 1.69 \times 10^{-4} \hspace{1cm} (6.17)$$

We vary the fraction of βs from 0.001 to 1 while keeping the number of βs fixed at 1000. This is to simulate the roughly constant β rate under the ^{210}Po peak. For each fraction we generate 1000 trials, where for each trial we combine the β distribution (with 1000 events) and corresponding α distribution, and fit them to a double Gaussian. This mimics the first step of the statistical subtraction applied to the data. The results from the fit of each trial are then stored in a histogram for each fit parameter. Once all 1000 trials for a given fraction are completed, the mean of the histogram for each fit parameter and the RMS is calculated.

Figure 6.12 shows the result of such a simulation for the fit parameter corresponding to the fitted number of βs. The central value on the plot is the mean of the histogram for each fraction and the error bars are the RMS of the histogram. The black data points are the result of the fits when all the Gaussian parameters are left free, while the red data points are the result of fixing the Gaussian means to their true simulated value. One can see from this plot that the fitted number of βs is biased, and the bias increases as the fraction of βs decreases. The bias is reduced however, if the means of the Gaussians are correctly fixed. Extracting some numbers from the plot, we find that the fitted number of βs, when all parameters are left free is within 0.6% of the true value, for fractions greater than 0.3.
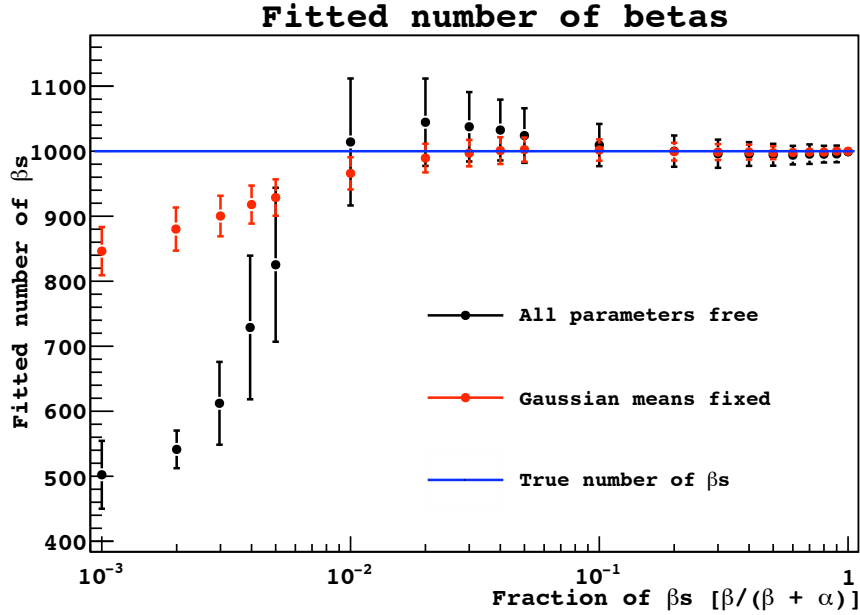
Figure 6.12: Simulation results for the fitted number of βs versus the fraction of βs simulated, when fitting a double-Gaussian distribution with two Gaussians. The true number of β simulated is 1000. Central values and errors are the mean and standard deviation of the distribution for a thousand trials. Black data points present the results when all parameters are left free. For the red data points, the means of the Gaussians were fixed to the true value.

Since fixing the means greatly reduces the bias, especially for fractions less than 0.01, we would like to fix the means using the data in the mostly-β section of the spectrum. To check how accurate the fitted means are in this region, we can use the result of the simulation for the fitted mean of the β Gaussian, shown in Figure 6.13. The fitted mean is seen to follow the same trend as the the fitted number of βs, indicating that the shifting of the mean is mostly responsible for the bias in the fits. We find that the fitted mean of the βs is accurate to within 0.6% for fractions greater than 0.3.

In spectral regions where the β fraction is above 0.3, we can therefore trust the fit results for both the number of βs and the mean of the β Gaussian to better than 0.6%, even in the worst case of parameters chosen.

Fitted mean of betas
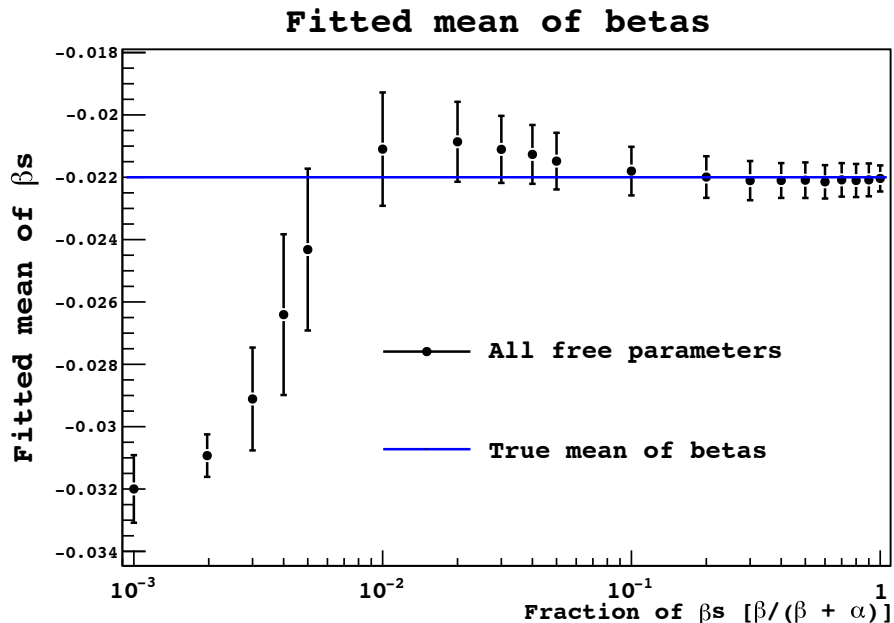
Figure 6.13: Simulation results for the mean of the β distribution when fitting a double-Gaussian distribution with two Gaussians. The true mean of the β simulated distribution is -0.022. Details in text.

6.4.1.3   Sensitivity to ^{14}C pileup

Pulse shape discrimination using the Gatti parameter is most effective when there are only two types of backgrounds that are accurately represented by the reference shapes. If an additional species of events is present, the Gatti parameter distribution of those events will not have the statistical properties described in Eq. 4.20 and the statistical subtraction based on the shape of the Gatti parameter distribution will not work. This is especially a problem for pileup events, where the small time separation between two distinct scintillation events causes them to be considered as a single event. The valley between the ^{14}C endpoint and the ^{210}Po peak is strongly populated by such ^{14}C pileup events. The scintillation time profile of these events is distorted and they have Gatti parameter distributions extending from standard β-like values to positive values well past the α distribution mean. Figure 6.14 (left) shows the Gatti parameter distribution for events between 100 and 105 photoelectrons. The non-Gaussian tail extending above 0.05 is due to ^{14}C pileup (the rate of ^{210}Po αs

241

in this energy range is negligible, though there may be a small contribution from ^{238}U and ^{232}Th decay chain αs). The rate of pileup events slowly decreases at higher energies, as can be seen from the Gatti parameter distribution between 130 and 135 photoelectrons (Figure 6.14, right). As was estimated in Section 3.2.2, the rate of pileup events above 145 photoelectrons is negligible, which is why we only use the statistically subtracted spectrum in the energy range above 145 p.e.
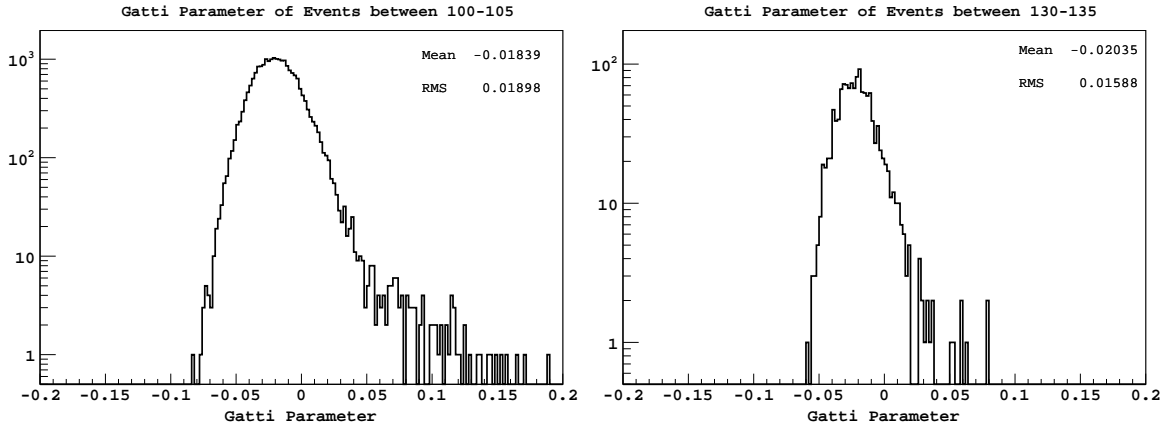
Figure 6.14: Left: Gatti parameter distribution for events between 100 and 105 photoelectrons. The non-Gaussian tail extending above 0.05 is due to ^{14}C pileup events. Right: Gatti parameter distribution for events between 130 and 135 photoelectrons. The contribution of pileup events has reduced, decreasing the number of observed events with Gatti parameter above 0.05. The only contribution of αs at these energies is from the small rate of decay chain isotopes. Compare with the distributions at higher energies in Figure 6.5.

6.5 Gatti Parameter Cut

In addition to the statistical subtraction described in the section above we have also tried to apply a cut on the Gatti parameter of events to remove αs. Unlike the statistical subtraction, a single cut on the Gatti parameter cannot completely separate the α and β populations due to the large overlap in the distributions. However it can significantly decrease the α population, thereby reducing the dependence of the fit result on the detailed modeling of the response function (specifically the tails of the ^{210}Po peak). Since the α contamination will not be completely removed, we will need

to fit the spectrum of residual αs that fall below the cut. In order to do this we must chose a value for the Gatti parameter cut such that not only is a negligible fraction of βs removed, but also such that the cut efficiency for αs is constant, so that the α spectrum is not distorted. A convenient way to define such a cut is to simply use the linear fit to the mean of the α Gatti parameter distributions (see Figure 6.7)

$$g_{cut} = 0.028939 + 1.67 \times 10^{-6} \cdot q \tag{6.18}$$

where q is the recorded charge of the event. Given that the largest value for the mean of the β Gatti parameter is < -0.02 and the corresponding fitted standard deviations are < 0.016 above 100 p.e., the fraction of βs that fall above the cut is negligible. Figure 6.15 shows the energy spectrum of the events that fall above and below the Gatti parameter cut.

6.5.1 Comparison with Statistical Subtraction

While the Gatti parameter cut is not as effective as the statistical subtraction, it makes less assumptions about the data. While the statistical subtraction requires that we know the true Gatti parameter distributions, the simple cut only makes two assumptions:

- We assume that the tails of the β distribution are sufficiently small such that only a negligible fraction of β events extend beyond three standard deviations.

- We assume that the fraction of α events above and below the mean do not change significantly with energy.

We note that both these assumptions are automatically satisfied if the distributions are assumed to be Gaussian, as is done for the statistical subtraction. Thus,
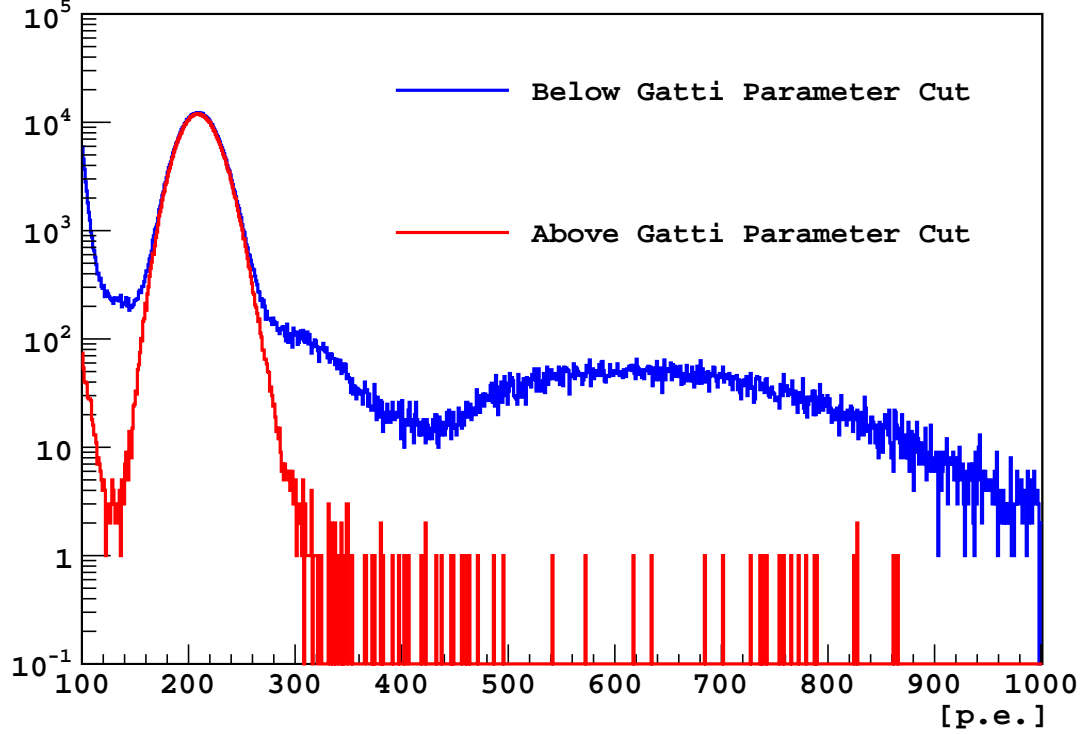
Figure 6.15: Spectra of events that fall below the Gatti parameter cut (blue) and above (red). The increase in events above the cut at low energies (< 130 p.e.) is due to ^{14}C pileup events.

fitting the spectrum with the Gatti parameter cut provides a cross-check on the statistical subtraction.

6.6 Spectral Fitting

6.6.1 Energy spectra

6.6.1.1 Solar Neutrino Spectra

As discussed in Section 3.1, the solar neutrino energy spectra are obtained from [39]. In order to convert the neutrino energy spectra into the observed electron-recoil energy spectra we use the cross-sections given in [62], which includes loop-level radiative corrections. The best estimate for the values of the constants have changed since [62]

was published, and the new values [63], are given in Table 3.2. Using these new, more precise values, the uncertainty in the total ^{7}Be elastic scattering cross-section is approximately 0.03%. The uncertainties in the parameters also affect the differential cross-section and therefore the shape of the neutrino spectra, though the effect on the fit results for ^{7}Be was less than 0.02%.

Since the elastic scattering cross-sections differ for ν_e and ν_μ, in order to calculate the recoil energy spectrum, one must know the ratio of ν_μ to ν_e, which amounts to specifying the survival probability P_{ee}. The value for the survival probability for each species of solar neutrino is calculated using the analytical expression derived in [40]. We have ignored Earth-matter effects and have used the vacuum oscillation parameters $\Delta m^2 = (7.59 \pm 0.20) \times 10^{-5}$ and $\sin^2(2\theta) = 0.87 \pm 0.03$ [1].

We briefly comment here on the seemingly circular logic of using a value for P_{ee} while attempting to make a measurement of the same. While a value for the electron neutrino survival probability is required in order to create the electron recoil spectrum for the spectral fit, the specific value used has little effect on the overall shape. Figure 6.16 shows the change in the shape of the ^{7}Be electron recoil spectrum for $\pm 1\sigma$ changes in the neutrino oscillation parameters. The change is found to be less than 0.05% throughout the spectrum. For the CNO electron recoil spectrum, which has a much smaller contribution to the spectral fit, the effect can be as large as $\sim 0.3\%$ near the end point. We have evaluated the effect of varying the oscillation parameters on the spectral fit results and found that the fitted ^{7}Be interaction rate changes by about $\pm 0.07\%$.

6.6.1.2 Background Energy Spectra

Table 6.8 lists the background β energy spectra, $S_\beta(E)$, used in the spectral fit and the source from which it was obtained. For monoenergetic γ and α background, we
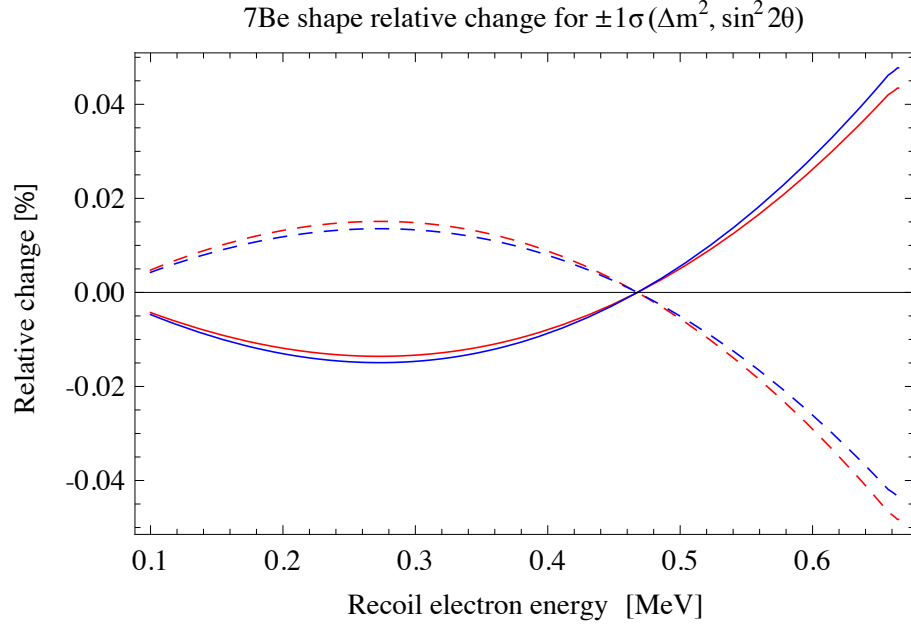
Figure 6.16: Effect of varying neutrino oscillation parameters on the ^{7}Be electron recoil spectrum. The red lines have Δm^2 changed by $+1\sigma$, blue lines by -1σ. $\sin^2(2\theta)$ is changed by $+1\sigma$ in the solid lines, -1σ in the dashed lines. Central values and errors for the neutrino oscillation parameters are taken from the Particle Data Group [1].

use a simple δ-function:

$$S_\alpha(E) = \delta(E - E_\alpha) \tag{6.19}$$

$$S_\gamma(E) = \delta(E - E_\gamma) \tag{6.20}$$

$S_\beta(E)$	Source	Notes
^{85}Kr	T.O.I.	SF: $(W^2 - 1) + (W_0 - W)^2$
^{210}Bi	T.O.I.	SF: $1 + 0.578W + 28.46/W - 0.658W^2$ [106]
^{11}C	T.O.I.	Quenching of positron annihilation γs left free
^{214}Pb	T.O.I.	See Table 5.3 for γ quenching
^{14}C	T.O.I.	SF: $1 + 1.24(W_0 - W)$ [107]
^{40}K	[108]	3rd Forbidden Decay

Table 6.8: β energy spectra for backgrounds in fit. T.O.I indicates the standard β spectrum was obtained from the Table of Isotopes [109], SF refers to the shape factor applied, W is the total energy of the β particle (in rest mass units) and W$_0$ is the total energy available for the decay (in rest mass units).

6.6.2 Charge Spectra

The conversion from an energy spectrum $S(E)$ to a normalized charge spectrum $S(q_N)$ is given by:

$$S(q_N) = \int S(E)P(q_N|E)dE \tag{6.21}$$

where $P(q_N|E)$ is the response function (described in detail in Chapter 5, summarized in Section 5.5) which depends on both the energy and type of particle.

6.6.3 Fit Procedure

The data histogram is first rescaled by dividing the contents and uncertainties of each bin by the total exposure (673.62 days $\times$ 75.70 tons = 510.0 day $\times$ 100 tons). The histogram is then fit by comparing the scaled data histogram to the sum of all the charge spectra included in the fit. We perform three different fits with different levels of α reduction. The first fit is performed on the entire spectrum without any pulse shape cuts, the second is with a cut on the Gatti parameter, outlined in Section 6.5, and the third is with the statistical subtraction described in Section 6.4. The standard configuration for each of the fits is given in Table 6.11 and will be briefly described below:

- Fit Range

  The lower edge of the fit range (145 p.e.) was chosen to include as much of the valley between the ^{14}C endpoint and the ^{210}Po peak while avoiding ^{14}C pileup events (see Section 3.2.2) which are hard to model in terms of Gatti parameter and position reconstruction. The higher edge of the fit range (650 p.e.) was extended until the external background rate (see Figure 3.1, Section 3.2.11) became a significant fraction (> 0.05) of the ^{11}C rate.

- Bin Width

  The bin width (5 p.e.) was chosen for the statistically subtracted spectrum such that there were enough β events in each bin to be able to fit the Gatti parameter distribution, while small enough to not lose information about the spectral shape. For the other fits, the default was kept at 5 p.e., for ease of comparison.

- Minimization Method

  By default, the fit was performed by minimizing the χ^2 of the charge spectra with respect to the data. Even with a bin width of 2 p.e., there are more than 20 counts in each bin such that the χ^2 approximation is valid and the reduced χ^2 can be used a goodness-of-fit test. As part of the systematics test, a likelihood fit was also performed. The minimization routine used was the MIGRAD algorithm in MINUIT. No significant change was noticed in either the location of the minima or the uncertainties when other minimizers within MINUIT were tried.

- Response Function Parameters

  Leaving the response function parameters g_i free in the fit greatly slows down the fitting procedure since every time one of the parameters is varied, the spectral shape of each of the species has to be recomputed. In order to enable the fit to converge in a reasonable amount of time, we have tried to keep the number of free resolution parameters to a minimum. In the standard configuration we have fixed parameter g_4, related to the third central moment of the spatial and temporal distribution of the light conversion probability (see Section 5.5), to zero. For the final fits to spectra where the ^{210}Po peak is clearly visible (the entire spectrum and the spectrum with the Gatti parameter cut) we have left g_1, g_2 and g_3 free, whereas for intermediate tests we have fixed g_3 to previ-

ously obtained values. For the spectrum with the statistical subtraction, there is no longer any species with large enough statistics to accurately determine the response function parameters. We have therefore fixed all the resolution parameters g_i to the average of the values obtained from the other fits.

- Solar Neutrino Rates

  Besides the rate of the ^{7}Be neutrino interaction, the rates of all other solar neutrino spectra are fixed to the value given by the GS98 solar model in [17]. The ^{8}B neutrino spectrum is not included in the fit due to its negligible contribution (see Figure 6.30). From this point on in this thesis, unless specifically mentioned, the quoted values for the ^{7}Be rate refer to the fitted rate for the 0.862 MeV branch. The rate should be multiplied by 1.04 to obtain the total rate, including the 0.384 MeV branch.

- ^{210}Po Peak Position

  Since the ^{210}Po peak is such a dominant feature in the energy spectrum, the position can be determined to much higher accuracy from the fits to data than from the empirical quenching given by Eq. 5.105, and is therefore left free in the fit.

- ^{11}C Quenching

  Like the ^{210}Po peak, the ^{11}C spectral shape is clearly visible which allows the starting point of the ^{11}C to be determined by the data. The starting point can also be calculated from the known energy of the two annihilation γs and the effective γ-ray quenching (Eq. 5.100) which was calculated independently using the source calibration data (see Table 5.3). By leaving the starting point free in the fit, we can test the quenching model used in Section 5.2.2 and study some of the systematics related to the energy scale (see Section 6.8.3.2).

- ^{238}U Daughters above ^{222}Rn

  All α decays in the chain, within the fit energy range, were included since a localized peak can strongly affect the number of counts in a single bin. For each β emitting isotope in the chain, we estimated the contribution to the fit by assuming all ^{238}U daughters to be in secular equilibrium at a rate of 0.57 cpd/100 tons (see Section 3.2.6.1). A discussion of the true rates of these isotopes can be found in the fit results section (Section 6.7). A summary of all the isotopes in the decay chain, their primary decay branch, and whether or not they were included in the fit is given in Table 6.9. We note that only a single peak was used for each α emitting isotope since most branches of the decays fell within 5-10 p.e. of the dominant branch. In Figure 6.30 we show the known spectra that were excluded from the spectral fit and an estimation of their contribution. The effect of excluding these species is analyzed in Section 6.8.3.3.

Species	Decay mode	$E_\alpha / E_{\beta+\nu}$ [MeV]	E_γ [MeV]	BR %	Fit status
^{238}U	α	4.19		71	Excluded: Below fit range
^{234}Th	β	0.199		78	Excluded: Below fit range
^{234m}Pa	β	2.27		98	Excluded: Low fit rate†
^{234}U	α	4.78		71	Included
^{230}Th	α	4.69		76	Included
^{226}Ra	α	4.78		94	Included
^{222}Rn	α	5.49		100	Included
^{218}Po	α	6.00		100	Included
^{214}Pb	β	0.67	0.35	48	Included
^{214}Bi	β	1.51	1.76	40	Excluded: Removed by cuts
^{214}Po	α	7.83		100	Excluded: Removed by cuts
^{210}Pb	β	0.02	0.05	84	Excluded: Below fit range
^{210}Bi	β	1.16		100	Included
^{210}Po	α	5.31		100	Included

Table 6.9: List of ^{238}U daughters and primary decay branches. The energies listed in the second column are the peak energies for α decays and endpoint energies for β decays. The final column states whether the decay spectrum was included in the fit or the reason for its exclusion. †Spectra that are excluded due to low rates in the fit region are shown in Figure 6.30 and the impact of excluding these species is described in Section 6.8.3.3.

- ^{222}Rn and ^{222}Rn Daughters

  The rates of these species are assumed to be in secular equilibrium at the value determined from the ^{214}Bi-Po coincidences (see Section 3.2.6.1).

- ^{232}Th Daughters

  As in the case of the ^{238}U daughters, all α decays within the fit range are included, represented by a single peak for each isotope. The β decay spectra were excluded due to their small contribution in the fit range. A summary of all the isotopes in the decay chain, their primary decay branch, and whether or not they were included in the fit is given in Table 6.10. Figure 6.30 shows the known spectra that were excluded from the spectral fit and an estimation of their contribution. The effects of excluding these species is studied in Section 6.8.3.3.

Species	Decay mode	$E_\alpha/E_{\beta+\nu}$ [MeV]	E_γ [MeV]	BR %	Fit status
^{232}Th	α	4.01		77	Excluded: Below fit range
^{228}Ra	β	0.04	0.01	50	Excluded: Below fit range
^{228}Ac	β	1.16	0.97	30	Excluded: Low fit rate†
^{228}Th	α	5.42		72	Included
^{224}Ra	α	5.69		95	Included
^{220}Rn	α	6.29		100	Included
^{216}Po	α	6.78		100	Included
^{212}Pb	β	0.34	0.24	82.5	Excluded: Low fit rate†
^{212}Bi(64%)	β	2.25		55	Excluded: Removed by cuts
^{212}Po	α	8.78		100	Excluded: Removed by cuts
^{212}Bi(36%)	α	6.05		25	Included
^{208}Tl	β	1.80	3.20	49	Excluded: Low fit rate†

Table 6.10: List of ^{232}Th daughters and primary decay branches. The energies listed in the second column are the peak energies for α decays and endpoint energies for β decays. The final column states whether the decay spectrum was included in the fit or the reason for its exclusion. †Spectra that are excluded due to low rates in the fit range are shown in Figure 6.30 and the effects of excluding these species is studied in Section 6.8.3.3.

- α Decay Rates

  For all α emitters whose decay rate is fixed in the fit, the rate is reduced by half

in the spectrum with the Gatti parameter cut, and set to zero in the spectrum where the statistical subtraction was applied.

- Cosmogenics

  As estimated in Section 6.2.3.2, besides ^{11}C, the only other cosmogenic isotope with a significant rate in the final spectrum fit range is ^{7}Be, which is included in the fit. The spectra for some of the other cosmogenic isotopes that were excluded from the fit are shown in Figure 6.30. We have analyzed the consequence of leaving these spectra out of the final fit in Section 6.8.3.3.

- External Backgrounds

  The external background spectra (see Section 3.2.11) were excluded from the fit due to the difficulty in analytically modeling the energy spectra, as well as to avoid the complications arising from having to include different response function parameters due to their strongly non-uniform spatial distribution (see Section 5.3). In order to minimize their contribution, the fit range was limited to below 650 p.e. The impact of excluding these species is later studied in Section 6.8.3.3.

Parameter	Value		
	Entire	Gatti Cut	Stat. Sub
Histogram Parameters			
Fit Start	145 p.e.		
Fit End	650 p.e.		
Bin Width	5 p.e.		
Offset	0 p.e.		
Energy Scale Parameters			
Light Yield	Free		
Response Function Shape	Modified Gaussian		
Response Function Parameter g_1	Free	Free	Fixed
Response Function Parameter g_2	Free	Free	Fixed
Response Function Parameter g_3	Free	Free	Fixed
Response Function Parameter g_4	0		
Quenching Parameterization	Eq. 5.98, Table 5.2		
^{11}C Quenching	Free		
^{210}Po Quenching	Free	Free	Fixed
Solar Neutrinos			
pp Count Rate	133		
CNO Count Rate	5.07		
pep Count Rate	2.75		
^{7}Be Count Rate	Free		
^{238}U Daughters			
^{234}U, ^{230}Th, ^{226}Ra Count Rate	X†	X†/2	0.00
^{222}Rn, ^{218}Po Count Rate	1.62	0.81	0.00
^{214}Pb Count Rate	1.62		
^{210}Bi Count Rate	Free		
^{210}Po Count Rate	Free		
^{232}Th Daughters			
^{228}Th, ^{224}Ra, ^{220}Rn, ^{216}Po Count Rate	Y†	Y†/2	0.00
^{212}Bi α Count Rate	0.05	0.02	0.00
Cosmogenic Isotopes			
^{7}Be Count Rate	0.35		
^{11}C Count Rate	Free		
Other Backgrounds			
^{85}Kr Count Rate	Free		
^{40}K Count Rate	Free		

Table 6.11: Standard Fit Configuration. When only one value is listed, it applies to all three fit methods. All count rates are given in counts/day/100 tons. †Rates were varied based on different assumptions listed in text.

6.7 Fit Results

It has been found that a key ingredient in obtaining an accurate fit result is to determine the true count rate of isotopes in the long-lived decay chains. Based on the ^{214}Bi-Po and ^{212}Bi-Po coincidence rates during stable detector periods, it has been estimated that, assuming secular equilibrium, the decay rate of the ^{238}U and ^{232}Th chains is (0.57 ± 0.05) and (0.13 ± 0.03) cpd/100 tons respectively (see Sections 3.2.6.1, 3.2.6.2). However, due to the long-lived isotopes in the ^{238}U chain, secular equilibrium may not necessarily hold, so these rates may not apply to all the isotopes in the ^{238}U chain above ^{222}Rn. In order to try and independently evaluate the rate, we have inverted the α cut described in Section 6.5 and fit the α spectrum using the known α decays in the chains. We have fixed the rate of the αs below ^{222}Rn since the rate is well determined by the number of observed ^{214}Bi-Po coincidences and we strongly expect secular equilibrium to hold within those isotopes. To avoid having degeneracies in the fit (all the αs are very close in energy) we have tied all the isotopes above ^{222}Rn to have the same rate and similarly tied all the α emitting isotopes in the ^{232}Th chain. We have also extended the lower limit of the fit range by 10 photoelectrons to better constrain the low energy αs. Unfortunately the presence of pileup restricts the fit to above 135 p.e. The fit result is shown in Figure 6.17. Taking into account a 50% acceptance rate for the α cut, we obtain an equilibrium rate of (0.28 ± 0.07) cpd/100 tons for ^{234}U, ^{230}Th and ^{226}Ra from the ^{238}U chain and (0.12 ± 0.03) cpd/100 tons for ^{228}Th, ^{224}Ra, ^{220}Rn and ^{216}Po from the ^{232}Th chain.

The fitted rates of the αs from the ^{232}Th chain, which is mostly constrained by the high energy ^{216}Po α peak, is in good agreement with the rate obtained from the ^{212}Bi-Po coincidences. This provides some confirmation that the isotopes at the higher end of the chain are in secular equilibrium with the ^{212}Bi-Po decays and also increases our confidence in the fitting procedure. Assuming secular equilibrium above ^{228}Th, the fitted rate of (0.12 ± 0.03) cpd/100 tons corresponds to a ^{232}Th contamination of

$(3.4 \pm 0.9) \times 10^{-18}$ g/g.

The fitted rate of the αs from the ^{238}U chain differs from the asymptotic ^{214}Bi-Po coincidence rate by about 2.9σ. This indicates that secular equilibrium does not hold throughout the chain. We have assumed that all three isotopes, ^{234}U, ^{230}Th and ^{226}Ra, have the same decay rate, which is not necessarily true, but because they have very similar energies this assumption does not affect the fit results much. Assuming secular equilibrium above ^{234}U, the fitted rate of (0.28 ± 0.07) cpd/100 tons corresponds to a ^{238}U contamination of $(2.6 \pm 0.7) \times 10^{-18}$ g/g.
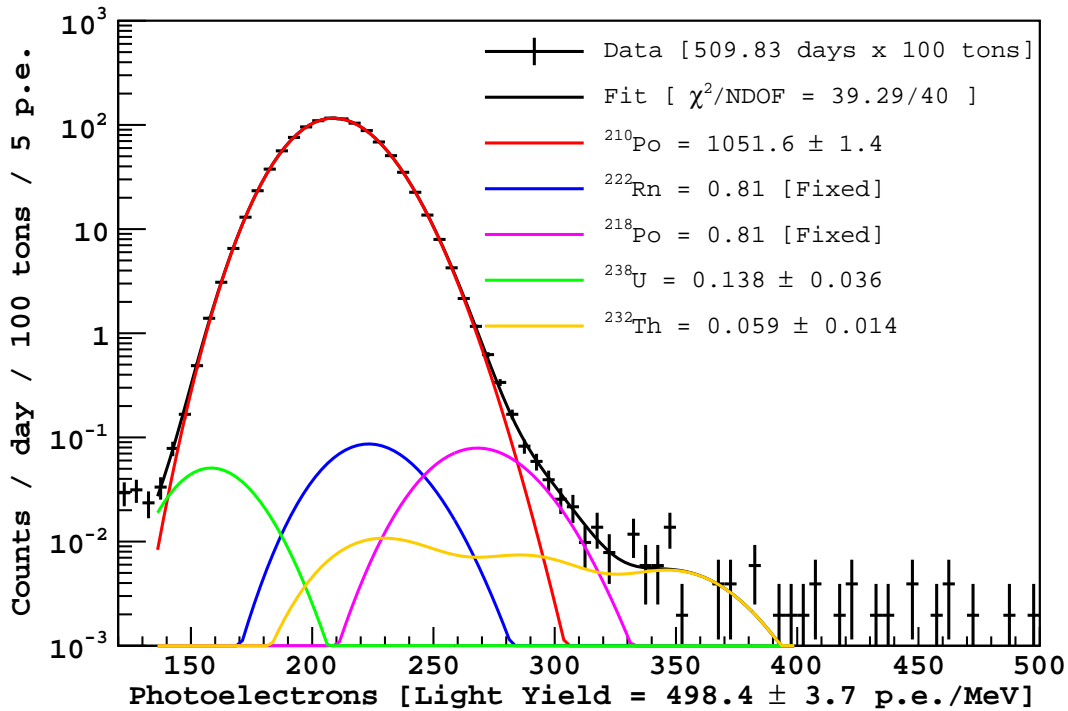

Figure 6.17: Spectral fit to α energy spectrum following the Gatti parameter cut. All rates are given in units of counts/day/100 tons. Positions of all α peaks, except for ^{210}Po, are fixed. The amplitudes of ^{222}Rn and ^{218}Po are fixed to values obtained from ^{214}Bi-Po coincidences. The acceptance rate for αs is 50%.

6.7.1 Entire Spectrum Fit

In the fit to the entire spectrum (without any pulse shape cuts to remove α decays)the α decays from the ^{238}U and ^{232}Th decay chains have a fairly significant contribution, especially with respect to ^{85}Kr. Since we are not certain about their rates, we have tried to evaluate the effect of these isotopes on the rest of the fit. First, we performed a fit assuming that the abundances of all isotopes above ^{222}Rn in the ^{238}U chain and all isotopes in the ^{232}Th chain are negligible within the scintillator. We also performed fits with the rates set either to the values obtained from assuming secular equilibrium or from the fit to the α spectrum. Table 6.12 summarizes the results of these tests. As the contribution from the decay chains is increased, the ^{85}Kr rate systematically decreases and the ^{7}Be rate increases correspondingly. In the absence of any better information regarding the isotope abundances, we have decided to use the values from the α fit as our baseline. The result of the fit is shown in Figure 6.18 and summarized in Table 6.15

Decay Chain αs	$(^{238}$U, ^{232}Th) [cpd/100 tons]	^{7}Be [cpd/100 tons]	^{85}Kr [cpd/100 tons]	^{210}Bi [cpd/100 tons]
None	(0, 0)	44.7 ± 3.1	32.3 ± 5.7	39.3 ± 2.9
α Fit	(0.28, 0.12)	46.3 ± 3.0	26.5 ± 5.9	39.3 ± 3.1
Sec. Eq.	(0.57, 0.13)	48.4 ± 2.9	20.0 ± 6.2	39 ± 12

Table 6.12: Effect of varying the contribution of αs from the ^{238}U (above ^{222}Rn)and ^{232}Th decay chains in the fit to the entire spectrum. For the specific isotopes considered, see Table 6.11. Sec. Eq. denotes that the rates were fixed to the values estimated from Bi-Po coincidences, assuming secular equilibrium. The ^{7}Be rate is only for the 0.862 MeV branch.
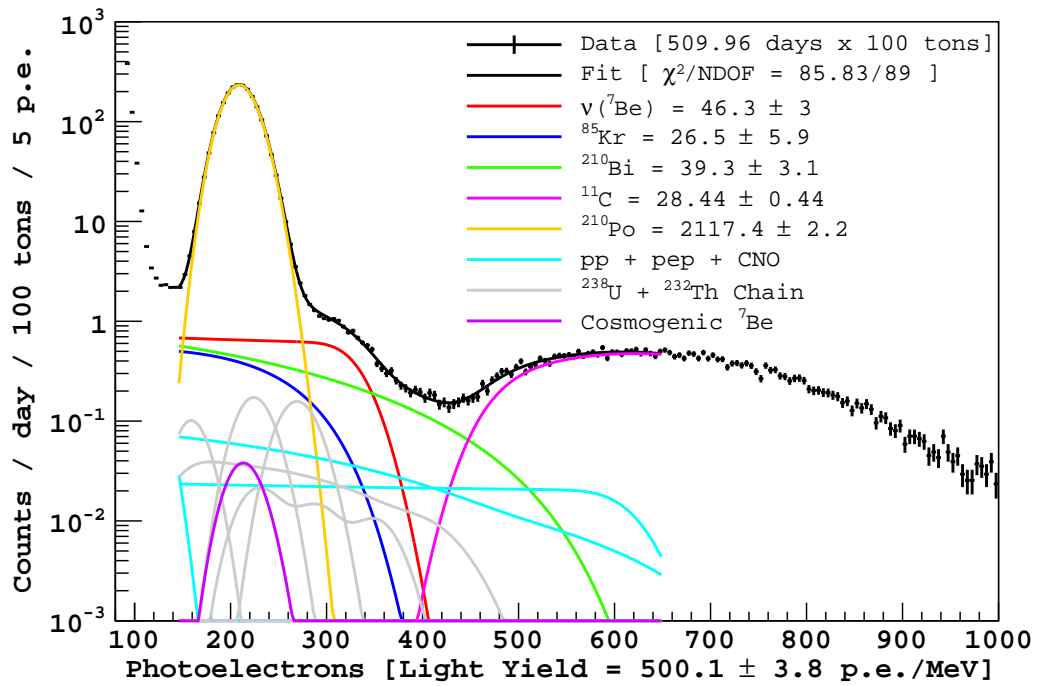
Figure 6.18: Spectral fit to energy spectrum without the application of any cuts to remove α decays. All rates are given in units of counts/day/100 tons. The rates of ^{238}U chain isotopes above ^{222}Rn and all ^{232}Th chain isotopes are set to the values obtained from the α spectral fit.

6.7.2 α Cut Fit

As was done for the fit to the entire spectrum, we have tried to evaluate the effect of the ^{238}U and ^{232}Th chains on the fit to the spectrum after the α cut (described in Section 6.5). Table 6.13 summarizes the results of the different tests. Compared to the spectrum without the α cut, the α decays from the ^{238}U and ^{232}Th decay chains are less significant with respect to the other species, which reduces their impact on the fit results. We note that the fit results presented in the recently published paper [86] do not include any contribution from the ^{232}Th decay chain or the sections of the ^{238}U chain above ^{222}Rn. The published values are therefore very similar to the first row of Table 6.13 (though the α cut used in [86] removes a larger fraction of αs than the cut used here). As before, we will use the results that fix the decay chain rates to the ones determined from the α fit as our baseline. The fit is shown in Figure 6.19 and the values summarized in Table 6.15.

We note that the fitted values for the resolution parameters and ^{210}Po quenching are in good agreement for the fits with and without the α cut and that the rate of the ^{210}Po after the α cut is $(50.4 \pm 0.1)\%$ of the original rate. These results justify our use of the same response function before and after the cut and for scaling the fixed α rates by 50%.

Decay Chain αs	$(^{238}$U, ^{232}Th) [cpd/100 tons]	^{7}Be [cpd/100 tons]	^{85}Kr [cpd/100 tons]	^{210}Bi [cpd/100 tons]
None	(0, 0)	44.7 ± 2.6	30.8 ± 5.1	38.0 ± 2.8
α Fit	(0.14, 0.06)	45.4 ± 2.6	27.9 ± 5.2	38.0 ± 2.9
Sec. Eq.	(0.29, 0.07)	46.6 ± 2.6	24.4 ± 5.3	38.3 ± 2.9

Table 6.13: Effect of varying the contribution of αs from the ^{238}U and ^{232}Th decay chains (above ^{222}Rn and ^{220}Rn respectively) in the fit to the spectrum with the α cut applied. Sec. Eq. denotes that the rates were fixed to the values estimated from Bi-Po coincidences, assuming secular equilibrium. The ^{7}Be rate is only for the 0.862 MeV branch.
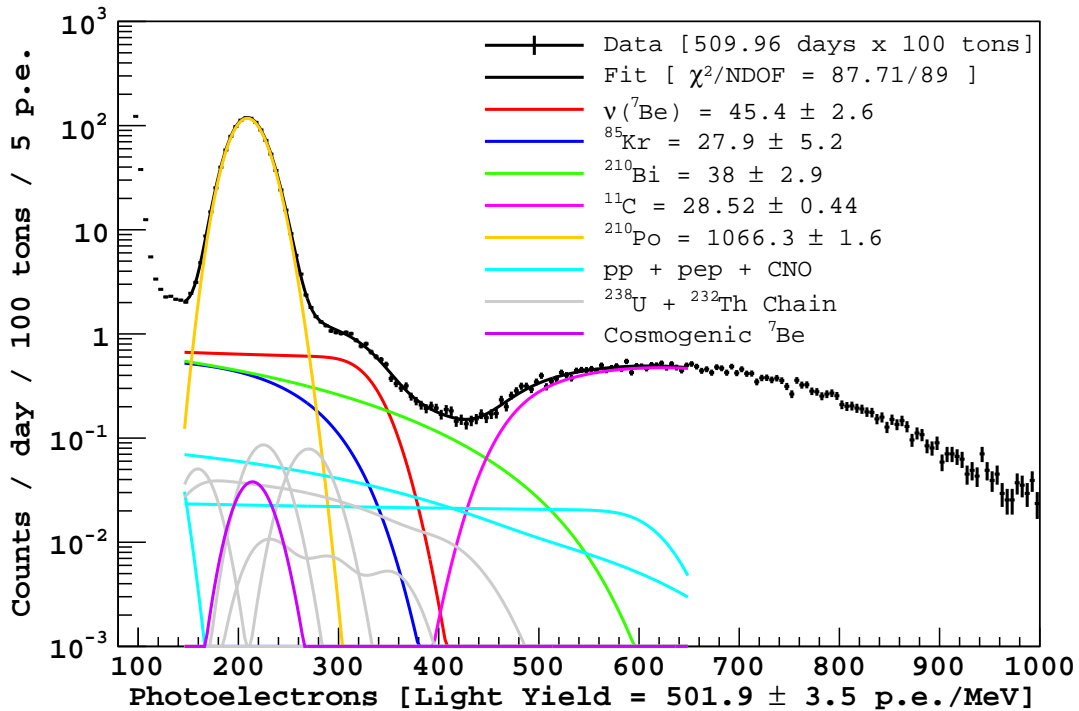
Figure 6.19: Spectral fit to energy spectrum after the application of the Gatti parameter cut to reduce the α decays. All rates are given in units of counts/day/100 tons. The rates of ^{238}U chain isotopes above ^{222}Rn and all ^{232}Th chain isotopes are set to the values obtained from the α spectral fit.

6.7.3   Statistical Subtraction Fit

For the fit to the statistically subtracted spectrum we do not have to worry about the decay chain αs as the have all been removed from the spectrum (or, at the very least, reduced to a negligible rate). We have fixed all the resolution parameters to the average of the values obtained from the previous two fits, since without the presence of the ^{210}Po peak, there is no longer a distinct spectral feature to constrain their values. The fit is shown in Figure 6.20 and the values summarized in Table 6.15.

6.7.3.1   Tests of Statistical Subtraction

In order to check if the statistical subtraction over or under subtracts the number of αs in the spectrum we have left the amplitude of the ^{210}Po spectrum free in the fit

(allowing it to also be negative) while fixing its position to the average of the other two fits. The best fit value for the residual ^{210}Po rate is -0.9 ± 0.3. This equates to a $(0.041 \pm 0.014)\%$ over-subtraction which is within the sensitivity of the tests performed in Section 6.4.1. Figure 6.21 shows the fit to the statistically subtracted spectrum (the same as in Figure 6.20) in linear scale, such that the small negative contribution from ^{210}Po is visible.

Due to a strange coincidence, the position of the cosmogenic ^{7}Be γ falls almost directly under the ^{210}Po peak. As a result of this unfortunate alignment, we are not able to independently disentangle the rate of cosmogenic ^{7}Be from a possible over-subtraction of the ^{210}Po αs. Setting the rate of cosmogenic ^{7}Be to zero, we obtain a value of -0.5 ± 0.3 for the residual ^{210}Po rate, which gives an estimate of the lower limit of the over-subtraction.

Leaving the ^{210}Po free in the fit to the subtracted spectrum assumes that any bias in the subtraction will be directly proportional to the number of αs. While the simulations in Section 6.4.1.2 indicated that this was the case, we have also performed an additional test in which we simply ignore the data in the energy region under the ^{210}Po peak (160 p.e. - 265 p.e.) where we expect a possible bias. The results, listed in Table 6.14 are consistent with the standard fit, indicating that the fit results are not greatly affected by any possible bias in the statistical subtraction.

Fit	^{7}Be [cpd/100 tons]	^{85}Kr [cpd/100 tons]	^{210}Bi [cpd/100 tons]
Standard	45.0 ± 2.0	29.2 ± 3.5	37.0 ± 2.6
Excluding ^{210}Po region	45.2 ± 2.3	28.7 ± 4.2	36.9 ± 2.6

Table 6.14: Comparison of fit results with, and without including the ^{210}Po peak region (160 p.e. - 265 p.e.) in the fit. Results for ^{11}C (not listed) do not change. The ^{7}Be rate is only for the 0.862 MeV branch.
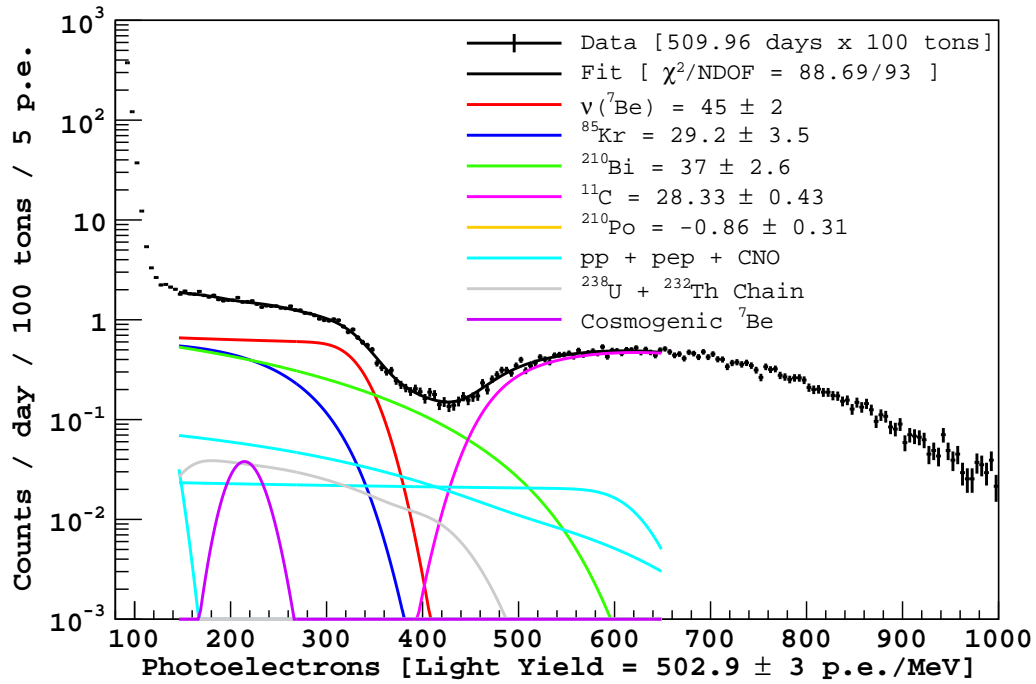
Figure 6.20: Spectral fit to energy spectrum after the statistical subtraction of α decays. All rates are given in units of counts/day/100 tons.
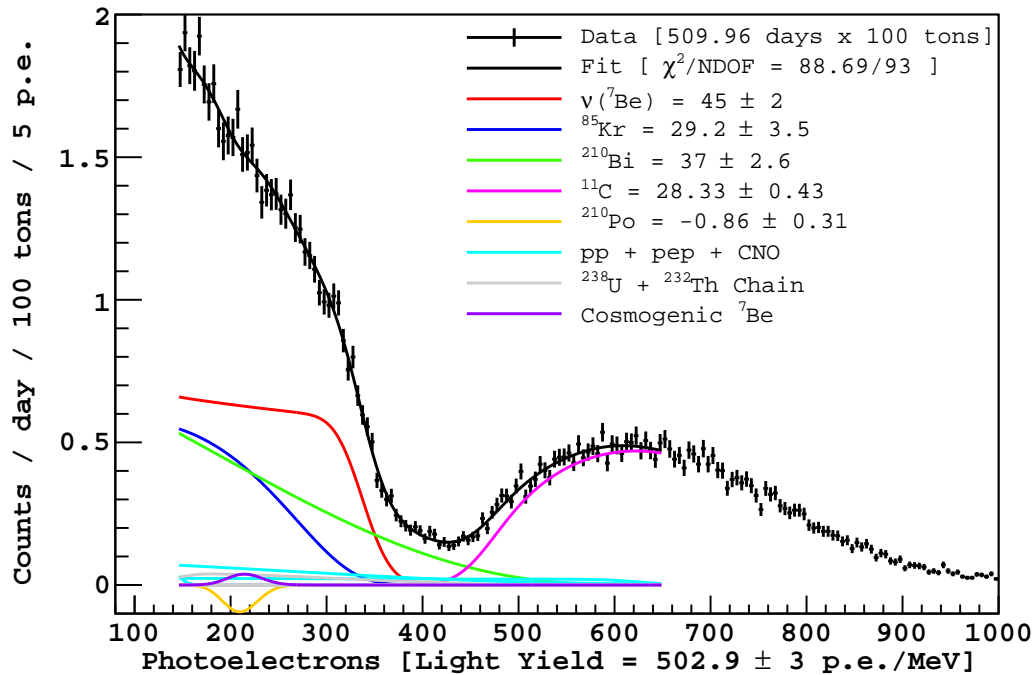

Figure 6.21: Spectral fit to energy spectrum after the statistical subtraction of α decays, in linear scale. All rates are given in units of counts/day/100 tons.

6.7.4 Summary and Comparisons

Parameter	Value		
	Entire	Gatti Cut	Stat. Sub.
Energy Scale Parameters			
Light Yield [p.e./MeV]	500.1 ± 3.8	501.9 ± 3.5	502.9 ± 3.0
Response Function g_1	1.550 ± 0.003	1.551 ± 0.004	Fixed (1.551)
Response Function g_2	3.11 ± 0.09	3.02 ± 0.13	Fixed (3.07)
Response Function g_3	2×10^{-13}	1×10^{-11}	Fixed (0)
Response Function g_4		Fixed (0)	
^{11}C Quenching	0.887 ± 0.008	0.884 ± 0.008	0.882 ± 0.007
^{210}Po Quenching	0.0791 ± 0.0006	0.0788 ± 0.0005	Fixed (0.0789)
Solar Neutrinos			
^{7}Be Count Rate	46.3 ± 3.0	45.4 ± 2.6	45.0 ± 2.0
^{210}Pb Daughters			
^{210}Bi Count Rate	39.3 ± 3.1	38.0 ± 2.9	37.0 ± 2.6
^{210}Po Count Rate	2117 ± 2	1066 ± 2	-0.86 ± 0.31
Cosmogenic Isotopes			
^{11}C Count Rate	28.44 ± 0.44	28.52 ± 0.44	28.33 ± 0.43
Other Backgrounds			
^{85}Kr Count Rate	26.5 ± 5.9	27.9 ± 5.2	29.2 ± 3.5
^{40}K Count Rate	1×10^{-9}	3×10^{-10}	1×10^{-12}
Goodness of Fit			
χ^2 / NDOF	85.83 / 89	87.71/ 89	88.69 / 93
p Value	0.575	0.519	0.607

Table 6.15: Standard Fit Results. All count rates are given in counts/day/100 tons. The ^{7}Be rate is only for the 0.862 MeV branch. All uncertainties listed are values returned directly by MINUIT from the fit. For a discussion of the systematic uncertainties, see Section 6.8.2.

As can be seen by the results of the different fits, summarized in Table 6.15, the values obtained for each of the fitted parameters are fairly consistent. We note that while the differences are smaller than the given uncertainties, the data sets are not independent. In fact, the only difference between the data in the three fits is the α content. Since the fraction of events that are αs in the fit region is about 97%, the statistically subtracted spectrum is a small subset of the entire data spectrum. While the exact correlation between the spectra has not been evaluated, the good agreement between the fits increases our confidence in the result. The species with the largest

difference between the fits, as well as the largest fractional uncertainty is ^{85}Kr. The fitted rate for ^{85}Kr is strongly determined by the count rate in the valley between ^{14}C and ^{210}Po, which is very sensitive to the α content in the spectrum. We point out that the ^{85}Kr rate from the fits is in very good agreement with the independent estimate of the contamination from the delayed coincidences: 30.4 $\pm$ 5.3 (stat) $\pm$ 1.3 (sys) cpd/100 tons (see Section 3.2.3 for details). For the parameter of interest, ^{7}Be, the fitted rate spans a range of 1.3 cpd/100 tons (2.8%). For the purpose of conducting various systematics tests, described in the next section, we had to pick a single fit method as our baseline for comparison. Since there is some uncertainty as to the true contamination of the ^{238}U and ^{232}Th decay chains, and the rate of αs in those chains have a strong effect on the fit result for the entire spectrum as well as the α cut spectrum, we believe that the result from the statistically subtracted spectrum is the most trustworthy. For this reason all further checks and tests were performed on the statistically subtracted spectrum.

For completeness, Figure 6.22 shows the fit to the statistically subtracted spectrum on an energy scale, while Table 6.16 gives the correlations between the fit components, as calculated by the minimization program MINUIT. Finally, we attempt to fit the data energy spectrum without the inclusion of an electron recoil spectrum from ^{7}Be neutrinos (Figure 6.23). As can be seen from the reduced χ^2, the fit is very poor. In addition, the fitted ^{85}Kr value is in strong disagreement with the independent measurement from delayed coincidences and the light yield is much higher than that measured by the calibration sources (492 $\pm$ 2 p.e./MeV). Thus the observed data is incompatible with the absence of ^{7}Be neutrinos.
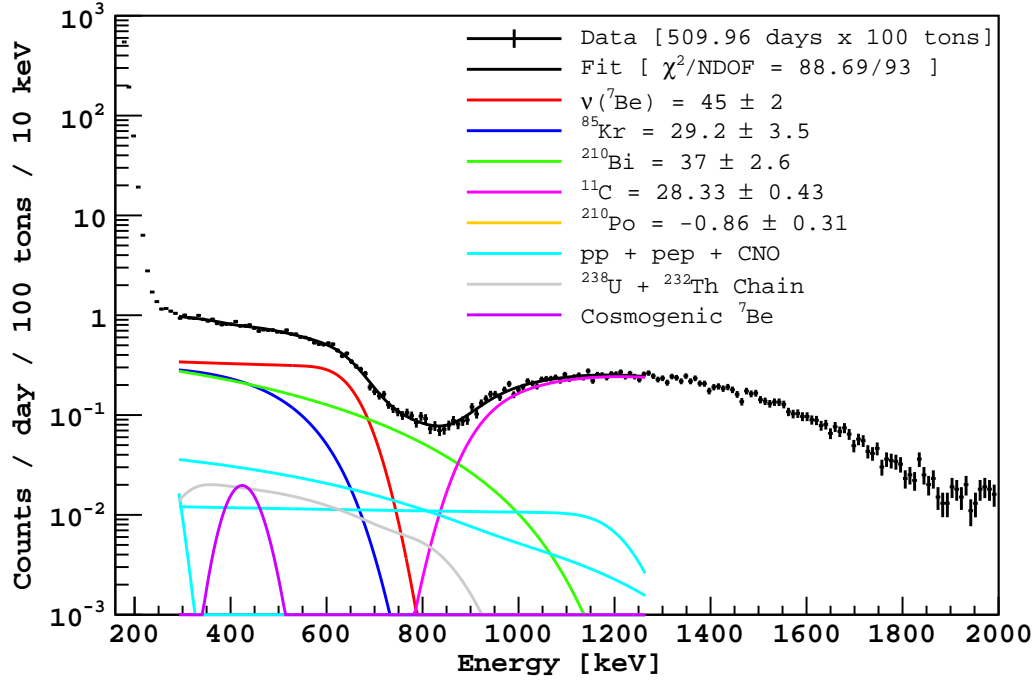
Figure 6.22: Spectral fit to energy spectrum after the statistical subtraction of α decays, shown on an energy scale. All rates are given in units of counts/day/100 tons.

	L.Y.	^{11}C Quen.	^{7}Be	^{85}Kr	^{210}Bi	^{11}C	^{210}Po	^{40}K
L.Y.	1.000	-0.874	-0.516	0.825	-0.770	0.267	-0.095	0.004
^{11}C Quen.	-0.874	1.000	0.346	-0.739	0.802	0.015	0.085	0.002
^{7}Be	-0.516	0.346	1.000	-0.693	0.066	-0.195	0.170	0.002
^{85}Kr	0.825	-0.739	-0.693	1.000	-0.691	0.210	-0.373	0.010
^{210}Bi	-0.770	0.802	0.066	-0.691	1.000	-0.134	0.078	-0.024
^{11}C	0.267	0.015	-0.195	0.210	-0.134	1.000	-0.025	-0.005
^{210}Po	-0.095	0.085	0.170	-0.373	0.078	-0.025	1.000	-0.002
^{40}K	0.004	0.002	0.002	0.010	-0.024	-0.005	-0.002	1.000

Table 6.16: Correlation matrix for the free parameters of the spectral fit, as determined by the minimization program MINUIT.
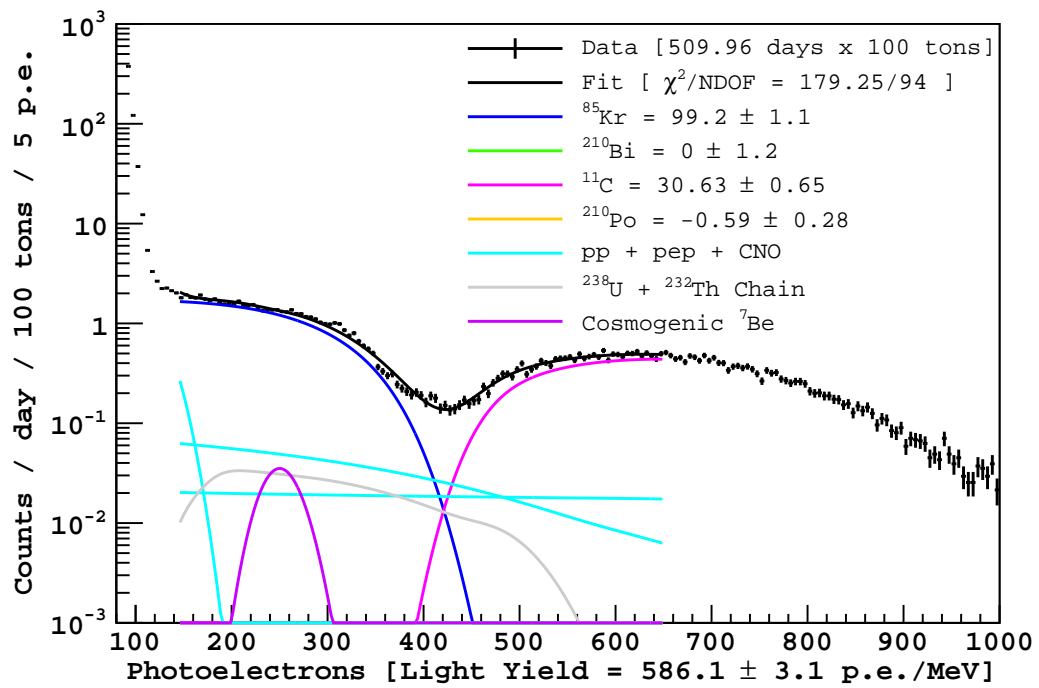
Figure 6.23: Spectral fit to energy spectrum, without the inclusion of an electron recoil spectrum from ^{7}Be neutrinos. All rates are given in units of counts/day/100 tons.

## 6.8 Checks, Systematics and Uncertainties

6.8.1 Consistency Checks

Two independent consistency checks were performed on the data and fit results.

6.8.1.1 Fitting Individual Time Periods

The entire chain of analysis, starting from the event selection to the statistical subtraction was performed independently on the 7 different periods listed in Table 6.1 (periods 1a and 5a were excluded due to low statistics). The spectra were then fit, using the same method that was applied to the entire data set. The results for the main fit components are shown in Figure 6.25. For all the components except ^{210}Bi (whose level increased throughout the data-taking period) we have fit a constant line, shown in black, through all seven periods. For comparison, we have also overlaid the 1σ band (red) for the best fit result for all periods combined. Both ^{7}Be and ^{85}Kr, as well as the energy scale parameters, show good agreement with the hypothesis of a constant value through all periods, as well as good agreement with the fit result for all periods. The fitted ^{11}C rate displays a non-Gaussian distribution around its mean value. This is due to the fact that ^{11}C is cosmogenic and is often produced in large bursts that do not follow a Poisson process [72].

We have also included, for comparison (but not in the above-mentioned constant fits), results for period 8, which extends from 14th February 2010 to 2nd May 2010 (Runs 12489 - 12940) and has a pre-cut livetime of 68.5 days. This period was included in the analysis used in the recent publication [86] but has been excluded from this analysis for the following reasons:

- Laben Firmware Change

  Between period 7 and 8 the firmware on the Laben boards was changed as part of an upgrade. During the July 2011 Borexino general meeting it was

shown that this change introduced extra hits for each event, as compared to the old firmware. This has the effect of increasing the ^{210}Po peak position by about 4 hits. Since these extra hits had very low recorded charge, no effect is directly visible in the charge variable. However since a lot of the selection cuts (most notably the position reconstruction and the Gatti parameter) depend on the number of hits and not the charge, the extra hits can still affect the final energy spectrum. It is currently not clear whether these hits are physical or the result of faulty firmware, though even if the hits are physical, our entire energy calibration, position reconstruction, and event selection, were tuned using the old firmware.

- In mid March 2010, during period 8 ($\sim$ Run 12626), the Inner Vessel was filled with about 9 m^3 of pure PC (without the PPO wavelength shifter) from the top. Due to the lack of PPO, events occurring in the region of the newly filled scintillator were recorded at a lower effective energy, as compared with events in the rest of the Inner Vessel. While the added scintillator seemed to have remained outside of the fiducial volume, fairly well separated from the rest of the Inner Vessel (stratified above $z \sim 3.25$ m - see Figure 6.24), it is possible that some of these events with lower reconstructed energy, especially those under the top end cap, may have mis-reconstructed within the fiducial volume, changing the spectral shape.

From Figure 6.25 one can see that the fit result of ^{85}Kr for period 8 (3.4 ± 12.0) is significantly lower than that of other periods, and the ^{7}Be, whose fit result is anti-correlated with ^{85}Kr, is significantly higher (58.7 ± 6.3). The fitted lightyield is also lower than average for this period. While the differences from other periods are only on the order of two standard deviations, and could therefore be statistical fluctuations, we also note that fitting the entire spectrum, without any α subtraction, for this period gives a poor goodness-of-fit (p-value = 0.03).
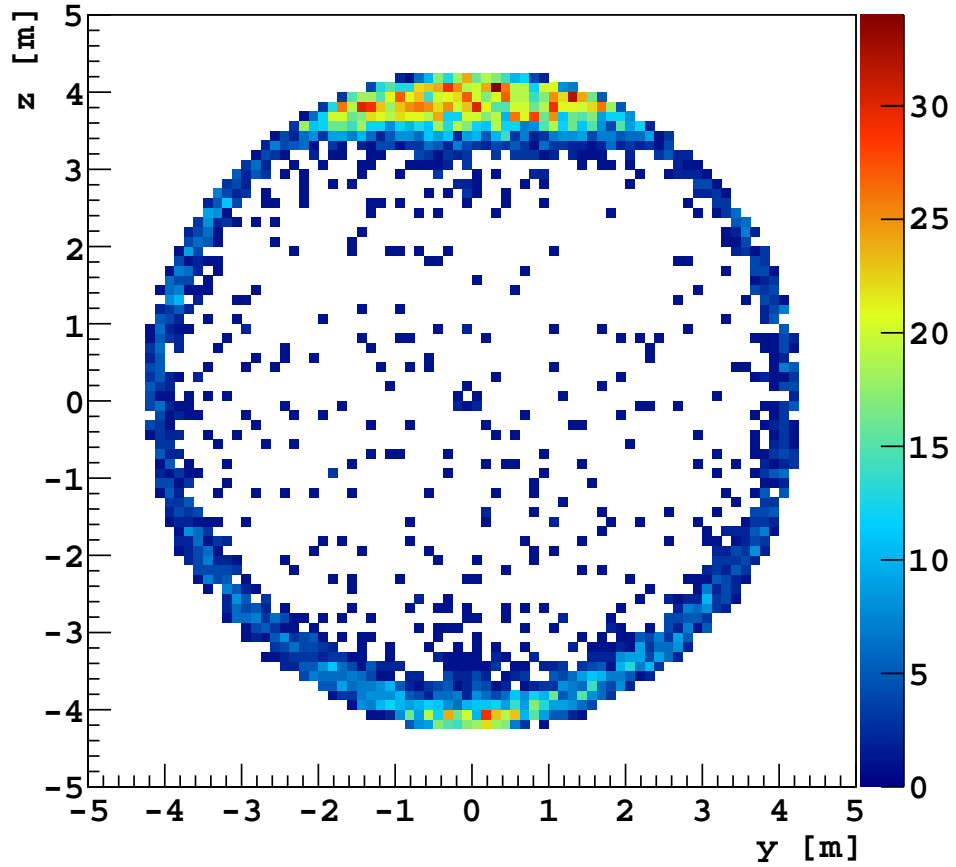
Figure 6.24: Spatial distribution (in the $z - y$ plane, $|x| < 0.5$ m) of events in the 140 - 150 p.e. energy region (^{14}C-^{210}Po valley) for runs in period 8, following the filling of the Inner Vessel with pure PC in March 2010. The layer of newly added scintillator (~ 9 m^3) is clearly visible from the high rate of events at $z > 3.25$ m. These events are thought to be ^{210}Po decays, degraded in energy due to the lack of wavelength shifter (PPO) in the added scintillator.

Due to the combination of the firmware change (whose effects are still being investigated), the addition of pure pseudocumene (without PPO), and the anomalous results of the fits, it was decided that it is safer to exclude this period from this analysis. For completeness, the fit results for all periods, including period 8, are shown in Table 6.17. We point out that, including period 8, we obtain values in closer agreement with those presented in [86] which also included period 8.

Periods	^{7}Be [cpd/100 tons]	^{85}Kr [cpd/100 tons]	^{210}Bi [cpd/100 tons]	^{11}C [cpd/100 tons]
1 - 7	45.0 ± 2.0	29.2 ± 3.5	37.0 ± 2.6	28.33 ± 0.43
1 - 8	46.4 ± 1.9	26.8 ± 3.4	40.5 ± 2.6	28.12 ± 0.41

Table 6.17: Comparison of fit results when including / excluding period 8. A firmware change was applied to DAQ electronics between period 7 and 8.

6.8.1.2 Fitting Reduced Fiducial Volume

In order to study the effect of external backgrounds and non-uniform light conversion within the fiducial volume we also attempted a fit on a reduced fiducial volume with a radial cut at 2.5 m and a vertical cut to exclude regions with $|z| > 1.0$ m. The new fiducial volume has a volume of 37.2 m^3 with a corresponding mass of 32.7 tons. The spectrum was fit using the same method that was applied to the entire data set and the results are shown in Table 6.18.

Fiducial Vol.	^{7}Be [cpd/100 tons]	^{85}Kr [cpd/100 tons]	^{210}Bi [cpd/100 tons]	^{11}C [cpd/100 tons]
$r < 3.021$ m $|z| < 1.67$ m	45.0 ± 2.0	29.2 ± 3.5	37.0 ± 2.6	28.33 ± 0.43
$r < 2.5$ m $|z| < 1.0$ m	48.8 ± 3.0	37.1 ± 11.5	18.4 ± 18.5	27.61 ± 0.96

Table 6.18: Comparison of fit results between the standard fiducial volume (75.7 tons) and a reduced fiducial volume (32.7 tons).

We see that the results are comparable to the fit using the standard fiducial volume, though the uncertainties on the ^{85}Kr and ^{210}Bi rates are much larger. Note that the data sets are not statistically independent; the reduced fiducial volume is a subset (43%) of the standard one.

6.8.2 Statistical Uncertainty

The uncertainties returned by the fitting routine (MIGRAD in MINUIT) include correlations between all other free parameters. Thus the values listed in the previous sections include the uncertainty in the energy scale (namely the fiducial-volume-
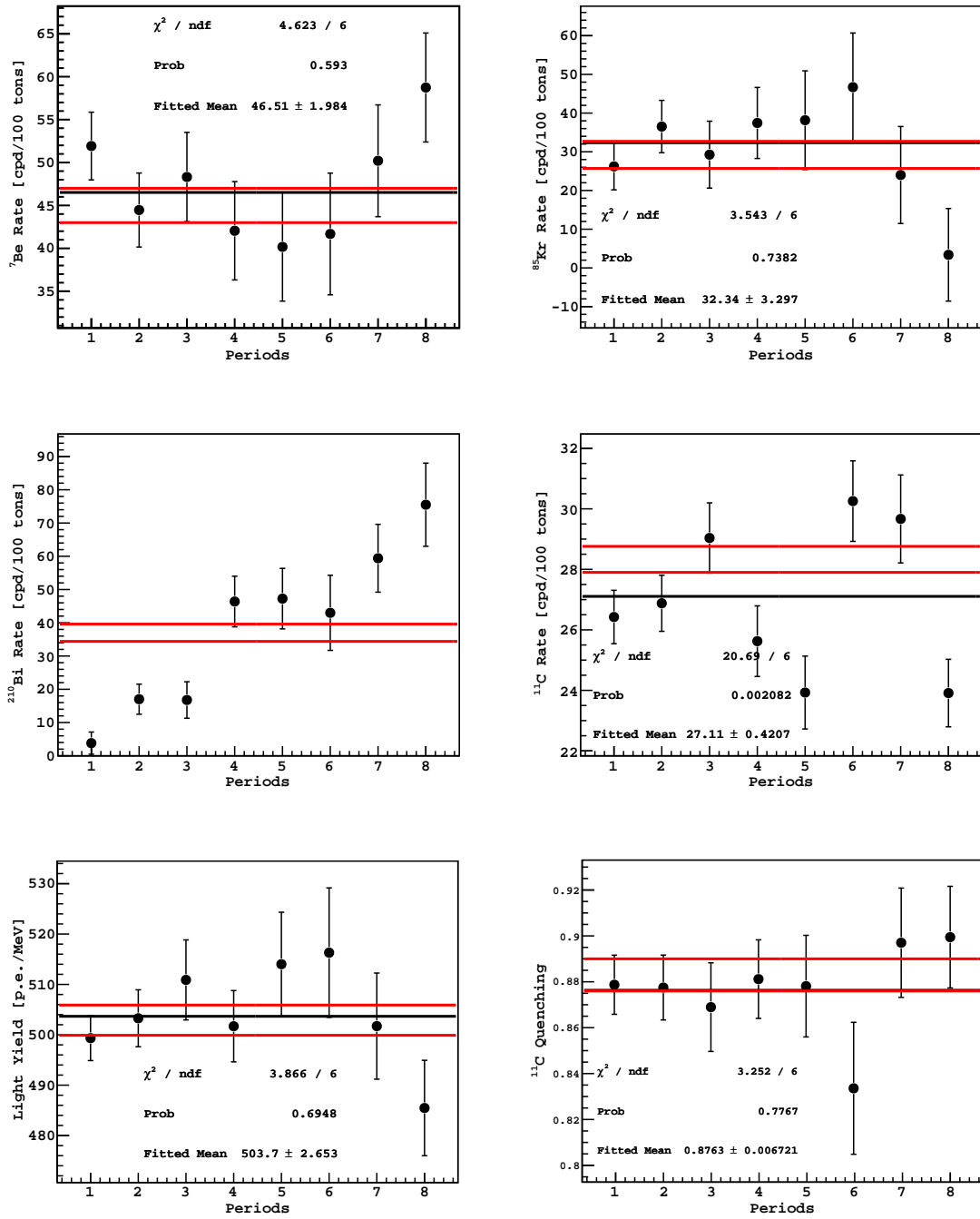
Figure 6.25: Fit results for individual periods. Statistics displayed in text box are for a fit to a constant value across all periods (shown as black horizontal line). The region between the red lines depicts the 1σ band around the best fit value for all periods combined. Values for period 8 are only shown for reference - they are not included in the fit.

averaged detector lightyield and the ^{11}C quenching). To determine only the statistical component of the uncertainty of the ^{7}Be rate, as well as the backgrounds, we fixed all energy scale parameters in the fit (to their best-fit values) such that the only free parameters were the amplitudes of the various spectra. Using this method we estimate a statistical uncertainty of 1.6 cpd/100 tons (3.6%) in the ^{7}Be rate. The statistical uncertainties for the main components of the fit are shown in Table 6.19. By taking the difference (in quadrature) between the statistical and systematic uncertainties, we obtain an uncertainty of 2.7% for the free energy scale parameters of the fit (see Section 6.8.3.2 for more details).

Free Energy Scale Params	^{7}Be [cpd/100 tons]	^{85}Kr [cpd/100 tons]	^{210}Bi [cpd/100 tons]	^{11}C [cpd/100 tons]
None (Stat. Unc.)	45.0 ± 1.6 (3.6%)	29.2 ± 2.0 (6.8%)	37.0 ± 1.5 (4.1%)	28.33 ± 0.35 (1.2%)
LY, ^{11}C (Ene. Unc.)	45.0 ± 2.0 (2.7%)	29.2 ± 3.5 (9.8%)	37.0 ± 2.6 (5.7%)	28.33 ± 0.43 (0.9%)

Table 6.19: Comparison of the fit results with (top) / without (bottom) the energy scale parameters fixed. The uncertainties obtained with all energy scale parameters fixed are taken as the best estimate of the statistical uncertainty in the fitted rates. The difference (in quadrature) between the uncertainties with the energy scale parameters free and fixed are taken as the estimates of the uncertainty due to the energy scale parameters (see Section 6.8.3.2).

6.8.3   Systematic Uncertainty

6.8.3.1   Fit Parameters

In order to evaluate the effect of the various choice of parameters made during the fit procedure, such as binning, fit range etc, as well as the rate of the fixed species in the fit, we performed hundreds of fits, simultaneously varying each of the parameters within acceptable ranges and studied the results. We have listed the different parameters that were varied below, and summarized them in Table 6.20.

- Bin Width

The bin width was alternated between 5 and 10 photoelectrons. We could not reduce the bin width smaller than 5 photoelectrons due to the statistics required for the statistical subtraction.

- Response Function Parameters

  The response function parameters were randomly chosen from a Gaussian distribution whose mean and variance were obtained from the fits without the statistical subtraction of αs (see first two columns of Table 6.15).

- ^{210}Po Quenching

  The ^{210}Po quenching, which determines the position of the ^{210}Po peak on the electron energy scale, was also randomly chosen from a Gaussian distribution whose mean and variance were obtained from the fits without the statistical subtraction of αs (see first two columns of Table 6.15).

- Offset

  The presence of PMT dark noise can cause an offset from zero in the energy scale. In order to prevent this, we have subtracted the estimated number of dark hits in each event. This estimation is done statistically (there is no way to identify a specific hit as dark noise) and an error in the estimate can cause there to be an overall offset in the spectrum. Given the average overall dark rate of 550 kHz for all PMTs, we expect (and therefore subtract) about one dark hit per event. To study the effect of a possible offset we varied the offset by a random number picked from a Gaussian with a mean of 0 and a standard deviation of 1 photoelectron.

- Fit Range

  Both the start and end points of the fit range were varied to study their effect on the fit results. The end point was varied from 600 to 800 photoelectrons. While there is evidence of external backgrounds above 650 photoelectrons, higher end-

points had a negligible effect on the fit. On the other hand, the fit results are sensitive to the starting point of the fit. Figure 6.26 shows the fitted ^{7}Be rate as a function of the fit starting point, which was varied uniformly between 130 and 170 photoelectrons. Each point represents the mean ^{7}Be rate with the corresponding starting point, averaged over all other parameters that were simultaneously varied. The error bars are the standard deviations of the distributions. The rate is found to be fairly stable for starting points in the range of 140 to 165 photoelectrons. The results for fits starting below 140 p.e. are not reliable due to the presence of ^{14}C pileup which affects the statistical subtraction (no pileup spectrum was included in the fit). There is a large jump in the fitted ^{7}Be rate for fits starting at 170 p.e. Individual fits at higher starting values also return comparably high values for the ^{7}Be rate. The cause of this is currently unknown, but could be due to biases in the statistical subtraction under the ^{210}Po peak. Further investigation is warranted, but for this analysis we have decided to restrict the fit range between 140 and 165 photoelectrons, where the statistical subtraction is known to be reliable. We recall the previous test, in which the ^{210}Po peak region was excluded from the fit, returned consistent results, indicating that biases in the subtraction under the ^{210}Po peak do not significantly change the results when the fit is started below the ^{210}Po energy.

- ^{214}Pb Rate

  The ^{214}Pb count rate, was randomly picked from a Gaussian distribution whose mean and variance were obtained from the ^{214}Bi-Po coincidence method described in Section 3.2.6.1.

- Solar Neutrino Rates

  The solar neutrino rates for *pp*, *pep* and CNO solar neutrinos, that are fixed in the fit, were chosen from Gaussian distributions whose mean and variance
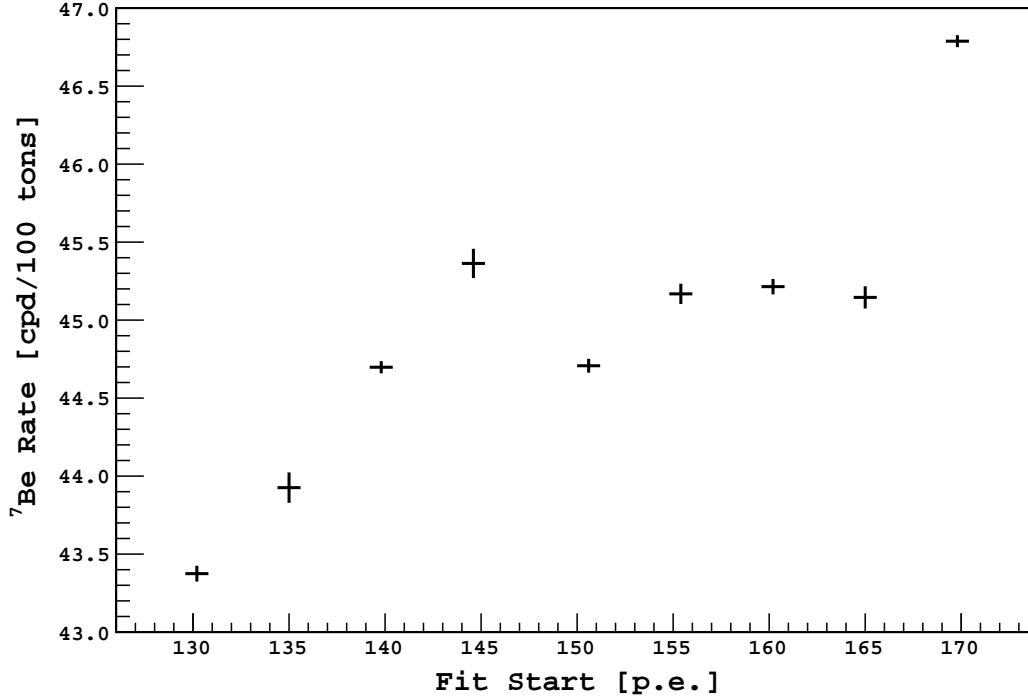
Figure 6.26: Dependence of the fitted ^{7}Be rate on the starting point of the fit. Fits starting below 140 p.e. are affected by ^{14}C pileup which leads to unreliable results. The large increase in the fitted rate for fits starting at 170 p.e. is not well understood, but is possibly related to small biases in the statistical subtraction of αs.

were taken from [17]. Correlations between the neutrino fluxes were introduced based on the values from [64].

- Background Spectra

  We alternated the shape factor used for the first forbidden transition ^{85}Kr β decay between the standard (see Table 6.8) and the shape factor proposed in [110].

  We note that there is a recent paper, [111], with an alternative description of the ^{210}Bi shape factor as compared to the previous standard found in literature [106]. Comparing fits performed with the new shape factor to the standard, we find that the fitted ^{7}Be rate changes by less than 0.5%, though the ^{210}Bi rate increases by about 8%. Since the effect on the ^{7}Be rate is negligible, we have

chosen to use the older results [106] based on the better documented and studied magnetic spectrometer measurements.

- Minimization Method

  We alternated the fit method between a standard χ^2 minimization and a negative log-likelihood minimization that assumed a Poisson distribution of counts in each bin.

Parameter	Values Assigned
Histogram Bin Width	5 p.e. or 10 p.e.
Response Function Parameter g_1	Gaussian (1.5505, 0.0024)
Response Function Parameter g_2	Gaussian (3.0672, 0.0795)
^{210}Po Quenching	Gaussian (0.07894, 0.00041)
Offset	Gaussian (0, 1) [p.e]
^{85}Kr Spectrum	Shape Factor: Standard or [110]
Fit Start	Uniform (140, 165) [p.e]
Fit End	Uniform (600, 800) [p.e]
^{214}Pb Count Rate	Gaussian (1.62, 0.06) [cpd/100 tons]
Solar Neutrino Rates	Central Values: Gaussian ([17])
	Correlations: [110]
Minimization Method	χ^2 or Poisson Likelihood

Table 6.20: List of fit parameters varied in order to study the associated systematic uncertainty. Gaussian (μ, σ) indicates that the value was randomly assigned from a Gaussian distribution with mean μ and variance σ^2. Uniform (a, b) indicates that the value was randomly chosen from a uniform distribution ranging from a to b, inclusive.

The effect of varying the above fit parameters on the ^{7}Be rate is shown in Figure 6.27. We see that the fitted rate ranges from 43.6 to 45.9 cpd/100 tons, depending on the combinations of parameters used for the fit. Taking the standard deviation of the distribution as an estimate of the 1σ systematic uncertainty related to the fit parameters, we have listed the results in Table 6.21.

6.8.3.2   Energy Scale

The uncertainty related to the free energy scale parameters in the fit (the fiducial-volume-averaged detector lightyield and the ^{11}C quenching) can be estimated by tak-
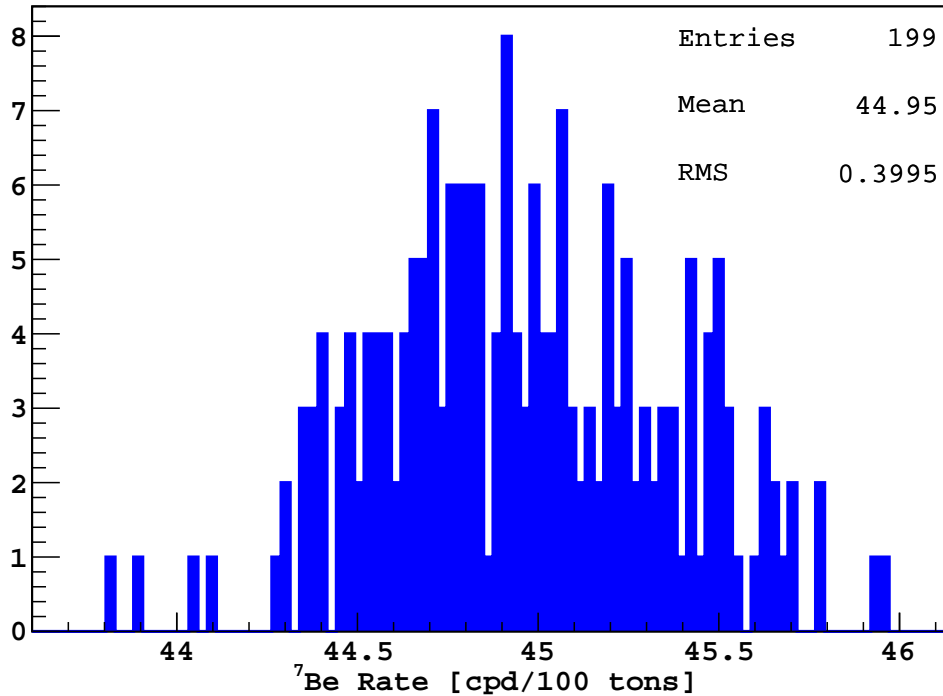
Figure 6.27: Distribution of the fitted ^{7}Be rates when the fit parameters (listed in Table 6.20) are simultaneously varied. The standard deviation of the distribution is taken as the estimate of the systematic uncertainty associated with the fit parameters.

ing the difference, in quadrature, between the uncertainties when the parameters are left free and when they are fixed. Referring to Table 6.19, we see that for the ^{7}Be rate this gives an uncertainty estimate of $\sqrt{2.0^2 - 1.6^2} = 1.2$ cpd/100 tons, equivalent to a 2.7% fractional uncertainty. The corresponding uncertainty for the other main components of the fit are listed in parenthesis in the second row of Table 6.19.

Along with the lightyield and the ^{11}C quenching, there are also systematic uncer-

Fit Parameters	^{7}Be	^{85}Kr	^{210}Bi	^{11}C
Uncertainty	%	%	%	%
1σ	0.88	3.8	4.5	0.5

Table 6.21: 1σ systematic uncertainties related to the fit parameters, for the main components in the fit. Values are obtained from the standard deviation of the distribution of fit results when simultaneously varying the fit parameters. For example see Figure 6.27 for the ^{7}Be distribution.

tainties related to the Cherenkov light emission (see Section 5.2.1.2) and the non-linear relationship between the charge variable and the true number of photoelectrons (see Section 5.2.3). Due to computational constraints we were unable to leave these parameters free in the fit and had to vary them manually to estimate the associated uncertainties. We performed a fit in which the effective quenching ignored the contribution of Cherenkov light, and also one in which the non-linear factor b was set to zero. The results of the fits are summarized in Table 6.22. Though these changes represent fairly extreme cases for the energy scale, we have chosen to use them as conservative 1σ uncertainties. Since both the tests caused the fit results to change in the same direction we have chosen to symmetrize the uncertainties by introducing a shift in the central value, using the rules prescribed in [112]. For one-sided uncertainties σ_i, the central value is shifted by an amount equal to half the sum of the uncertainties $(\frac{1}{2}\Sigma\sigma_i)$. The variance of the new central value is then given by $\frac{3}{4}\Sigma\sigma_i^2$. The result of the symmetrization is shown in the last row of Table 6.22.

Fit Type	^{7}Be % Change	^{85}Kr % Change	^{210}Bi % Change	^{11}C % Change
No Cherenkov	+1.0	-1.4	+0.72	-0.36
$b = 0$	+0.82	-1.4	+0.48	-0.14
Combined	$+0.91 \pm 1.1$	-1.4 ± 1.7	$+0.60 \pm 0.75$	-0.25 ± 0.33

Table 6.22: Effect of varying the fixed energy scale parameters (Cherenkov light contribution and non-linear charge response) on the main fit components. For details about the energy scale parameters, see Section 5.2. The last row gives the combined uncertainty, symmetrized according to the rules prescribed in [112]. The first number in each column is the fractional shift in the central value, and the second column represents the fractional uncertainty in the new central value.

The combined systematic uncertainties related to the energy scale (for both free and fixed parameters) are calculated by adding the uncertainties from Tables 6.19 and 6.22 in quadrature. The shift in the central value comes directly from the asymmetric errors in the fixed parameters. The results are summarized in Table 6.23.

| Energy Scale | ^{7}Be | ^{85}Kr | ^{210}Bi | ^{11}C |
Uncertainty	%	%	%	%
Shift (δ)	+0.91	-1.4	+0.60	-0.25
1σ	2.9	9.9	5.7	0.96

Table 6.23: Combined energy scale systematics for both the free (Table 6.19) and fixed energy scale parameters (Table 6.22). The first row gives the fractional shift in the central value calculated from the asymmetrical uncertainties related to the fixed parameters while the second row gives the total uncertainty, added in quadrature.

Comparison to source calibration data   As discussed in Section 5.2, the energy scale used for the fit is obtained from the γ source calibration data and Birk's Model for scintillation light (there is also a small contribution from Cherenkov light). Birk's model has two free parameters, a linear scaling, referred to as the lightyield, and a term responsible for the non-linear response, referred to as kB. From the γ source calibration data we obtained a detector lightyield, at the center of the detector of 488.5 ± 1.6 p.e./MeV (see Section 5.2.2). Including the non-uniform light collection within the fiducial volume of 1.008 ± 0.002 (see Section 5.3) we predict a lightyield of 492 ± 2 p.e./MeV. However, leaving the lightyield free in the fit gives a value of 502.9 ± 3.0 p.e./MeV, about 3σ away from the source calibration data. Similarly, the quenching parameter for ^{11}C, which was left free in the fit, fits to a value of 0.882 ± 0.007, which is about 2σ away from the one obtained from the γ source calibration data (0.901 ± 0.006).

This discrepancy could be reasonably explained by a shadowing effect, in which the apparatus for the source insertion system blocks some of the light. However the ^{11}C starting point, which is determined by the number of photoelectrons produced by two 511 keV γ rays, in the data (502.9 p.e/MeV $\times 0.882 \times 1.022$ MeV $= 453$ p.e.) is in good agreement with the value obtained from the source calibration (492 p.e/MeV $\times 0.9011 \times 1.022$ MeV $= 453$ p.e.). Thus it seems that while the two parameter Birk's Model describes the γ energy scale well, the β energy scale prefers a higher detector lightyield.

In order to study this effect, we performed a fit in which the ^{11}C quenching was fixed to the central value of the source calibration. This resulted in an increase in the ^{7}Be fitted rate by 2 cpd/100 tons, more than 4% of the nominal value. However, as expected, the goodness of fit is considerably worse. Carrying out a likelihood ratio test on the fits, with and without the ^{11}C quenching fixed, we find that the central value of the ^{11}C quenching, as obtained from the source calibration data, is ruled out at the 99.5% C.L. Since this central value is obtained from the same method we use to calculate our β energy scale (see Section 5.2), this brings into question the accuracy of the energy scale model. Fortunately, the signal and background fit rates are not sensitive to the non-linearity of the β energy scale (as opposed to the ^{11}C starting point). Varying the kB parameter within 1σ of its best fit value changes the ^{7}Be fit result by less than 0.2%. As a model independent check, we also performed a fit assuming no non-linearity in the β energy scale (kB = 0). Even in this extreme case, the ^{7}Be value changed by only 1.9%.

The reason for the tension between the source calibration data and the ^{7}Be analysis dataset is currently unknown, but it has a large effect on the fitted ^{7}Be value (see Figure 6.28). As a check, we included the source calibration result as a constraint on the value for the ^{11}C quenching by adding a term:

$$\chi_c^2 = \left(\frac{^{11}\text{C Quenching} - 0.901}{0.006} \right)^2 \tag{6.22}$$

to the overall χ^2 of the fit. Figure 6.29 shows the profile of the original χ^2 (shown in black) as the ^{11}C quenching is fixed to various values around the minimum (0.882 ± 0.007). The red data points show the modified profile after the addition of the constraint term χ_c^2. The new minimum is located at a ^{11}C quenching value of 0.893±0.001. We then redid the standard fit, fixing the ^{11}C quenching to the new value and obtained the results listed in Table 6.24. Since all of the changes are smaller than the

uncertainty related to leaving the lightyield and ^{11}C quenching free in the fit (see values in parenthesis in the second row of Table 6.19) we have chosen not to include an additional uncertainty associated with this effect. However we do strongly recommend a much more detailed analysis of the energy scale in order to understand the origin of the discrepancy between the calculated β and γ energy scale.
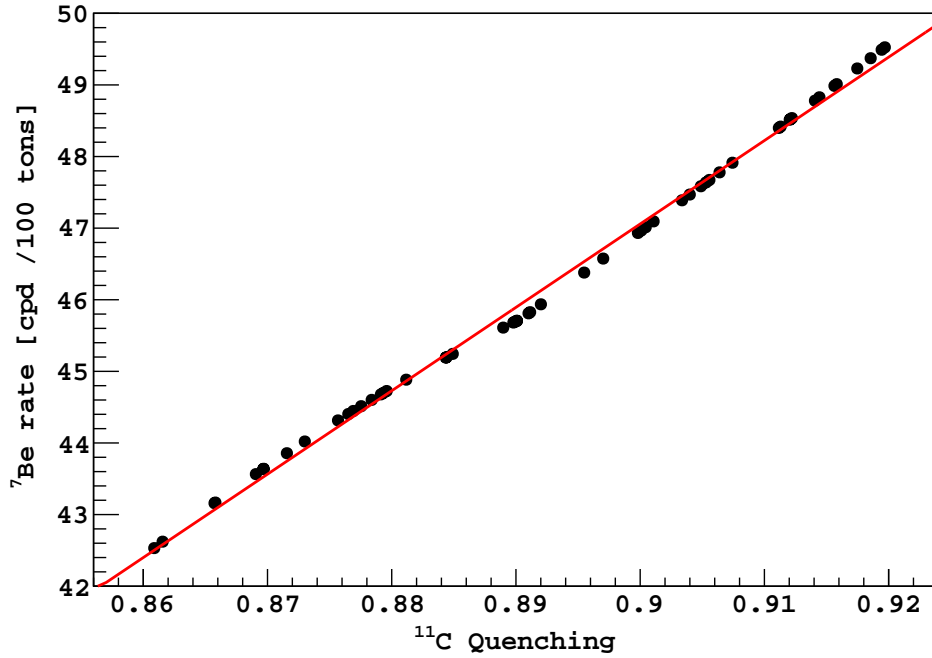
Figure 6.28: Dependence of the fitted ^{7}Be rate on the value of the ^{11}C quenching in the fit. Red line shows a linear fit to the data.

^{11}C Quench.	^{7}Be [cpd/100 tons]	^{85}Kr [cpd/100 tons]	^{210}Bi [cpd/100 tons]	^{11}C [cpd/100 tons]
Left Free	45.0 ± 2.0	29.2 ± 3.5	37.0 ± 2.6	28.33 ± 0.43
Fixed (0.893)	46.1 ± 2.0 ($+2.4\%$)	26.4 ± 9.8 (-9.6%)	38.3 ± 15.6 ($+3.5\%$)	28.28 ± 0.64 (-0.2%)

Table 6.24: Change in fit values for main components, when ^{11}C quenching is fixed to the value obtained from applying the source calibration data constraint (see Figure 6.29).
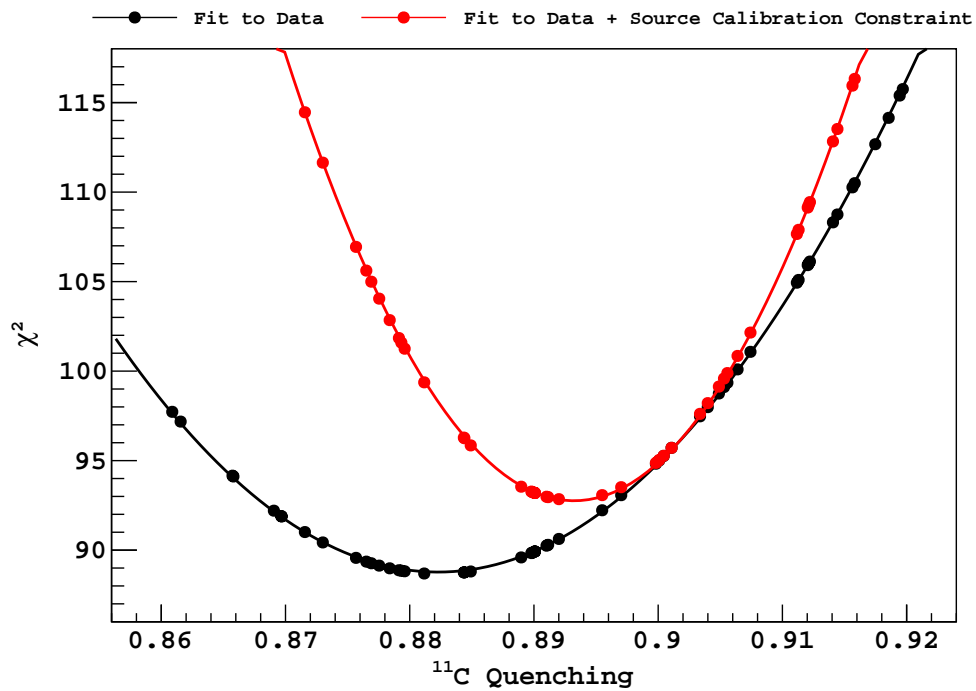
Figure 6.29: Black: Minimized χ^2 versus different (fixed) values of the ^{11}C quenching. Red: Modified χ^2 distribution , including constraint on ^{11}C quenching value based on source calibration data (see Eq. 6.22). Solid lines are second-order polynomial fits to the data.

6.8.3.3 Excluded Spectra

Figure 6.30 shows the internal backgrounds that were excluded from the spectral fit due to their small contribution in the fit region. The rates for the cosmogenic isotopes are set to the values given in Section 6.2.3.2, while the isotopes from the long-lived decay chains of ^{238}U and ^{232}Th are fixed assuming secular equilibrium throughout the chain (see Sections 3.2.6.1, 3.2.6.2). The rate of electron recoils from ^{8}B neutrinos is set to the value predicted by the LMA-MSW solution. For comparison we also show the expected ^{7}Be spectrum (red). We note that the spectra are obtained directly from Geant4 [113] and are not convolved with the detector energy response function. The energy scale is also not completely accurate since the individual γ and α energies have not been quenched, however this has a minimal effect on the shape of the background in the fit energy range (290 - 1300 keV). Most of these background spectra were excluded from the fit because their exact rate is not known, and is too small to be accurately determined by the spectral fit. In order to estimate the effect of excluding these spectra, a constant spectrum at a rate of 1×10^{-2} cpd/100 tons/10 keV (mimicking the estimated total excluded background spectrum in Figure 6.30) was added to the fit. The relative change in the results of the fit are given in Table 6.25 for the major components.

To study the effects of excluding the external background we performed a fit using the *g4bx* Monte Carlo simulated background spectra for ^{40}K, ^{214}Bi and ^{208}Tl (see Figure 3.1). The rates were fixed to the estimates from independent fits to high energy regions of the spectrum (Table 3.7 in Section 3.2.11) and the energy scale for the Monte Carlo spectrum was fixed (unlike the rest of the species for which the lightyield and ^{11}C quenching is left free.) The relative change in the fitted rate for the major components is shown in Table 6.25.

While it seems counter-intuitive for the fitted ^{7}Be rate to increase when additional backgrounds are included at a fixed rate, it can be explained by studying the different

Excluded Backgrounds
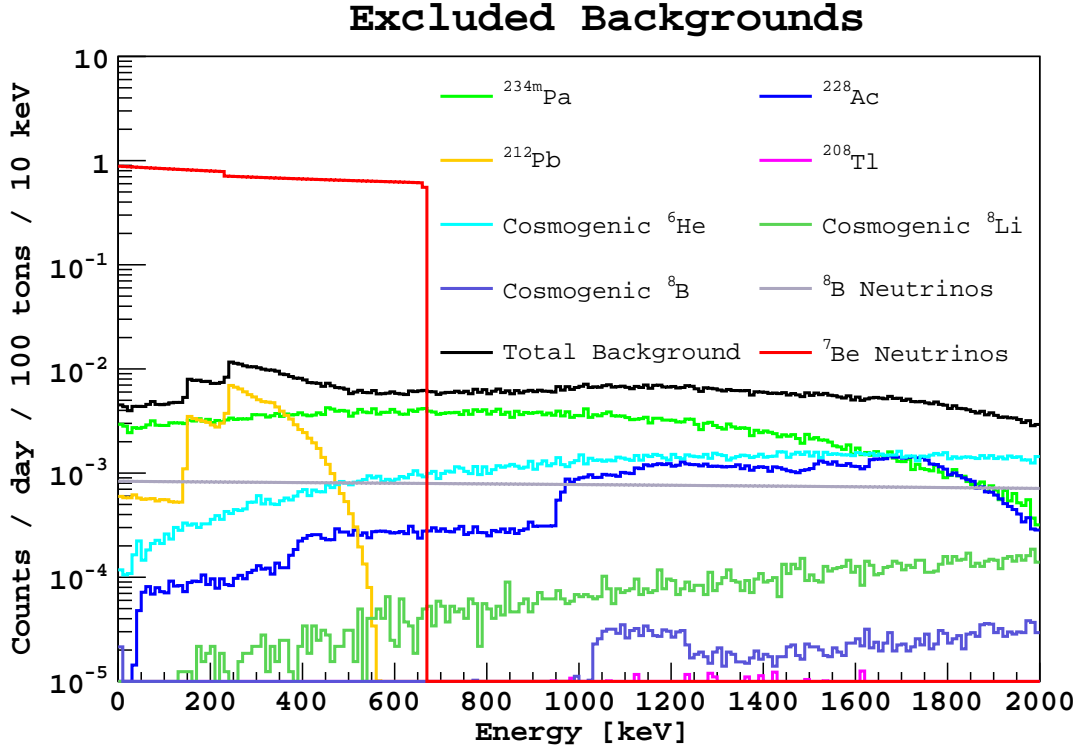
Figure 6.30: Known internal backgrounds that were excluded from the fit. The rates of the cosmogenic isotopes were taken from Section 6.2.3.2. Cosmogenic isotopes with expected residual rates below 0.05 cpd/100 tons are not shown. The rates of the decay chain isotopes were obtained assuming secular equilibrium (see Sections 3.2.6.1, 3.2.6.2). Solar neutrino rates are calculated using the LMA-MSW solution with the ^{7}Be spectrum (red) shown for reference. The energy spectra do not include the detector energy resolution or quenching of γs and αs.

spectral shapes of the fit components. For the fit components that dominate in a single energy region, such as ^{210}Bi in the ^{7}Be - ^{11}C valley, and ^{11}C at higher energies, the fitted rate expectedly decreases when other backgrounds are included in those regions. If ^{210}Bi decreases, the ^{7}Be and ^{85}Kr rates are then forced to increase to compensate in the lower energy regions. Since there is some uncertainty in the rates of the internal and external backgrounds, we have decided to take the difference between completely excluding them, and including them at our current best estimates, as a systematic uncertainty. The inclusion of neglected backgrounds create a one-sided uncertainty for all the components, and we once again symmetrize the uncertainties by introducing a shift in the central value [112], as was done for the energy scale in the previous

Fit	^{7}Be % Change	^{85}Kr % Change	^{210}Bi % Change	^{11}C % Change
Incl. Internal Flat Bkgd.	+ 0.64	+5.5	-7.8	-1.5
Incl. External Bkgd.	+ 0.86	+4.65	-5.9	-3.5
Incl. Int. & Ext. Bkgd.	+ 1.51	+10.6	-14.5	-5.2
Symmetrized Unc.	$+0.75 \pm 1.3$	$+5.3 \pm 9.2$	-7.3 ± 12.6	-2.6 ± 4.5

Table 6.25: Relative change in fit results when including estimates for internal and external backgrounds. The first row shows the results for a flat spectrum (1×10^{-2} cpd/100 tons/10 keV), designed to mimic the sum of all the neglected internal backgrounds. The second row lists the change when ^{40}K, ^{214}Bi and ^{208}Tl external background spectra (spectra generated by the *g4bx* MonteCarlo program, rate set to the values in Table 3.7 of Section 3.2.11) are included in the fit. The third row shows the results when both are simultaneously included, and the last row gives the symmetrized uncertainties [112], where the first number in each column is the fractional shift in the central value, and the second column represents the fractional uncertainty in the new central value.

section. The resulting changes are listed in the final row of Table 6.25.

6.9 Results

Using the central values from our baseline fit to the statistically subtracted spectrum (see Sections 6.7.3 and 6.7.4) and the various statistical and systematic uncertainties, summarized in Table 6.26, we obtain a final result for the measured ^{7}Be rate as 45.4 ± 1.6 (stat) ± 1.5 (sys) cpd/100 tons. The combined uncertainty on the central value is 4.9%. The final result for the other main components of the fit are listed in Table 6.27. Systematic errors are always hard to estimate and often include some degree of hand-waving and gut instincts. While we have tried to be as accurate as possible in evaluating the systematics, when there has been some ambiguity we have tried to err on the side of caution, perhaps leading to a larger coverage than the intended 1σ gold standard of 68%. As empirical evidence of the validity of the systematic uncertainty, we report that of the many hundreds of attempted variations on the analysis procedure, not a single central value fell outside the quoted 3σ range (99.7% C.I.) of the systematic uncertainty: [40.8 - 50.0] cpd/100 tons.

Source	Shift %	Uncertainty %	Reference Section
Statistical		3.6	6.8.2
Livetime		0.054	6.2.4
Annual Variation	+ 0.03		6.1.1
Fiducial Volume	- 0.81	0.78	4.3.1.1
Scintillator Density		0.045	2.1.2.2
Trigger Efficiency		< 0.1	6.2.3.1
Cut Sacrifice	+ 0.04	0.02	6.2.3.1
Residual Muons		< 0.026	6.2.3.2
Excluded Spectra	+ 0.75	1.3	6.8.3.3
Oscillation Parameters		0.07	6.6.1.1
Differential Cross Section		< 0.02	6.6.1.1
Fit Parameters		0.88	6.8.3.1
Energy Scale	+ 0.91	2.9	6.8.3.2
Total Systematic	+ 0.92	3.4	
TOTAL	+ 0.92	4.9	

Table 6.26: Summary of uncertainties related to the measured ^{7}Be neutrino interaction rate. The first column lists the source of the uncertainty, and the second and third columns give the corresponding fractional shift in central value and error. Details regarding each evaluation can be found in the section referenced in the last column. The systematic uncertainties are combined assuming no correlation between each source.

Comparing the results to the previous published measurement of the ^{7}Be rate after 192 days of data taking, 49 ± 3 (stat) ± 4 (syst) cpd/100 tons [114], we see that the systematic uncertainty has been greatly reduced. In particular, the uncertainty related to the fiducial mass has reduced from 6% to 0.8% and the energy scale uncertainty has been decreased from 6% to 2.9%. These reductions in the systematic uncertainty are mostly due to the series of calibration campaigns that took place since

Component	Central Value [cpd/100 tons]	Statistical Uncertainty [cpd/100 tons]	Systematic Uncertainty [cpd/100 tons]
^{7}Be	45.4	1.6	1.5
^{85}Kr	30.1	2.0	4.2
^{210}Bi	34.2	1.4	5.0
^{11}C	27.3	0.3	1.3

Table 6.27: Final results for the main signal and background components in Borexino. A itemized description of the individual systematic uncertainties for the ^{7}Be rate can be found in Table 6.26. Uncertainties for the other components were calculated in the same way.

the previous publication.

The ^{7}Be result presented here is fairly close to the value, $46.0\pm1.5(\text{ stat})^{+1.5}_{-1.6}$ (syst) cpd/100 tons, presented in the recent publication by the collaboration *"Precision measurement of the ^{7}Be solar neutrino interaction in Borexino"* [86], though the values for some of the other components differ. The main reason for the difference is that while a lot of the analysis described here was used for the publication, some of the work was carried out beyond the set cut-off date, as part of a continued study. During this period we have tried to address several issues, that we were either unable to study in time for the publication, or were raised soon after. The main differences in the analysis procedures are listed below:

- The analysis used for the publication included an additional period beyond the data set presented here. The issue regarding the implementation of the new DAQ firmware (see Section 6.8.1.1) only came to our attention in July 2011, after the finalization of the analysis for the publication. While the additional period is only a small fraction (9%) of the total livetime, it can be seen from the values in Table 6.17 that it has a large effect (3%) on the fitted ^{7}Be central value. We note that the ^{210}Bi rate continued to increase during this period, leading to the higher central value in the publication.

- At the time of the publication, the contribution of the αs in the heavy element decay chains to the spectrum (see Section 6.7.2) was not taken into account. This has a fairly large effect on the fit results for spectra in which the αs have not been statistically subtracted (see for example Table 6.13). This caused a higher fitted rate for the ^{85}Kr contribution, and correspondingly lower ^{7}Be values in those fits. A large portion of the uncertainty described as "Fit Methods" in [86] is due to the difference between fitting a spectrum with a partial α cut (but not including all the decay chain αs) and fitting the statistically subtracted spectrum. We should point out that the α cut used in [86] removed a larger

fraction of αs than the one used here and so the exact magnitude of the effect can not be determined.

- The systematic uncertainty related to the true size of the fiducial volume was evaluated differently and the possible radial bias of the CCD camera reconstruction, described in Section 4.3.1.1, was not included at the time of publication. We also note that we have chosen to symmetrize the uncertainties and shift the central value, while asymmetric errors were used for the publication. For the purpose of comparison to the values listed in Table 6.26, the asymmetric uncertainties $\left(^{+0.5}_{-1.3}\right)$ in [86], if symmetrized, correspond to a shift in the central value by -0.4% and a systematic uncertainty of ±1.1%.

- The effect of neglecting background rates from internal and external radioactive isotopes, as well as some cosmogenics (Section 6.8.3.3), was only recently evaluated and therefore not included in the uncertainty presented in [86]. We note that besides having a significant contribution to the uncertainty in the ^{7}Be rate, this is the source of the dominant uncertainty in the ^{210}Bi and ^{11}C rates.

As a reminder, many of the changes listed above were solely the work of the author, and are not necessarily endorsed by the entire collaboration.

In conclusion, we remark that the analysis and result presented here represents the first precision ($< 5\%$) measurement of the ^{7}Be solar neutrino interaction rate and achieves the primary goal of the Borexino experiment, first conceived in 1989.

Chapter 7

Implications

In the previous chapter we discussed the details of the measurement of the ^{7}Be neutrino interaction rate in Borexino yielding a result of 45.4 ± 1.6 (stat) ± 1.5 (sys) cpd/100 tons. Here we will compare that measurement to the predictions of the Standard Solar Model as well as the LMA-MSW neutrino oscillation framework. We will also study the implications of this measurement on the determination of the survival probability at different energies by combining results from different experiments. As with the previous chapter, we will restrict ourselves to discussing the 0.862 MeV ^{7}Be neutrinos, unless explicitly mentioned. We will also only consider the widely accepted three neutrino scenario.

7.1 ^{7}Be Neutrino Flux

The experimental result discussed in the previous chapter measured the rate of interaction of the ^{7}Be neutrinos through neutrino-electron elastic scattering. In order to convert this rate into a neutrino flux, we must include the cross section for the interaction as well as the number of target electrons:

$$R = \left(\Phi_{\nu_e} \sigma_{\nu_e} + \Phi_{\nu_{\mu,\tau}} \sigma_{\nu_{\mu,\tau}} \right) n \tag{7.1}$$

where R is the measured interaction rate, Φ_{ν_e} is the electron neutrino flux, $\Phi_{\nu_{\mu,\tau}}$ is the combined muon and tau neutrino flux, σ_x is the total electron scattering cross section for the corresponding neutrino flavor and n is the number of electrons in the target. Since the scattering cross section is different for ν_e, as compared to ν_μ and ν_τ, we cannot determine the total neutrino flux, but only the relationship between the fluxes of the different neutrino flavors. We can rewrite the above equation as:

$$\Phi_{\nu_e} = -\frac{\sigma_{\nu_{\mu,\tau}}}{\sigma_{\nu_e}}\Phi_{\nu_{\mu,\tau}} + \frac{R}{\sigma_{\nu_e}n} \tag{7.2}$$

This linear relationship is shown in Figure 7.1 (blue band), where we have used the measured interaction rate of $R = (45.4 \pm 2.2)$ cpd/100 tons, $\sigma_{\nu_e} = (5.7828 \pm 0.0025) \times 10^{-45}$ cm^2, $\sigma_{\nu_{\mu,\tau}} = (1.28204 \pm 0.00077) \times 10^{-45}$ cm^2 (see Section 3.1.1.1) and $n = (3.307 \pm 0.003) \times 10^{31}$ electrons/100 tons. The slope of the band is given by the ratio of the scattering cross sections (0.22) and the width is the 1σ uncertainty, including the correlation between the cross section uncertainties ($\rho = -0.74$). The y-intercept, $\Phi_{\nu_e} = (2.75 \pm 0.13) \times 10^9$ cm^{-2} sec^{-1}, gives the predicted neutrino flux in the case of no oscillations. We note that we have so far not made any assumptions regarding astrophysical models of the Sun or neutrino oscillations. The only theoretical input is the neutrino-electron scattering cross sections, which are known to very high precision. In the next two sections we will compare this result with the Standard Solar Model and neutrino oscillation parameters. This will be done in two ways: first we will assume the validity of the Standard Solar Model and, combining its predictions with the current ^{7}Be measurement, predict a value for the electron neutrino survival probability, independent of the neutrino oscillation parameters. Alternately, using the LMA-MSW oscillation framework in conjunction with the ^{7}Be result, we will predict a ^{7}Be neutrino flux to be compared to the Standard Solar Model.
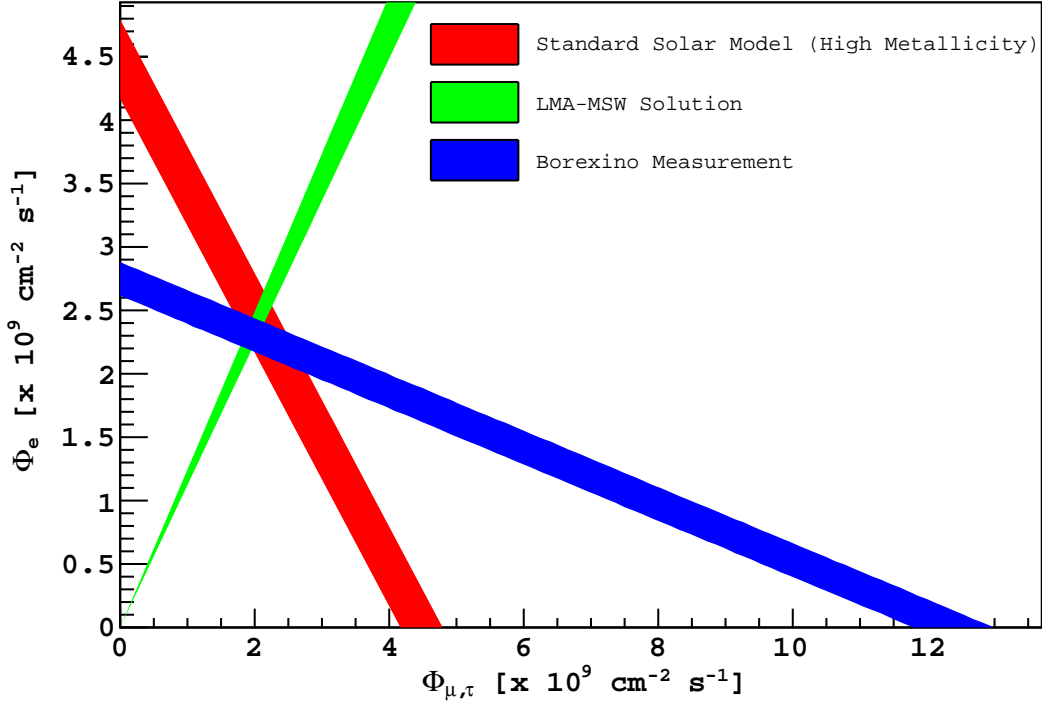
Figure 7.1: Relationship between the flux of electron and other neutrino flavors, for 0.862 MeV ^{7}Be neutrinos. The blue band shows the current experimental result for the ^{7}Be neutrino interaction rate (Eq 7.2). The red band shows the flux prediction based on the Standard Solar Model [17] (Eq 7.3). The green band shows the relationship between the fluxes assuming the LMA-MSW oscillation framework [40] (Eq 7.6). The vertical width of each band represents the 1σ uncertainty in the electron neutrino flux as calculated from the corresponding equation. The intersection points of the blue band with the others are listed in Table 7.1.

7.2 Standard Solar Model

In the high metallicity framework of the Standard Solar Model (SSM), the predicted total ^{7}Be neutrino flux at Earth is $\Phi(\text{SSM}) = (4.48 \pm 0.31) \times 10^9$ cm^{-2} sec^{-1} [17]. Given this constraint on the total flux, we can write the relationship between the electron neutrino flux and the flux of the other flavors as:

$$\Phi_{\nu_e} = -\Phi_{\nu_{\mu,\tau}} + \Phi(\text{SSM}) \tag{7.3}$$

The above equation is plotted in Figure 7.1 (red band), where the width of the band is solely determined by the 7% uncertainty in the SSM flux. One can see that given the precision of the current ^{7}Be neutrino rate measurement (5%), the SSM model uncertainty is larger than the experimental uncertainty. The large separation between the y-intercepts of the blue and red band indicates the significance at which the no-oscillation hypothesis is ruled out (5.1 σ).

The intersection of the blue and red bands give the best estimates for the fluxes of the different neutrino flavors, based on the SSM ^{7}Be neutrino flux. Combining Eqs. 7.2 and 7.3 we can calculate the electron neutrino survival probability as:

$$P_{ee}(\text{SSM}) \equiv \frac{\Phi_{\nu_e}}{\Phi(\text{SSM})} \tag{7.4}$$

$$= \frac{R - \Phi(\text{SSM})\sigma_{\nu_{\mu,\tau}}n}{\Phi(\text{SSM})(\sigma_{\nu_e} - \sigma_{\nu_{\mu,\tau}})n} \tag{7.5}$$

By randomly picking each of the parameters from a normal distribution around the central value and accounting for the uncertainties and correlations we obtain a value of $P_{ee}(\text{SSM}) = 0.507 \pm 0.068$.

7.3 LMA-MSW

Assuming the large mixing angle (LMA) solution for neutrino vacuum oscillations and the validity of the Mikheyev-Smirnov-Wolfenstein (MSW) description for oscillations in matter, one can calculate the electron neutrino survival probability using a density profile for the neutrino production region. Using the analytical approximation found in [40] (neglecting Earth matter effects), with the best estimates for the vacuum oscillation parameters prior to this measurement [1], we obtain a value of $P_{ee}(\text{LMA})$

$= 0.542 \pm 0.013$. We can then express the different neutrino fluxes as:

$$\Phi_{\nu_e} = \frac{P_{ee}(\text{LMA})}{1 - P_{ee}(\text{LMA})} \Phi_{\nu_{\mu,\tau}} \qquad (7.6)$$

The predicted ratio is overlaid on Figure 7.1 (green band) with the width determined by the errors on the neutrino vacuum oscillation parameters. We can combine Eqs. 7.2 and 7.6 to calculate the total ^{7}Be neutrino flux:

$$\Phi(\text{LMA}) \equiv \Phi_{\nu_e} + \Phi_{\nu_{\mu,\tau}} \qquad (7.7)$$

$$= \frac{R}{(P_{ee}(\text{LMA})\sigma_{\nu_e} + (1 - P_{ee}(\text{LMA}))\sigma_{\nu_{\mu,\tau}})n} \qquad (7.8)$$

By once again randomly picking each of the parameters from a normal distribution around the central value and accounting for the uncertainties and correlations we obtain a value for the total ^{7}Be neutrino flux of $\Phi(\text{LMA}) = (4.27 \pm 0.22) \times 10^9$ cm^{-2} sec^{-1}.

	0.862 MeV ^{7}Be Flux $[10^9$ cm^{-2} sec$^{-1}]$	$P_{ee}(0.862$ MeV$)$
SSM	4.48 ± 0.31	$\mathbf{0.507 \pm 0.068}$
LMA-MSW	$\mathbf{4.27 \pm 0.22}$	0.542 ± 0.013

Table 7.1: Final results for the ^{7}Be neutrino flux and electron neutrino survival probability at 0.862 MeV. The numbers in regular typeface are the predictions from the theory while the numbers in bold are the values obtained by combining the predictions with the measurement presented here. The first row uses the latest Standard Solar Model [17] while the second row values are determined the LMA-MSW neutrino oscillation framework [40].

Comparing the values of $\Phi(\text{SSM})$ and $\Phi(\text{LMA})$, as well as $P_{ee}(\text{SSM})$ and $P_{ee}(\text{LMA})$ in Table 7.1 we see that the two different input assumptions, combined with the ^{7}Be measurement presented here, agree at the 1σ level.

Finally we briefly remark on the solar metallicity controversy. The present result is shown along with the SSM predictions for both the high and low metallicity scenarios

in Figure 7.2 (along with the 8B measurements from SNO and Super-Kamiokande).
It can be seen that given the current theoretical and experimental uncertainties, the
predicted flux obtained from combining the present ^{7}Be result with the LMA-MSW
solution $[(4.27 \pm 0.22) \times 10^9 \text{ cm}^{-2} \text{ sec}^{-1}]$ cannot help distinguish between the low
$[(4.09 \pm 0.29) \times 10^9 \text{ cm}^{-2} \text{ sec}^{-1}]$ and high $[(4.48 \pm 0.31) \times 10^9 \text{ cm}^{-2} \text{ sec}^{-1}]$ metallicity
solutions.
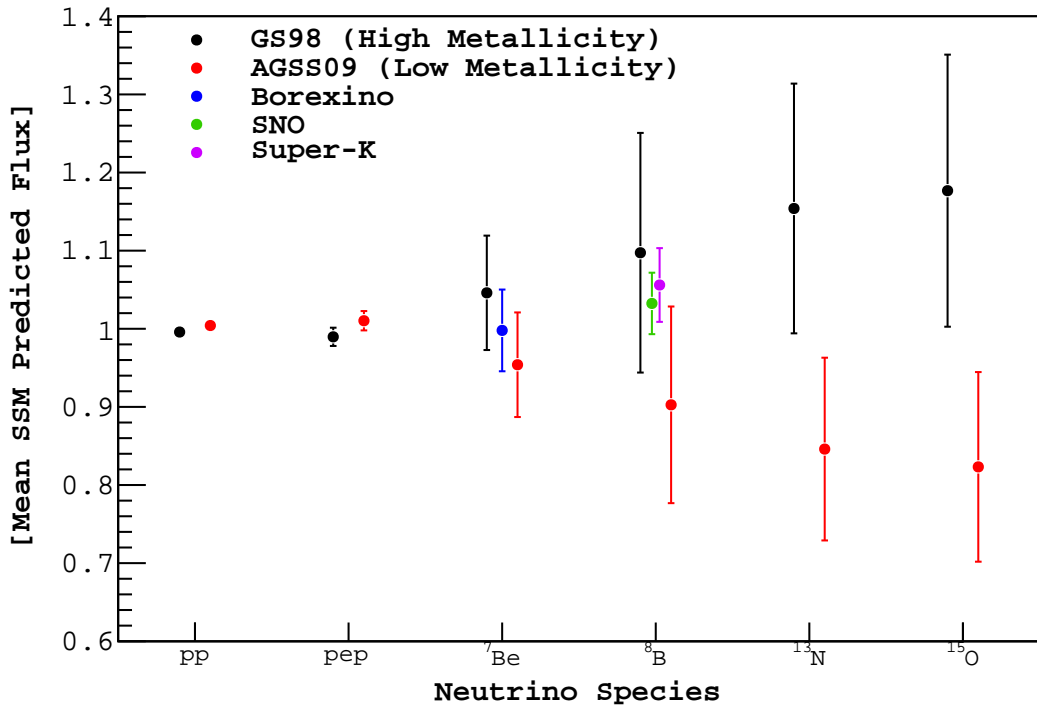

Figure 7.2: SSM predicted neutrino fluxes for the high (black) and low (red) metallicity
scenarios [17]. The present ^{7}Be measurement is shown along with the latest SNO [115] and
Super-Kamiokande ([116] using the P_{ee} value at 10 MeV from [115]) results. The values
have been scaled to the mean value of the high and low metallicity predictions for each
species.

7.4 Global Analysis of Electron Neutrino Survival Probability

In this section we will use the current ^{7}Be measurement, in conjunction with the results from other solar neutrino experiments to calculate the electron neutrino survival probability as a function of energy. We will adopt the formalism in [117] where the solar neutrino experimental results are analyzed independently of neutrino oscillation parameters. First we will use the combined results from various solar neutrino detectors to obtain the survival probability at high and intermediate energies. Next, using additional inputs from the latest Standard Solar Model [17], we calculate the survival probability at intermediate and low energies.

7.4.1 Formalism

Consider a generic detector that measures solar neutrinos in such a way that it can neither distinguish between different types of neutrinos (eg. pep, ^{7}Be, ^{8}B) nor between the different neutrino flavors. In such a detector the total measured rate of events will be given by:

$$R = \sum_i \Phi_i n \int S_i(E)[P_i(E)\sigma_{\nu_e}(E) + (1 - P_i(E))\sigma_{\nu_{\mu,\tau}}(E)]dE \qquad (7.9)$$

where the index $i = \{pp, {}^7\text{Be}, pep, {}^{13}\text{N}, {}^{15}\text{O}, {}^{17}\text{F}, {}^8\text{B}, hep\}$ runs over the different neutrino species, E is the incoming neutrino energy, $S_i(E)$ is the normalized neutrino energy spectrum, $P_i(E)$ is the energy-dependent electron neutrino survival probability and the detection cross sections $\sigma_{\nu_x}(E)$ include the detector sensitivity. For energy ranges in which the neutrino survival probability is relatively constant, we can approximate the above formula by adopting an average survival probability P_i such

that we have:

$$R = \sum_i \Phi_i n \left[P_i \int S_i(E) \sigma_{\nu_e}(E) dE + (1 - P_i) \int S_i(E) \sigma_{\nu_{\mu,\tau}}(E) dE \right] \tag{7.10}$$

$$= \sum_i \Phi_i n \left[P_i \langle \sigma_{\nu_e} \rangle_{S_i} + (1 - P_i) \langle \sigma_{\nu_{\mu,\tau}} \rangle_{S_i} \right] \tag{7.11}$$

where $\langle \sigma_{\nu_x} \rangle_{S_i}$ indicates the spectral-averaged neutrino detection cross section. Similarly we can define the expected rate from the SSM, assuming no oscillations ($P_i = 1$), as:

$$R(\text{SSM}) \equiv \sum_i \Phi_i(\text{SSM}) n \langle \sigma_{\nu_e} \rangle_{S_i} \tag{7.12}$$

We can then define the ratio of the measured to the predicted rates as:

$$R' \equiv \frac{R}{R(\text{SSM})} \tag{7.13}$$

$$= \sum_i \left[\epsilon_i \beta_i P_i + \eta_i \beta_i (1 - P_i) \right] \tag{7.14}$$

where β_i is the flux normalized to the SSM prediction, and ϵ_i and η_i are the fractional rates corresponding to the electron and other neutrino flavor interactions respectively:

$$\beta_i \equiv \frac{\Phi_i}{\Phi_i(\text{SSM})} \tag{7.15}$$

$$\epsilon_i \equiv \frac{\Phi_i(\text{SSM}) \langle \sigma_{\nu_e} \rangle_{S_i}}{\sum_i \Phi_i(\text{SSM}) \langle \sigma_{\nu_e} \rangle_{S_i}} \tag{7.16}$$

$$\eta_i \equiv \frac{\Phi_i(\text{SSM}) \langle \sigma_{\nu_{\mu,\tau}} \rangle_{S_i}}{\sum_i \Phi_i(\text{SSM}) \langle \sigma_{\nu_e} \rangle_{S_i}} \tag{7.17}$$

Note that with these definitions, the fractional rates for electron neutrinos are normalized: $\Sigma \epsilon_i = 1$.

7.4.2 Solar Neutrino Experiments

We are now in a position to discuss the results from the various solar neutrino detectors. The chlorine-based detector operated by Ray Davis in the Homestake mine detected neutrinos through the inverse beta decay reaction:

$$\nu_e + {}^{37}\text{Cl} \rightarrow e^- + {}^{37}\text{Ar} \qquad (7.18)$$

The reaction only takes place for electron neutrinos ($\eta_i = 0$) and has a energy threshold of 0.814 MeV, making it insensitive to the low energy pp neutrinos ($\epsilon_{pp} = 0$). No energy information is available and so neutrinos of different types cannot be distinguished. The measured rate is therefore the total interaction rate for all neutrinos. The expected fractional rates, given the latest Standard Solar Model [17], are given in Table 7.2 and the fractional product of the neutrino fluxes and the detection cross section (ϵ_i prior to the integration of the numerator) are shown in the top panel of Figure 7.3. As can be seen from the values in Table 7.2 and Figure 7.3, the measured rate is dominated by ${}^8\text{B}$ neutrinos, due to the large enhancement in the capture cross section at high energies. The total measured rate from the Homestake experiment is taken to be 2.56 ± 0.23 SNU[1] [118].

Like the Homestake experiment, the gallium based experiments (GALLEX, SAGE and GNO) also detect neutrinos through inverse beta decay ($\eta_i = 0$):

$$\nu_e + {}^{71}\text{Ga} \rightarrow e^- + {}^{71}\text{Ge} \qquad (7.19)$$

In this case the threshold energy (0.233 MeV) is low enough to also be sensitive to pp neutrinos, but as with the chlorine detector, individual neutrino types cannot be distinguished. The expected fractional rates, given the latest Standard Solar Model [17], are given in Table 7.2 and the fractional rate profiles of the neutrino interactions

---

[1]1 SNU (Solar Neutrino Unit) is defined as 10^{-36} neutrino captures per target atom per second.
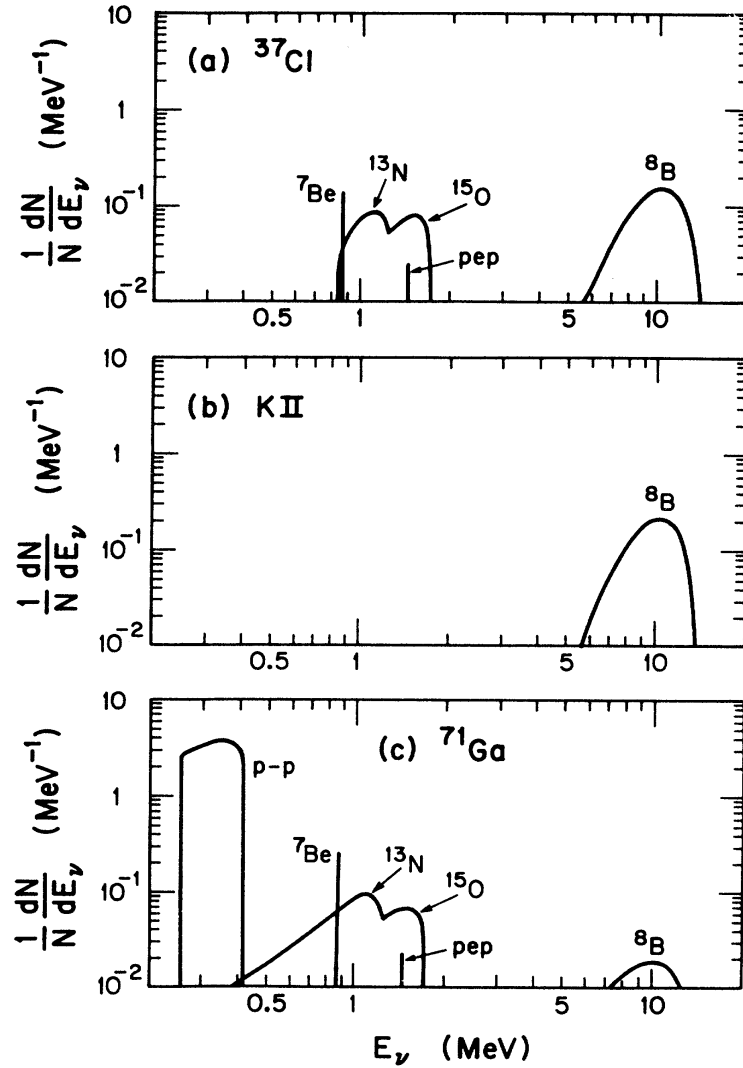
Figure 7.3: Product of neutrino fluxes and the detection cross section versus neutrino energy for different experiments, assuming the SSM predicted neutrino fluxes without oscillations. Top Panel: Homestake chlorine detector. Middle Panel: Kamiokande-II. Bottom Panel: Gallium based experiments. The continuum sources are given as fractional differential spectrum while the line sources are shown as fractions of the total rate. The Kamiokande-II distribution includes the effect of detection efficiencies and energy resolution. Plot taken from [119].

(ϵ_i prior to the integration of the numerator) are shown in the bottom panel of Figure 7.3. For the measured rate we have taken a weighted average of the SAGE [120] and GNO [121] results and the new reevaluation of the GALLEX measurement [122] to obtain a rate of 66.2 ± 3.0 SNU.

Super-Kamiokande is a water Cherenkov detector, that detects neutrinos through

Neutrino	SSM		Homestake		SAGE/GALLEX/GNO	
	Φ_i	δ_i	$\langle\sigma_{\nu_e}\rangle_{S_i}$	ϵ_i	$\langle\sigma_{\nu_e}\rangle_{S_i}$	ϵ_i
	[cm^{-2}sec^{-1}]	%	[10^{-46}cm^2]		[10^{-46}cm^2]	
pp	5.98×10^{10}	0.6	0.0	0.000	11.72	0.553
^{7}Be	5.00×10^9	7	$2.14^\dagger$	0.135	71.7	0.283
pep	1.44×10^8	1.2	16.0	0.029	204	0.023
^{13}N	2.96×10^8	14	1.67	0.006	60.4	0.014
^{15}O	2.23×10^8	15	6.80	0.019	113.7	0.020
^{17}F	5.52×10^6	17	6.86	< 0.001	113.9	< 0.001
^{8}B	5.58×10^6	14	1.14×10^4	0.806	2.40×10^4	0.106
hep	8.04×10^3	30	4.41×10^4	0.004	7.14×10^4	< 0.001

Table 7.2: Flux and rate information for different solar neutrino species. The second column lists the total flux, Φ_i, and fractional uncertainties, δ_i, for each of the neutrino species according to the latest SSM [17]. The third column lists the energy-averaged product of the detection cross section and neutrino spectra, $\langle\sigma_{\nu_e}\rangle_{S_i}$, as well as the rate fraction, ϵ_i, for the different species in the Homestake chlorine detector. The fourth column lists the corresponding numbers for the gallium based detectors SAGE, GALLEX and GNO. Values for the spectral-averaged detection cross sections are taken from [39,123]. †The 10.3%, 0.384 MeV, branch falls below the detection threshold.

the elastic scattering of electrons. Since the recoiling electrons are detected through the emission of Cherenkov light, the detection threshold is roughly 5 MeV, making it sensitive to only high energy neutrinos ($\epsilon_i = \eta_i = 0$ for $i \neq {}^8$B, hep). The interaction occurs with all flavors of neutrinos, but the cross section for electron neutrino scattering is roughly 6 times larger ($\eta_{8B} = 0.156 \cdot \epsilon_{8B} = 0.156$). We have used a weighted average of the results from the three phases of Super-Kamiokande [116] for a measured ^{8}B flux of: $\Phi_{8B} = (2.35 \pm 0.05) \times 10^6$ cm^{-2} sec^{-1} (assuming no oscillations).

The SNO experiment was also a water Cherenkov detector but it uses heavy water as the target. It was unique in that it could detect neutrinos through three different interactions:

$$\text{CC: } \nu_e + d \ \rightarrow p \ + p + e^- \tag{7.20}$$

$$\text{NC: } \nu_x + d \ \rightarrow n \ + p + \nu_x \tag{7.21}$$

$$\text{ES: } \nu_x + e^- \rightarrow e^- + \nu_e \tag{7.22}$$

The charged current (CC) reaction only occurs for electron neutrinos ($\eta_i = 0$), while the neutral current interaction (NC) is equally sensitive to all neutrino flavors ($\eta_i = \epsilon_i$). As in Super Kamiokande, the elastic scattering (ES) cross section is roughly 6 times larger for electron neutrinos, than for other flavors. The combination of the different channels allows for the direct measurement of the ^{8}B flux and survival probability. We have used the most recent result from the SNO collaboration [115] which combines the measurements from all three phases to give a flux of $\Phi_{8B} = (5.25 \pm 0.20) \times 10^6$ cm^{-2}sec^{-1} and a survival probability (at 10 MeV) of $P_{8B} = 0.32 \pm 0.02$.

Finally, we include the Borexino ^{7}Be measurement that is the topic of this thesis. We remind the reader that the charged current elastic scattering cross section is roughly 4.51 times larger than the neutral current cross section ($\eta_{7Be} = 0.222 \cdot \epsilon_{7Be}$) at the 0.862 MeV energy of ^{7}Be neutrinos. We will only consider the ^{7}Be rate measurement from Borexino as the measurement of the ^{8}B rate [77] is much less sensitive than that from Super-Kamiokande or SNO.

7.4.3   Data-Only Analysis

In order to make an analysis of the results of the different neutrino experiments, independent of the neutrino oscillation parameters, we will group together different neutrino types into three categories, depending on their average energy. *pp* neutrinos will be considered low energy, with flux Φ_L and survival probability P_L. ^{7}Be, *pep*, ^{15}O, ^{13}N and ^{17}F neutrinos are grouped together as intermediate energy neutrinos (Φ_I, P_I) and finally ^{8}B and *hep* neutrinos are together categorized as high energy (Φ_H, P_H). With this convention, the index i in Eq 7.14 now runs over the three energy regions: low, intermediate and high.

Comparing the detector sensitivities shown in Figure 7.3, we see that the energy profile of the ^{8}B rate is very similar in the chlorine, gallium and Kamiokande ex-

periments. This is due to a coincidence in which the detection efficiency for water Cherenkov detectors drops off at low energies in a similar way to the neutrino capture cross sections. This allows us to reasonably use a single (rate averaged) high energy survival probability P_H for all of the high energy neutrino detectors.

Also, due to the 0.814 MeV energy threshold energy for the neutrino capture on ^{37}Cl, the intermediate energy neutrinos measured by the Homestake experiment are restricted within the range of 0.8 - 1.8 MeV (see Figure 7.3). Given that 73% of the detected intermediate energy neutrinos at Homestake are predicted to be ^{7}Be neutrinos, and that the neutrino survival probability is expected to change by less than 7% (based on the LMA-MSW solution) over that energy range, the use of a single survival probability, P_I, for the Borexino and Homestake experiments is also reasonable. The lower threshold (0.233 MeV) in gallium means that the detectors are sensitive to CNO neutrino down to lower energies. However, due to the decreasing cross section with energy, the detection rate for CNO neutrinos is highest near the end points (see Figure 7.3).

Experiment	ϵ_L	ϵ_I	ϵ_H	η_L	η_I	η_H	R'
Homestake	-	0.190	0.810	-	-	-	0.32 ± 0.03
SAGE/GALLEX/GNO	0.553	0.341	0.106	-	-	-	0.52 ± 0.02
Super-Kamiokande	-	-	1.000	-	-	0.156	0.42 ± 0.01
SNO (Combined)							0.94 ± 0.04
Borexino	-	1.000	-	-	0.222	-	0.61 ± 0.03

Table 7.3: Rate fractions for different solar neutrino experiments. The values ϵ_i give the fractional rate of events in the low, intermediate and high energy regions for electron neutrinos, and η_i is the corresponding number for muon and tau neutrinos. The final column lists the measured rate relative to the unoscillated SSM predictions. See Eqs 7.14 and 7.15 for the definition of each of the parameters. Sources used for the measured rates of each of the experiments can be found in Section 7.4.2.

The fractional rates for each of the experiments in the energy regions defined above are summarized in Table 7.3, along with the ratio of the measured flux to the unoscillated Standard Solar Model predictions. Using these values, the system of

equations corresponding to Eq 7.14 is:

$$R'_{Cl} = 0.32 \pm 0.03 = 0.190\beta_I P_I + 0.810\beta_H P_H \qquad (7.23)$$

$$R'_{Ga} = 0.52 \pm 0.02 = 0.553\beta_L P_L + 0.341\beta_I P_I + 0.106\beta_H P_H \qquad (7.24)$$

$$R'_{SK} = 0.42 \pm 0.01 = 0.844\beta_H P_H + 0.156\beta_H \qquad (7.25)$$

$$R'_{SNO} = 0.94 \pm 0.04 = \beta_H \qquad (7.26)$$

$$P_{SNO} = 0.32 \pm 0.02 = P_H \qquad (7.27)$$

$$R'_{BX} = 0.61 \pm 0.03 = 0.778\beta_I P_I + 0.222\beta_I \qquad (7.28)$$

As can be seen, the SNO measurements directly give the relative rate ($\beta_H(SNO) = 0.94 \pm 0.04$) and survival probability ($P_H(SNO) = 0.32 \pm 0.02$) in the high energy region. Note that we can also obtain P_H by combining the Super-Kamiokande result with the SNO flux measurement: $P_H(SK, SNO) = 0.34 \pm 0.02$. Since the results are consistent, we will use the weighted average $P_H = 0.33 \pm 0.01$ for the remainder of this analysis. For the radiochemical experiments, the relevant term at high energies is the electron neutrino flux on Earth, relative to the SSM: $\beta_H P_H$. Combining the results from SNO, including correlations (see Table VIII of [115]), we get $\beta_H P_H(SNO) = 0.30 \pm 0.01$, while combining data from Super-Kamiokande and SNO we get $\beta_H P_H(SK, SNO) = 0.32 \pm 0.01$. Once again we will use the weighted average: $\beta_H P_H = 0.31 \pm 0.01$.

For the intermediate energy survival probability we can combine the value of $\beta_H P_H$ with the measurement from the chlorine detector to obtain $\beta_I P_I = 0.38 \pm 0.16$. Using the Borexino result presented here, we obtain the values $\beta_I = 1.43 \pm 0.57$ and $P_I = 0.27 \pm 0.21$. Note that the ^{7}Be survival probability predicted in the LMA-MSW framework is 0.542 ± 0.013 (see Section 7.3) and the survival probability obtained by combining the ^{7}Be measurement with the predicted SSM flux is 0.507 ± 0.068 (see Section 7.2). We point out that combining this latest ^{7}Be measurement with previous

results from other solar neutrino experiments, we have obtained a determination of the electron neutrino survival probability in the intermediate energy range (0.8 - 1.8 MeV) using only experimental results, albeit with large uncertainties.

Due to the lack of multiple measurements of the pp neutrinos, it is not possible to disentangle the Standard Solar model predictions from the survival probability at low energies. Combining the values for the gallium experiments with the Homestake and $\beta_H P_H$ measurements listed above, one obtains $\beta_L P_L = 0.65 \pm 0.11$.

7.4.4 Standard Solar Model Constraints

In this section we will estimate the electron neutrino survival probabilities using the Standard Solar Model predicted fluxes (see Table 7.2) as an additional constraint.

As mentioned earlier, due to the lack of available experimental data, the survival probability at low energies is currently completely undetermined from data alone. If we add, as input, the well determined SSM prediction for the pp neutrino flux ($\beta_L = 1.000 \pm 0.006$), then, using the values calculated in the previous section, we obtain a low energy survival probability of $P_L = 0.65 \pm 0.11$.

We have now calculated the survival probability in all three energy regions, using only the SSM pp neutrino flux as input. However, the uncertainty on the intermediate energy survival probability is large (78%). We can reduce this uncertainty by also including the SSM predicted flux at intermediate energies. Since the intermediate energy interactions are dominated by ^{7}Be in the Homestake and gallium experiments, we will use the SSM uncertainties for the ^{7}Be flux ($\beta_I = 1.00 \pm 0.07$). Excluding the results from Borexino, the Homestake experiment gives a value of $P_I = 0.38 \pm 0.16$ when combined with the $\beta_H P_H$ value and the SSM prediction. If the rate from this Borexino ^{7}Be measurement is included, we can combine it with the SSM prediction to get an intermediate survival probability of $P_I = 0.51 \pm 0.07$ (as calculated previously in Section 7.2). Note that the inclusion of Borexino has reduced the fractional

uncertainty from 42% to 13%.

We can also recalculate the low energy survival probability from the gallium experiments, using the SSM flux predictions at low and intermediate energies, the $\beta_H P_H$ value, and Borexino. The new value gives $P_L = 0.57 \pm 0.05$, reducing the uncertainty from 16% to 9%. Note that without Borexino, the additional input of the SSM predicted intermediate energy flux does not help constrain the low energy survival probability.

The SSM prediction for the high energy neutrino flux was not included since the uncertainty in the prediction (14%) is significantly larger than that of the direct measurement by SNO (4%).

The various predictions, with and without the SSM inputs and with and without Borexino are summarized in Table 7.4 and the results with the SSM constraints are depicted in Figure 7.4.

	Data Only			SSM Inputs		
	P_L	P_I	P_H	P_L	P_I	P_H
Before BX	-	-	0.33 ± 0.01	0.65 ± 0.11	0.38 ± 0.16	0.33 ± 0.01
After BX	-	0.27 ± 0.21	0.33 ± 0.01	0.57 ± 0.05	0.51 ± 0.07	0.33 ± 0.01

Table 7.4: Electron neutrino survival probabilities in the low, intermediate and high energy regions. The first column lists the values obtained independent of oscillation parameters or SSM flux predictions. The second column includes SSM fluxes for the low and intermediate energy regions. The first row lists the results excluding any inputs from Borexino, while the second row includes the measurement of the ^{7}Be rate described in this thesis. The values obtained with SSM inputs are shown in Figure 7.4.
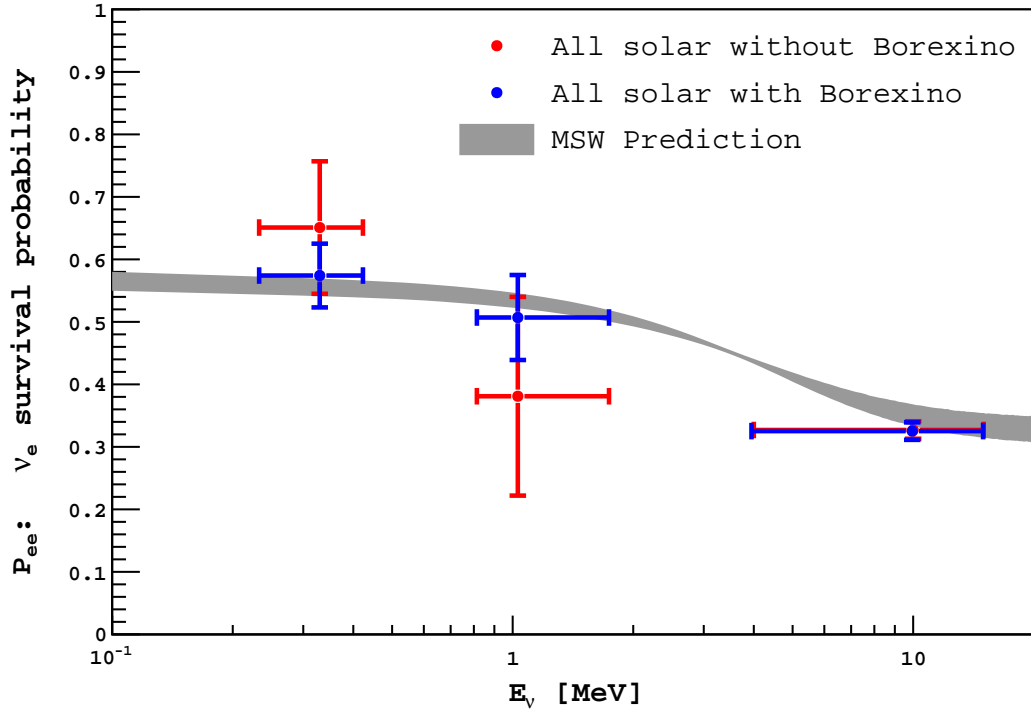
Figure 7.4: Electron neutrino survival probability as a function of energy. Data points are calculated using the formalism in [117] wherein the measurements from different solar neutrino experiments are combined, in conjunction with the SSM, to estimate the survival probability at low, intermediate and high energies, independent of models for neutrino oscillation parameters. The red points indicate the best estimates without including Borexino data, and the blue points include the measurement of the ^{7}Be rate described here. The value at high energy is unaffected by the recent Borexino measurement. The grey band represents the LMA-MSW 1σ prediction for the ^{8}B neutrino production region. Details of the inputs and the calculation can be found in Section 7.4, with the final values given in Table 7.4.

Appendices

Appendix A

List of Event Selection Cuts

1. Muons Cosmogenics and Post-Muon Noise

   if (muon_internal)

       tag and drop event

   if ($\Delta t_\mu < 300$ms)

       if (muon_internal and not muon_special_d1)

           restart 300ms window and drop event

       else

           drop event

2. Zero cluster events and Clustering consistency

   if (n_cl_echidna $= 0$ $\|$ n_cl_m4 $= 0$ $\|$ n_cl_echidna $\neq$ n_cl_m4)

       drop event

   (n_cl_echidna = laben.n_clusters, n_cl_m4 = GetNM4Events ())

3. Search for sequences of fast coincidences (2 ms) in 1.5 m radius

   if ($\Delta t < 2$ms && $\Delta s < 1.5$m)

       drop events

4. Keep only trigger type $= 1$

if ($\texttt{trg\_type} \neq 1 \parallel \texttt{btb\_inputs} \neq 0$)

    drop event

($\texttt{trg_type} = $ trigger.trgtype, $\texttt{btb_inputs} = $ trigger.btb_inputs)

5. Drop multi cluster events

if ($\texttt{n\_clusters\_echidna} \neq 1$)

    drop event

6. Start time of cluster

if !($\text{t}_{min} < \texttt{cluster\_time}$ - $\texttt{trigger\_time} < \text{t}_{max}$)

    drop event

with $\text{t}_{min} = $ -6100, -16100, -16240

and $\text{t}_{max} = $ -4800, -15300, -15700 for run $< 6562, < 12422, \geq 12422$

(cluster_time = laben.clusters.start_time, trigger_time = laben.trigger_time)

7. Drop crate noise

if ($\texttt{m4\_laben\_hitdist\_1\_crate\_frac} > 0.75$)

    drop event

8. FV cut

if ($\texttt{r\_lngs} > 3.021$)

    drop event

(r_lngs = laben.clusters.position_lngs.GetR ())

9. Z cut

if ($|\texttt{z\_lngs}| > 1.67$)

    drop event

(z_lngs = laben.clusters.position_lngs.z)

10. Geometrical uniformity

if $\left(\texttt{beta\_recon} > 0.02657 + e^{(-1.306 - 0.01728\,\texttt{charge\_m4})} + e^{(-3.199 - 0.001738\,\texttt{charge\_m4})} \right)$

drop event

(beta_recon = m4s.laben__hitdist__chargebeta__recon_1,

   charge_m4 = m4s.laben__cluster__npe_corrected)

11. Spherical Harmonics

if $\left(\texttt{sh\_power\_1} > 0.1192215 + e^{(12.3571 - 0.3.4926\,\texttt{n\_npmts})} + e^{(-0.611803 - 0.0114214\,\texttt{n\_npmts})}\right)$

   drop event

(n_npmts = normalized_npmts)

12. N Peaks

if $(\texttt{n\_peaks} > 1)$

   drop event

13. Q/Qrec

if $!\left(0.6 < \frac{\texttt{charge}}{\texttt{qrec}} < 1.6\right)$

   drop event

(charge = laben.NormalizeCharge (laben.clusters.charge_short))

  qrec $\equiv$ -2000 ln (1 - $\frac{\texttt{npmt\_short}}{2000}$) $\times$ (1 + 0.11 ln (1 - $\frac{\texttt{npmt\_short}}{2000}$))

  npmt_short = laben.NormalizePmts (laben.clusters.npmts_short))

14. M4 strange events

if $\left(\frac{\texttt{charge\_noavg\_m4}}{\texttt{charge\_m4}} < 0.5 \frac{\texttt{good\_charge\_channels\_m4}}{\texttt{n\_live\_pmts\_m4}}\right)$

   drop event

(charge_noavg_m4 = m4s.laben__cluster__npe_noavg_corrected,

  good_charge_channels_m4 = m4s.good_charge_chans,

  n_live_pmts_m4 = m4s.live_pmts)

Appendix B

Muon Tagging Definition

Definitions of muon cut variables:

muon_internal: muon_internal_strict or muon_internal_special

muon_internal_strict: need n_clusters > 0

  if `trigger_type` $= 1$

   require muon_mtb or muon_mcr or muon_idf

  if `trigger_type` $= 2$

   require `nhits_short` > 80

muon_mtb: require `btb_inputs` $\&$ 4

muon_mcr: if `is_muon_alligned`

  require `muon_has_cluster`

muon_idf: need $n\_clusters > 0$

    if $nhits\_short\_norm > 2100$

      require $mean\_time\_short > 100$ and $gatti < 0.55$

    else if $nhits\_short\_norm \geq 900$

      require $peak\_time > 30$

    else if $nhits\_short\_norm > 80$

      require not is_buffer and $peak\_time > 40$

is_buffer: need $n\_clusters > 0$

    require $nhits\_short\_norm < 200$ and $z\_lngs > 4$ and $gatti < 0.2$

muon_internal_special: muon_internal_special_d1 $\parallel \ldots \parallel$ muon_internal_special_d5

muon_internal_special_d1: need $trigger\_type \leq 2$

    if $n\_raw\_hits > 200$ $trigger\_type$

      require $n\_decoded\_hits < 0.05$ n_raw_hits

muon_internal_special_d2: need $trigger\_type \leq 2$

    if $n\_decoded\_hits > 100$

      require btb_inputs & $0xFB$

muon_internal_special_d3: need $trigger\_type = 1$ and $cluster\_id = 0$

    require $0 < start\_time + gate\_start < 1700$

    $(gate\_start = 6000$ for run < 6562

      $= 16500$ for $6562 \leq$ run < 14366

      $= 15400$ for run $> 14366)$

muon_internal_special_d4: need $trigger\_type \leq 2$ and $n\_clusters > 0$

    require $mean\_time\_short > 200$

muon_internal_special_d5: need $trigger\_type = 1$ and $n\_clusters = 0$

    require muon_mtb or muon_mcr

Bibliography

[1] K. Nakamura et al. Review of particle physics. *J. Phys.*, G37:075021, 2010.

[2] J. Dunkley, R. Hlozek, J. Sievers, V. Acquaviva, P.A.R. Ade, et al. The Atacama Cosmology Telescope: Cosmological Parameters from the 2008 Power Spectra. *Astrophys.J.*, 739:52, 2011.

[3] Samoil Bilenky. *Introduction to the Physics of Massive and Mixed Neutrinos*. Number 817 in Lecture Notes in Physics. Springer, 2010.

[4] E. Komatsu et al. Seven-Year Wilkinson Microwave Anisotropy Probe (WMAP) Observations: Cosmological Interpretation. *Astrophys.J.Suppl.*, 192:18, 2011.

[5] J. Angrik et al. *KATRIN design report 2004*. Wissenschaftliche Berichte. Forschungszentrum Karlsruhe, 2005.

[6] John N. Bahcall. *Neutrino Astrophysics*. Cambridge University Press, 1989.

[7] C.F. von Weizsacker. Uber Elementumwandlungen im Innern der Sterne II. *Physikalische Zeitschrift*, 39:633–646, 1938.

[8] H. A. Bethe. Energy Production in Stars. *Phys. Rev.*, 55:434–456, Mar 1939.

[9] E. G. Adelberger, A. Garcia, R. G. Hamish Robertson, et al. Solar fusion cross sections. II. The pp chain and CNO cycles. *Rev. Mod. Phys.*, 83:195–245, Apr 2011.

[10] Ko Abe. The XMASS Experiment. *AIP Conference Proceedings*, 1182(1):268–271, 2009.

[11] D.N. McKinsey and K.J. Coakley. Neutrino detection with CLEAN. *Astroparticle Physics*, 22(5-6):355 – 368, 2005.

[12] Mark C Chen. SNO and SNO+. *AIP Conference Proceedings*, 944(1):25–30, 2007.

[13] Michael Wurm, Franz von Feilitzsch, Marianne Goeger-Neff, Tobias Lachenmaier, Timo Lewke, Quirin Meindl, Randolph Moellenberg, Lothar Oberauer, Juha Peltoniemi, Walter Potzel, Marc Tippmann, and Juergen Winter. The Physics Potential of the LENA Detector. *arXiv:1004.3474v1 [physics.ins-det]*, April 2010.

[14] Christian Grieb and R.S. Raghavan. Probing the temperature profile of energy production in the sun. *Phys.Rev.Lett.*, 98:141102, 2007.

[15] L. C. Stonehill, J. A. Formaggio, and R. G. H. Robertson. Solar neutrinos from CNO electron capture. *Phys. Rev. C*, 69:015801, Jan 2004.

[16] John N. Bahcall. The luminosity constraint on solar neutrino fluxes. *Phys. Rev. C*, 65:025801, Jan 2002.

[17] Aldo M. Serenelli, Wick C. Haxton, and Carlos Pena-Garay. Solar models with accretion. I. Application to the solar abundance problem. *arXiv:1104.1639v1 [astro-ph.SR]*, April 2011.

[18] C. Giunti and C.W. Kim. *Fundamentals of Neutrino Physics and Astrophysics*. Oxford University Press, 2007.

[19] Eric G. Adelberger, Sam M. Austin, John N. Bahcall, A.B. Balantekin, Gilles Bogaert, et al. Solar fusion cross-sections. *Rev.Mod.Phys.*, 70:1265–1292, 1998.

[20] Aldo Serenelli. Solar neutrinos and the sun. *arXiv:1109.2602v1 [astro-ph.SR]*, 09 2011.

[21] B. Pontecorvo. Inverse beta processes and nonconservation of lepton charge. *Sov. Phys. JETP*, 7:172–173, 1958.

[22] B. Pontecorvo. Neutrino experiments and the question of leptonic-charge conservation. *Sov. Phys. JETP*, 26:984–988, 1968.

[23] Samoil M. Bilenky and B. Pontecorvo. Lepton Mixing and Neutrino Oscillations. *Phys. Rept.*, 41:225–261, 1978.

[24] Andrew G. Cohen, Sheldon L. Glashow, and Zoltan Ligeti. Disentangling Neutrino Oscillations. *Phys. Lett.*, B678:191–196, 2009.

[25] E. Kh. Akhmedov and A. Yu. Smirnov. Neutrino oscillations: Entanglement, energy-momentum conservation and QFT. *arXiv:1008.2077v3 [hep-ph]*, October 2010.

[26] Evgeny Kh. Akhmedov and Alexei Yu. Smirnov. Paradoxes of neutrino oscillations. *Phys. Atom. Nucl.*, 72:1363–1381, 2009.

[27] C. Giunti. Energy and momentum of oscillating neutrinos. *Mod. Phys. Lett.*, A16:2363, 2001.

[28] Harry J. Lipkin. Quantum theory of neutrino oscillations for pedestrians: Simple answers to confusing questions. *Phys. Lett.*, B642:366–371, 2006.

[29] Alessandro Strumia and Francesco Vissani. Neutrino masses and mixings and... *arXiv:hep-ph/0606054v3*, April 2010.

[30] L. Wolfenstein. Neutrino oscillations in matter. *Phys. Rev. D*, 17:2369–2374, May 1978.

[31] S. P. Mikheyev and A. Y. Smirnov. Resonance enhancement of oscillations in matter and solar neutrino spectroscopy. *Yadernaya Fizika*, 42:1441–1448, 1985.

[32] Felix Boehm and Petr Vogel. *Physics of Massive Neutrinos.* Cambridge University Press, 1987.

[33] Rabindra N. Mohapatra and Palash B. Pal. *Massive Neutrinos in Physics and Astrophysics.* World Scientific Publishing, Third edition, 2004.

[34] S. T. Petcov and S. Toshev. Three neutrino oscillations in matter: Analytical results in the adiabatic approximation. *Phys. Lett.*, B187:120, 1987.

[35] S. T. Petcov. An analytic description of three neutrino oscillations in matter with varying density. *Phys. Lett.*, B214:259, 1988.

[36] J. N. Bahcall and P. I. Krastev. Does the sun appear brighter at night in neutrinos? *Phys. Rev. C*, 56:2839–2857, Nov 1997.

[37] J. N. Bahcall, C. M. Gonzalez-Garcia, and C. Pena-Garay. Before and After: How has the SNO NC measurement changed things? *Journal of High Energy Physics*, 7:54, July 2002.

[38] M. B. Smy, Y. Ashie, S. Fukuda, et al. Precise measurement of the solar neutrino day-night and seasonal variation in Super-Kamiokande-I. *Phys. Rev. D*, 69:011104, Jan 2004.

[39] John Bahcall. John Bahcall Website. http://www.sns.ias.edu/~jnb/SNdata/sndata.html.

[40] P. C. de Holanda, Wei Liao, and A. Yu. Smirnov. Toward precision measurements in solar neutrinos. *Nucl. Phys.*, B702:307–332, 2004.

[41] Alexander Friedland, Cecilia Lunardini, and Carlos Pena-Garay. Solar neutrinos as probes of neutrino-matter interactions. *Physics Letters B*, 594(3-4):347 – 354, 2004.

[42] A. Palazzo and J. W. F. Valle. Confusing nonzero θ_{13} with nonstandard interactions in the solar neutrino sector. *Phys. Rev. D*, 80:091301, Nov 2009.

[43] Kevin B. McCarty. *The Borexino Nylon Film and the Third Counting Test Facility.* PhD thesis, Princeton University, June 2006.

[44] G. Bellini et al. Muon and Cosmogenic Neutron Detection in Borexino. *JINST*, 6:P05005, 2011.

[45] G. Alimonti et al. The Borexino detector at the Laboratori Nazionali del Gran Sasso. *Nucl. Instrum. Meth.*, A600:568–593, 2009.

[46] G. Ranucci. Private Communication.

[47] L. Oberauer, C. Grieb, F.von Feilitzsch, and I. Manno. Light concentrators for Borexino and CTF. *Nuclear Instruments and Methods in Physics Research Section A: Accelerators, Spectrometers, Detectors and Associated Equipment*, 530(3):453 – 462, 2004.

[48] J. Benziger et al. The nylon scintillator containment vessels for the Borexino solar neutrino experiment. *Nucl. Instrum. Meth.*, A582:509–534, 2007.

[49] J.B. Birks. *The Theory and Practice of Scintillation Counting*, volume 27 of *International Series of Monographs on Electronics and Instrumentation*. Pergamon Press, 1964.

[50] Michael Clinton Johnson. *Scintillator Purification and Study of Light Propagation in a Large Liquid Scintillation Detector*. PhD thesis, Princeton University, June 1998.

[51] G Alimonti, C Arpesella, M Balata, et al. Light propagation in a large volume liquid scintillator. *Nuclear Instruments and Methods in Physics Research Section A: Accelerators, Spectrometers, Detectors and Associated Equipment*, 440(2):360 – 371, 2000.

[52] National Institute of Standards and Technology. *TRC Tables-Hydrocarbons*. U.S. Dept. of Commerce, Technology Administration, 2000.

[53] Andrea Pocar. *Low Background Techniques and Experimental Challenges for Borexino and its Nylon Vessels*. PhD thesis, Princeton University, November 2003.

[54] Aldo Ianni. Personal Communication.

[55] M. Chen, F. Elisei, F. Masetti, U. Mazzucato, C. Salvo, and G. Testera. Quenching of undesired fluorescence in a liquid scintillator particle detector. *Nuclear Instruments and Methods in Physics Research Section A: Accelerators, Spectrometers, Detectors and Associated Equipment*, 420(1-2):189 – 201, 1999.

[56] B. Caccianiga, Y. Koshio, and S. Manecki. Estimation of the FV systematic error (Internal Borexino Report). https://borex.lngs.infn.it/Doc/memos/memos.shtml, 2011.

[57] V Lagomarsino and G Testera. A gateless charge integrator for borexino energy measurement. *Nuclear Instruments and Methods in Physics Research Section A: Accelerators, Spectrometers, Detectors and Associated Equipment*, 430(2-3):435 – 446, 1999.

[58] Steve Hardy. *Measuring the ^7Be Neutrino Flux From the Sun: Calibration of the Borexino Solar Neutrino Detector*. PhD thesis, Virginia Polytechnic Institute and State University, March 2010.

316

[59] Szymon Manecki. Vessel analysis: Volumes and leak rates (Internal Borexino Report). https://borex.lngs.infn.it/Doc/general_meetings/2010-03/szymon.manecki_Vessel_Volume_GM_Gran_Sasso_2010.pptx, March 2010.

[60] Szymon Manecki. Personal Communication, September 2011.

[61] Chiaro Ghiano, Aldo Ianni, Alessandro Razeto, and Igor Machulin. Detection feasibility of Charge Current interactions on ^{13}C in massive high purity Liquid Scintillator neutrino detectors (Internal Borexino Report). http://borex.lngs.infn.it/Doc/general_meetings/2011-03/carbon13.pdf, March 2011.

[62] John N. Bahcall, Marc Kamionkowski, and Alberto Sirlin. Solar neutrinos: Radiative corrections in neutrino - electron scattering experiments. *Phys. Rev.*, D51:6146–6158, 1995.

[63] Alex Wright. The Uncertainty in the Neutrino-Electron Elastic Scattering Cross Section (Internal Borexino Report), 2011.

[64] Evalyn Gates, Lawrence M. Krauss, and Martin J. White. Treating solar model uncertainties: A consistent statistical analysis of solar neutrino models and data. *Phys. Rev.*, D51:2631–2643, 1995.

[65] Ludmila Wilhelmová, Milan Tomášek, and Karel Stukheil. The measurement of low concentrations of Kr-85 in atmospheric air samples. *Biological Trace Element Research*, 43(1):725–730, 1994.

[66] M. Hirota, K. Nemoto, A. Wada, and Y. Igarashi. Spatial and Temporal Variations of Atmospheric ^{85}Kr Observed During 1995-2001 in Japan: Estimation of Atmospheric ^{85}Kr Inventory in the Northern Hemisphere. *Journal of Radiation Research (Tokyo)*, 45:405–413, 2004.

[67] S. Hardy and S. Zavatarelli. The ^{85}Kr contamination through the delayed coincidence analysis (Internal Borexino Report). http://borex.lngs.infn.it/Doc/ general_meetings/2010-06/zavatarelli_hardy_krypton.pdf, June 2010.

[68] C. Arpesella et al. First real time detection of ^{7}Be solar neutrinos by Borexino. *Phys. Lett.*, B658:101–108, 2008.

[69] Cristiano Galbiati et al. Cosmogenic C-11 production and sensitivity of organic scintillator detectors to pep and CNO neutrinos. *Phys. Rev.*, C71:055805, 2005.

[70] T. Hagner et al. Muon induced production of radioactive isotopes in scintillation detectors. *Astropart. Phys.*, 14:33–47, 2000.

[71] S. Abe et al. Production of Radioactive Isotopes through Cosmic Muon Spallation in KamLAND. *Phys. Rev.*, C81:025807, 2010.

[72] Richard Saldanha. Reduction of ^{11}C background in Borexino (Pre-Thesis Project). Princeton University, 2009.

[73] S. Zavatarelli. Updated report on the backgrounds before/after the Water Extraction (WE) purification campaigns (Internal Borexino Report), January 2011.

[74] J. Benziger et al. A Scintillator Purification System for the Borexino Solar Neutrino Detector. *Nucl. Instrum. Meth.*, A587:277–291, 2008.

[75] G. Zuzel, H. Simgen, and G. Heusser. Ar and Kr concentrations in nitrogen as a measure of the 39Ar and 85Kr activities in connection with the solar neutrino experiment. *Applied Radiation and Isotopes*, 61(2-3):197 – 201, 2004. Low Level Radionuclide Measurement Techniques - ICRM.

[76] M. Ambrosio et al. Measurement of the residual energy of muons in the Gran Sasso underground laboratories. *Astropart. Phys.*, 19:313–328, 2003.

[77] G. Bellini et al. Measurement of the solar 8B neutrino rate with a liquid scintillator target and 3 MeV energy threshold in the Borexino detector. *Phys. Rev.*, D82:033006, 2010.

[78] G. Bellini et al. Observation of Geo-Neutrinos. *Phys. Lett.*, B687:299–304, 2010.

[79] C. Arpesella et al. Measurements of extremely low radioactivity levels in BOREXINO. *Astropart. Phys.*, 18:1–25, 2002.

[80] M.J. Berger, J.H. Hubbell, S.M. Seltzer, J. Chang, J.S. Coursey, R. Sukumar, D.S. Zucker, and K. Olsen. XCOM: Photon Cross Section Database (version 1.5). URL: http://physics.nist.gov/xcom, June 2011.

[81] M. Buizza Avanzini. [8]B neutrino measurement above 2 MeV through an unbinned and multivariate maximum likelihood fit (Internal Borexino Report). https://borex.lngs.infn.it/Doc/general_meetings/2011-07/MBA_June2011_8B.pdf, July 2011.

[82] pep Working Group. Measurement of the pep and CNO neutrino interaction rates in Borexino (Internal Borexino Report), 2011.

[83] Rene Brun and Fons Rademakers. ROOT – An object oriented data analysis framework. *Nuclear Instruments and Methods in Physics Research Section A: Accelerators, Spectrometers, Detectors and Associated Equipment*, 389(1-2):81 – 86, 1997. New Computing Techniques in Physics Research V.

[84] B. Caccianiga et al. A multiplexed optical-fiber system for the PMT calibration of the Borexino experiment. *Nucl. Instrum. Meth.*, A496:353–361, 2003.

[85] N. Balakrishnan and C. R. Rao. *Handbook of Statistics*, volume 16, 17. Elsevier Science B.V., 1998.

[86] G. Bellini et al. Precision Measurement of the ^{7}Be Solar Neutrino Interaction Rate in Borexino. *Physical Review Letters*, 107(14), 2011.

[87] S. Bonetti, B. Caccianiga, P. Lombardi, and G. Ranucci. Results of the Milano position reconstruction code using an effective index of refraction n = 1.7 (Internal Borexino Report). https://borex.lngs.infn.it/Doc/memos/memos.shtml, February 2008.

[88] Henning Back. *Internal Radioactive Source Calibration of the Borexino Solar Neutrino Experiment.* PhD thesis, Virginia Polytechnic Institute and State University, September 2004.

[89] E. Gatti and F. de Martini. A New Linear Method of Discrimination between Elementary Particles in Scintillation Counters. *Nuclear Electronics*, 2:265–276, 1962.

[90] Daniel Bick. *Setup of a Drift Tube Muon Tracker and Calibration of Muon Tracking in Borexino.* PhD thesis, University of Hamburg, 2011.

[91] G. F. Knoll. *Radiation Detection and Measurement*, page 114. John Wiley and Sons, 3rd edition, 2000.

[92] Oleg Smirnov. Energy reconstruction and energy resolution in Borexino: Addendum No.1 to Echidna report 08 March 2008 (Internal Borexino Report).

[93] J. B. Birks. Scintillations from Organic Crystals: Specific Fluorescence and Relative Response to Different Radiations. *Proceedings of the Physical Society A*, 64:874–877, October 1951.

[94] M.J. Berger, J.S. Coursey, M.A. Zucker, and J Chang. ESTAR, PSTAR and ASTAR: Computer Programs for Calculating Stopping-Power and Range

Tables for Electrons, Protons, and Helium Ions (version 1.2.3). URL: http://physics.nist.gov/Star, June 2011.

[95] Hai Du, Ru-Chun Amy Fuh, Junzhong Li, L. Andrew Corkan, and Jonathan S. Lindsey. PhotochemCAD: A Computer-Aided Design and Research Tool in Photochemistry. *Photochemistry and Photobiology*, 68(2):141–142, 1998.

[96] A. Chavarria. Borexino's events above 3 MeV and first detection of solar ^{8}B ν-e scattering in an organic liquid scintillator target (Pre-Thesis Project). Princeton University, December 2009.

[97] J. M. Los Arcos and F. Ortiz. kB: a code to determine the ionization quenching function Q(E) as a function of the kB parameter. *Computer Physics Communications*, 103:83–94, June 1997.

[98] Mach4 and LNGS. ^{7}Be Analysis Internal Borexino Report, June 2011.

[99] F. Ortiz, J. M. Los Arcos, A. Grau, and L. Rodríguez. Monte Carlo simulation of the spectral response of beta-particle emitters in LSC systems. *Nuclear Instruments and Methods in Physics Research Section A: Accelerators, Spectrometers, Detectors and Associated Equipment*, 312(1-2):109 – 113, 1992.

[100] H. O. Back et al. Pulse-shape discrimination with the Counting Test Facility. *Nucl. Instrum. Meth.*, A584:98–113, 2008.

[101] JPL. Jet Propulsion Laboratory Horizons On-Line Ephemeris System (Version 3.36). http://ssd.jpl.nasa.gov/horizons.cgi.

[102] Szymon Manecki and Richard Saldanha. Post-Muon Noise (Internal Mach4 Report). https://argus.princeton.edu/groups/borex/wiki/6b930/Jun_18_2010, https://argus.princeton.edu/groups/borex/wiki/8fb16/July_08_2010.html, June 2010.

[103] Lawrence D. Brown, T. Tony Cai, and Anirban DasGupta. Interval Estimation for a Binomial Proportion. *Statistical Science*, 16(2):pp. 101–117, 2001.

[104] M. Pallavicini, A. Caminata, S. Davini, and L. Ludhova. Trigger Efficiency Study (Internal Borexino Report). http://borex.lngs.infn.it/Doc/general_meetings/2011-03, March 2011.

[105] D. Franco, G. Consolati, and D. Trezzi. Positronium signature in organic liquid scintillators for neutrino experiments. *Phys. Rev.*, C83:015504, 2011.

[106] Helmut Paul. Shapes of beta spectra. *Nuclear Data Sheets. Section A*, 2(3):281 – 298, 1966.

[107] V. V. Kuzminov and N. Ja. Osetrova. Precise Measurement of 14C Beta Spectrum by Using a Wall-less Proportional Counter. *Physics of Atomic Nuclei*, 63(7):1292–1296, 2000.

[108] W. H. Kelly, G. B. Beard, and R. A. Peters. The beta decay of K40. *Nuclear Physics*, 11:492 – 498, 1959.

[109] S.Y.F. Chu, L.P. Ekstrom, and R.B. Firestone. Database WWW Table of Radioactive Isotopes. http://nucleardata.nuclear.lu.se/nucleardata/toi, February 1999.

[110] Jack P. Davidson. The First Forbidden Shape Factor and the $f_n t$ Products for Beta-Decay. *Phys. Rev.*, 82:48–51, 1951.

[111] A. Grau Carles. Beta shapefactor determinations by the cutoff energy yield method. *Nuclear Instruments and Methods in Physics Research Section A: Accelerators, Spectrometers, Detectors and Associated Equipment*, 551(2-3):312 – 322, 2005.

[112] G. D'Agostini. Asymmetric Uncertainties: Sources, Treatment and Potential Dangers. *arXiv:physics/0403086*, 2004.

[113] Geant4 Collaboration. Geant4. http://geant4.web.cern.ch/geant4.

[114] C. Arpesella, H. O. Back, M. Balata, et al. Direct Measurement of the ^{7}Be Solar Neutrino Flux with 192 Days of Borexino Data. *Phys. Rev. Lett.*, 101:091302, Aug 2008.

[115] SNO Collaboration. Combined Analysis of all Three Phases of Solar Neutrino Data from the Sudbury Neutrino Observatory. *arXiv:1109.0763v1 [nucl-ex]*, 09 2011.

[116] K. Abe et al. Solar neutrino results in Super-Kamiokande-III. *Phys.Rev.*, D83:052010, 2011.

[117] V. Barger, D. Marfatia, and K. Whisnant. Testing the LMA solution with solar neutrinos independently of solar models. *Phys. Lett.*, B617:78–86, 2005.

[118] B. T. Cleveland et al. Measurement of the solar electron neutrino flux with the Homestake chlorine detector. *Astrophys. J.*, 496:505–526, 1998.

[119] V. Barger, R. J. N. Phillips, and K. Whisnant. Reexamination of neutrino oscillation solutions to the solar-neutrino problem. *Phys. Rev. D*, 43:1110–1128, Feb 1991.

[120] J. Abdurashitov. Measurement of the solar neutrino capture rate with gallium metal. III. Results for the 2002–2007 data-taking period. *Physical Review C*, 80(1), 2009.

[121] M. Altmann et al. Complete results for five years of GNO solar neutrino observations. *Phys. Lett.*, B616:174–190, 2005.

[122] F. Kaether, W. Hampel, G. Heusser, J. Kiko, and T. Kirsten. Reanalysis of the GALLEX solar neutrino flux and source experiments. *Phys. Lett.*, B685:47–54, 2010.

[123] John N. Bahcall. Gallium solar neutrino experiments: Absorption cross-sections, neutrino spectra, and predicted event rates. *Phys.Rev.*, C56:3391–3409, 1997.